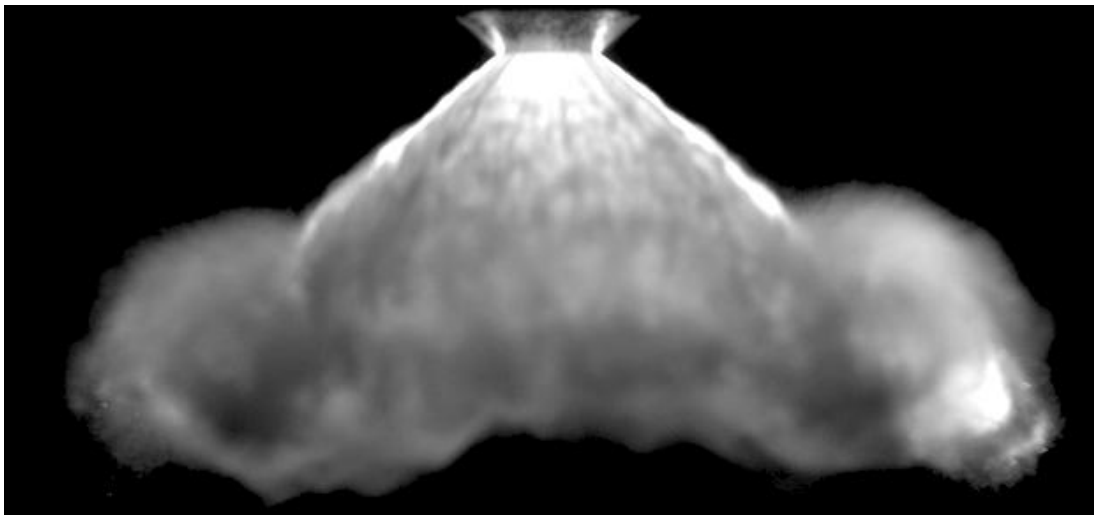
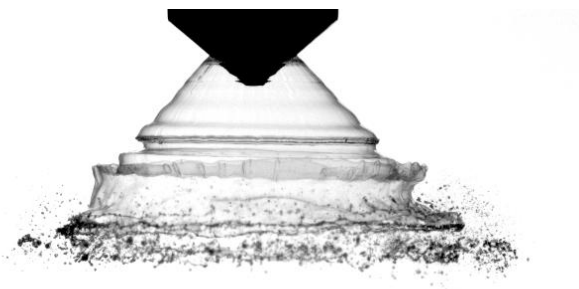


DISS. ETH NO. 20852

**Experimental characterization of the two phase flow of a  
modern, piezo activated hollow cone injector**



Andreas Schmid  
2012



DISS. ETH NO. 20852

**Experimental characterization of the two phase flow of a  
modern, piezo activated hollow cone injector**

A dissertation submitted to the  
ETH ZURICH  
for the degree of  
Doctor of Sciences

presented by  
ANDREAS MANUEL SCHMID  
Dipl. Masch.-Ing. ETH Zürich  
born April 21<sup>st</sup>, 1979  
citizen of Ausserberg and Raron, VS, Switzerland

accepted on the recommendation of  
Prof. Dr. Konstantinos Boulouchos, ETH Zürich, examiner  
Prof. Dr. Ulrich Spicher, Universität Karlsruhe, GER, co-examiner  
Dr. Graham Wigley, Loughborough University, UK, co-examiner

2012



*Mine Eltru gwidmut,  
sowiä dum Öscheni, Polini, Gerli und Henriki.*



# Preface

The present work was carried out at the Laboratory of Aerothermochemistry and Combustion Systems (LAV) at the Swiss Federal Institute of Technology (ETH) Zurich, Switzerland and in the framework of a transnational, industrial project with BMW Forschung und Technik GmbH, Germany.

My very special thanks go to Prof. Dr. Konstantinos Boulouchos, head of LAV, for his tremendous support in every possible way, innumerable fruitful and inspiring exchanges and for providing a well equipped and most enjoyable working environment.

I also want to thank Prof. Dr. Ulrich Spicher for the instructional time during the NoNO<sub>x</sub> Project, for the interest in my work and for being one of my co-referents. In Loughborough, UK, (Hirnsdorf, Austria by now) I thank especially Dr. Graham Wigley for the salutary hours in his lab, followed by fruitful discussions about PDA, sprays and spray simulations, and for being one of my co referents.

My sincerest thanks also go to Dr. Christian Lämmle for countless highly appreciated and most instructive discussions and the support as well as an experienced lead through the project. Special thanks also go to Dr. Bruno Schneider for an outstanding support in the solution of technical, optical, software and spray related problems. Special thanks also go to Dr. Yuri Wright for lots of academic and IT advises, climbing experiences and discussions.

The NoNO<sub>x</sub> project (in which framework the present work has been carried out) was lead and guided by Walter Hübner and Dr. Udo Gerke from BMW. Many thanks for the possibility to participate in such an interesting and extraordinary project. RWTH Aachen, University of Duisburgh-Essen, University of Karlsruhe and ETH Zürich have been working together for 3 years with the

result of a new and promising approach to CAI combustion. This time during the NoNOx project was a very intense and instructional experience with a lot of demanding meetings and sometimes demanding discussion with a last *Absacker*, or two, to all participants my thanks.

Dr. Kai Herrmann for tons of good advises, for the great help in the organisation and the sharing of experimental equipment and for my first job.

Within the LAV, there are so many people I would like to thank for a great time the list would be too long. Let me therefore thank you in general for the litres of coffee, kilos of cake, hours of good conversations, films, sports, beers in dark, smoky bars, fast moments on different racetracks in Europe and Switzerland, bike trails in the cold, wet dark...

On the private side I would like to thank my girlfriend Sabrina, for enduring me and for supporting me throughout the most intense phases of this thesis. Dr. Thomas Eggel and his family for their warm welcomes, hot *Flämmli*s, even hotter discussions and for believing in me and my academic way. To Dr. Christian Hutter, Dr. Cédric Hutter, Dr. Karol Prikopsky, Dipl. Masch.-Ing. Simon Segat and Dipl. Masch.-Ing. Matthias Siegrist my sincerest thank for a great time at ETH (and aside), it would have been worthless without you.

Furthermore, I would like to thank all my friends, cousins and colleagues for the inspiring and forward directing, most pleasurable moments ‘out of the office’ and for being there.

Last but not least, I thank my sister Sandra and my parents Pauli and Mario who supported my studies and to whom I dedicate this work.



*Dissertation: Hochtrainieren der Frustrationsgrenze*

# Abstract

Focus of this study is the experimental investigation of liquid fuel sprays at Otto engine relevant conditions. In a state-of-the-art constant volume chamber, the high pressure high temperature cell (HTDZ) at ETH Zürich, laser optic methods have been applied to investigate the spray of an A-injector (outwardly opening, pintle-type, hollow cone injector) in particular the influence that gas density, injection pressure, needle lift and fuel properties have on the spray under evaporating and non-evaporating conditions. At University of Loughborough LDA and PDA (Laser and Phase-Doppler Anemometry) data for atmospheric conditions were obtained to provide detailed information on droplet velocity and diameter. The fuel exiting an A-injector has a distinctive string-like structure. These strings are not steady in the beginning of the injection (as they wander around) but stabilize after very short time. The A-injector produces toroidal vortices in the air surrounding the spray which carry very small droplets (non-evaporating conditions). These vortices can be strong enough to influence the spray in subsequent phases. Along the nominal propagation direction of the liquid phase, different zones with increasing droplet size form. Gas density shows strong influence on spray morphology and spray propagation. Injection pressure has negligible influence on spray shape but a much stronger one on spray tip penetration, size of circumferential vortices and droplet size. The spray shows also strong dependency on needle lift; the spray becomes thicker towards higher needle lift while break up length are bigger. The experimental results indicate that correlations from established literature on multihole injectors describe the physics of an A-injector only partially. For example the influence of needle lift on spray breakup is overestimated while the gas density is not taken into account. Therefore a new correlation for A-injectors is presented in this work.

# Zusammenfassung

In der vorgelegten Arbeit wurden experimentelle Untersuchungen zur Ausbreitung des eingespritzten Brennstoffs einer Hohlkegeldüse für die Benzindirekteinspritzung unter motornahen Bedingungen durchgeführt. In einer modernen Konstantvolumenkammer, der Hochtemperatur- Hochdruckzelle (HTDZ) der ETH Zürich, wurde mittels laseroptischer Verfahren das Gemischbild einer A-Düse (nach aussen öffnende, piezo-gesteuerte Hohlkegeldüse) unter verdampfenden und nicht verdampfenden Bedingungen untersucht. An der Universität Loughborough wurden mittels Laser und Phasen-Doppler Anemometrie Tropfengeschwindigkeit und -durchmesser unter atmosphärischen Bedingungen bestimmt. Das Spraybild hat eine strähnige Struktur die charakteristisch ist für die A-Düse. Die Position dieser Strähnen ist anfangs zeitlich variabel. Während des Beginns der Einspritzung wandern sie in tangentialer und radialer Richtung, stabilisieren sich jedoch nach kurzer Zeit. An den Flanken des Hohlkegels bildet sich ein toroidaler Wirbel in der Luft. Dieser transportiert sehr kleine Tropfen (nichtverdampfende Bedingungen). Entlang der Strahlachse bilden sich mit zunehmender Distanz Zonen mit steigender Tropfengrösse. Die Gasdichte hat einen starken Einfluss auf das Spraybild und die Strahlausbreitung. Der Einspritzdruck beeinflusst die Geschwindigkeit der Strahlausbreitung und damit Tropfen- sowie Wirbelgrösse. Grösserer Nadelhub macht den Spray dichter und vergrössert die Aufbruchlänge des Sprays. Es zeigte sich, dass bekannte Korrelationen für Mehrlochdüsen die physikalischen Vorgänge einer A-Düse nur teilweise beschreiben. Die Einflüsse auf Eindringtiefe der Strahlspitze sowie auf den Strahlaufbruch werden nur ungenügend wiedergegeben. Aus diesen Gründen wurde neu eine Korrelation für die A-Düse erarbeitet, die aus Messwerten genommen wurde. Die Voraussagen über die Eindringtiefe der flüssigen Phase stimmen sehr gut mit den Messungen überein.



---

# Contents

<b>1</b>	<b>INTRODUCTION.....</b>	<b>1</b>
<b>2</b>	<b>FUNDAMENTALS .....</b>	<b>6</b>
<b>2.1</b>	<b>Direct Injection in Otto engines.....</b>	<b>6</b>
2.1.1	History of the Otto engine and the Direct Injection.....	6
2.1.2	Direct Injection with homogenous charge.....	7
2.1.3	Direct Injection with stratified charge.....	8
<b>2.2</b>	<b>State of the art .....</b>	<b>12</b>
2.2.1	Physics of the atomisation .....	12
2.2.2	Internal nozzle flow .....	13
2.2.3	Primary breakup.....	16
2.2.4	Secondary breakup.....	24
2.2.5	Internal nozzle flow and primary breakup in an A-injector .....	29
2.2.6	Atomisation with the A-injector .....	33
<b>3</b>	<b>MEASUREMENT INSTRUMENTATION.....</b>	<b>37</b>
<b>3.1</b>	<b>Phase Doppler Anemometry .....</b>	<b>41</b>
3.1.1	Light scattering on spherical particles.....	42
3.1.2	LDA Measurement Principles .....	44
3.1.3	Determination of the particle velocity.....	45
3.1.4	Determination of the particle size .....	46
3.1.5	Determination of Measurement volume size.....	47
3.1.6	Selection of scattering angle.....	48
3.1.7	Selection of the velocity measurement range .....	50
3.1.8	Selection of the size measurement range .....	51
3.1.9	PDA layout on the experiment .....	51
3.1.10	Limitations and inaccuracies of the PDA technique.....	52
3.1.11	Data evaluation .....	56
3.1.12	Software.....	56
<b>3.2</b>	<b>2D light section technique/Mie scattering .....</b>	<b>57</b>
<b>3.3</b>	<b>Shadowgraphy.....</b>	<b>57</b>
<b>4</b>	<b>EXPERIMENTAL SETUP.....</b>	<b>62</b>
<b>4.1</b>	<b>High Temperature High Pressure Cell (HTDZ) .....</b>	<b>62</b>
<b>4.2</b>	<b>Optical setup in the cell.....</b>	<b>65</b>
<b>4.3</b>	<b>PDA setup.....</b>	<b>70</b>
<b>4.4</b>	<b>Fuel path.....</b>	<b>72</b>

<b>5</b>	<b>RESULTS AND DISCUSSION .....</b>	<b>74</b>
<b>5.1</b>	<b>Reference case .....</b>	<b>77</b>
5.1.1	Reproducibility of the Spray structure .....	77
5.1.2	Spray shape of an A-injector .....	79
5.1.3	Streak Behaviour.....	82
5.1.4	Spray Penetration of the reference case .....	84
5.1.5	Influence of injection duration on vortex development .....	87
5.1.6	Droplet size and velocity distribution .....	88
5.1.7	Measurement grid .....	89
5.1.8	External observation of a streak by means of sample number .....	90
5.1.9	Development of the streaks inner structure.....	91
5.1.10	Cone and Spray Angles .....	94
5.1.11	Inside a streak .....	96
5.1.12	Droplet size distribution along a streak.....	98
5.1.13	Vapour phase .....	101
5.1.14	Evaporation and Vapour Phase.....	103
<b>5.2</b>	<b>Influence of gas density .....</b>	<b>107</b>
5.2.1	Influence of gas density on spray morphology.....	107
5.2.2	Influence of air density on spray tip penetration .....	109
5.2.3	Influence of air density on evaporation rate .....	110
<b>5.3</b>	<b>Influence of injection pressure.....</b>	<b>111</b>
5.3.1	Influence of injection pressure on spray morphology.....	111
5.3.2	Influence of injection pressure on spray tip penetration .....	114
5.3.3	Influence of injection pressure on droplet size distribution .....	115
5.3.4	Influence of injection pressure on evaporation rate.....	116
<b>5.4</b>	<b>Influence of needle lift.....</b>	<b>117</b>
5.4.1	Influence of needle lift on spray morphology .....	117
5.4.2	Influence of the needle lift on spray tip penetration .....	120
5.4.3	Influence of a variation of the needle lift on droplet sizes .....	121
5.4.4	Influence of needle lift on evaporation rate.....	122
<b>5.5</b>	<b>Influence of fuel properties .....</b>	<b>124</b>
5.5.1	Influence of fuel properties on spray penetration .....	126
5.5.2	Influence of fuel properties on droplet sizes .....	126
5.5.3	Influence of fuel properties on evaporation.....	127
<b>5.6</b>	<b>Comparison with literature .....</b>	<b>128</b>
5.6.1	New correlation for spray penetration.....	129
<b>6</b>	<b>CONCLUSIONS AND OUTLOOK .....</b>	<b>137</b>
	<b>NOMENCLATURE .....</b>	<b>142</b>
	<b>Abbreviations.....</b>	<b>142</b>

**Symbols.....143**

**REFERENCES..... 146**

**7 APPENDIX..... 156**

**7.1 Fuel properties .....156**

**7.2 Injection rates and needle lifts .....156**

**7.3 Distortion of Shadowgraphy images.....159**

**7.4 PDA settings .....160**

**7.5 List of publications.....165**

**7.6 Curriculum vitae.....166**





# 1 Introduction

*May you live in interesting times*

*-Unknown source*

This ancient Chinese curse describes very well the past decades in automotive engineering. Since the introduction of the Clean Air Act in 1971 [1], engine manufacturers have been forced to further reduce the emissions of their engines (vehicles, resp.) almost every 5 years. Since July 1<sup>st</sup> 1992 Euro-standards have been introduced to the European Union and Switzerland.

		CO [g/km]	HC [g/km]	HC+NO <sub>x</sub> [g/km]	NO <sub>x</sub> [g/km]	PM [g/km]
<b>Diesel engine</b>						
<b>Euro 1</b>	01.07.1992	2.72	-	0.97	-	0.14
<b>Euro 2, IDI</b>	01.01.1996	1	-	0.7	-	0.08
<b>Euro 2, DI</b>	01.01.1996 a)	1	-	0.9	-	0.1
<b>Euro 3</b>	01.01.2000	0.64	-	0.56	0.5	0.05
<b>Euro 4</b>	01.01.2005	0.5	-	0.3	0.25	0.025
<b>Euro 5</b>	01.09.2009	0.5	-	0.23	0.18	0.005
<b>Euro 6</b>	01.09.2014	0.5	-	0.17	0.07	0.005
<b>Otto engine</b>						
<b>Euro 1</b>	01.07.1992	2.72	-	0.97	-	-
<b>Euro 2</b>	01.01.1996	2.2	-	0.5	-	-
<b>Euro 3</b>	01.01.2000	2.3	0.2	-	0.15	-
<b>Euro 4</b>	01.01.2005	1	0.1	-	0.08	-
<b>Euro 5</b>	01.09.2009	1	0.1	-	0.07	0.005 b)
<b>Euro 6</b>	01.09.2014	1	0.1	-	0.07	0.005 b)

**Table 1 – Exhaust gas regulations of the European Union [2]**

Table 1 shows the definition of the Euro standards and its corresponding allowed emission amounts. Today Euro 5 is necessary to bring a car onto the European market. Since 1971 the allowed mass of hydrocarbons being emitted by an Otto engine went from 1 g/km down to 0.1 g/km. This is a reduction by

one order of magnitude. The emissions of carbon monoxide were reduced from 18 g/km down to 1 g/km. A look at a single car model, a Volkswagen Golf GTI, shows the development in engine technology (Figure 1-1). In the last 30 years the curb weight was increased by 65 % (the car became bigger, more comfortable and provides much higher safety) and the power of the car was increased by 89 %. In the same time the consumption of the car was reduced by 7.5 %, while fulfilling all clean air regulations.

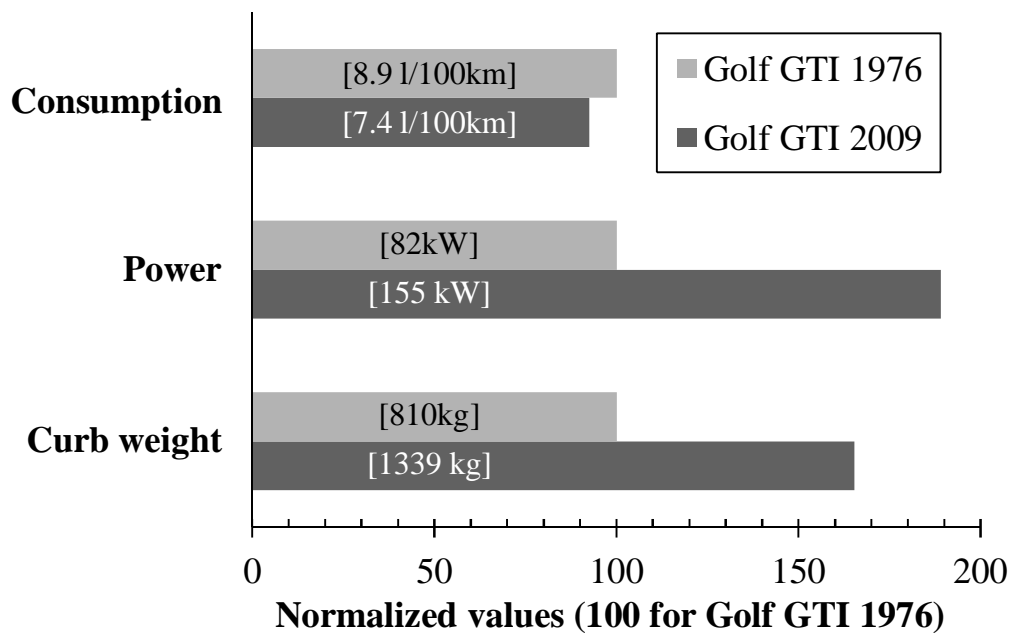


**Figure 1-1 – Development in power output, weight and fuel consumption on the basis of the VW Golf GTI [3]**

As their contribution to the Kyoto protocol [4], the European Automobile Manufacturers' Association (ACEA) made a voluntary commitment to reduce the  $CO_2$  emissions of an ACEA member fleet by 25 % down to 140 g/km by the year 2008. The Commission of the European Union now asked for 120 g/km by 2012. To achieve such goals while maintaining the Euro 5 and Euro 6 standards, different approaches are being investigated. For Otto engines there are three major directions in which industrial and academic research scientists are looking for additional reductions in fuel consumption.

A homogenous ( $\lambda = 1$ ) concept with an electric engine in a hybrid concept offers a low cost engine combined with a simple and well known exhaust treatment system (3 way catalyst). This offers the possibility to fulfil clean air regulations

and with a fuel saving hybrid concept an increase of the vehicles total efficiency. The reduction of the fuel consumption is depending on the application and the implementation of the hybrid concept. An intelligent control system is necessary to make use of the advantages offered by the combination of internal combustion (IC) and electrical engines. Different grades of hybridisation offer different advantages and disadvantages.

A downsized, turbocharged engine combined with direct injection, spark ignition (DISI) and variable valve train applied as a  $\lambda = 1$  - concept with a simple exhaust treatment system promises an alternative, less complex solution to hybrid systems. Mild hybridisation and intelligent measures (like start stop automatic) can help to achieve the goals of an increased efficiency of the entire propulsion system.

A rather radical approach has been adopted by several car manufacturers in the development of a complete new combustion mode: The main idea for this concept has come from the Diesel engines, where the homogenous charge compression ignition (HCCI) concept has been investigated for the past 25 years [5]. The corresponding concept for the Otto engine is called controlled auto ignition (CAI [6]). The idea is to achieve a homogenous ignition of the premixed gasoline air mixture. Instead of a flame front propagating through the cylinder like in a SI-engine, combustion proceeds in the form of a volume reaction all over the combustion chamber. Due to lean mixtures CAI promises less unburned hydro-carbons (UHC) close to the cylinder walls, which increases efficiency and reduces emissions. The minimization of regions with rich mixtures reduces particulate matter (PM) and  $\text{NO}_x$  emissions. The sensitivity of the ignition on various factors like changes in fuel quality, influence of neighbour cylinders due to pressure variations in the inlet and exhaust manifold, temperature variations and others make it necessary to know the cylinder pressure as well as temperature. These factors and the limited applicable range shown in Figure 1-2 have prohibited a production application of the technique until today. A promising option to better control CAI is the fuel direct injection (DI). Being such an influencing factor, the DI also offers possibilities to enlarge the applicable range of the CAI concept. Due to an adjustable cooling effect of the evaporating fuel the temperature of the cylinder mass can be adjusted.

Additionally the fuel can be injected in order to form either a homogenous or a stratified manner.

Overall, the fuel injection system must be highly flexible, combined with a high reproducibility and reliability. For the project in which frame the present work has been carried out (NoNO<sub>x</sub>-Project, [7]), a piezo-activated, outwardly opening hollow cone injector has been applied to inject the fuel directly into the cylinder. This type of injector offers several advantages such as a good atomisation, a fast response time (i.e. fast opening/closing for multiple injections), as well as variable needle lift and therefore a variable hydraulic diameter that offers the possibility to inject very small amounts of fuel, combined with a very high reproducibility. New combustion methods increasingly demand the injection of small amounts as this is state of the art in Diesel applications (e.g. pilot injections against Diesel “knocking” or post injection to heat the exhaust treatment system). Therefore the focus for this work has been set on the investigation of small injections (5 mg) to understand the influence on spray characteristics and spray quality.

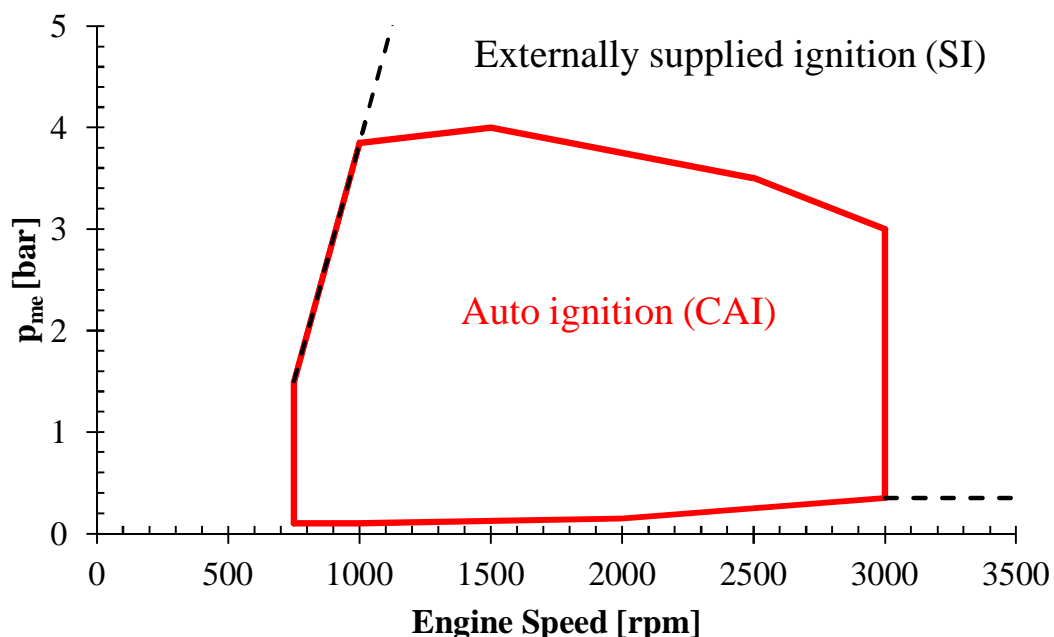


**Figure 1-2 – Application range for CAI [19]**

To optimise the injection process and to increase combustion efficiency, the factors influencing the behaviour of the liquid and the vapour phase have to be understood. Works in the past have shown that the hollow cone injectors form a rather complex spray [8], [9], [10], [11] or [12]. Annular vortices have a major

influence on the spray further downstream. The vortices themselves are strongly influenced by the liquid phase and its interaction with the surrounding air. The nature of these effects and their influence on the spray is only partially understood.

Therefore the goal of this work is the experimental investigation of selected effects (e.g. needle lift, rail pressure, gas density and temperature) on the spatial evolution of the spray and qualitatively on the formation and development of the injection driven flow-field and evaporation in a quiescent environment. This has been done by studying the spray on a macroscopic level under engine like conditions in the HTDZ, the high temperature high pressure cell of the ETH Zürich, as well as on a microscopic level under atmospheric conditions at Loughborough University, UK.

The present work is divided into three sections:

### **State of the art (Chapter 2)**

This chapter is an introduction into the basics of sprays, in Direct Injection Engines and today's knowledge about automotive sprays. This covers the spray mechanics as well as the empiric correlations usually employed for the calculation of the spatial spray distribution.

### **Experiment and measurement instrumentation (Chapter 3 & 4)**

In this part a short overview on available measurement techniques is given and an introduction to the applied methods is made (i.e. Mie scattering, Shadowgraphy and Phase Doppler Anemometry). A brief introduction to the constant volume chamber (HTDZ) is given and the optical setup of the experiment is explained.

### **Results and Discussion (Chapter 5 & 6)**

The results produced in the experiments are shown and compared to literature data. A correlation for the estimation of spray tip penetration is presented, the spray shape under different conditions is discussed, droplet velocity and diameter are shown and a method for the estimation of the vapour phase is introduced. Afterwards the results of the experimental investigations are analyzed and discussed.

## 2 Fundamentals

*There is nothing so practical as a good theory*

- Jack Welsh

### 2.1 Direct Injection in Otto engines

#### 2.1.1 History of the Otto engine and the Direct Injection

The first description of a 4 stroke piston engine found is from 1862 by *Beau de Rochas* [13]. In 1867 *Nikolaus August Otto* applied for the first patent of an atmospheric gas engine, which he realised a couple of years later in 1876 in the “Gasmotoren-Fabrik Deutz” in Deutz, Germany and patented it 1877 [14]. 1877 Otto also patented the idea of bringing in the fuel directly into the cylinder [13]. 1886 *Gottlieb Daimler*, *Carl Benz* and *Wilhelm Maybach* developed the first gasoline engines and used them in the first known automotive application. These engines were still supplied with gasoline out of a constant level- or float type carburettor. 1898 the first experiments with gasoline direct injection have been carried out using the *Haselwander*- method [15]. The first practical application of an Otto engine with gasoline direct injection (direct injected spark ignited, DISI) was by *Junkers* in 1914 [13]. The first engines serially equipped with gasoline direct injection were the *Junkers Fo.2*-engines for the speedboats of the German Navy in 1917. In 1934 *Daimler-Benz* began with the development for the *DB 600*-engine. In cooperation with *l’Orange* and later with *Bosch*, the first multihole injectors have been developed. The superior performance of a DISI engine was shown 1939 when the absolute velocity record was established first by *Hans Dieterle* (746.6 km/h) on a *Heinkel He 100* and later by *Fritz Wendel* (755.1 km/h) on a *Messerschmitt Me 209*, both equipped with a *DB 601* direct injection engine. In 1954 *Daimler-Benz* brought the *300 SL* sports car with a DISI in serial-production. After several successful applications in race cars [16],

[17], research in direct injection was almost completely abandoned during the 1960 and 70s. This was mainly due to the low fuel prices and the development of the cheaper intake-manifold injection. Related to stratified charge combustion the DISI method found its way back to the automotive application in 1995. First Japanese (Mitsubishi, Toyota) and later European and North-American car manufacturers (VW, Audi, GM, a. o.) introduced their 4 stroke Otto engines with gasoline direct injection. In the beginning especially stratified mixture has been applied but due to the limited benefits in fuel economy in practical operation, the cost-intensive exhaust gas treatment ( $NO_x$ -catalyst) as a result of the lean operation and the higher Particular Matter (PM) emission, the stratified application could not be established. Instead almost all manufacturers employ nowadays engines with a homogeneous and stoichiometric ( $\lambda = 1$ ) charge, the advanced ones being equipped with direct injection systems.

### **2.1.2 Direct Injection with homogenous charge**

Bringing in the fuel directly into the cylinder offers new possibilities to influence temperature, volumetric efficiency and pressure in the cylinder even prior to combustion. Major advantage of fuel direct injection is the cooling effect due to evaporation in the cylinder which helps to reduce knocking. The cooling effect in the cylinder during the air intake and the lower volume of the liquid fuel compared to the evaporated fuel increases the volumetric efficiency. Additionally a big drawback which comes along with the injection into the intake manifold can be neutralized as the cooling of the gas upstream of the inlet valve results in an unfavourable pressure drop over the inlet valve [18]. The option of cooling the charge during the compression offers the possibility to increase the compression ratio, which increases the efficiency. Alternatively, the compression ratio can be kept almost constant while the engine is supercharged to produce more power. This allows reducing the engine size while maintaining the power output (downsizing) [19]. Furthermore the direct injection allows the better evaporation of the fuel due to the hot cylinder walls. In addition no wall film dynamics due to spray impingement on the wall – as is the case for injection in the intake manifold – is present, which reduces UHC emissions and helps to increase efficiency, while assuring  $\lambda=1$  operation within tight limits for every cylinder and every cycle.

### 2.1.3 Direct Injection with stratified charge

One major drawback of the Otto engine compared to the Diesel principle is the difference in the control of the load. A Diesel engine is quality controlled, i.e. there is no throttling of the intake air at part load. If more power is demanded, this is achieved by injecting more fuel, resulting in a lower overall air-to-fuel ratio ( $\lambda$ );  $\lambda \geq 2.8$  in part load down to  $\lambda \approx 1.1$  for full load. Otto engines on the other hand are quantity-controlled, due to the limited flammability range of the premixed charge. To achieve a stable combustion  $\lambda$  needs to remain within the flammability range of the used fuel, e.g. for gasoline between  $\lambda \geq 0.6$  up to  $\lambda \leq 1.6$  (roughly, this is also depending on other factors such as ignition energy and cylinder temperature for example).

The ideal stratified mode offers a way to control the load of an Otto engine qualitatively with the global lambda. The engine runs at a high global lambda  $\lambda \geq 1.6$ , where a stable combustion cannot be achieved in homogenous mode. But instead of filling the whole cylinder with a homogenous air - gas mixture, the fuel is brought in locally, close to the spark plug. Building a dense cloud of fuel gas around the spark plug, with a local lambda within the flammability range of the given fuel, a DISI engine operated in stratified mode works like a Diesel engine (quality controlled). This results in better efficiency, as the engine can be dethrottled and therefore the volumetric efficiency can be increased. The air around the fuel cloud acts like an insulating layer thus the wall heat losses can be reduced [19]. Furthermore this layer separates the unburned cloud from the walls and crevice volumes, thereby preventing the flame from reaching the quenching distance and therefore from being extinguished by the walls. This increases the efficiency of the engine even more and reduces the amount of unburned hydrocarbons (UHC).

Depending on how the mixture transport to the spark plug is realised, the stratified methods are divided into *wall guided*, *air guided* and *spray guided* stratified direct injection (Figure 2-1). Often the practical applications can't be related clearly to one method, as the stratification is realised by a combination of mechanisms [20], [21], [19], [22].





**Figure 2-1 – Principle stratification applications: a) wall guided, b) air guided, c) spray guided [24]**

### 2.1.3.1 Wall guided

Most of the direct injection engines of the first, modern generation (after 1990) are designed based on the wall guided principle. For this method a special piston shape leads the partly liquid, partly gaseous fuel cloud towards the spark plug (Figure 2-1 a). The injector is usually positioned below the intake valves to give the spray more time to evaporate. Hereby larger zones of processed (atomised, evaporated and with air mixed fuel), ignitable fuel reach the spark plug what makes the method more robust against cycle to cycle variations. Because of the strong interaction between the fuel and the piston it can occur that in disadvantageous situations liquid fuel remains on the piston until the exhaust valves open. This increases the amount of UHC in the exhaust gases. Therefore the spray evaporation is often enhanced by combining the wall guided method with the air guided one, by using a tumble or swirl flow in the cylinder [19], [22]. Due to the special piston shape, the method can be optimised for a limited range in engine speed only.

### 2.1.3.2 Air guided

For air guided methods the fuel transport to the spark plug is mainly accomplished by the air flow generated in the inlet manifold and the inlet valves. A special shaped piston surface supports the air flow (Figure 2-1 b). Due to the strong interaction between the air flow and the spray, fuel evaporation is significantly enhanced and the wetting of the piston can be prevented. The air guided, stratified direct injection employs a tumble and/or a swirl flow. Depending on how the inlet channels are controlled, the vortex in the cylinder

rotates either around an axis coaxial to the cylinder axis (swirl) or parallel to the piston surface (tumble) [22]. The drawback of the air guided methods is the dependency of the in cylinder air flow on engine speed. This can partially be avoided by a sophisticated intake manifold which allows turning the swirl or tumbling on and off (Figure 2-2). Another disadvantage of the air guided principle is the tumble or swirl flow itself as the corresponding flow patterns decrease the volumetric efficiency of the engine which leads to penalties in power density and fuel efficiency [19].

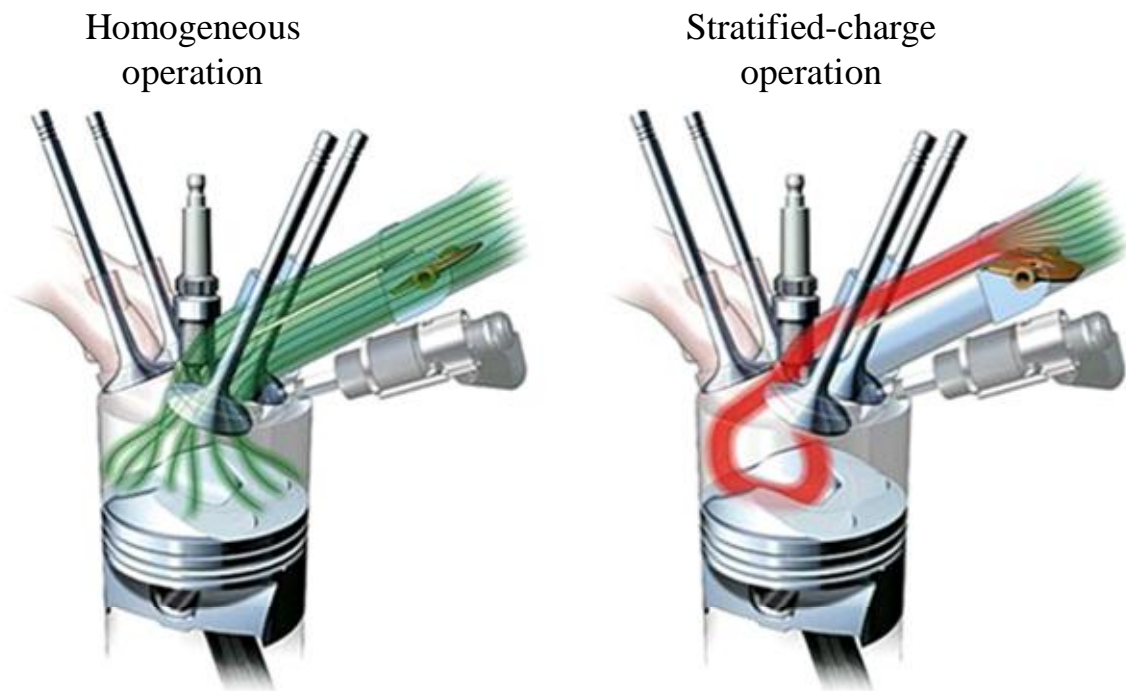


**Figure 2-2 – Switch to change between Homogenous and stratified operation [23]**

### 2.1.3.3 Spray guided

Expert opinion suggests that the spray guided method is the only principle which can tap the full potential of the stratified charge combustion [25], [26], [27], [28]. As it has much smaller deficits such as wall and/or piston wetting, expensive piston shapes or control mechanisms in the inlet channels to influence the in-cylinder flow pattern, the spray guided method promises least efficiency losses with the highest potential for a cost effective serial application of direct injection. Therefore the spray guided direct injection methods are called “direct injection of the second generation” even though research has been going on for the last 30 years for which an exhausting overview is documented in [29]. The

idea is to ensure a confined cloud of fuel close to the spark plug without the use of complex flow conditions in the cylinder and the therefore necessary complex piston surface design. This can be achieved by means of a strong interaction between the fuel and the air, which is usually applied by higher injection pressures. What has been known in the development of Diesel engines for years, and found its best application in the Common Rail Injection System [30], emerged as important for gasoline applications, as well; the higher the injection pressure, the better the atomisation process becomes. Especially for the stratified case the increase in injection pressure offers a promising potential [31] (though there are inherent limitations such as the lubrication of the high pressure pump or viscosity issues which still prevent series application for very high pressure above 100 MPa with gasoline type fuels). Today two injector types are used for the spray guided stratification: Multihole injectors (e.g. Figure 2-3, left side) are cost efficient devices offering a wide range of possibilities to design the spray shape [33]. The injector is small, simple and provides a reproducible spray morphology.



**Figure 2-3 – GDI Multihole Injector (left) [32] and the Piezo hollow cone injector applied in the present work (right)**

The piezo activated, hollow cone injector (or A-injector; Figure 2-3, right side) on the other hand is a flexible, high precision device. It is therefore quite expensive but comes with a very high reproducibility. It forms, as suggested by the name, a hollow cone of fuel. Due to its piezo actuation the injector has the potential for very short opening and closing times and very short injection durations (hence small quantities), what allows the application of multiple

injections. Further the piezo technology offers the variation of needle lift and therefore a variable cross section of the injection area. This can be used to control the flow through the injector and therefore control and even shape the injection rate as was shown in [34] and as will further be discussed later.

## 2.2 State of the art

### 2.2.1 Physics of the atomisation

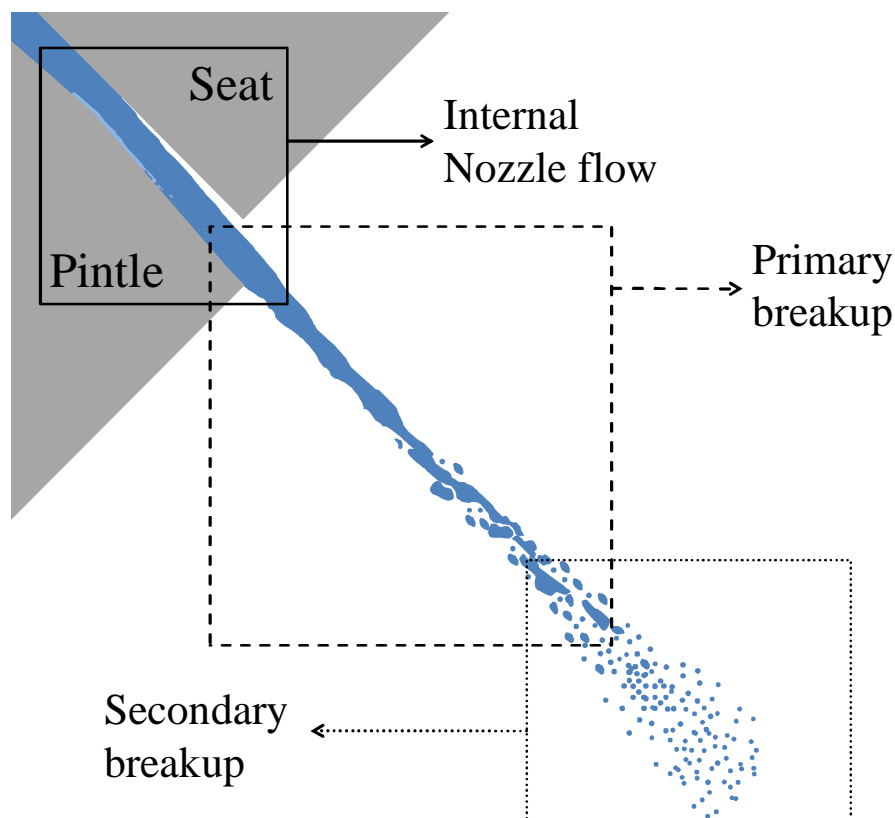


**Figure 2-4 – Schematic cut through the nozzle of an A-injector, showing the three stages in the atomization process**

Even though the geometry of the injector differs completely from plane orifice injectors, the physical processes seem to be quite similar. In analogy to the injection with a cylindrical nozzle-hole type injector, the atomisation process in the A-type injector can roughly be divided into three stages [41]:

- The *internal nozzle flow* can be very complex and is influenced by such factors like the internal injector geometry, the pressure in the rail and the mass flow rate through the nozzle, the surface roughness in the injector

etc. The internal nozzle flow influences the whole spray formation and breakup process.

- During the *primary breakup* or liquid breakup, the liquid core exiting the nozzle is broken up into ligaments, blobs and the first droplets. The driving forces behind the primary breakup are cavitation and the turbulence within the liquid phase, especially at high velocities in the nozzle, which are provoking wave structures and therefore an increased liquid surface area, giving rise to instabilities leading to the break-up process itself
- The *secondary breakup* or droplet breakup involves the interaction between the droplets and the surrounding gas as well as the interaction of the droplets with each other. The droplets formed in the primary breakup are broken up further, due to the shear stress and instabilities induced by the relative velocity between droplets and air or due to the collision with other droplets.

Figure 2-4 gives a schematic overview of these three stages. In the following chapters these will be discussed in more detail.

## **2.2.2 Internal nozzle flow**

Even though the flow in a Diesel injector is quite different from the one through an A-injector, the physics that forces the liquid through the injector are essentially the same. The examination of the internal flow field in Diesel injectors can therefore provide useful insight towards a better understanding of the A-injector. Diesel injectors are quite well investigated and the physics behind their internal nozzle flow is qualitatively understood. Therefore the basics of the internal nozzle flow will be discussed here on the example of such an injector.

### **2.2.2.1 Velocity profile**

Figure 2-5 shows the velocity profile for a turbulent, incompressible flow through a nozzle. The fuel velocity in the axis is given by the Bernoulli principle:

$$u_{nozzle} = u_{Bernoulli} = \sqrt{\frac{2 \cdot \Delta p_{inj}}{\rho_{liquid}}} \quad (1)$$

where  $\Delta p_{inj}$  is the pressure drop over the nozzle ( $p_{Rail} - p_b$ ) and  $\rho_{liquid}$  is the density of the liquid phase.

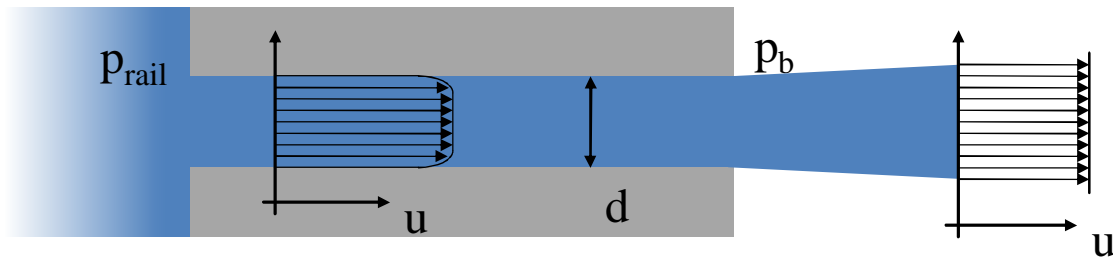


Figure 2-5 – Ideal velocity profile inside a nozzle

### Reynolds number

The Reynolds number  $Re$  describes the relation between the inertial and the viscous forces. For flows the *critical Reynolds number* ( $Re_{crit} = 2'300$  for liquid or gaseous flows through circular tubes) defines whether the flow is turbulent or laminar.  $Re$  is calculated with a characteristic length  $l$ , a characteristic velocity  $u$  and the kinematic viscosity  $\nu$  of the fluid:

$$Re = \frac{u \cdot l}{\nu} \quad (2)$$

The rail pressure pushes the liquid through the nozzle towards the exit. For very low injection pressures and therefore low Reynolds numbers ( $Re < Re_{crit}$ ), the flow field in an injector is laminar and has a Haagen-Poiseuille velocity profile. For very high Reynolds numbers ( $Re \gg Re_{crit}$ ), a turbulent flow with a velocity profile as in Figure 2-5 is seen. Diesel injectors easily reach Reynolds numbers bigger than 10'000 (In [41], Reynolds numbers were between 25'000 and 60'000). But for the most technical applications, the nozzle hole is quite short (in the order of 3 to 6 times the orifice diameter). Therefore the turbulent flow cannot fully develop – the turbulent core of the jet is shrouded by “quasi laminar” streaming layers [41].

### 2.2.2.2 Cavitation and hydraulic flip

The higher the velocity in the nozzle, the more turbulence is generated. Above a certain velocity, cavitation occurs. Cavitation describes the process when in liquid flows the local static pressure drops below the vapour pressure. Single bubbles start to form; foams or even films of evaporated liquid can develop. For cavitation in cylindrical nozzles, a large body of literature exists; e.g. [43], [44], [45]. The *Cavitation Number*  $CN$  is an indicator offering a way to estimate the probability for cavitation to occur and its intensity [46]. Its definition is as follows:

$$CN = \frac{p_d - p_v}{\frac{1}{2} \cdot \rho \cdot u_{liquid}^2} \quad (3)$$

Where  $CN$  is the cavitation number,  $p_d$  is the static pressure at the reference section,  $p_v$  is the vapour pressure of the working fluid at 25°C,  $\rho$  is the density of the working fluid and  $u_{liquid}$  is the bulk velocity at the reference cross-section. As the static pressure at the reference section is not always known, the definition by [47] is commonly employed in engineering considerations:

$$CN = \frac{p_{rail} - p_b}{p_b - p_v} = \frac{\Delta p_{inj}}{p_b - p_v} \quad (4)$$

where  $p_{rail}$  is the pressure in the rail,  $p_b$  is the back pressure and  $p_v$  is the vapour pressure. The  $CN$  value, above which cavitation occurs depends on the nozzle geometry, the fuel properties and fuel condition (pressure, density). For Diesel injectors cavitation occurs for  $0.5 \leq CN \leq 5$  (depending on the nozzles geometry and the up- and downstream conditions) and increases with higher  $CN$ . If the rail pressure is increased and the velocity in the nozzle rises, cavitation becomes stronger, filling more of the nozzles cross area. When the nozzle is completely filled with vapour phase (cavitation), a further increase of injection pressure does not increase the fuel mass flow anymore and a condition called *supercavitation* is reached. Maximum mass flow is reached because the high injection velocity reaches the reduced speed of sound in the multiphase flow of the cavitating fluid (also see [48] and [49] for detailed information). Under supercavitating conditions, injectors achieve a maximum spray angle and a very good atomization (Figure 2-6 b).

If the injection pressure is further increased it can occur that the liquid flow in the nozzle becomes totally detached from the nozzle walls. This condition is called a *total hydraulic flip*. Real injectors generally exhibit a highly distorted and/or too asymmetric flow field for total hydraulic flip to occur. The nozzles remain in a fully cavitating state. Only for injectors with a single, axially arranged nozzle as it is often used in experimental investigations, a partial or hydraulic flip could be observed [41].

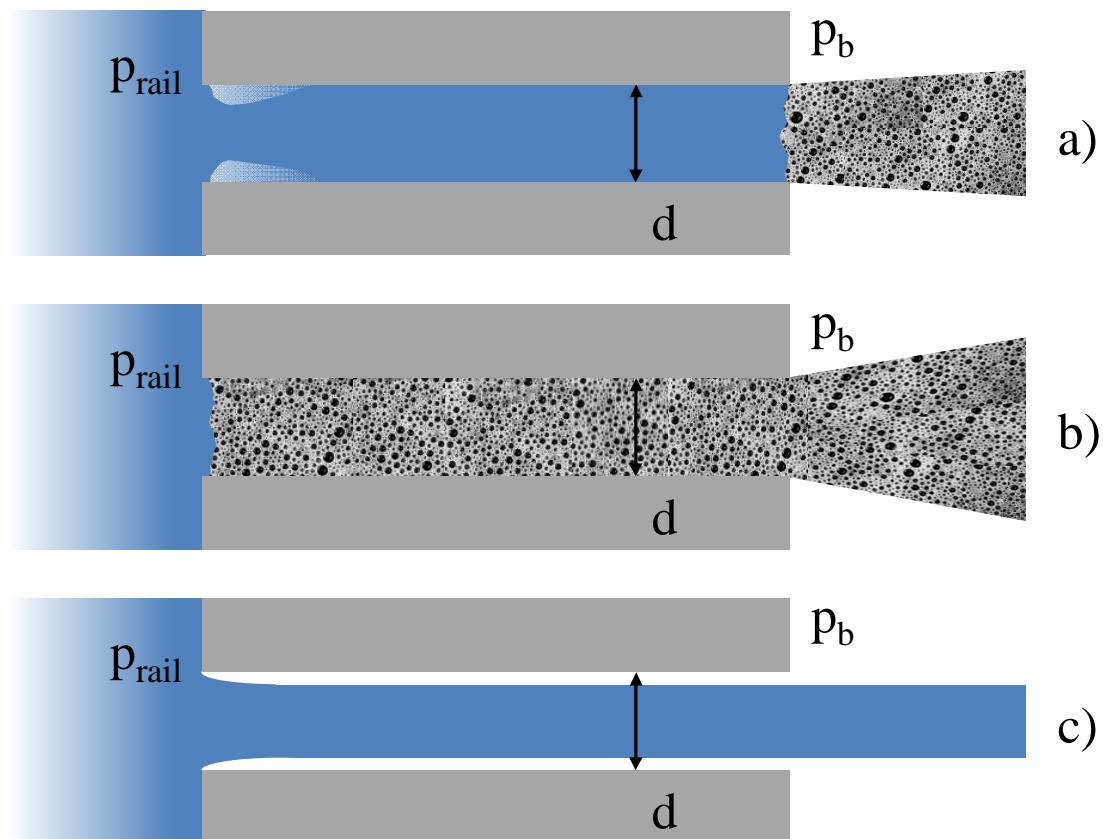


Figure 2-6 – a) Cavitating nozzle, b) nozzle in super cavitation state, c) hydraulic flip

### 2.2.3 Primary breakup

As soon as the liquid phase exits the nozzle, the surrounding gas and processes within the liquid phase – or more precisely the interplay between aerodynamic forces, surface tension and viscosity of the liquid – start to disintegrate the surface and break up the liquid core into ligaments, blobs and large droplets. This process is therefore called primary or liquid breakup. It is characterised by the following dimensionless numbers:



### Weber number

The *Weber number* describes the relation between inertial and surface tension forces. It is defined as:

$$We = \frac{d \cdot \rho \cdot u_{rel}^2}{\sigma} \quad (5)$$

With  $d$  as the diameter of the droplet (or the nozzle),  $\rho$  as the density of the air (or the liquid),  $u_{rel}$  the relative velocity between the droplet (or the liquid jet) and the surrounding air and  $\sigma$  as the surface tension of the liquid.

For droplets there is a *critical Weber number* which allows an estimation of the smallest droplets to encounter under the given parameters (For liquids with low viscosity this is  $We_{crit} = 12.5$  ).

### Ohnesorge number

The *Ohnesorge number* ( $Oh$ ) describes the relation between the damping characteristics of the viscous forces and the surface tension.  $Oh$  is depending on the fluid properties and geometric conditions, only.

$$Oh = \frac{\eta}{\sqrt{\sigma \cdot \rho \cdot d}} = \frac{\sqrt{We}}{Re} \quad (6)$$

These characteristic numbers allow a classification of the breakup regimes proposed by Ohnesorge in 1937 [50]. In the double logarithmic *Ohnesorge diagram* the different breakup regimes are separated by straight lines. Three different spray regimes have been identified; *Rayleigh regime*, *wind-induced regime* and the *atomization regime*. In [51] a further classification by differentiating between first and the second wind-induced breakup regimes is proposed. Figure 2-7 shows the classification of the breakup regimes in the Ohnesorge diagram and the conditions for the experiments carried out in this work with the hollow cone, outward opening injector. The injection pressure ( $\Delta p_{inj}$ ) was varied between 6 and 18 MPa, the needle lift has been varied from 10 to 50  $\mu\text{m}$  and the air density was set as 2.2, 6.6 and 13.2  $\text{kg/m}^3$  to reflect relevant engine conditions. The classification lines should not be understood as solid lines, defining a clear boundary between the different regimes. They

represent the locations where transition between two regimes occurs in a qualitative way. The experiments performed within the framework of this thesis have been plotted as well. As can be seen they are all in the atomization regime. The low rail pressure cases (injection pressure 0.7 MPa) are in the second wind-induced Breakup regime.

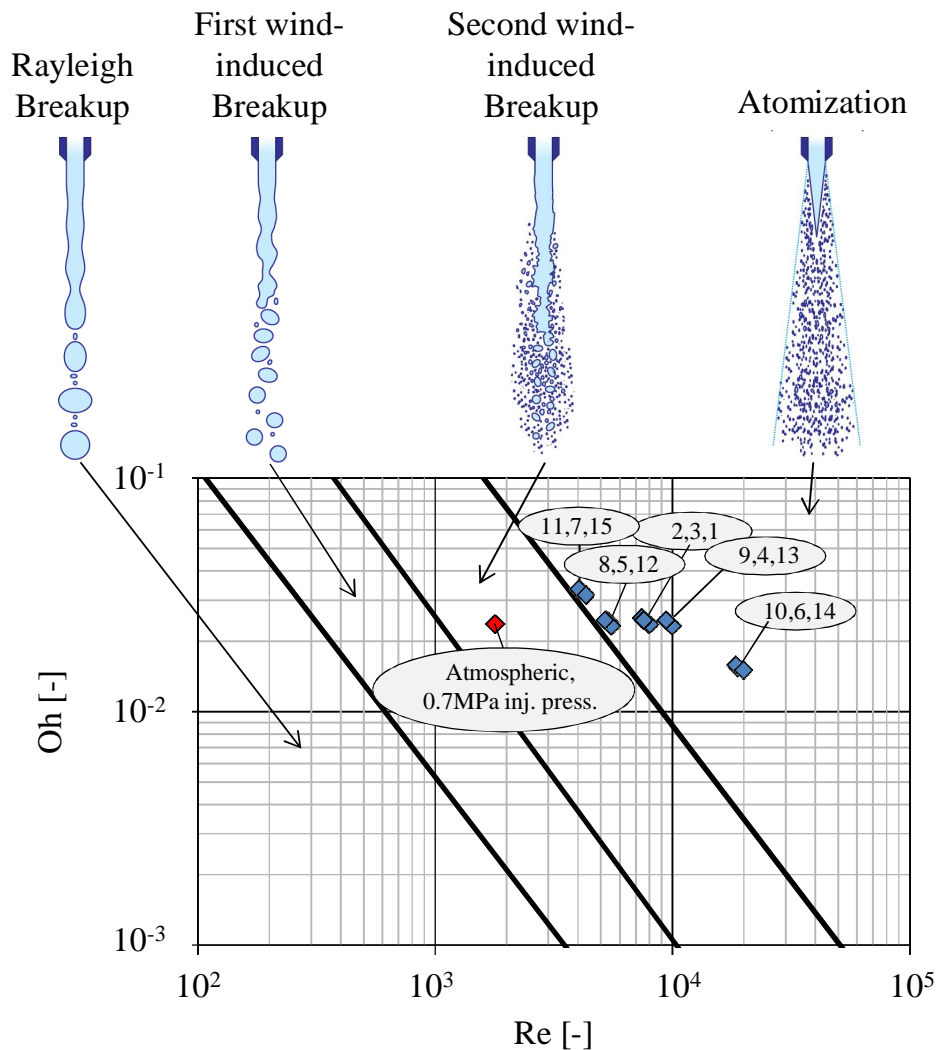


**Figure 2-7 – Ohnesorge diagram with breakup regime and the conditions of the experiments conducted for the present work (including the low pressure case shown in Figure 2-12 and Figure 5-2), also see Table 3**

### 2.2.3.1 The Breakup regimes - classification

#### Rayleigh breakup

For very low injection velocities the surrounding gas has a very small or almost no influence on the spray breakup. The dominant effect in this regime is the surface tension. Small disturbances in the liquid lead to growing axial symmetric oscillations in the liquid which finally leads to the breakup of the jet. The

droplets generated in this regime are typically in the size of  $d_p \approx 2 \cdot d_0$  where  $d_p$  denote the size of the particle (droplet) and  $d_0$  the nozzle diameter (hydraulic diameter), respectively [41].

### **First wind-induced breakup**

At increased relative velocity between jet and surrounding gas the aerodynamic forces have stronger influence on the jet. Therefore the higher shear forces additionally deform the liquid surface. The distribution of the static pressure along the surface intensifies the effect of the oscillations generated by the surface tension and the breakup occurs earlier. The boundary between first wind-induced and Rayleigh breakup is defined at  $We_{gas} = 0.4$ . The size of the resulting droplets is still in the range of the nozzle diameter [41].

### **Second wind-induced breakup**

A further increase of the jet velocity intensifies the instabilities – induced by the shear stress and the distribution of the static pressure – in the jet. Additional to the axial symmetric oscillations transversal waves travel along the jet. *Kelvin-Helmholtz* instabilities evoke waves on the surface of the jet. These instabilities occur due to the relative velocity between the liquid phase and the surrounding gas. This relative velocity causes shear stress in the liquid phase and thus creates waves on its surface. Due to these waves small droplets are ripped out of the jet surface (surface stripping, compare Figure 2-10). The boundary to the first wind-induced breakup is defined as:  $We_{gas} = 1.2 + 3.4 \cdot Oh^{0.9}$  [53]. The resulting droplets in this regime are clearly smaller than the nozzle diameter [41].

### **Atomisation**

For direct injecting automotive applications atomisation constitutes the most important breakup regime. A characteristic of this regime is a completely broken up surface of the jet exiting the nozzle. The liquid core<sup>1</sup> itself (which can be visualised by special optical techniques [54], [56] or by electric conductivity measurement [57]) remains short (a few  $d_0$ ) and is distracted very fast by several effects, as will be discussed later. The atomisation regime is defined as

---

<sup>1</sup> In the current work the liquid core is defined as the connected volume attached to the nozzle.

$We_{gas} > 40$ . The resulting droplets are much smaller than the nozzle diameter. Hiroyasu and Arai [55] divided the atomisation regime further into an incomplete spray region close to the boundary to the second wind-induced breakup and a complete spray region towards higher injection velocities and Reynolds numbers [41].

### 2.2.3.2 Mechanisms influencing the liquid breakup process

#### **Aerodynamic effects**

The influence of aerodynamic effects on liquid breakup is depending on the relative velocity between liquid and air. The higher the relative velocity is, the stronger are the forces involved. Kelvin-Helmholtz instabilities occur due to the relative velocity between the liquid phase and the surrounding gas. This relative velocity induces shear stress in the liquid phase and thus creates waves on its surface. On the spray surface these waves grow until they are strong enough to extract large droplets out of the surface.

#### **Internal nozzle flow**

As soon as the (turbulent) spray exits the nozzle, the radial velocity components within the liquid phase start to disturb the surface and form waves and instabilities. These disturbances on the surface are enhanced but not provoked by the aerodynamic effects (Injections into vacuum chambers showed these instabilities, too [58]).

As discussed earlier (page 13, the velocity distribution in the nozzle) the velocity profile inside the nozzle is not fully developed. A quasi-laminar flow around the turbulent core is observed. These instabilities take time to reach the surface, which is why the deformation of the surface and the decay of the liquid core need a couple of nozzle diameters to occur (It takes time for the instabilities to reach the surface, this time is often expressed as the distance travelled as a function of the nozzle diameter).

As soon as the liquid exits the nozzle, the velocity profile starts to change and forms a more or less uniform velocity distribution in the liquid phase (as a result of the missing walls which give velocity  $u = 0$  as a boundary condition) and a

plug-flow occurs. The shear forces and the associated momentum exchange between the layers with different velocities lead to radial pressure gradients which are destabilising the liquid core. This relaxation of the velocity profile is almost unaffected by the surrounding gas and depends on the internal nozzle flow, only [47].

### Cavitation and hydraulic flip

As discussed before (Chapter 2.2.2.2), cavitation has its cause in the internal nozzle flow. After the liquid exits the nozzle, cavitation has a strong effect on the liquid breakup as it enhances the turbulence in the nozzle upstream. Collapsing cavitation bubbles produce strong pressure waves and so called “*micro jets*” in the liquid [59]. These help to break up the liquid core but can damage the nozzle as they have an erosion effect on the nozzle walls.

Increased cavitation results in a wider spray angle [60], a stronger air entrainment can be observed and usually a better atomisation, too. When the entire nozzle is filled with cavitation, the *super-cavitation* state is reached and the maximum spray angle arises. A further increase of the injection pressure does not increase the mass flow through the injector. But if the pressure rises above a certain level, the injector can switch into a hydraulic flip. This results in a very poor atomisation and long penetration of the jet.

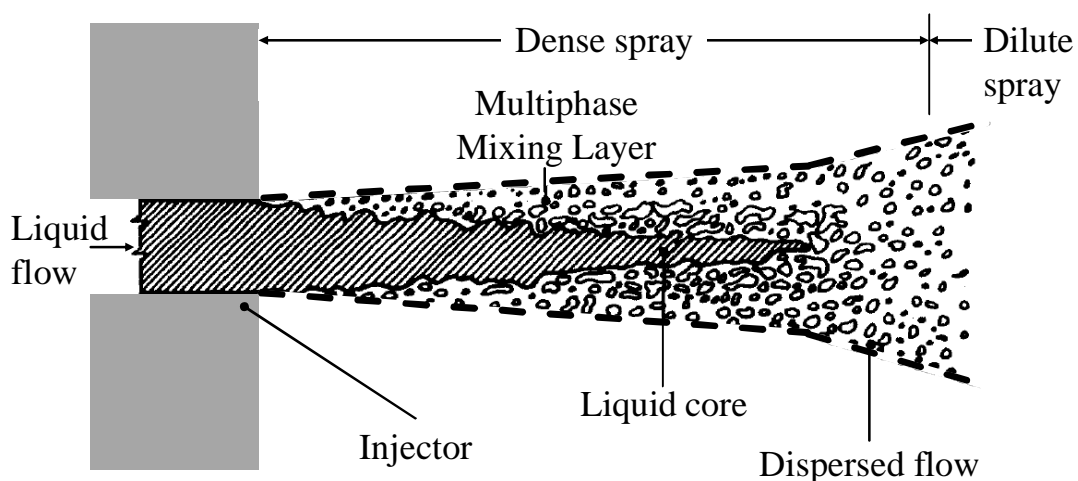


Figure 2-8 – Sketch of the near-injector region of a pressure-atomised spray in the atomisation breakup regime [65]

As illustrated in Figure 2-8 the *liquid core* ideally consists of the liquid single phase exiting the nozzle and ligaments, blobs, and first small droplets detaching from it. The gas fraction in this region is very small resulting in the aerodynamic effects playing a small role. In reality the liquid core contains not exclusively vapour liquid but also fuel vapour from cavitation further upstream. Therefore the liquid breakup is dominated by imploding cavity bubbles and the remaining turbulent flow structure from the internal nozzle flow. For Diesel injectors the time, or alternatively, the distance (often expressed as multiples of the nozzle diameter) needed to break up the liquid core can be calculated with (semi-) empirical correlations like [61], [61], [62] or [63]. Until reaching the breakup length the penetration of the spray tip increases linearly with time, which implies a constant tip velocity.

After the breakup the liquid core is fractured into smaller structures (e.g. ligaments etc.) which interact with the slow gas phase (slow compared to the injection velocity). For experiments under Diesel-like conditions this breakup length can be detected as illustrated in Figure 2-9.

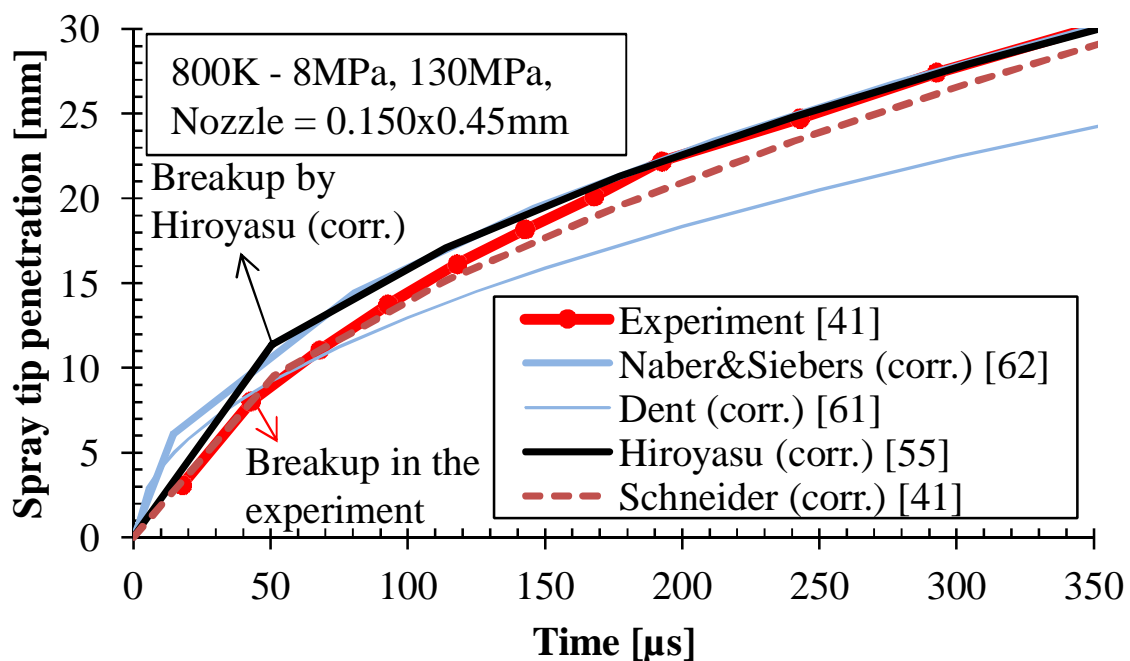


Figure 2-9 – Spray tip penetration for a Diesel Injector (Experiments and Correlations) [41]

[41] found best agreement with his measurements in [55] where breakup time is defined as:

$$t_{Breakup} = 28.65 \cdot \frac{\rho_{liquid} \cdot d_0}{\sqrt{\rho_{gas} \cdot \Delta p_{inj}}} \quad (7)$$

Here  $d_0$  is the nozzle diameter,  $\Delta p_{inj}$  is the injection pressure (i.e. the pressure drop over the nozzle), and  $\rho$  are the gas and liquid density. An empirical constant accommodates the nozzle design. The breakup length is defined as:

$$s_{Breakup} = 11.17 \cdot \left( \frac{2 \cdot \rho_{liquid}}{\rho_{gas}} \right)^{0.5} \cdot d_0 \quad (8)$$

and for  $t < t_{Breakup}$  the penetration of the spray tip is:

$$s_{(t)} = 0.39 \cdot \left( \frac{2 \cdot \Delta p_{inj}}{\rho_{liquid}} \right)^{0.5} \cdot t \quad (9)$$

while the velocity of the tip is:

$$u_{Tip} = \dot{s}_{(t)} = 0.39 \cdot \left( \frac{2 \cdot \Delta p_{inj}}{\rho_{liquid}} \right)^{0.5} \quad (10)$$

In the different correlations Bernoulli's flow velocity formula (1) stands out. [55] claimed a linear dependence of breakup length on exit velocity at the nozzle. This is not fully correct, as was already stated by [41] where it could be shown that the velocity is dependent from the density of the gas phase, which is missing in Hiroyasu's correlation (9).

For the penetration beyond the breakup length or after the breakup time, Hiroyasu suggests a square root dependence as an approximation to the experimental spray tip, hence for  $t > t_{Breakup}$  the penetration is calculated by:

$$s_{(t)} = 2.95 \cdot \left( \frac{\Delta p_{inj}}{\rho_{gas}} \right)^{0.25} \cdot (d_0 \cdot t)^{0.5} \quad (11)$$

## 2.2.4 Secondary breakup

### 2.2.4.1 Theory

Once droplets have been formed, the breakup mechanisms for hollow-cone injectors are the same as for multi-hole injectors. Therefore the droplet breakup will be explained with the help of work done on Diesel injectors (e.g. [65], [66] or [41]).

The droplets formed in the primary breakup, due to the disintegration of the liquid core, may undergo secondary breakup; they collapse then into smaller drops. The relevant forces in this phenomenon are those related with surface tension, viscosity, inertia and surface instabilities responsible for wave growth.

Depending on the local liquid to gas ratio (void fraction) and velocity ratios, different mechanisms dominate the droplet breakup. A macroscopic view on the breakup allows a classification into different flow regimes [65] as illustrated in Figure 2-8. As the liquid structures break up and air is entrained, the *dense spray region* is relevant. The gas fraction is still very low, leaving almost no space for the droplets. This leads to a variety of droplet - droplet interactions. When two droplets interact during flight, several events may occur. The droplets may experience bounce, stable coalescence, temporary coalescence followed by disruption or fragmentation, depending on the value of Weber number, collision angle and the fluid properties. Examples of these events are sketched in [67]. Even though the liquid fraction is dominant, the gas fraction within the dense spray is high enough to allow the breakup of the bigger droplets and irregular formed liquid fractions.

Further downstream in the *dilute spray* the liquid volume fraction decreases down to a level where collision effects become less important. As the chance for two droplets to collide becomes quite small, the aerodynamic effects become the major breakup mechanism. Droplets entering this regime have been broken-up to a diameter which allows the surface tension to give the droplets a spherical shape.

Further downstream, in the *very dilute spray*, the liquid fraction has become very small. Collision effects have no effect anymore on the breakup. Most of the droplets have decelerated to relative velocities which cannot transfer enough



energy into the liquid phase to further break up the droplets. But the aerodynamic drag still acts as a decelerating force.

The driving force behind the droplet break-up grows with the second power of the relative velocity to the surrounding gas. The responsible aerodynamic effects known for this breakup are the Rayleigh-Taylor and the Kelvin-Helmholtz instabilities.

The *Rayleigh-Taylor* instability is a “fingering” instability of an interface between two fluids of different densities, which occurs when the light fluid is imposing pressure upon the heavy fluid [71], [72], [73]. As long as the boundary layer between the liquid and the gaseous phase remains smooth, the droplet is

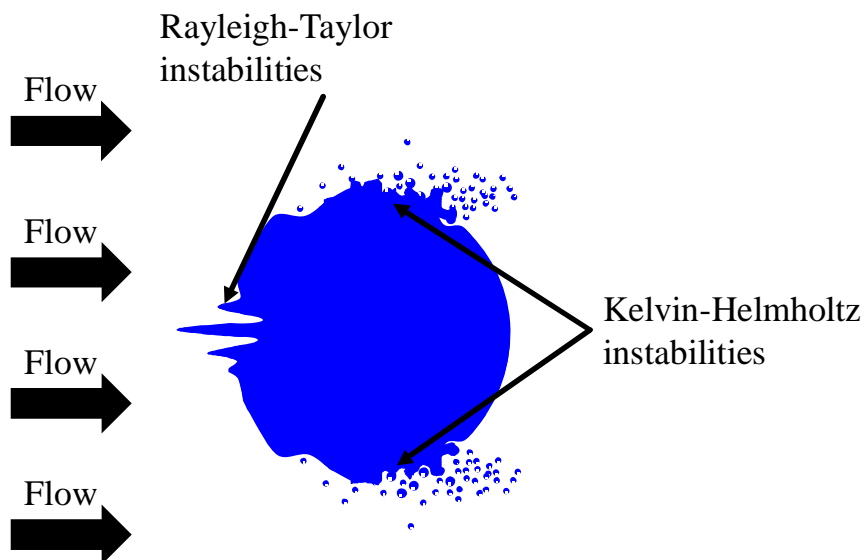


**Figure 2-10 – Different types of droplet instabilities (according to [69] and [70])**

stable. But smallest disturbances induce the growth of fingers which lead to the droplet break up. The Rayleigh-Taylor instability forms on the front side of the droplet and acts perpendicular to the relative velocity.

As mentioned earlier, Kelvin-Helmholtz instabilities occur due to the relative velocity between the liquid phase and the surrounding gas and act parallel to the droplet surface. On the droplet surface this can lead to the building of small droplets, or waves grow until they tear the droplet apart. Depending on the Weber number one or the other effect has more influence on droplet breakup:

As can also be seen in Figure 2-10 neither of the two effects has a significant influence on droplet breakup at low Weber numbers. Above  $We > 100$  the Kelvin-Helmholtz effect starts to strip off small droplets from the surface on the side of the droplets. Above  $We > 350$  the Rayleigh-Taylor instability gains strong influence and leads to catastrophic breakup, while the Kelvin-Helmholtz help disintegrate the droplets on the side.

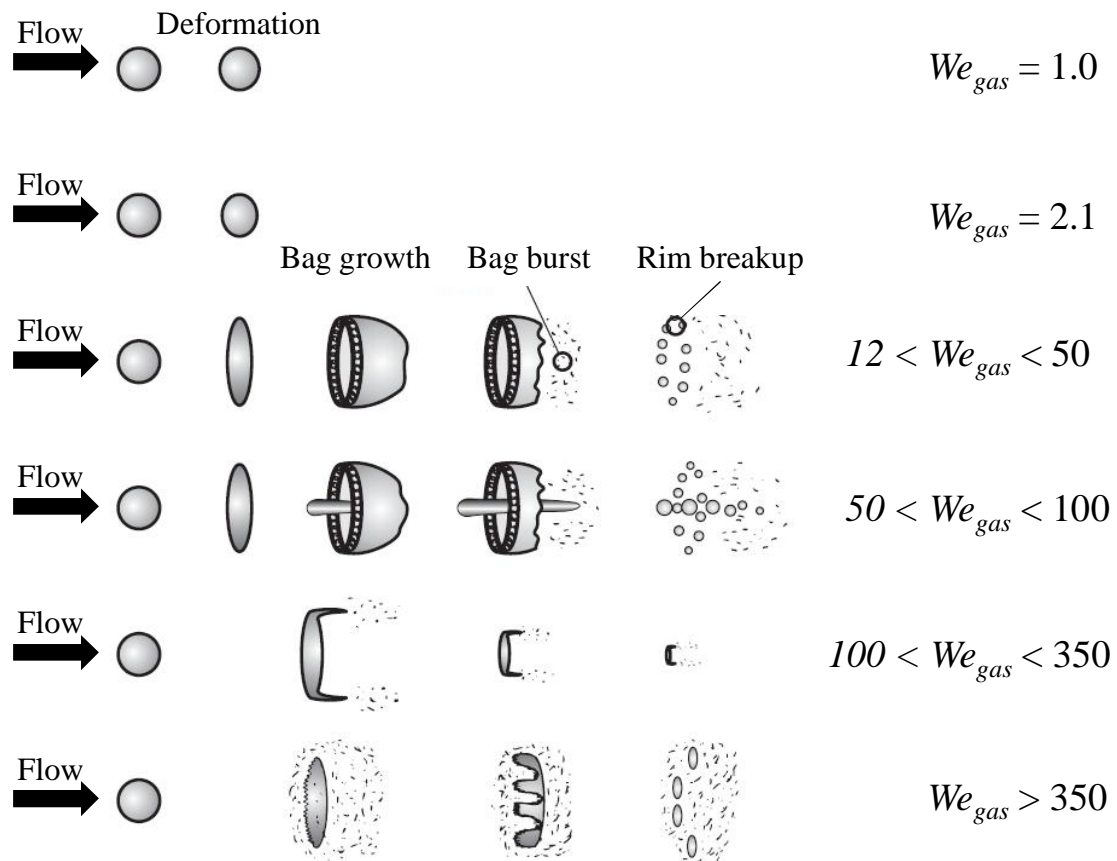


**Figure 2-11 – Droplet deformation and breakup up regimes according to [65], [66]**

The force stabilising the droplets is surface tension. It pulls the droplet together and forces its surface into a spherical shape. The viscosity of the liquid dampens the waves occurring within the droplet and slows down the deformation of the droplet. The higher the viscosity is, the more stable the droplet becomes. Like the primary breakup, the droplet breakup mechanisms can be classified by different droplet breakup regimes. For Ohnesorge numbers  $Oh < 0.1$  the influence of the viscosity is small and the droplet breakup regimes can be classified according to the Weber number of the gas phase. Figure 2-11 shows the corresponding breakup mechanisms, according to [65] and [66].

For small Weber numbers  $We_{gas} < 12$  the droplets are deformed (flattened) due to their relative velocity to the gas. Under certain conditions a *vibrational breakup*<sup>2</sup> can occur. This breakup mechanism is very slow compared to the time domains the other breakup mechanisms occur. Towards higher Weber numbers the breakup becomes much faster, and the resulting droplets become smaller. For Weber numbers between  $12 < We_{gas} < 50$  the droplet is inflated like a bubble, forming a thin bag with a more massive toroidal rim at its beginning. The bag eventually bursts (*bag breakup*), forming a large number of small droplets [66]. A short time later the rim disintegrates, producing a small number of fragments. At higher Weber numbers  $50 < We_{gas} < 100$  in the middle of the bag a column of liquid is formed (stamen). Like the rim this stamen breaks up into larger droplets. *Sheet stripping* ( $100 < We_{gas} < 350$ ) is distinctly different from the bag breakup. The droplet gets deformed to a flat structure, without forming a bag. During this deformation and afterwards a thin sheet is continuously drawn from the periphery. Above Weber number  $We_{gas} > 350$  the droplet undergoes a *catastrophic breakup*; where the drag continuously erodes the droplets surface, while large-amplitude, long-wavelength waves ultimately penetrate and disintegrate the drop [65], [74].

The mechanisms described here are steady state. A Diesel injection on the other hand is transient. The droplets on the tip of the injection face the undisturbed gas phase. The initial relative velocities between droplet and gas phase are therefore very high. Once the spray plume is developed and steady state is reached, the droplets travel in the drag of the leading droplets. Their relative velocity to the gas phase is therefore reduced. Depending on the radial position in the spray this relative velocity is different. In the middle of the spray it is small, as the entrained gas is at a similar velocity as the liquid phase is. Towards the outside the gas velocity drops and therefore the relative velocity to the droplets becomes very high. On the outer region of the spray the droplet velocity decreases as well, so that the relative velocity between the two phases is small. The droplets face therefore several of these break-up regimes, depending on the relative

---

<sup>2</sup> "Oscillations develop at the natural frequency of the drop. It can occur that the flow field interacts with the droplet in such a way as to increase oscillation amplitude, which in turn causes the drop to decompose into few large fragments" [66]

velocity [41].

In an Otto engine, it is important to evaporate the whole liquid fuel before ignition and combustion take place. During combustion, liquid fuel would lead to soot emissions when the flame reaches it, or it is carried out into the exhaust system, where it has to be oxidised by a catalytic converter. This decreases the efficiency of an engine, as the fuel energy could not be used to produce work. To guarantee a fast evaporation of the liquid fuel, it is important to have a high surface-to-volume ratio. As the volume of a droplet decreases with the 3<sup>rd</sup> power to its radius and the surface by the 2<sup>nd</sup>, the surface to volume ratio is increased with smaller droplets. It is therefore important that the liquid phase breaks up to very small droplets. For shear breakup at low Ohnesorge numbers [75] defined a characteristic breakup time. It allows an estimation of the time between primary breakup and the drop size at which it doesn't undergo any further breakup. This characteristic time is defined as:

$$t_{char.Breakup} = d_0 \cdot \frac{\sqrt{\rho_{liquid} / \rho_{gas}}}{u_0} \quad (12)$$

where  $d_0$  denotes the initial droplet diameter and  $u_0$  the initial relative velocity between droplet and the surrounding gas.

The *Sauter Mean Diameter* (*SMD* or  $D_{32}$ ) characterises the surface to volume ratio of a spray. A droplet with the size of the *SMD* has the same surface to volume ratio as the total number of observed droplets. It is defined as:

$$d_{32} = \frac{\sum_{i=1}^n d_i^3}{\sum_{i=1}^n d_i^2} \quad (13)$$

The *mean diameter* ( $D_{10}$ ) is the arithmetic average of the droplet diameters and is defined as:

$$d_{10} = \frac{1}{n} \cdot \sum_{i=1}^n d_i \quad (14)$$

In [41] a review on different correlations of the droplet diameter was performed. It was stated that the influence of the different parameters varies in a significant range. According to these findings an estimation of the *SMD* is therefore very difficult and varies with the model applied. In [58] the available correlations

have been described more concretely: “*Many of the drop size equations published in the literature are of somewhat dubious value*”.

### 2.2.5 Internal nozzle flow and primary breakup in an A-injector

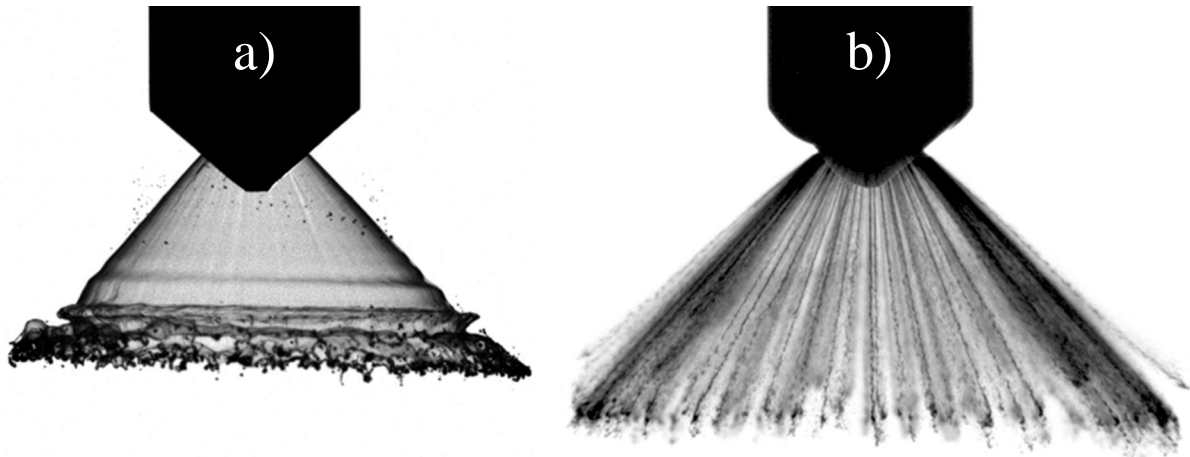


**Figure 2-12 – a) Liquid sheet from an A-injector at low injection pressure (0.7 MPa)  
b) Strings from an A-injector at higher injection pressure (12 MPa)**

For hollow cone injectors the influence of the inner-nozzle flow on the spray behaviour is very strong. From a cone shaped, continuous orifice like in the A-injector, a homogenous liquid sheet would be expected to exit the nozzle. For low injection pressures this is more or less true as can be seen on Figure 2-12 a). When following the liquid phase from the nozzle exit to the end, different regimes can be observed: A liquid sheet exits the nozzle. It starts to develop small waves which become stronger until they disintegrate the sheet and form ligaments and droplets. On the surface of the sheet slight longitudinal strings can be seen. According to [39], [42] these strings are formed by air bubbles and/or cavitation pockets in the gap between the pintle and the seat. At high injection pressures this effect is more pronounced. The pockets shape the liquid sheet into separated strings as can be observed in Figure 2-12 b).

During the injection, air is entrained from the outside region into the nozzle forming pockets. These pockets keep always attached to the nozzle exit and are distributed circumferentially around the nozzle. Individually they can either be attached to the seat or to the pintle. Depending on the position where these pockets form, the strings can move in radial and/or tangent direction. For instance, if the pockets of air are attached to the pintle, the strings formed run

over the pockets and are deflected away from the injector axis, increasing the cone angle [39].

At the seal band of the injector, where the cross section becomes smaller and due to the increased flow velocities the pressure locally drops below the fluid vapour pressure, cavitation pockets form. Unlike the entrained air, these pockets are detached from the nozzles exit line. They have a triangular shape with the appendix lying close to the seal band. As soon as the pockets become too big, they are carried away by the flow.

The two effects of cavitation and air entrainment seem to co-exist. So far, the influence one on the other could not be identified. In [39] it is not excluded that the entrained air and the cavitation form a multiphase flow condition that is referred to as ‘super cavitation’. The authors of [36] argue that the apparent cavitation in the conical nozzle region involves a ‘partial hydraulic flip’ phenomena, as due to cavitation and air entrainment, the sheet/the strings are fully detached from the nozzle walls over wide areas. The flow rate through an injector nozzle is calculated with:

$$\dot{m} = A_{nozzle} \cdot u_{liquid} \cdot \rho_{liquid} \quad (15)$$

For the A-injector the flow area depends on needle lift and the seat angle. It can be expressed as:

$$A_{nozzle} = \pi \cdot \varepsilon \cdot \sin(\alpha) \cdot r (2 - \varepsilon \cdot \sin(\alpha))$$

where  $\varepsilon$  is the needle lift,  $r$  is the radius of the orifice and  $\alpha$  is the seat angle (see for comparison Figure 2-13 on page 32 and Figure 5-58 on page 131). According to [76] the needle lift is in the range of 25 to 40  $\mu\text{m}$ .

Due to air entrainment, cavitation and boundary shear flow the effective flow rate in the injector is lower than the theoretical one. The discharge coefficient  $C_d$  specifies the ratio between the theoretical and the effective mass flow. It is defined as:

$$C_d = \frac{\dot{m}_{eff}}{\dot{m}_{theor}} = \frac{A_{eff} \cdot \rho_{eff} \cdot u_{eff}}{A_{theor} \cdot \rho_{theor} \cdot u_{theor}} \quad (16)$$

Cavitation and air entrainment (Figure 2-13, left) reduce the area of the liquid phase exiting the nozzle [39], [36], while bubbles in the fluid reduce the density

of the liquid phase. The area contraction coefficient  $C_a$  represents these losses, and is defined as:

$$C_a = \frac{A_{eff}}{A_{theor}} \quad (17)$$

Shear effects at the boundaries lead to a non-uniform velocity profile within the liquid phase (Figure 2-13). The corresponding reduction of the mean exit velocity is specified as:

$$C_v = \frac{u_{eff}}{u_{theor}} \quad (18)$$

Therefore:

$$C_d = C_a \cdot C_v$$

For cavitating nozzle flows, [43] found the velocity in the “vena contracta<sup>3</sup>” as:

$$u_{VC} = \sqrt{\frac{2 \cdot (p_{Rail} - p_{vapour})}{\rho_{liquid}}} \quad (19)$$

And therefore the discharge coefficient can be expressed (based on equation 2.3) as:

$$C_d = C_a \cdot \sqrt{\frac{p_{Rail} - p_{vapour}}{p_{Rail} - p_{back}}} = C_a \cdot \sqrt{1 + \frac{1}{CN}}$$

One big difference to the primary breakup of sprays exiting cylindrical nozzles is the conical liquid sheet exiting, rather than a jet. A Diesel injector for example has a more or less cylindrical jet exiting the nozzle, which is broken up by the effects discussed earlier. For a conical liquid sheet these effects do also exist, but additionally there is the effect of the increased radius of the sheet. When the sheet expands, its thickness is reduced in order to keep constant mass flow. While the sheet becomes thinner it becomes more sensitive to the surrounding gas (it becomes easier deflected due to the reduced mass flow and is easier affected by local pressure changes).

---

<sup>3</sup> The point in flow where the diameter of the stream is the least minimum

Another difference in the primary breakup is the variable geometry of the nozzle. Diesel or multihole injectors with their cylindrical nozzles have a fixed

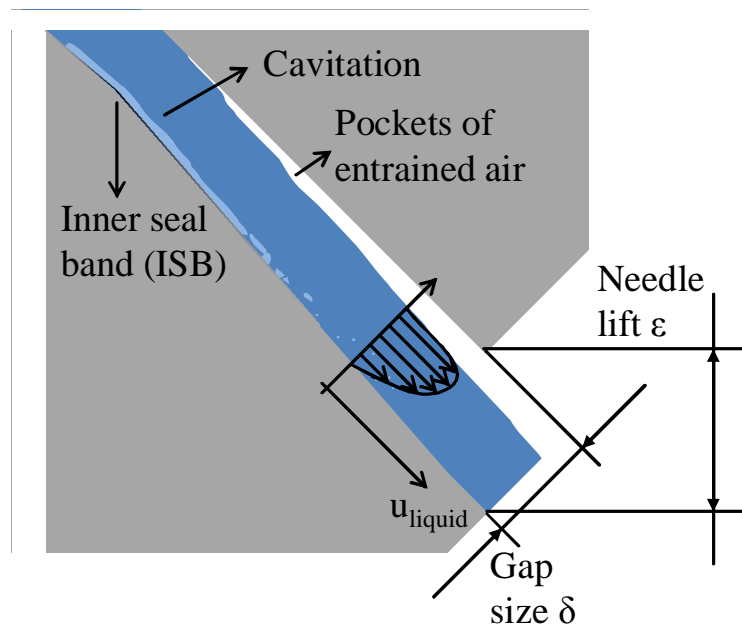


**Figure 2-13 – Internal nozzle flow: Area loss due to air entrainment and cavitation and velocity profile due to shear effects**

boundary. The A-injector has one fixed boundary to the liquid on the needle seat and a moving boundary to the pintle. As it is illustrated in Figure 2-13, the flow is attached onto the needle pintle on a longer range than on the seat above the flow (even if there are no pockets of air). [64] demonstrated with special prototype injectors the influence that a longer attachment either to the needle seat or to the pintle has on the cone angle. They investigated two prototype injectors, one with a larger inner seal band “+ISB” and one with a pintle smaller than the original so with a reduced distance to the inner seal band “-ISB”. In case of the larger pintle the fluid stayed longer attached to the pintle and the seal band was brought nearer to the nozzle exit than with the standard injector. In the other case with the smaller needle, the flow stayed longer attached to the needle seat and the seal band was brought higher upstream, away from the nozzle exit, compared to the standard injector.

The analysis of the cone angle showed a small increase in cone angle compared to the reference case for both nozzle types and also an increase in spray stability (shot to shot). The results show a strong dependency on backpressure. For atmospheric conditions the change in the spray image was very small. For an increased backpressure the differences become more noticeable. The standard



injector showed a much stronger sensitivity on the backpressure compared to the two prototype injectors. Its spray angle showed higher shot to shot variation with increasing backpressure. For the standard injector the mean cone angle is strongly reduced for increased backpressures (from  $87^\circ$  at 0.11 MPa down to  $78^\circ$  at 1.66 MPa) whereas the

-ISB varies from  $89^\circ$  to  $86^\circ$  and the +ISB even less, from  $89^\circ$  down to  $87^\circ$ .

For DISI engines and gasoline injectors a correlation for the penetration length of the liquid phase like Hiroyasu's (compare formula (7) and following on page 22) could not be found, whether for multi-hole nor for hollow cone injectors.

### 2.2.6 Atomisation with the A-injector

Since its presentation in 1998 [35], much effort has been directed towards improved understanding of the spray physics behind the atomisation (nozzle flow, string formation, first and secondary breakup) of the A-injector. But still there is a need for fundamental knowledge of the high pressure, hollow-cone sprays of A-injectors [36]. Injectors with cylindrical nozzles have been used and investigated for more than 100 years, nonetheless, some of the physics behind

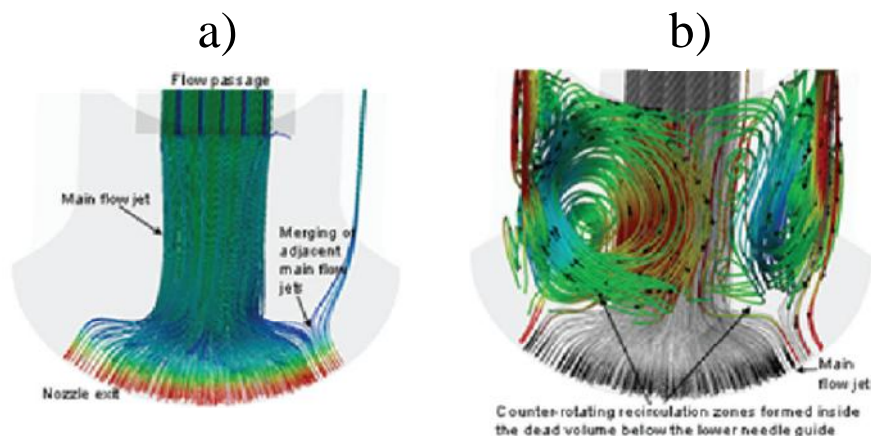


**Figure 2-14 – a) Flow streamlines inside a hollow cone nozzle. Main flow path of the standard design; b) recirculation zones formed below the guides (in colour scale; the streamlines of the main flow path are superimposed on the black-white scale)[42]**

are not yet fully understood (e.g. cavitation, atomisation processes) Despite these shortcomings, a number of empirical correlations have been proposed to describe spray morphology and time evolution of two-phase related quantities [37], [38]. Compared to the Diesel and gasoline multihole injectors for DI, the A-injector is quite new. Its nozzle geometry is completely different as it has no holes, but a pintle which builds a thin slit on a conical surface when lifted.

Therefore the hydraulic diameter is variable. Due to this and the different geometry cavitation and pockets of air occur with random sizes and at random spots in the region of the inner seal band [36], [39]. This results in a more complex nozzle flow. Furthermore the break up formation works differently as the breakup of a liquid sheet experiences more destructive influences than the classical breakup after a cylindrical nozzle [40].

Today the physics of the flow within the nozzle of an A-injector are still not fully understood. The size and physical boundary conditions of an injector nozzle make it very difficult to investigate the internal flow structures. Scale-up models made of transparent materials allow a look on the cavitation in a nozzle [39], [36], while numerical simulations help to understand how the flow inside the nozzle looks like [36], [42].

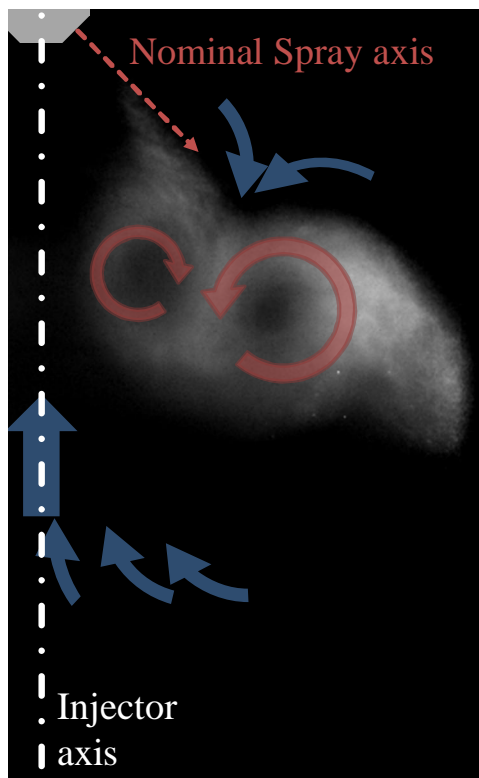


**Figure 2-15 – Vortices and air entrainment in the hollow cone of an A-injector after the injection has finished**

As in the case of Diesel or multi-hole injectors, the nominal penetration of an A-injector depends on the density of the surrounding gas, injection pressure, geometry of the injector and the properties of the injected fuel. A higher gas density has a stronger drag effect on the spray, which results in a slower tip velocity and a shorter spray tip penetration [77], [78], [79], [80], [81] or [82]. As could be expected and was stated by [55], higher injection pressure results in a higher spray tip velocity, which can also be seen with the A-injector [80]. Once the primary breakup is completed, the spray of a hollow cone injector is dominated by two large, toroidal and circumferential vortices. These entrain air from the outside of the cone into the spray, while the air underneath the injector (i.e. the inner part of the spray cone) is brought through a so called funnel flow towards the injector [77], [9], [10], [11], [12].

Figure 2-15 illustrates the flow conditions within the hollow cone. Use of PIV [10] visualised the parabolic path alongside which the vortex centre of the outer vortex propagates away from the injector. In [10] it is

also reported that the velocity of the funnel flow depends linearly on the injection pressure, with a velocity of about 2 m/s for an injection pressure of 10 MPa and 5 m/s for 20 MPa. In [79] the influences of different fuel types on spray propagation have been investigated. It was shown that liquids of higher viscosity and surface tension formed a vortex on the leading edge with a lower droplet density, whereas fuels with lower viscosity and surface tension showed a vortex which was merging with the spray tip, forming a dense cloud of droplets. The reason for this is not yet fully understood. As the A-injector is actuated by a piezo crystal it allows a very fast opening and closing of the needle. Therefore split injections in form of double, triple and even five injections have been investigated by [83], [10], [11], [84] and [34]. It was found that the axial penetration of the liquid phase (as well as of the evaporated, gaseous phase) can be reduced if the same amount of fuel is divided into two (or more) separate injections.

The droplet diameters produced by a piezo driven hollow cone injector are very small. Under atmospheric conditions and injection pressures between 12 and 20 MPa droplet sizes of  $D_{10} \leq 8$  and  $D_{32} \approx 16 \mu\text{m}$  can be achieved [11], [34]. Compared to a modern multi-hole gasoline injector which produces at same conditions and a nozzle hole diameter of  $140 \mu\text{m}$  droplets with  $D_{10} \approx 20$  and  $D_{32} \approx 50 \mu\text{m}$  [85] the piezo injector has a large advantage and a much better atomisation quality.

In the literature the knowledge on the breakup process and the toroidal vortices of an A-injector is very limited. Further no experimental data could be found describing the streaks behaviour or its inside structure. There is also lack in investigations of the needle lift and its influence on spray morphology, droplet size and vapour phase of an A-injector spray. Other important things like the evaporation process or the vapour phase of an A-injector under engine like conditions are described only partially. Engineering correlations are a great help to estimate spray penetration or droplet size (e.g. [41], [55], etc.). Unfortunately no such correlation could be found in literature for the A-injectors.

Therefore this work focuses on the investigation of the spray evolution and morphology under engine-like conditions. In combination with detailed, atmospheric investigations of the droplet size and velocity of an A-injector the goal is to better understand the breakup process, the liquid-air interactions and

the resulting flow patterns. Further the needle lift needs to be investigated more closely and its influence on spray penetration, droplet velocity and droplet diameter needs to be described. Another focus is set on the identification of different influences (injection pressure, gas density and fuel characteristic) on the spray tip velocity in order to describe a penetration correlation for pintle type hollow cone injectors.

On these grounds three main goals of the present work have been defined as:

- The description of the A-injectors general spray morphology and its distinguishing marks (the streaky structure) as well as the liquid-air interactions and flow patterns of the liquid and (so far visible) gaseous phase
- The quantification of the main influences on spray penetration of selected parameters; gas density, injection pressure fuel properties and needle lift
- The elaboration of an experimentally validated correlation to predict spray tip penetration describe the different influences on the parameters mentioned above

### 3 Measurement instrumentation

*There are three principal ways to lose money: wine, women and engineers.  
While the first two are more pleasant the third is far more the certain  
-Baron Rothschild*

Experimental investigations of automotive sprays under engine like conditions pose significant challenges to measurement technology. The investigated events take place in very short time scales ( $\mu\text{s}$  range), the droplets to be measured are very small ( $\mu\text{m}$  range) and very fast (up to 150 m/s) [41]. As the interaction between spray and the surrounding air is very strong, it is crucial not to influence either of them with the measurement.

Non- intrusive measuring systems, like optical methods, are therefore the most suitable for the investigation of Diesel or direct injected gasoline sprays. To investigate different aspects of the spray, a multitude of techniques are in use today delivering a variety characteristic information of the spray (e.g. spray structure, spray angle, penetration, density, momentum, droplet size and velocities, vapour density). Depending on the depth of investigation to be achieved for the various aspects of the spray, different combinations of techniques can be applied. An assortment of techniques will be shown here:

To investigate the morphology of the liquid phase such as penetration and cone angle, shadow imaging and 2D light section methods are proven techniques. Shadow imaging is a line-of-sight technique which needs a bright background illumination. This can be accomplished with a flash lamp, a luminous field, a widened laser beam or simply with an illuminated white surface.

The 2D light section technique allows a contactless measurement of the spatial expansion of a sprays liquid phase in a cross section of the spray. Depending on the application it offers a rather simple technique to look inside a spray and

reveal its internal structure. As discussed earlier a hollow cone spray has a very interesting interior as half of the spray structure and vortices lie on the inside of the hollow cone which a line of sight technique like shadow imaging, Shadowgraphy or Schlieren technique can not reveal.

The 2D section technique can be further divided into Mie scattering and PLIF (planar laser induced fluorescence). Mie scattering is an application of a 2D light section technique, which collects the scattered light from a laser sheet by means of a camera. It gives information about the location of the liquid phase boundaries, based on which penetration of the liquid phase can be determined. The second application of this technique is the PLIF. As opposed to Mie scatter, PLIF is a so called elastic optical method, which offers an easy way to suppress the influence of multiple scattered light. Using a band pass filter, the exciting laser light can be blocked while the fluorescent light can be recorded, which

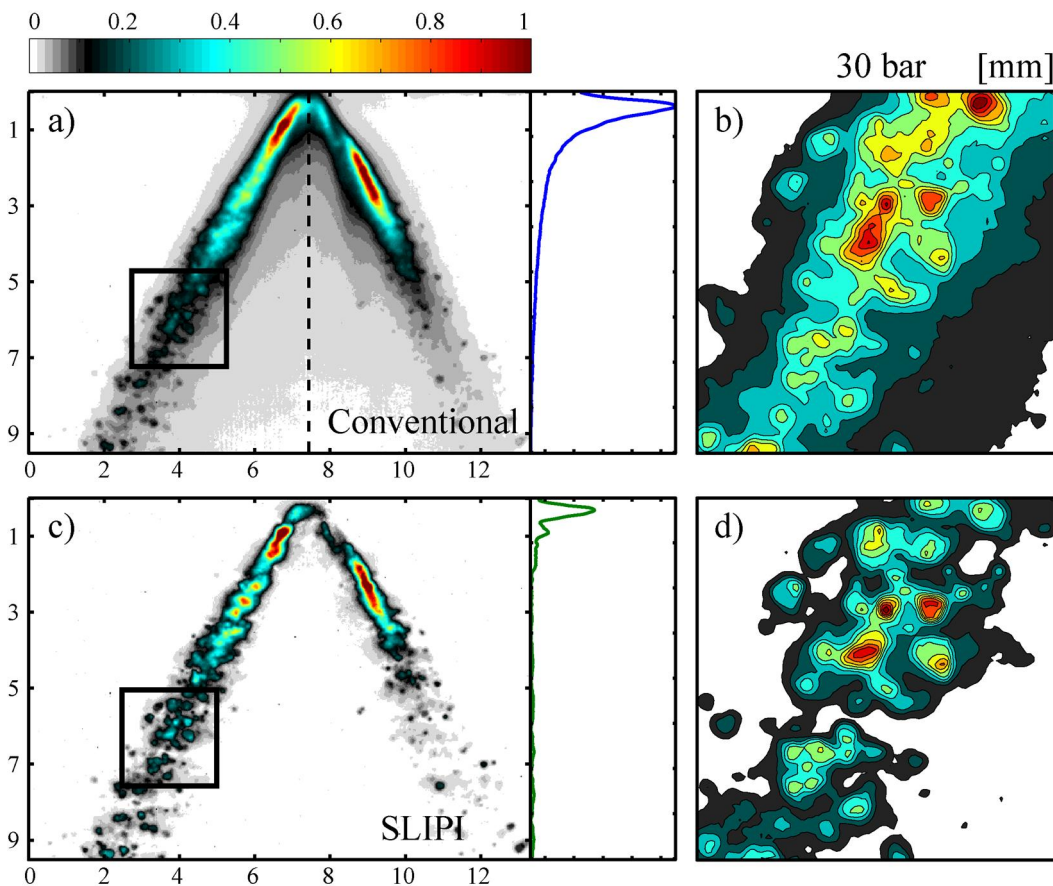


Figure 3-1 – Example of the SLIPI technique with a multihole injector [107]

strongly reduces multiply scattered light. Using tracers the application of PLIF methods give additional quantitative information, for example temperature [86], fuel concentration or air to fuel ratio [87]. The drawback of this method is the

small amount of light being emitted by fluorescence. This makes it necessary to use an intensifier to ensure sufficient levels of the recorded signal, which however reduces the spatial resolution of the image. A new technique called “Structured Laser Illumination Planar Imaging” (SLIPI) allows the identification and the quantification of multiply scattered light [90][107]. Therefore the images can be corrected accordingly (Figure 3-1). For this work the technique could not be used, as even the ultra fast SLIPI is still too slow for the investigation of the highly transient mechanisms in sprays.

Shadowgraphy and Schlieren technique are well suited to gain qualitative information not only about the liquid, but also the vapour phase of the spray. The images deliver information about the location of the vapour phase. As the methods make use of changes in the refractive index (due to density variations along the light path) a quantitative analysis requires that temperature and pressure gradients near the vapour phase to be very small. As line-of-sight methods, both Shadowgraphy and Schlieren integrate the information along the path through the spray [88]. Both techniques are based on parallel light beams, which can be produced either with a spherical lens, or by means of parabolic mirrors. The difference between the techniques lies in the optical arrangement between the camera and the measurement (compare Figure 4-5), where, for the Schlieren method the light is partly cut off, either with a knife edge or a (negative) pinhole. This increases the sensitivity on changes in densities. A third technique is Background Oriented Schlieren (BOS) as proposed by [89]. It is kind of a hybrid technique made of background imaging and Schlieren technique. Randomly distributed dots provide a background for the images of the experiment. Similar to PIV, the distortion introduced by the density variation between the background and the camera is calculated via cross correlation between an undistorted image and the image with the experiment. Based on the distortions the images intensity is then corrected and the Schlieren are made artificially, to visualise the intensity variations. The technique is very useful for large experiments where lenses or spherical mirrors would become too big and therefore too expensive. But due to the high recording frequency which has to be achieved for spray experiments, this technique would need a very powerful lamp to illuminate the background. Alternatively an increased gating time for the camera would decrease the accuracy of the setup.

All these presented techniques deliver time resolved information about the spatial propagation of the spray. Depending on the applied technique a selective cross section or an all-embracing two dimensional projection of the whole spray is provided. Based on the camera recording frequency, the expansion velocity of the liquid or the vapour phase can be determined.

In contrast, the following methods give quantitative information on droplet velocity or/and droplet diameter.

For highly time and spatially resolved investigations in small measurement volumes ( $\varnothing \approx 40 \mu\text{s}$ ), Laser Doppler Anemometry (LDA) and Phase Doppler Anemometry (PDA), are very well suited techniques, which also known as Laser/Phase Doppler Interferometry; LDI/PDI [91]). The techniques are strongly related. One big advantage of the methods is that they do not need to be calibrated. A disadvantage on the other hand is that if an entire flow field has to be measured, the measurement is very time consuming. For statistical reasons several injections have to be made at each position. This also requires a sophisticated translation stage to adjust the position of the measurement volume. Particle Image Velocimetry (PIV) in contrast, is a technique that provides a complete 2D velocity field in one step. Therefore tracing particles (glass spheres, oil droplets...) are seeded (as homogeneously as possible) into the flow. By means of a double exposure the path of the particles following the flow is visualised. Based on the time difference between the two exposures and cross correlation algorithms the direction and velocity of each particle and thus the velocity field can be derived. PIV is often used to visualize the flow field around the spray [41], [12]. Due to the high droplet velocities, the high droplet density and the inhomogeneity of the droplet distribution, the spray itself can only be used for the PIV in certain areas where the droplet density and the droplet velocity is small enough.

Another technique is the Laser Flow Tagging (LFT) [92]. In a first step a line is “written” into the flow field by a focused laser beam (due to absorption of the laser energy a certain molecule is dissociated and another molecule is being generated). In the second step an image is taken after a prescribed time step  $\Delta t$  visualising either the destroyed or the formed molecule (using laser spectroscopic methods such as Laser Induced Fluorescence (LIF) or Laser



Induced Incandescence (LII). The deformation that the line experiences provides information about the velocity distribution in the flow field [93].

In this work the following three optical techniques have been applied:

1. With the **Phase Doppler Anemometry** method local droplet size and velocity distributions have been measured at various positions along the spray at atmospheric conditions.
2. A **2D light section technique** based on Mie scattering has been used to visualize the spatial propagation of the liquid phase. With a high speed camera time resolved films of the injections have been made.
3. To have a qualitative impression on the behaviour of the vapour phase, a second camera was used to record time resolved **Shadowgraphy** images, showing both, liquid and gas phase distribution in the cell

These three techniques will be described more precisely in the following chapter.

### ***3.1 Phase Doppler Anemometry***

The Phase Doppler Anemometry (PDA) allows a non-contact, simultaneous measurement of both, droplet diameter and velocity at one location in the spray [41]. PDA is a further development of the Laser Doppler Anemometry (LDA). Today both techniques are state of the art and used in different scientific and engineering fields like fluid dynamics, combustion research, meteorology or process engineering. The main principle of both techniques is based on the detection and evaluation of the light scattered by objects passing a measurement volume which is generated by two crossed, coherent and linearly polarised laser beams. In addition to particle velocity, PDA also measures the particle diameter, if the droplets are spherical.

The PDA technique was introduced in 1975 [94], and many further developments have been reported in the literature (e.g.: [95], [96], [97] and [98])

The PDA investigations in this study have been carried out in collaboration with the University of Loughborough. In the following articles the basic principles of the PDA techniques is described.

### 3.1.1 Light scattering on spherical particles

The theory about light scattering can be divided in three major regimes. These differ in the relation between particle diameter  $d$  and the wavelength  $\lambda$  of the light.

- The Rayleigh scattering theory describes the scattering of light at very small particles (e.g. molecules) where ( $d \ll \lambda$ ). The Intensity of the scattered light is proportional to the sixth power of the diameter ( $d^6$ )
- The Lorentz-Mie theory describes the light scattering on spherical particles with a diameter bigger than the wavelength of light ( $d \geq \lambda$ ). In this case the light intensity is proportional to the second power of the droplet diameter, only ( $d^2$ ).
- For very large particles ( $d \gg \lambda$ ) geometrical optics can be applied instead of the Lorentz-Mie theory (Reflected and scattered light, Figure 3-2). Geometrical optics treats light as rays or straight lines travelling out from its source. (Reflection and refraction are described according to Snell's Law where for reflection the ray remains in plane of incidence with the angles of incoming light and the reflected light being the same. For refraction the angle of the transmitted beam is a function of the different refractive indexes:  $\frac{\sin \alpha_1}{\sin \alpha_2} = \frac{n_1}{n_2}$ )

Figure 3-2 shows a spherical object (e.g. gasoline droplet). The incoming light (monochromatic) hits the surface and is partially reflected and transmitted. Depending on the angle between the incoming light and the surface with the change in refractive index, the beams are reflected (or refracted) in different angles. Within the droplet the same effects further reflect and refract the light (first order and second order are the most important but some light still goes on even further).

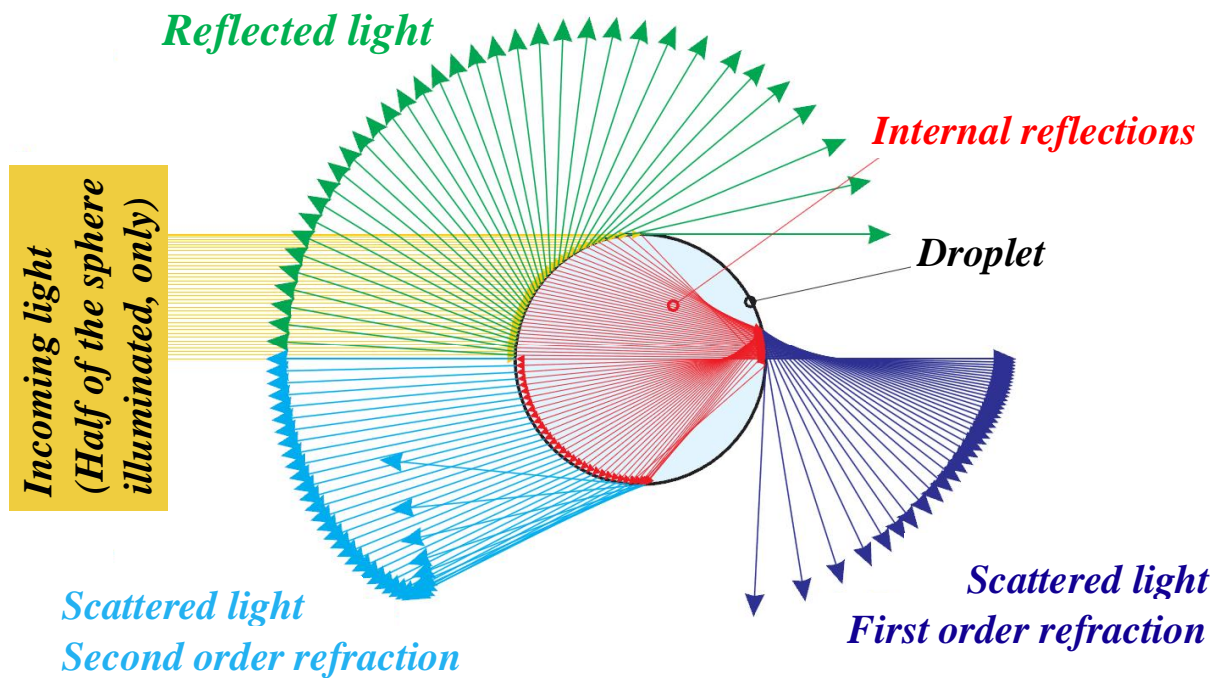


**Figure 3-2 –Conceptual image of light scattering of a single droplet in the Lorentz-Mie regime [41]**

Independent of the particle size, the polarisation of the incoming light has a large influence on the behaviour of the scattered light. The LDA and PDA technique work in the regime of the Lorentz-Mie scattering (i.e. particle size  $\geq$  wavelength of light). To calculate the particle diameter from the signals phase shift, PDA processors always use geometric optics, as the computing time would be tremendous, using the Lorentz-Mie theory. This on the other hand means that by measuring very small particles in certain circumstances, errors can occur (also see “Limitations and inaccuracies of the PDA technique”).

Figure 3-3 shows the intensity of the scattered light for a 5  $\mu\text{m}$  gasoline droplet in dependence of the scattering angle (air as surrounding media). The upper half of the diagram shows parallel polarised light, the lower one perpendicular polarised light. The scattering intensity is plotted logarithmically. In all calculations the real part of the refractive index was used, as the influence of absorption can be neglected, when using pure gasoline. Thereby special care needs to be taken to ensure that the fuel does not contain any additives which fluoresce or absorb light at the laser wavelengths. Parallel polarised light does not reflect any light under a certain angle, called the Brewster-angle. For gasoline under ambient conditions, this Brewster-angle lies at around  $70^\circ$ . The angle of the intensity of the second order reflected light for gasoline lies at about

150° and is called the rainbow angle. The Mie-scattering involves all geometric scattering orders and diffraction effects. The maxima and minima in the scattering light intensity are caused ‘internally’ by interference effects between the different scattering orders. The distinct dominance and the relative uniformity of the first order refracted light (for transparent particles) can be observed well.

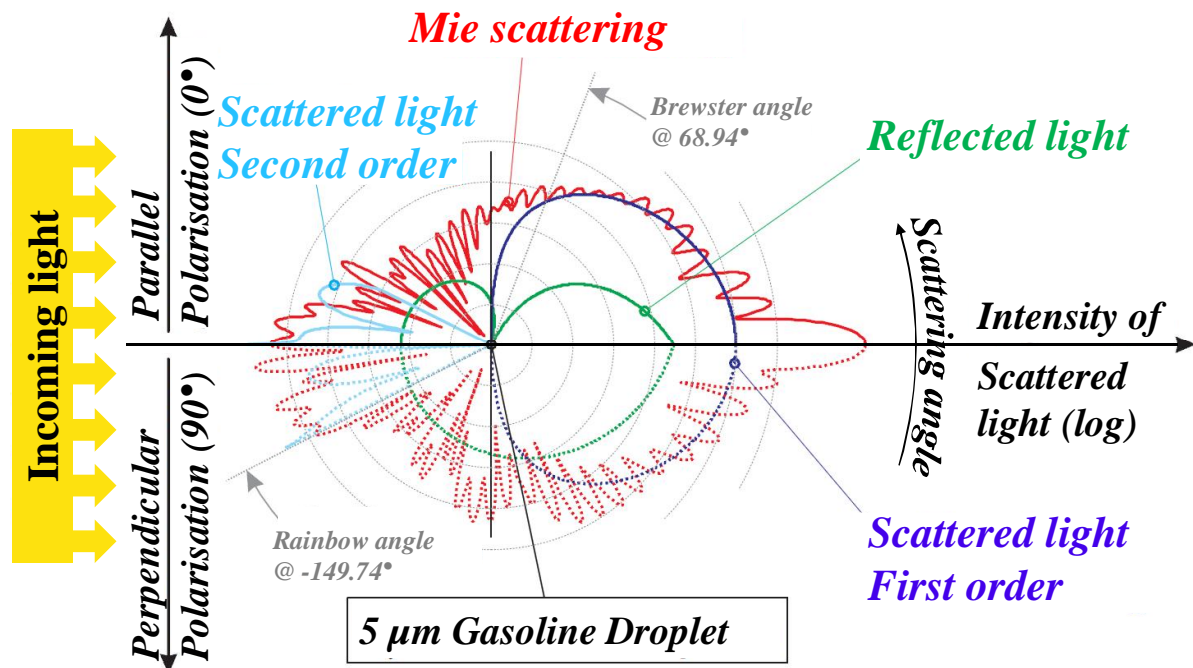


Figure 3-3 – Polar diagram of scattered light from a 5 μm gasoline droplet ( $n = 1.42$ ). The intensity of the scattered light is plotted logarithmically. Calculation according to [99], [41]

### 3.1.2 LDA Measurement Principles

The arrangement of the laser beams and the receiver optics is shown in Figure 3-4. The angles defining a PDA setup are shown, as well. The two laser beams coming from the transmitting optics are focused by the front lens of the system. In the focal point of the lens where the two laser beams cross, a *measurement volume* is formed due to the coherence and the linear polarisation of the two beam parts. This measurement volume basically consists of layers of constructive and destructive interference, so called *fringes*. A particle flying across these fringes will scatter light with a well defined modulation. This scattered light is collected by the receiving optics and converted to an electrical signal by a photomultiplier.

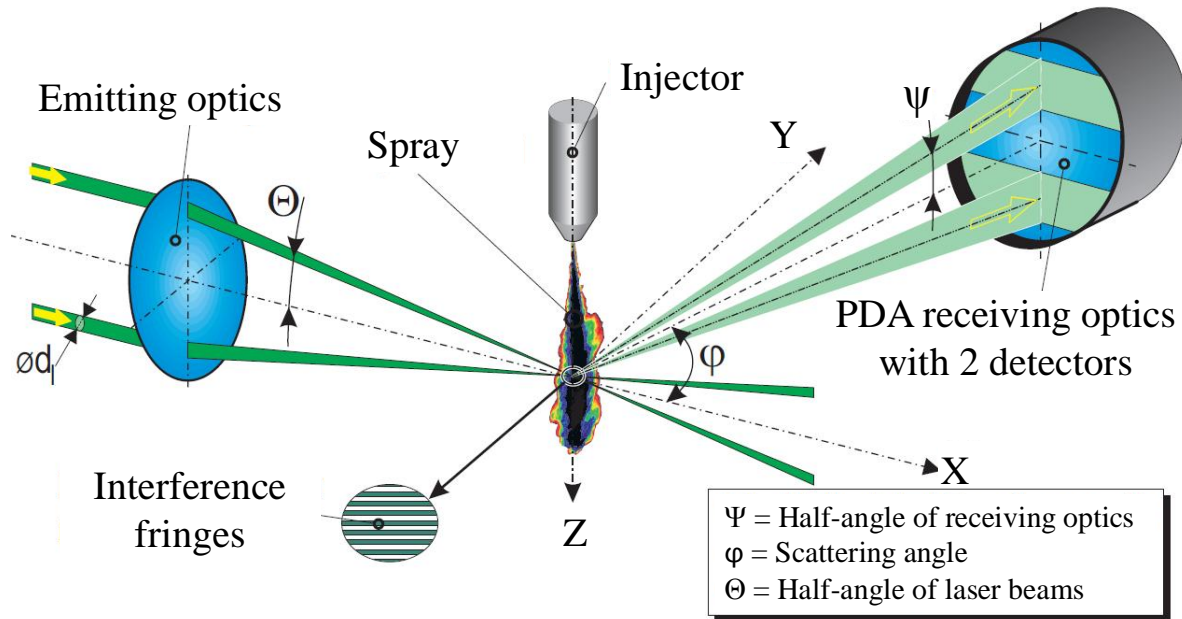


Figure 3-4 – Schematic of setup of the emitting and the receiving optics [41]

### 3.1.3 Determination of the particle velocity

The frequency of the light scattered by the particles travelling through a laser beam is shifted due to the velocity of the particle (Doppler Effect). However, this frequency shift is very small compared to the frequency of the light which makes it very difficult to measure it directly. Therefore current LDA/PDA measurement systems have a setup that uses the scattered light from two crossed laser beams. Due to interference between the scattered light from the two beams the effect of the Doppler shift can be found at a much lower frequency in the intensity modulation of the scattered light. However, instead of calculating the intensity modulation directly from the Doppler shifts it is much easier to use the fringe model: The fringe model simply looks at how the bright/dark layers in the measurement volume are scattered by the droplets. The spacing between the fringes depends on the laser wavelength and the angle between the two laser beams, only:

$$\text{Interference distance } d_f: \quad d_f = \frac{\lambda}{2 \cdot \sin(\Theta)} \quad (20)$$

A particle flying through the measurement volume produces a light burst with a certain frequency. This frequency is proportional to the particle velocity component perpendicular to the fringes:

Velocity component  $v$ : 
$$v = f_D \cdot d_f \tag{21}$$

So far this velocity component doesn't contain any information about the direction of the particles velocity. The latter can be determined by moving the fringes through the measurement volume. A particle standing still in the moving grid scatters light in the frequency which the fringes in the measurement volume have. If the particle moves with the fringes, the frequency of the scattered light is decreased and vice versa. This moving fringe pattern can be generated by shifting the frequency of one laser beam (typically  $10^{14}$  Hz) by 40 MHz. This shift is usually induced on the laser beam by a Bragg cell.

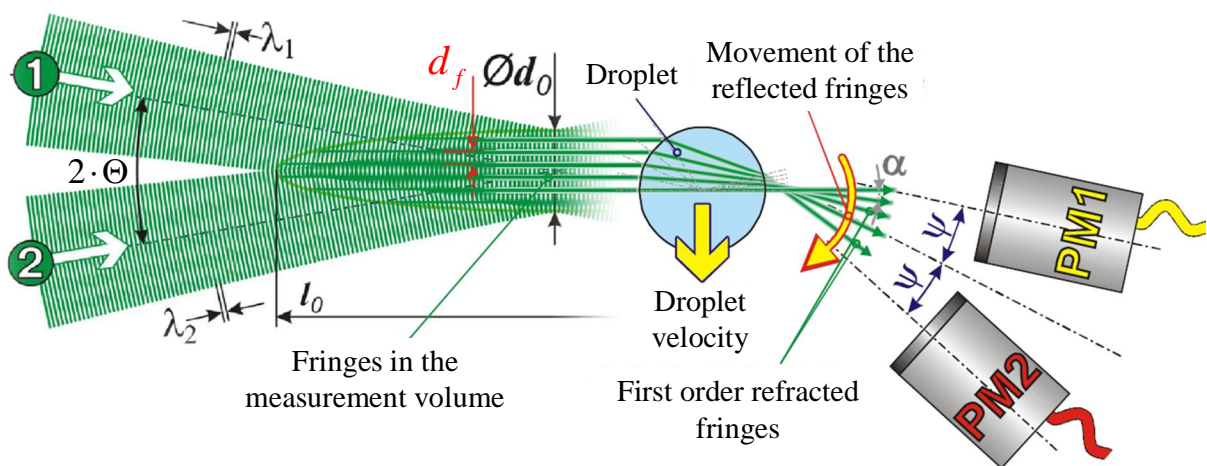


Figure 3-5 – Determination of the phase shift  $\Phi$  between the two photomultipliers [100]

### 3.1.4 Determination of the particle size

A droplet travelling through the measurement volume acts like a lens. It maps the scattered light of the fringes onto the photomultipliers. If the droplet (or the fringe pattern) is moving, then the phase shift between the two detectors is a function of the radius of curvature thus the diameter of the droplet. The phase shift is generated by the different angles of the scattered light to the detectors.

Using geometrical optics, the relation between the phase shift  $\Phi$  and the particle diameter  $d_p$  can be calculated for two scattered light orders:

Using the light reflected by the particle for sizing, the relation between particle diameter  $d_p$  and the phase shift  $\Phi$  can be calculated as follows:

$$\Phi = \frac{2 \cdot \pi \cdot d_p}{\lambda} \cdot \frac{\sin(\Theta) \cdot \sin(\Psi)}{\sqrt{2 \cdot (1 - q)}} \tag{22}$$

For light exiting the droplet after passing it once (1. Refracting order), the phase shift is calculated with:

$$\Phi = \frac{-2 \cdot \pi \cdot d_p}{\lambda} \cdot \frac{m \cdot \sin(\Theta) \cdot \sin(\Psi)}{\sqrt{2 \cdot (1+q) \cdot (1+m^2 - (m \cdot \sqrt{2 \cdot (1+q)}))}} \quad (23)$$

Whereas for  $q$  the following is applied:

$$q = \cos \Theta \cdot \cos \Psi \cdot \cos \varphi \quad (24)$$

And the refractive index ratio between particle and the environment is:

$$m = \frac{n_{particle}}{n_{environment}}; (m > 1) \quad (25)$$

Where  $\Phi$  denotes the measured phase shift,  $\varphi$  the scattering angle in the X-Y plane between the laser beams and the detectors,  $\Theta$  is half the angle between the two laser beams and  $\Psi$  is half the angle between the two detectors for the scattered light (see Figure 3-4).

For higher scattering orders no closed equation exists. [41].

### 3.1.5 Determination of Measurement volume size

The PDA measurement principle implies that the scattered light of one single droplet only, is detected by the receiving optics. Therefore the size of the measurement volume defines the maximum droplet density at which the technique still works. The smaller the measurement volume is, the higher is the chance to have only one droplet in it at a time (In fact the measurement volume should be smaller than the shortest distance between the droplets, to make sure one droplet left the measurement volume before the next droplet enters it). But at the same time it is better to have the measurement volume at least twice as big as the largest droplets in the spray. This is mainly due to the fact that the Gaussian intensity distribution in the laser beams can lead to measurement errors (see also chapter 3.1.10 on page 52). The use of three detectors at a scattering angle around  $70^\circ$  (Brewster's angle) minimizes this error.

The diameter of the measurement volume, i.e. the ellipsoid shape that two cylindrical objects form when they are crossed, is mainly depending on the

diameter  $d_1'$  of the laser beams in the focal point of the front lens. This is controlled by the lenses focal length  $f$ , the wavelength  $\lambda$  of the laser and the beam diameter of the parallel laser beams (more precisely the beam waist or beam focus) before the lens:

$$\text{Beam waist } d_1': \quad d_1' = \frac{4 \cdot \lambda \cdot F}{\pi \cdot d_1} \quad (26)$$

The diameter of the measurement volumes (length of the two short axis) correspond approximately the beam diameter  $d_1'$ . The ellipsoids length  $d_z'$  is defined by the angle between the two crossing laser beams:

$$\text{Length of measurement volume } d_z': \quad d_z' = \frac{d_1'}{\sin(\Theta)} \quad (27)$$

The PDA receiving optics reduces the effective (i.e. visible) length of the measurement volume with a slit diaphragm in the light path of the receiver (100 $\mu$ m in the used setup).

### 3.1.6 Selection of scattering angle

The quality of a PDA measurement is widely depending on the chosen observation angle (= scattering angle):

1. The order of the scattered light (reflection, first refraction order, second refraction order ...) chosen for the measurement has to be as dominant as possible.
2. The scattering light intensity under the chosen angle has to be sufficiently strong.
3. The relationship between the phase shift and the droplet diameter, which is calculated by the Mie-Lorentz theory, has to be non-ambiguous and linear.

A number of studies are reported in the literature, dealing with the question about the right scattering angle (e.g. [97], [101]). For investigations of hydrocarbon fuels ( $n \approx 1.42$ ), the optimal scattering angle lies in the range of the Brewster angle, thus approximately 70°. Choosing this angle and with setting the polarisation plane of the laser accordingly, the PDA receiving optics detect scattered light from the first order refraction, only. The relationship between the



phase shift and the droplet diameter is continuous and linear down to small droplet diameters (compare Figure 3-6).

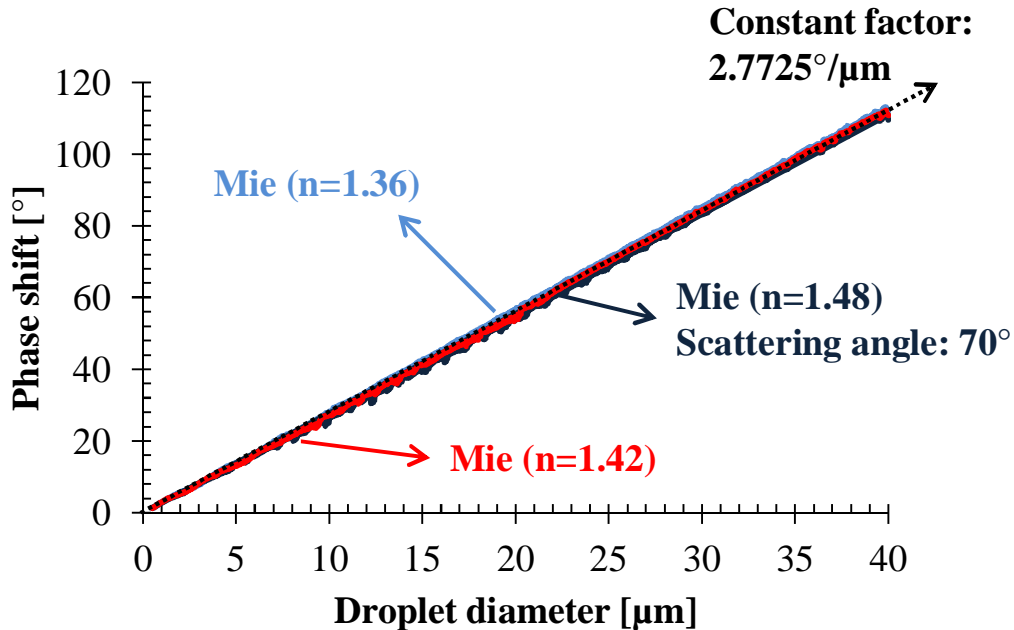


**Figure 3-6 – Relationship between scattering angle and droplet diameter for different refractive indices [41]**

Figure 3-6 shows the dependency between phase shift and droplet diameter for different refractive indices, calculated according to the Lorentz-Mie theory for a scattering angle of 70° (scattering light of the first refracting order). PDA measurements carried out employing this angle of 70° exhibit another characteristic: The phase diameter correlation is only weakly affected by changes of the refracting index, e.g. rising of the droplet temperature or changing composition of the droplet. As a consequence, the droplet temperature or fuel composition as a function of time does not necessarily need to be known for the droplet size measurement. This is especially important for evaporating conditions, where the droplet temperature is unknown and changes in time.

The distinct decline in the phase-diameter relationship for refracting indices lower than 1.3 is caused by the declining dominance of the intensity of the scattered light over the reflected light. A change in the refractive index from  $n = 1.48$  to  $n = 1.24$  effects a change in the Brewster angle from 68° up to 78°. An increased mixing of the orders of scattered light provokes an increased divergence from the linear phase diameter relationship.

A disadvantage using PDA measurements with an observation angle of  $70^\circ$  compared to the often employed  $30^\circ$  scattering angle is the loss of signal intensity by about one order of magnitude. But this can be compensated by an increase in laser power and accordingly high power sending optics.

### 3.1.7 Selection of the velocity measurement range

Besides the choice of the scattering angle, the angle between the two part beams has to be selected according to the requirements of the measurement. The angle between the two parts of the laser beam is chosen by the distance of the two parallel beams and the focal length of the systems front lens:

- PDA-processors have a limited signal frequency range. The bandwidth of the model used in this work ranges from 35 up to 80 MHz (relative to the 40 MHz). The velocity measurement range is coupled directly to the signal frequency range by the distance between the fringes in the measurement volume. Since for a given laser wavelength this distance depends on the angle between the laser beams only, the velocity measurement range consequently depends also on this angle only.
- The smaller the measurement volume, the bigger the maximum density in droplet number at which a PDA measurement is still possible (but in the mean time the data rate in the less dense peripheral zone of the spray decreases).
- According to the laws of the Gaussian optics, the diameter of the beam waist in the focal point of a lens is reciprocally proportional to the beam waist diameter in front of the lens (equation(26)). As the expansion of the laser beams in the deployed optical setup is directly depending on the distance of the parallel laser part beams, the following relationship is valid: The smaller the distance before the front lens, the larger the velocity measurement range. By reducing the distance, simultaneously the beams are expanded less, leading to an increased measurement volume and hence the measurable droplet density is reduced.
- A further factor, caused by the electronics limits the maximum velocities measurable: The droplet has to remain in the measurement volume for at least 270 ns in order to be recorded by the PDA processor. For the

measurement volume diameter of 39  $\mu\text{m}$  (as used in this measurements), this implies a maximum droplet velocity of 145 m/s.

Due to these opposing requirements, namely a preferably large velocity measurement range versus a measurement volume as small as possible satisfying higher droplet densities, a trade-off exists and an appropriate set-up must be carefully chosen, according to the conditions to be expected. The parameter sets utilised in the present experiments can be found in the Appendix (page 160)

### **3.1.8 Selection of the size measurement range**

As no phase shifts exceeding  $2\pi$  can be measured, the size measurement range is defined by the selection of the scattering angle and the arrangement of the detectors in the PDA measurement technique. In the applied Dantec PDA receiving optics the angle  $\Psi$  between the detectors can be reduced by adaptable slits and so the size measurement range can be doubled.

As the light intensity of the light scattered by the droplets is proportional to the second power of the droplet diameter ( $d \geq \lambda$ ), the maximum usable signal dynamic of the PDA processor can additionally narrow the effective droplet size range that can be measured.

### **3.1.9 PDA layout on the experiment**

The system used is divided in a commercial receiving optics from DANTEC (DANTEC 57X10 2D) and a non-commercial, high power transmitting optics which was designed by Dr. Graham Wigley et al [102]. The receiver was connected to a DANTEC 58N10-Enhanced Signal Processor.

The schematic diagram in Figure 3-7 and the image in Figure 4-8 show the PDA setup of the atmospheric spray rig at Loughborough University. The laser beam produced by a Coherent INNOVA-90-4 laser is separated in a green beam (514.5 nm) for axial velocities and a blue beam (488 nm) for the radial velocities. The beams are then individually focused (#6) into a Bragg cell (#5) which separates them into two part beams. The two separated part beams are then widened up to the designated beam distance (#7) and parallelised (#8). The four parallel part beams are recombined onto a common axis by a mirror system and focused into the measuring point by the front lens.

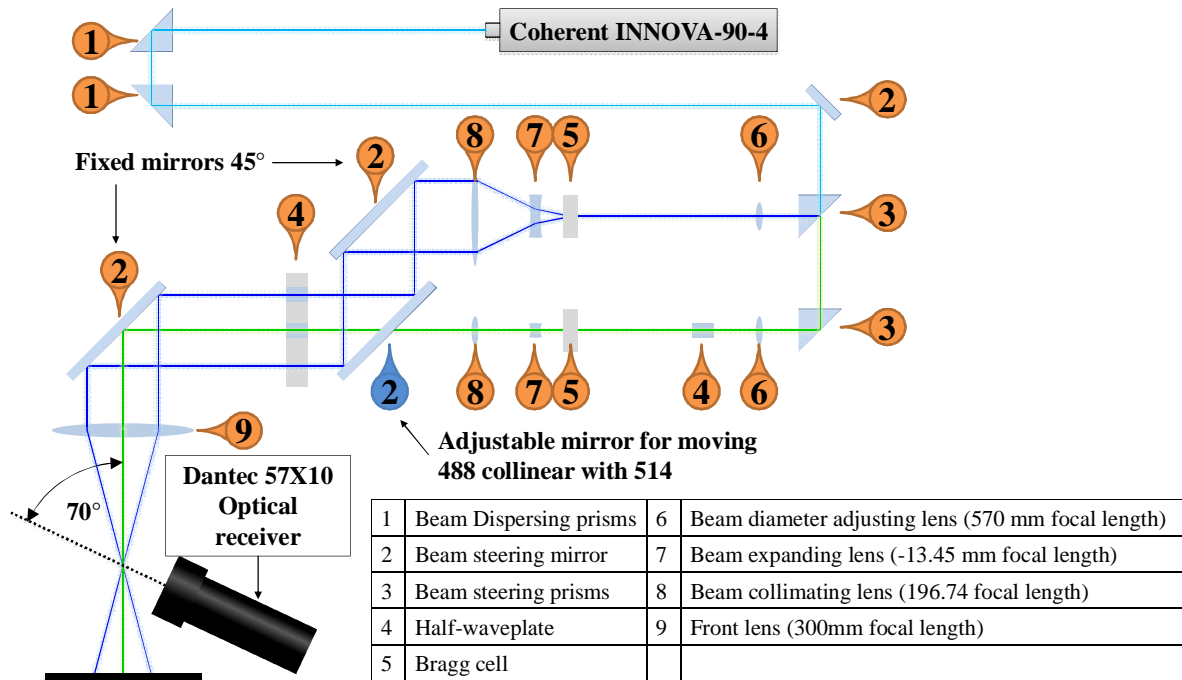


Figure 3-7 – Scheme of the PDA setup at Loughborough University

The scattered light exiting the measurement volume is collected by the optical receiver (Dantec 57X10) and converted by the photomultipliers into electrical signals.

The Dantec 58N50 PDA signal processor, interfaced with a PC using a Dantec 85G130 PC interface card first separates a droplets scattering light signal from the background noise. If a burst from a droplet is detected as such, the processor determines the frequency of the burst (droplet velocity) and the phase shift (droplet diameter) by a cross covariance function. Based on the quality demands defined by the operator, such as sphericity, maximum droplet diameter etc., the processor decides whether it accepts the signals as valid samples and sends them to the PC or whether it rejects them.

The parameter used for this work can be found in the appendix (page 160)

### 3.1.10 Limitations and inaccuracies of the PDA technique

The relationship between the measured variables (frequency and phase shift) and the actual values (velocity, diameter) is only depending on the chosen arrangement of the PDA setup, a calibration is not necessary. However, the following uncertainties and limitations have to be taken into account for the interpretation of the data. These influencing factors can be aroused by the

measurement technique itself or due to the application of the technique on the experiment:

- The size measurement works for spherical droplets, only. The PDA processor determines the phase shift of the scattered light from three different directions (Figure 3-8). The measurement is rejected, if the phase shift between the different detector combinations deviates too much (this is user defined). This results in the invisibility of strongly oscillating droplets, or droplets which have been deformed by the aerodynamic forces or of droplets which are about to break up.

In addition to the control of the size measurement, the utilisation of three detectors allows also an extension of the size measurement range:

The precise measurement is done by the two detectors with the largest distance from each other, D1 and D2. The ambiguity of the phase shift  $\Phi_{(1,2)} > 2\pi$  between detector D1 and detector D2 can be interpreted correctly as long as the phase shift between the closer detectors D1 and

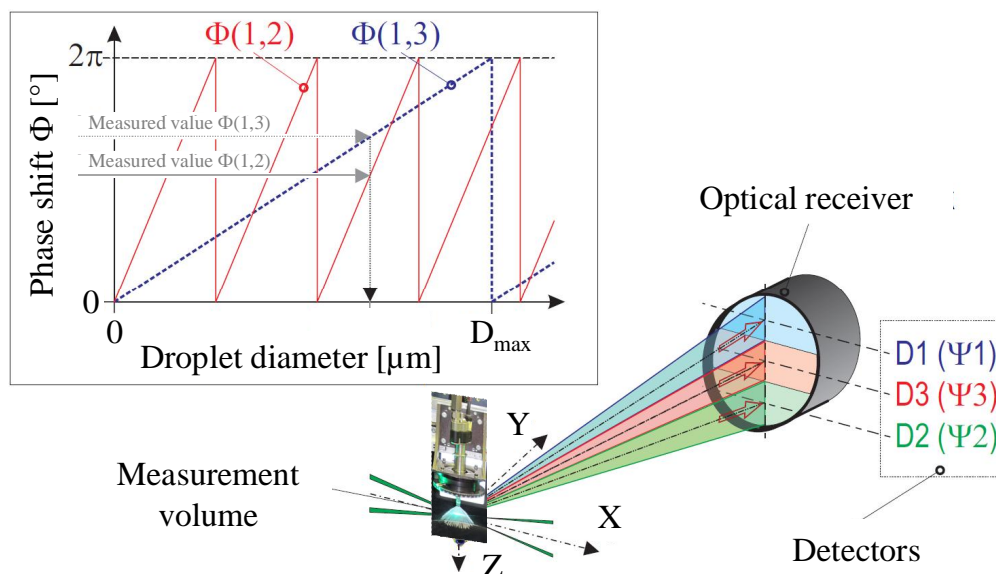


**Figure 3-8 – Increase of the measurement range and monitoring of the size measurement with the three detectors of the optical receiver [41]**

D3 is  $\Phi_{(1,3)} < 2\pi$  (Figure 3-8).

- The PDA processors use a constant factor between phase shift and droplet diameter to determine the droplet size. Figure 3-9 shows the percentage of

the divergence of this simplification from the effective phase shift calculated according to the Lorentz-Mie theory. The difference is smaller than  $\pm 5\%$  for a refractive index lower than 1.30. If the oscillations in the Lorentz-Mie-curves and the so generated peaks are taken into account, the difference is smaller than  $\pm 10\%$ .

- In very dense sprays a PDA measurement is not possible anymore: Often there is more than one droplet in the measurement volume and the resulting superimposed scattering light signal cannot be interpreted anymore by the PDA processor. Also the light on its way to the measurement volume can be weakened or bent so that the measurement volume can't be formed. Or the scattered light can't get to detector anymore and so the signal to noise level decreases until the signal is lost in the noise. Furthermore the general weakening of the scattered light intensity leads to

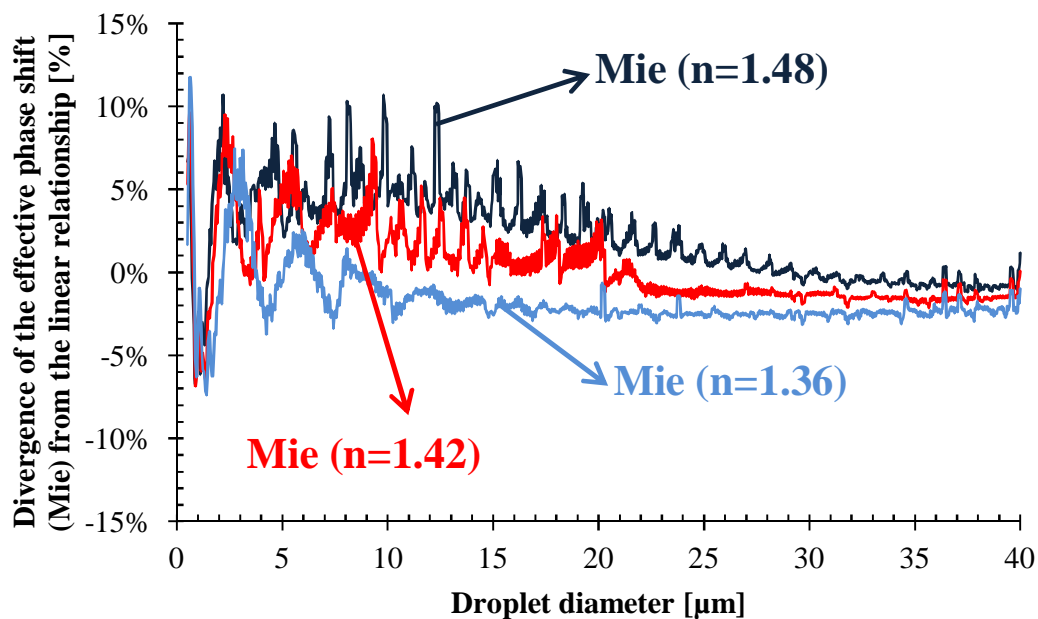


**Figure 3-9 – Relative error due to the effective phase shift from the linear simplification [41]**

a loss of signal for the small droplets, therefore the measured mean droplet diameter rises, even though nothing has changed on the injection system.

- The angles and dimensions of the PDA setup can only be measured to a given precision:

- An error of 0.5 mm in the distance between the parallel laser beams and the front lens causes an error in the velocity as well as the size measurement of 1.5 %.
- A discrepancy of one degree between the theoretical and the effective scattering angle leads to an error in the size measurement of 0.4 %.
- For the analysis of the measurement the PDA processor uses fixed levels of discretisation for velocity as well as size values. This can lead to large uncertainties for small droplets. (Typical quantitative values: 0.05 m/s per Bit for the velocity measurement (range ~140 m/s) and 0.2  $\mu\text{m}$  per Bit for the size measurement (range ~100  $\mu\text{m}$ ).

### **3.1.10.1 Trajectory effect**

Due to the Gaussian intensity distribution in the laser beam, a droplet does not get illuminated homogeneously over its surface. The relations between reflected and refracted scattering light intensities vary, depending on the position of the droplet in the measurement volume. As the phase – size relation is valid for the dominant scattered light, only, this leads to inaccurate measurements. This effect has to be taken account as soon as the expected droplet sizes are in the range of the measurement volume diameter or bigger. The detected droplets in this study were always much smaller than the diameter of the measurement volume. Therefore the trajectory effect does not noticeably influence the measurements. [103], [104], [105]

### **3.1.10.2 Slit effect**

The observable domain of the measurement volume can be reduced by means of an aperture in the light path of the receiver optics (cf. “Determination of Measurement volume size”, p.47). As discussed earlier, the PDA method needs either reflected, first order or second order refracted light. The composition of the scattered light produced by droplets at the border area of the observable domain varies, depending on the droplet position. If a droplet flies along this border of the visible slit, the dominance of the wrong scattering light (reflected) can lead to wrong measurements. Once again, the influence of this effect depends on the relation between droplet size and slit diameter.

For the setup used in this work (scattering angle  $70^\circ$ , first order refraction, three detectors for droplet size measurement) neither the slit, nor the trajectory effect had a big influence on the droplet size measurement. The measurement as close to the Brewster angle as possible minimized the influence of reflected light on the measurement.

The settings in the PDA software and the chosen setting affect the uncertainty of the results, as well. The settings used in this work can be found in the Appendix (Table 6 on page 160).

### **3.1.11 Data evaluation**

A data set for a PDA measurement consists of a series of single measurements composed of information about time of occurrence, velocity and size of each droplet. As per injection only few measurements accrue (depending on the position of the measurement volume in the spray), data from a number of realisations is compiled for subsequent evaluation. Afterwards the data is averaged over consecutive time bins (typically 10 to 50  $\mu\text{s}$ ) relative to start of injection. For each time step the differently quantified averaged velocities and diameters can be calculated. Depending on the information that is of interest, different values are obtained (e.g.  $D_{10}$ ,  $D_{21}$ ,  $D_{32}$ , Mean velocity).

### **3.1.12 Software**

For the PDA data acquisition and post-processing (measurement, validation and saving on the PC), DANTEC's SizeWare Version 2.4 was employed. The ensuing evaluation was carried out by means of existing software [106] and a Matlab code specifically developed in the framework of this thesis.



### ***3.2 2D light section technique/Mie scattering***

The 2D section technique applied in this work is based on Mie scattering (i.e. light scattered by particles in the order or larger than the wavelength of the light, compare chapter 3.1.1, page 43). Light from a laser sheet is scattered from liquid interfaces (e.g. droplets blobs, ligaments or the liquid core) exiting the nozzle. The scattered light from the particles is collected and recorded with a camera. Where a lot of liquid structures are the signal is strong, whereas regions with few droplets emit a weak light signal and the areas with gas or fuel vapour emit no light and appear as dark areas on the image. A drawback of the Mie scattering method is the non linearity of its signal. Bigger droplets reflect much more light than smaller ones do. Therefore this technique cannot be used to quantify the amount of droplets nor can it be inferred how the droplets look or how big they are which could indicate at which atomisation-state (e.g. still liquid core, in the primary atomisation regime, etc.) the spray in the observed region is. Another big drawback of the technique is multiple scattering. The light scattered on the liquid structures which is not captured by the camera or left the experimental zone via a window, is scattered on other liquid structures out of the plane of the laser sheet. This causes problems in quantifying the intensity measurements. With their hollow cone shape, A-injectors tend to multiple scattering, even more than multi-hole injectors [107]. Therefore droplets which are not in the measurement volume built by the laser sheet are visible and are therefore measured. This generates uncertainties in measurement of penetration length or spray/cone angle.

### ***3.3 Shadowgraphy***

The Shadowgraphy method allows the qualitative visualisation of the liquid and the vapour phase of the spray. It combines the characteristics of the Schlieren method with those of the shadow imaging technique. All three techniques are sensitive to density variations. Back light imaging or shadow imaging has the lowest sensitivity to these variations as its background consists of diffuse light and the Schlieren effect is just an unwanted side effect (compare Figure 3-13). The Schlieren method on the other hand is the most sensitive technique to density variations as it works only with the deflected rays but does not directly

visualize the liquid phase. Shadowgraphy is a mixture of both methods and benefits of the advantages of both techniques, the visualization of density variations using Schlieren method and Shadow imaging for the liquid phase.

### Schlieren principle

The light rays travelling through the experimental region get deflected by changes in refractive indices along their path as principally shown in Figure 3-10. The degree of deflection is an integration of the changes in refracting indices along the path as described in formula(28). The Schlieren technique cuts off this deflected light rays with a knife edge. As the light is missing on the image plane, a dark spot will appear instead, as illustrated in Figure 3-11, and where two rays hit the same spot it will be brighter than its surrounding.

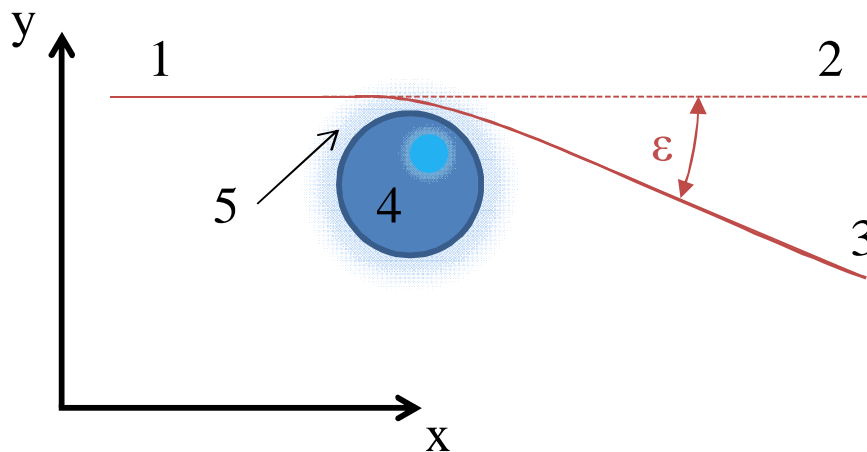


**Figure 3-10 – Ray of Light travelling through the density variations around an evaporating droplet**

- 1 = Ray of light before the experimental region
- 2 = Theoretical light path after experimental region
- 3 = Actual light path after experimental region
- 4 = Droplet
- 5 = Evaporated fuel layer around the droplet

The deflection  $\epsilon$  is described as

$$\epsilon = \frac{1}{n} \cdot \int \frac{\partial n}{\partial y} \cdot \partial x \quad (28)$$

With the refractive index in gases defined as

$$n - 1 = k \cdot \rho \quad (29)$$

And for gas mixtures

$$\frac{(n-1)}{\rho} = \sum_j k_j \cdot m_j \quad (30)$$

With

n = Refractive index

$\rho$  = Gas density in [kg/m<sup>3</sup>]

k = Gladstone-Dale coefficient [m<sup>3</sup>/kg] (e.g. Nitrogen k=0.00024 m<sup>3</sup>/kg)

m = Mass fraction

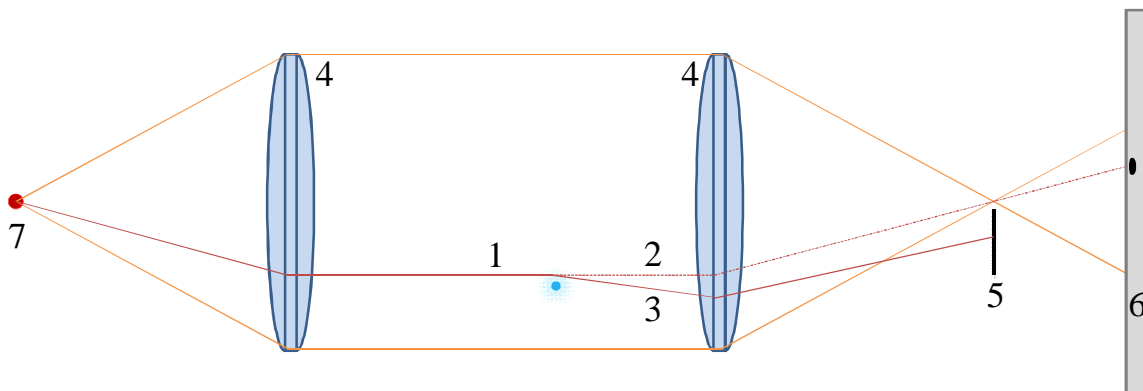


**Figure 3-11 – Lens based Schlieren setup**

1 = Ray of light before the experimental region

2 = Theoretical light path after experimental region

3 = Actual light path after experimental region

4 = Spherical lens

5 = Knife edge

6 = Image plane

7 = Point light source

The degree of cut-off defines the sensitivity of the Schlieren method. Figure 3-12 shows a cut-off variation for the same, non evaporating conditions (300K) in the HTDZ (isooctane as fuel). A knife edge was held into the beam, until the beam area in the focal point was cut-off by 0%, 50%, 90% and 110%, where the percentage stands for the part of the diameter of the light beam in the focal point. With no cut-off (which is actually called the Shadowgraphy method) no Schlieren can be seen for the non evaporating conditions. As a small part of the isooctane is evaporating, even at ambient temperatures, Schlieren start to show when the knife edge is moved more and more into the focal point of the second

lens. At 50% cut-off a small amount of vapour can be seen at the back of the main spray. If the cut-off is increased to 90%, this cloud of evaporated fuel shows more clearly. As soon as the whole beam is blocked by the knife edge, no more “ballistic photons” reach the camera. Only the light beams which are deflected around the knife edge can be seen. On the tips of the different streaks a lot of refracted light can be seen. One could say that these are changes in refracting index due to the vapour cloud around the evaporating droplets of isooctane, which is partly true. The light which can be seen at the back of the main spray – in the vortex which is following the injection – has most probably been deflected by the vapour. Around the spray tips, on the other hand, most of this effect comes from diffraction at the droplets. Here most of the droplets are freshly formed and didn’t have enough time to evaporate. Especially when compared to the case with 90% cut-off no light at all can be seen in these regions.

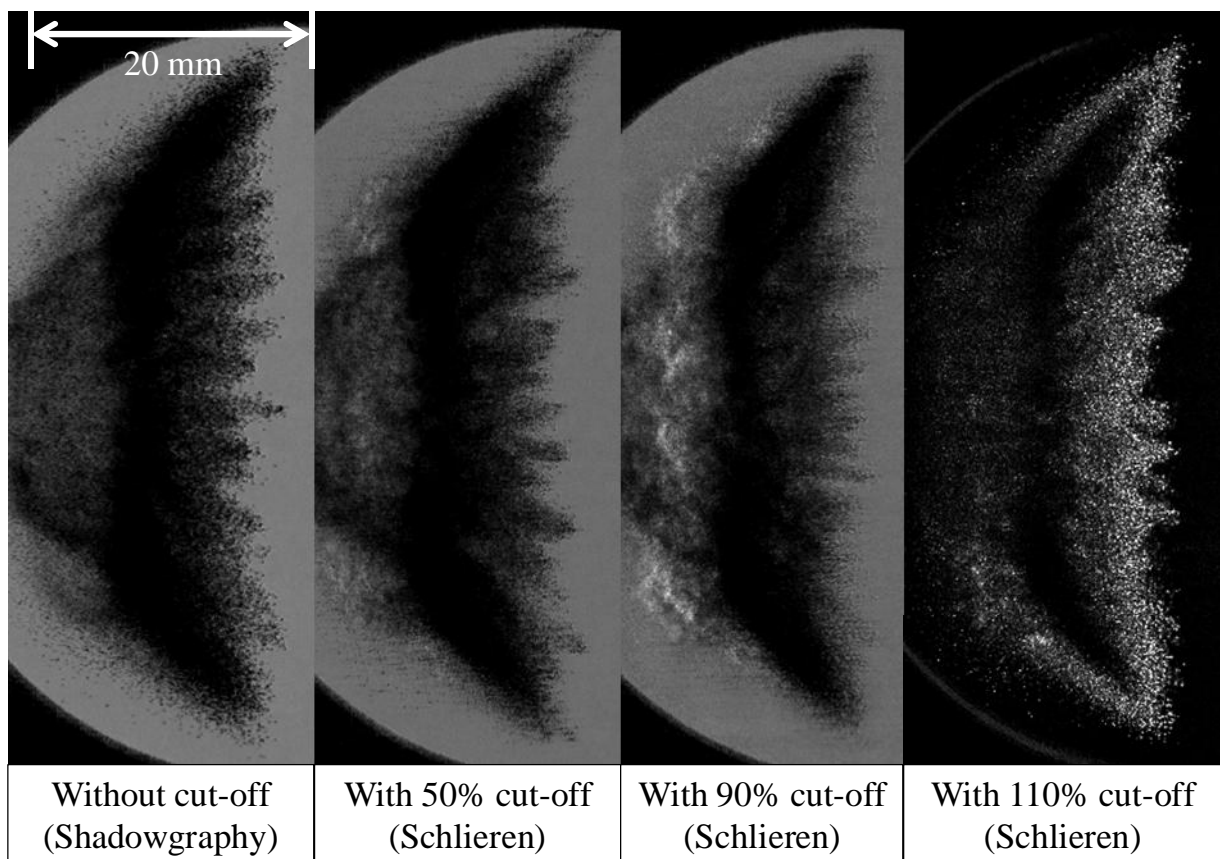


**Figure 3-12 – Knife edge cut-off variation for non evaporating conditions (atmospheric, injection pressure 12MPa, isooctane, needle lift 23  $\mu\text{m}$ ): Outer left image without cut-off, outer right image with full cut-off**

Schlieren effects can also occur when using the shadow imaging technique. If the density variations are too strong (high density, high temperature and high swirl) and the optical path through this region of strong changes in density is too long, the Schlieren effect can be observed even despite the highly dispersed background, as can be seen Figure 3-13. The sharp edges of the windows start to be covered by wavy structures and the dark region behind the edge has the same intensities as the white background. Like a mirage the white background wafts over the dark edge of the window. The conditions within the HTDZ are not as hot, dense and turbulent as in the Spray Combustion Chamber. Therefore such effects are not expected.

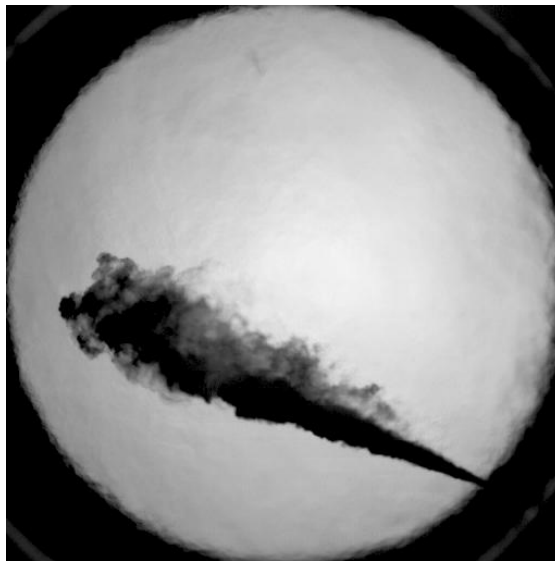


**Figure 3-13 – Schlieren in a shadow image due to high density variations in the Spray Combustion Chamber (SCC) at Wärtsilä Switzerland Ltd [107]**

Shadowgraphy represents a compromise between the sensitivity of the Schlieren and the ability to visualize liquid spray of the background imaging technique. For non evaporating conditions the Shadowgraphy shows the liquid phase of the spray and under evaporating conditions it shows the liquid and the vapour phase. As under evaporating conditions the differentiation between the two phases is not well defined, the Shadowgraphy was used to determine the vapour phase and the Mie images were used to find the liquid phase. Being a 2D light section technique, the Mie method has another advantage. Other than the Shadowgraphy it is a real 2D picture. It shows only droplets which are in the plane of the laser sheet (if multiple scattering is neglected). Shadowgraphy on the other hand shows the integrated information over the whole spray. This is very important when the inner and outer structure are investigated.

## 4 Experimental setup

*“You know, these kids today come out of graduate school, and they are whizzes with Computer Aided This and That, and they do courses in science theory and math and software design ... but they don’t get to bend tin. Not only that; they’ve never seen anything fail before. In engineering, experience gained is directly proportional to the amount of equipment ruined.”*

*-Stephen Baxter*

### 4.1 High Temperature High Pressure Cell (HTDZ)

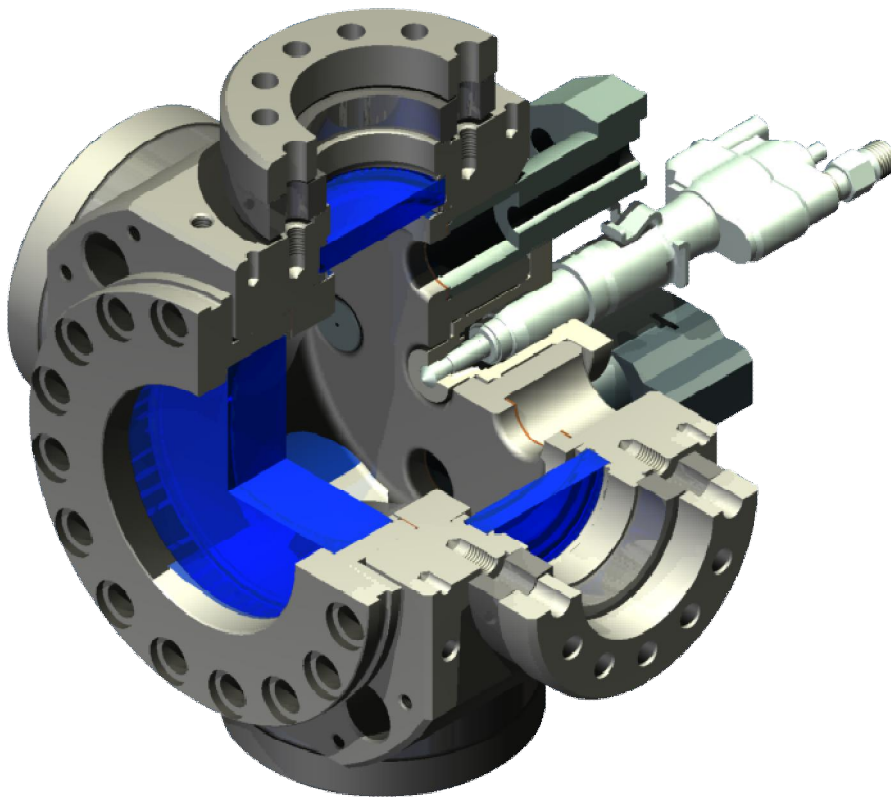


**Figure 4-1 – Isometric view of the HTDZ with mounted A-injector**

The Shadowgraphy and Mie experiments made for the present work have been carried out in a constant volume, high temperature and high pressure cell (in German *Hochtemperatur Hochdruckzelle: HTDZ*). The cell allows a wide variation of pressure and temperature combinations. Designed for the investigation of Diesel sprays, the pressure can be varied from 0.1 to 8 MPa (before combustion) and the wall temperatures can be set up to 800 K which results in gas temperatures of about 750 K (without H<sub>2</sub>-pre combustion). Pressure and temperature can be set independently to simulate engine like conditions [41]. The cell body, the sapphire windows and the measurement equipment are designed to withstand diffusive and premixed combustion with end pressures up to 20 MPa. Figure 4-1 shows an Isometric view of the HTDZ and Figure 4-2 gives a schematic overview of its conceptual scheme.

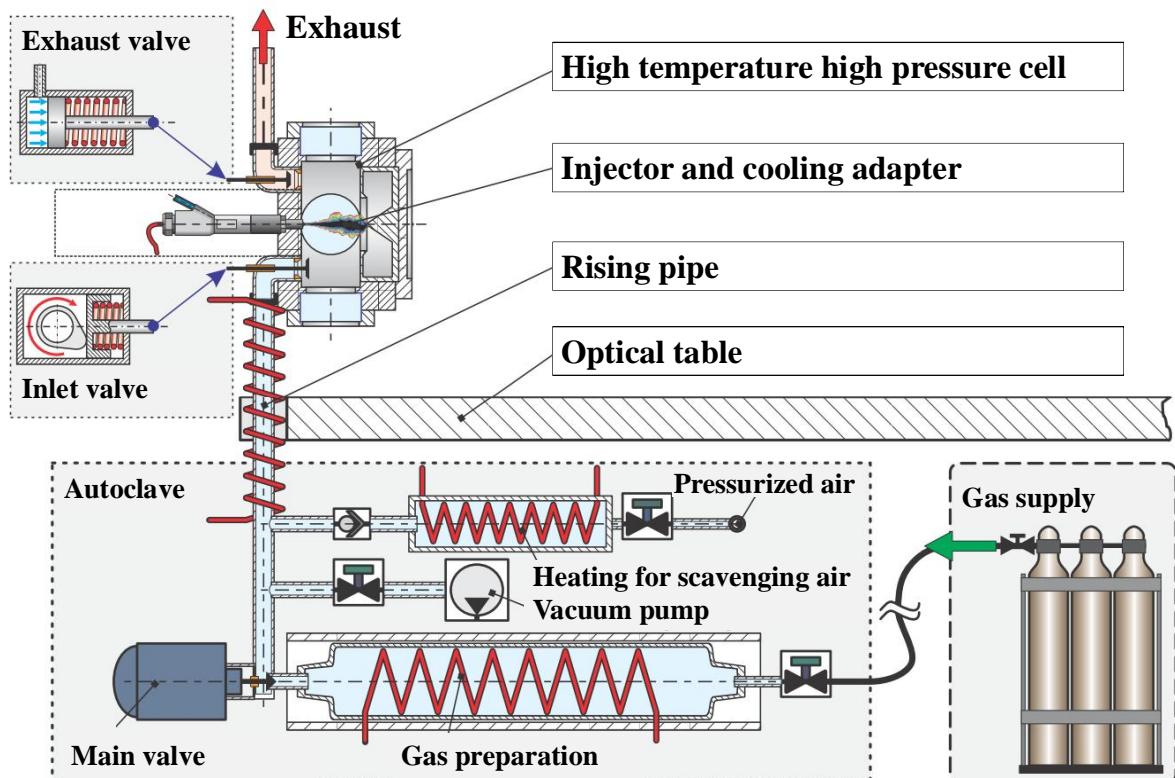


Figure 4-2 – Scheme of the HTDZ

The combustion chamber with the injector tip protruding out of its rear wall has a bore of 110 mm and is 40 mm deep. Together with the pockets formed by the windows and additional crevice volumes it forms a constant volume capacity of about 0.5 litres. The combustion chamber is optically accessible from five sides; a big sapphire window (optical width 90 mm) is in front of the injector and four small sapphire windows (optical width 42 mm) allow the optical access from the

side, perpendicular to the injector axis. The injector is mounted horizontally in a cooling adapter, so that the temperature of the in injector and therefore the temperature of the fuel can be controlled independently from the temperature of the cell body. The rear wall also houses the inlet valve under the injector and the exhaust valve on top of it. Both valves are pneumatically actuated. The inlet valve is shaped like a common automotive inlet or exhaust valve and it opens into the combustion chamber. The exhaust valve opens in the other direction (into the exhaust pipe) and acts so also as a safety valve, in case the chamber pressure exceeds a given value.

<b>Parameter</b>	<b>Specification</b>
Diameter/Width	Ø 110 mm /40 mm
Volume	≈ 0.5l
Temperature range	300–700K (without $H_2$ -pre combustion)
Pressure (before combustion)	0.1 - 8 MPa
Pressure (after combustion)	≤ 20 MPa

**Table 2 – Summary of the most important parameters of the constant volume cell**

For a constant volume cell the gas preparation is quite complex. An autoclave preconditions the gas (air,  $N_2$  or any non combustible, bottled gas) with the temperature and pressures necessary to achieve the conditions set by the user. To control the pressure insight the cell, a water cooled Kistler 7061BK precision pressure sensor [108] was used. As for the optical investigations only four of the five windows were necessary, the fifth which is underneath the cell body was replaced by a dummy. In this dummy the pressure sensor and a K-type temperature element were mounted. This position for the pressure measurement was necessary because the strong vibrations in the cell body caused by the valves can be seen on the pressure trace (perpendicular to the measurement axis, the sensitivity of the piezo sensors to noise is much smaller).



## 4.2 Optical setup in the cell

To obtain information of the Mie scattering and the Shadowgraphy technique at the same time, the two methods have been used simultaneously. Two LaVision HSS6 high speed cameras have therefore been installed perpendicular to each other. To guarantee a uniform light intensity for both sides of the spray, the laser sheet was projected from the front side of the chamber onto the needle tip of the injector. Perpendicular to the laser sheet parallel light for the Shadowgraphy technique was set up, as can be seen in Figure 4-3.

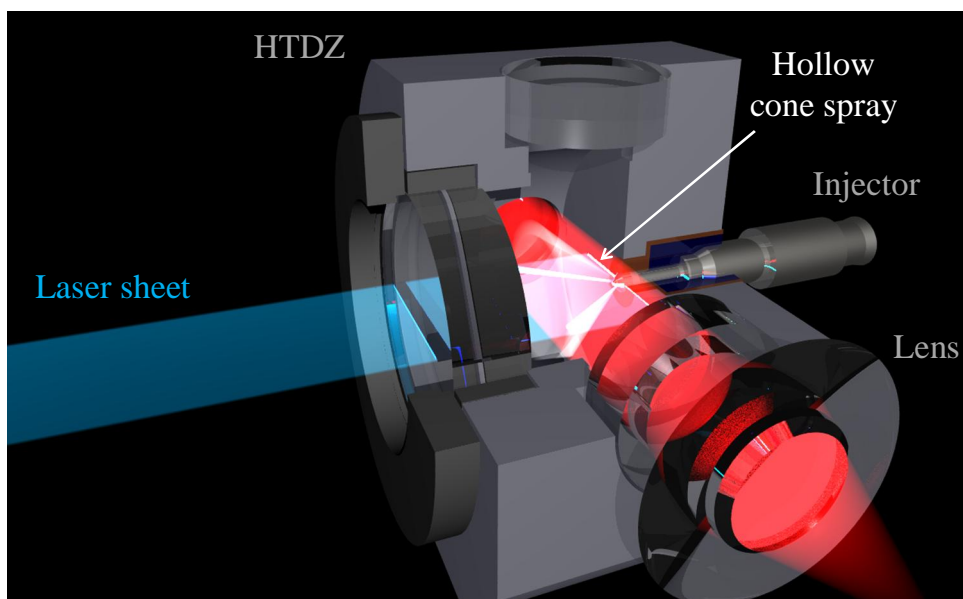


**Figure 4-3 – Mie and Shadowgraphy light path at the HTDZ**

This setup allows the observation of the inside of the spray and the outer contour at the same time. The combination of the two measurement techniques allows the investigation of the liquid phase via Mie scattering while the Shadowgraphy delivers a look on the outer shape of the liquid and delivers qualitative information about the vapour phase. Another advantage of this arrangement is the possibility to investigate the hollow cone from two sides at the same time, what makes it easier to detect eventual irregularities.

The two high speed cameras have been operated at 20 kHz frame rate, with an image gating of 8.333  $\mu$ s. Despite the short exposure time the signal was strong enough for a proper evaluation. The reason for this lies in the combination of suitable laser wavelengths with sufficient power.

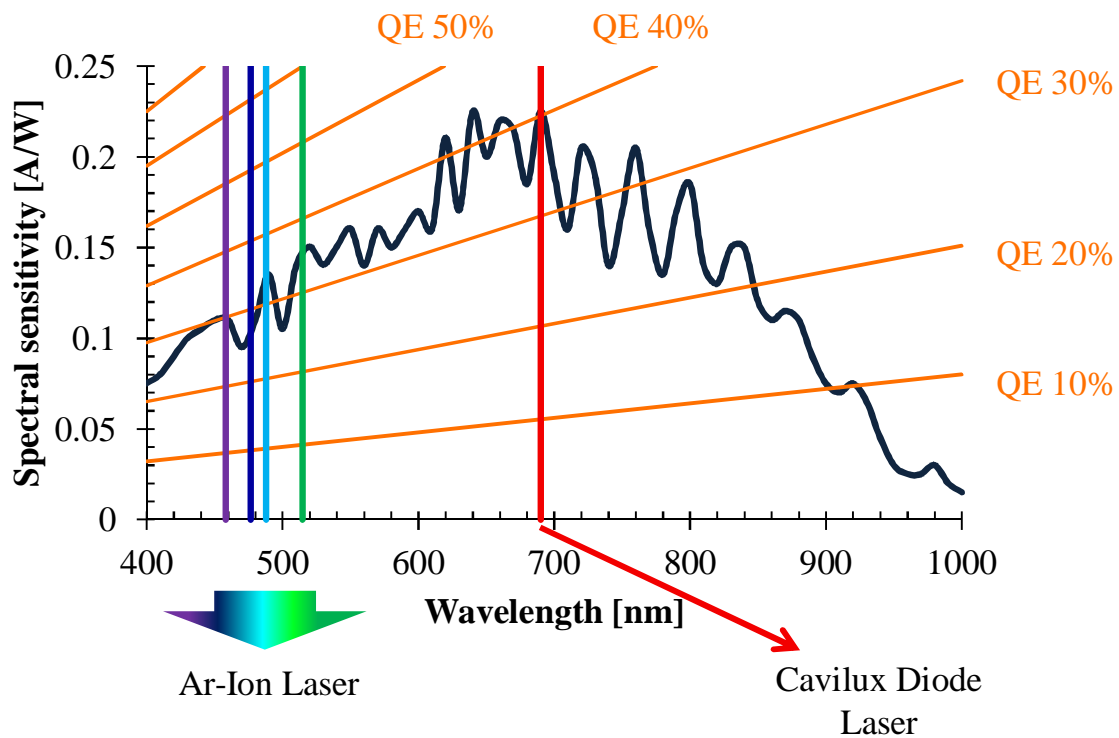


**Figure 4-4 – Response curve of a HSS6 CMOS chip compared to the wavelengths of the lasers used (with permission of LaVision)**

Figure 4-4 shows the response curve of a HSS6 CMOS chip. It shows the spectral sensitivity of the chip on the vertical axis plotted over the wavelength. The sensitivity is defined as Ampere exiting the chip per Watt of photons hitting it [109]. The red lines indicate the quantum efficiency. Quantum efficiency is defined as the photons probability to produce charge carriers. The higher the photons frequency is, the higher is its energy and therefore the higher is its chance to produce a charge carrier. As can be seen in Figure 4-4 the camera has not the same sensitivity over all wavelengths. To get a stronger signal the wavelength of the laser is chosen at a local maximum of the chips intensity. As can be seen, the wavelength of the Cavilux diode laser (690 nm) for the Shadowgraphy lies at the cameras absolute maximum sensitivity, with quantum efficiency over 40 %. Also for the Mie scattering technique most of the light captured by the chip on or close to a local maximum. The two strongest wavelengths of the Ar<sup>+</sup>- laser (Spectra physics; 514.5 nm with 43 % and 488 nm with 20 % of total power) lie both within a local maximum with more than 30 % of quantum efficiency.

The total all-lines power output of the Ar<sup>+</sup>-laser was 3W. Using the setup shown in Figure 4-5 (blue light path) the laser beam was widened in the horizontal direction by a plano concave, cylindrical lens ( $f = -75$  mm) with anti reflective coating (AR 455 – 515 nm). Four dielectric mirrors were used to guide the beam around the optical table and to make the optical path long enough to widen the

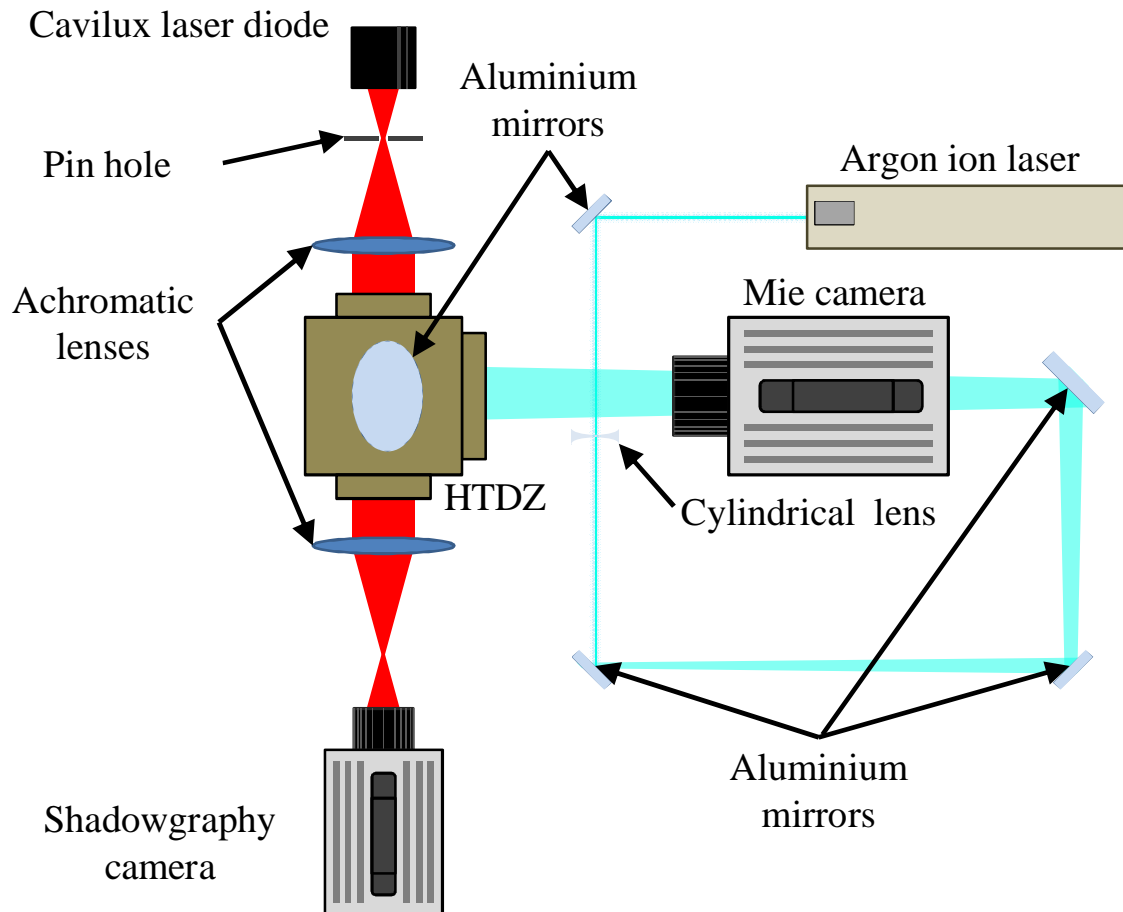


**Figure 4-5 – Light paths of the Mie and Shadowgraphy setup**

laser beam as much as needed. The strong widening of the sheet by the cylindrical lens allows (due to the Gaussian intensity distribution) a uniform intensity distribution and so a more uniform illumination of the spray. 1,100 mm before the injector tip, the light sheet is focused perpendicular to the sheet by a plano convex cylindrical lens ( $f=1,000$  mm) to generate a very thin light sheet. This guarantees a long and thin measurement volume for sharp images and the best resolution of the droplets.

The light scattered at the particles is collected with the high speed camera. This was run with a spatial resolution of 512 x 512 Pixel. Together with the objective lens used (Tamron, 80-110mm) a spatial resolution of 0.0862 mm/Pixel could be

achieved. The CMOS chip has a dynamic range of 12 bit (4,096 steps). The exposure time can be varied from the minimum of 0.1 ms up to  $1/f$  ms (depending on the given frequency of the camera). For the Mie scattering technique it was set to 8.333  $\mu$ s. Assuming a maximal velocity of 100 m/s the Spray tip covers almost 10 pixels during exposure time. The lateral of the spray never reaches these high velocities and can therefore be detected very accurately.

The images have been post-processed with a commercial software code [110] and Matlab code. Two signal intensities have been employed to characterise the spray: Pixels with intensity higher than 100 counts are considered as spray, pixels with counts higher than 1,500 have been treated as dense spray. This dense spray consists of areas with a high number of droplets, further they can contain ligaments, blobs and even liquid core, where it still exists. It is the regime from first to early second breakup. These thresholds have been chosen by comparison with the LDA measurements. Figure 4-6 shows a cross section view of 10 averaged Mie images, at an axial distance of 2.5 mm underneath the needle tip (atmospheric conditions, 12 MPa injection pressure, 23  $\mu$ m needle

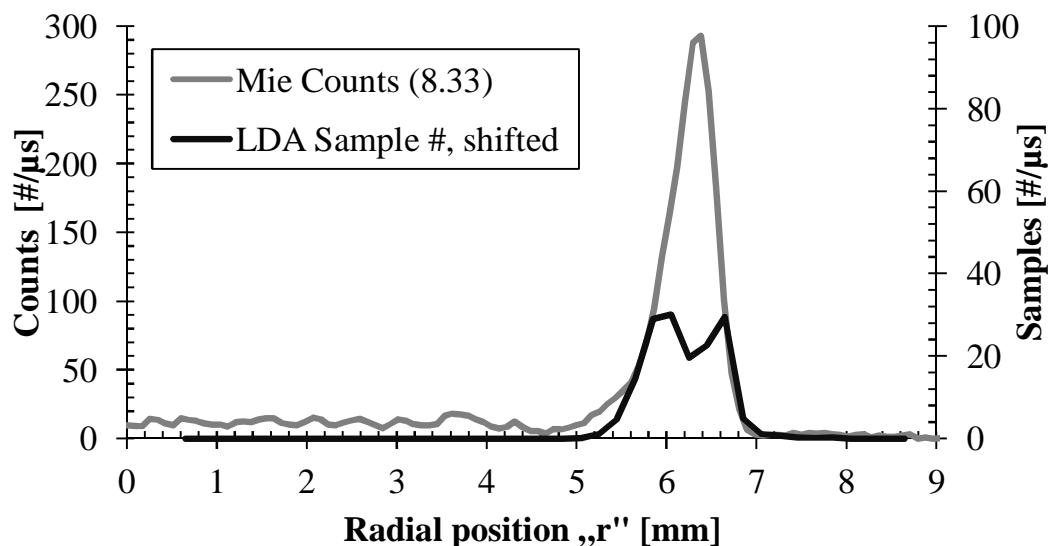


**Figure 4-6 – Cut through Mie image at axial distance  $z=2.5$  mm compared with LDA measurement at axial distance  $z=2.5$**

lift). The image was taken 150  $\mu$ s after start of injection (SOI). The counts have been divided by the exposure time resulting in counts/ $\mu$ s (gray line). On the same graph the sample numbers of an LDA measurement under the same

conditions at the same distance under the injection tip is plotted (black line). The values are in samples/ $\mu$ s to achieve an objective comparison between the two measurement techniques. On the inner side the Mie measurement has a completely different behaviour than the LDA measurement.

On the outside of the spray both techniques show very similar structure of the spray. Towards the inner of the streak the LDA signal stops rising while the Mie scattering light still increases until it reaches a maximum at 6.4 mm. On the inner side the side of the streak is again reproduced very well from both techniques. But from 5.4 mm on the Mie signal stays higher than the LDA droplet number. This is not possible as no droplets are present, especially in the region towards the injector axis. The light measured with the Mie method comes from multiple scattering events on the streaks located behind and before the measurement plane [90].

To make sure that this scattered light will not affect the measurement, the threshold was set to 100 counts for the outside. On the inner side an evaluation of the measurements was not possible, as a differentiation between the scattered and the multiply scattered light (scattered from other sources) cannot be made.

### **The Shadowgraphy setup**

Figure 4-5 shows the path of the Shadowgraphy setup (red path). A Cavilux® Diode laser, driven at a frequency of 20 Kilohertz and with a wavelength of 690 nm, was focused on a pinhole. In combination with translucent glass on the side towards the lens, the setup simulated a point light source. This point light source was set into the focal point of a first lens (focal length 400mm, clear aperture 95mm) in such a way that that a beam of parallel light was produced, which was sent through the HTDZ. On the camera side a second lens of the same type was used to focus the light back into the objective lens (Sigma,  $f = 2.8$ , focal length 105 mm) of the second HSS6 high speed camera, which was driven in parallel mode with the Mie camera (20 kHz, 512 x 512 pixel). In front of the objective lens, a narrow band pass filter (centre wavelength 690nm) was used to block the light of the  $\text{Ar}^+$ -laser and the ambient light. The setup resulted in a spatial resolution of 0.08584 mm/Pixel. Due to the short laser pulses – 0.04  $\mu$ s – the Shadowgraphy images become very sharp. The spray tip covers a

distance of only 4  $\mu\text{m}$  in this time, which is within far less than a pixel. The laser pulse was fired 2.5  $\mu\text{s}$  after the exposure time of the camera had started. For the evaluation of the Shadowgraphy images a comparison with the Mie scattering method has been performed. The threshold for the Shadowgraphy measurement has been set in such a way that both techniques qualitatively show a similar behaviour. Figure 4-7 shows the penetration curve of an evaporating case, measured with both techniques. Bearing in mind that the two techniques show measurements of different parts of the spray hollow cone, the two curves show very similar behaviour.

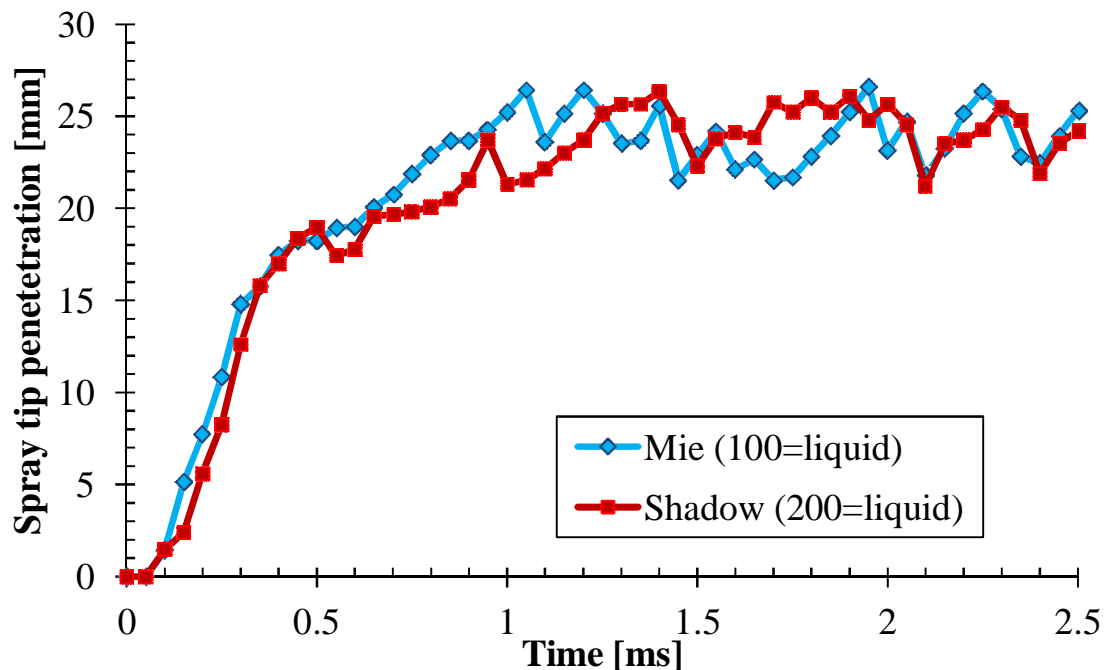
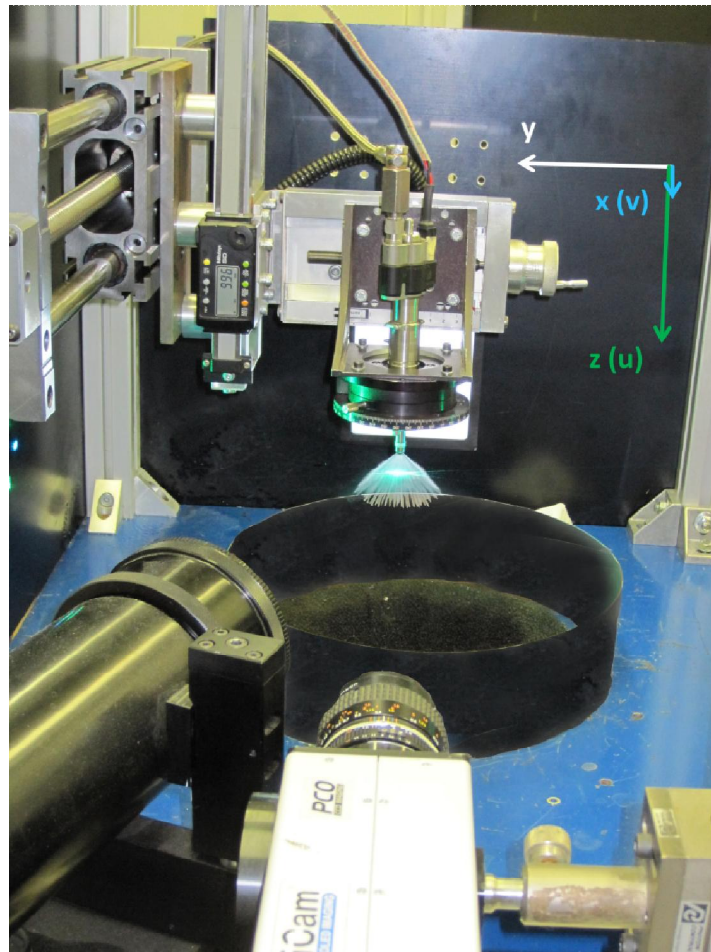


Figure 4-7 – Nominal penetration of the liquid phase under evaporating conditions; measured via Mie scattering (blue) and Shadowgraphy method (red)

### 4.3 PDA setup

In the atmospheric spray rig at Loughborough University 1D-LDA/PDA and 2D-PDA measurements were performed to produce the droplet size and axial and radial velocity fields as a function of time and space. Figure 4-8 shows the setup of the atmospheric spray rig and the PDA system. In the middle the hollow cone spray can be seen, crossing the measurement volume. The injector is rigidly held in a rotation stage, mounted on a precision 3-dimension orthogonal traverse system, visible in the upper half of Figure 4-8. The origin of the measurement grid was located directly under the tip. In a defined grid, the

injector was traversed electronically along its x axis on the following z levels: 2.5, 5, 10, 15, 20 and 30 mm. This way the spray was moved on a radial path through the measurement volume on different axial heights. The detector, in the



**Figure 4-8 – Image of the PDA system and the spray rig**

lower left corner of Figure 4-8, was mounted at an angle of  $70^\circ$  relative to the laser beams as described in the foregoing subchapter (Selection of scattering angle, p.48).

This was chosen to have a small influence on drop size measurements due to changes in the refraction index (e.g. change in temperature, inhomogeneities in fuel mixture, etc.). Table 6 in the appendix gives an overview concerning the settings and specifications of the PDA system.

For the PDA measurements, the rig was operated for 50 seconds at an injection frequency of 5 Hz. In this way, 250 experiments have been carried out at each grid position, to make sure enough samples could be acquired.

To have a control over the measurement volumes position in the spray, a flash screen behind the spray illuminated the spray in order to take shadow images

with a PCO Sensicam. As illustrated in Figure 4-9, the shadow image gives a good view about the measurement volumes position relative to the streaks.

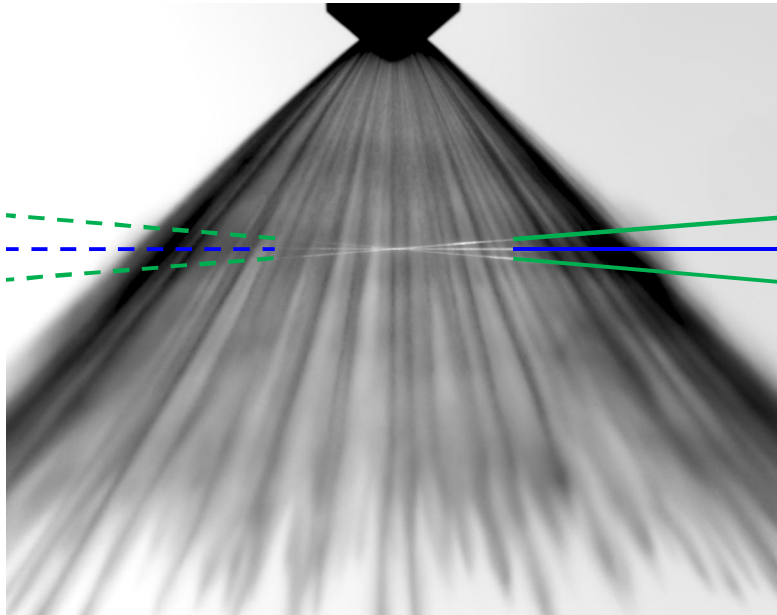


**Figure 4-9 – Shadow image of the hollow cone spray and the four crossing laser beams forming the two measurement volumes**

### ***4.4 Fuel path***

To have reproducible conditions within the fuel system, the fuel pressure for the measurements in the HTDZ was achieved with pressurised nitrogen. A piston in a cylinder transmitted the pressure from the nitrogen to the fuel. A high pressure tube transported the fuel to the injector. A pressure sensor Kistler 4075A was mounted 200mm before the injector. This allowed a very precise measurement of the fuel pressure in the rail and allowed a good estimation of the fuel pressure at the needle.

To control the fuel temperature, the injector was embedded in a cooling adapter. A constant flow of cooling water surrounded the injector and isolated the cold injector from the hot walls of the cell body. The temperature of the cooling water can independently be adjusted. A measurement temperature of an injector dummy showed that the injector tip inside the cell has the same temperature as the cooling water in the adapter.

The Piezo-activated hollow cone injector (A-injector) is a very flexible tool to bring fuel into the cylinder in a controlled, exact and reproducible way. The big advantage thereby is the piezo stack which is used to open the needle. Its lift as



well as its opening and closing characteristic can freely be chosen and combined. To do so, a Direct Injection Control Unit (DICU) was used to charge the piezo crystal and expand it. The DICU allows the generation of five and more different injections in one cycle. The needle lift, the shape of the lift and the closing velocity as well as their shape can independently be set for each of these five injections.

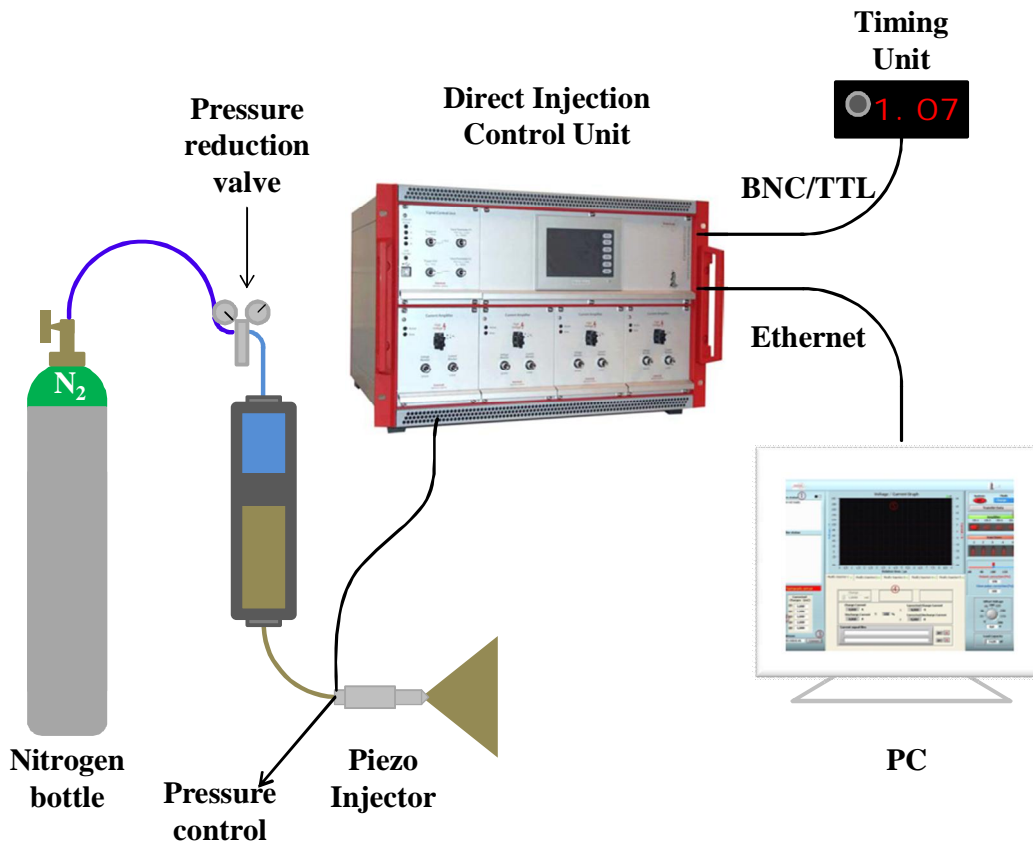


Figure 4-10 – Schematic of the fuel path

## 5 Results and Discussion

*If we knew what it was we were doing, it would not be called research, would it?*  
*-Albert Einstein*

This chapter is divided into different sub chapters. An overview over the measurement conditions and the variations made in this work is given in the first part. The second part deals with the general spray of an A-injector: Spray reproducibility, temporal behaviour of the strings, spray morphology and droplet size distribution. The following chapters present the influence of the operating conditions (gas density, gas temperature, injection pressure, needle lift, fuel properties) on spray morphology and droplet size distribution. In the last chapter a correlation is presented which allows the prediction of spray tip penetration as a function of time.

### Measurement Conditions

The injection of small amounts of fuel has become state of the art in modern Diesel engines [111]. For a pilot injection a small amount of fuel is injected into the cylinder before the main injection, to reduce the premixed combustion noise, the characteristic Diesel “knocking”. Post injections are used to heat up the exhaust after treatment system or to regenerate the PM-filter [112], [113].

Also in gasoline direct injection applications the use of small amounts of fuel becomes more and more important and helps to realize new combustion strategies, such as HCCI/CAI or similar strategies [7]. To help to understand the physics behind injections with small mass, the experiments shown in this work were performed with a fuel mass of 5 mg (with reference needle lift of 23  $\mu\text{m}$  this corresponds to an injection duration of 390  $\mu\text{s}$ ).

To properly investigate the influence of different parameters on spray shape and penetration, one was varied independently. Starting from a *reference point*

(reference operating condition) which was chosen in the middle of the varied range, the influence of the variations was studied individually while keeping the other parameters constant. A spray for Direct Injection applications faces different surrounding gas properties. During an early injection the density in the cylinder is nearly or sub-atmospheric. The late injection, shortly before top dead centre, faces a high gas density. If the injection takes place during the compression stroke, the density will vary between these two conditions. Three different cylinder conditions (gas density: 2.2, 6.6 to 13.2 kg/m<sup>3</sup> Figure 5-1) were chosen on the base of a real combustion process which can be found on an experimental single cylinder engine [7]. Figure 5-1 shows the pressure trace of a new combustion process. The idea behind the new combustion process is to produce more reactive elements during the gas exchange phase. Therefore a negative valve overlap during gas exchange top dead centre (geTDC) is generated: Instead of opening inlet and exhaust valves together which would scavenge the cylinder with fresh air, the exhaust valves are closed before geTDC and before the inlet valves open. Therefore the exhaust gas is compressed again and due to this compression the gas is heated up again. A small amount of fuel is injected into this environment. The high temperatures and the rest oxygen of the  $\lambda \approx 1.4$ -combustion, let the small fuel cloud partly undergo the first ignition [115], [116]. During this process the stable molecules are converted in an

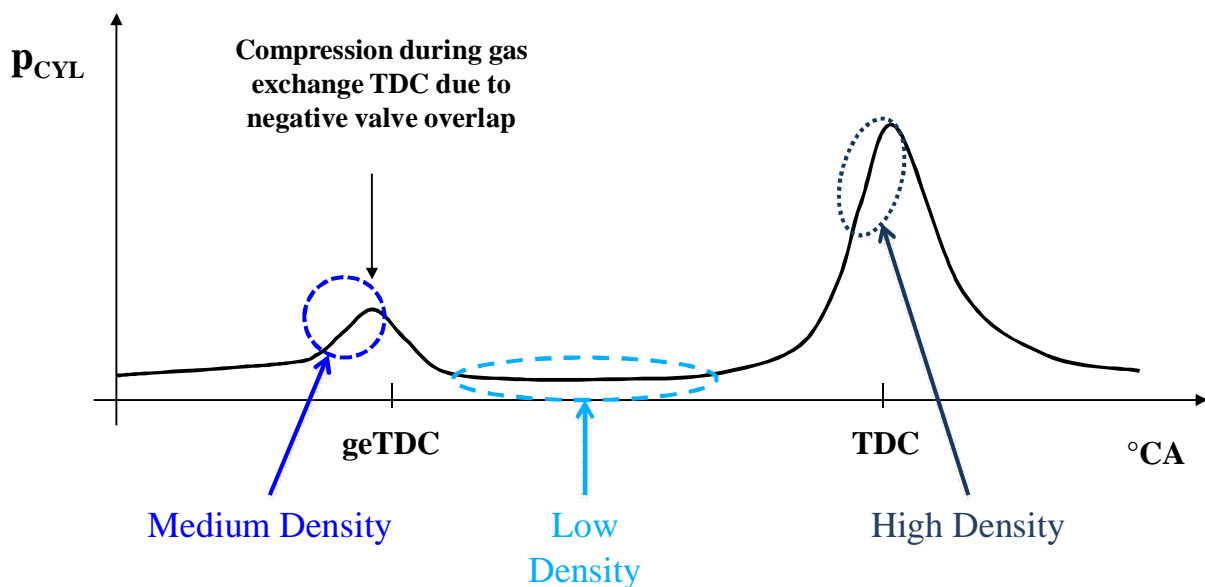


**Figure 5-1 – Conceptual pressure evolution of a CAI combustion process**

exothermic reaction into less stable components (e.g. formaldehyde). Due to the opening of the inlet valves the mixture is cooled down and any ongoing process is stopped.

During the filling process the main amount of fuel is injected into the cylinder. When the inlet valves are closed and the gas is compressed again, the mixture is heated up until it ignites itself. The point when this ignition starts can be influenced by the main injection. The products built in the geTDC-process are supporting this self ignition and stabilize it. In a one cylinder engine a stable CAI-operation could be demonstrated. The present work was conducted in the framework of this research project. Therefore the reference conditions were defined at a density of  $\rho = 6.6 \text{ kg/m}^3$ , which corresponds to in-cylinder conditions during geTDC due to the negative valve overlap. In the HTDZ this was achieved with the back pressure of  $p_{\text{HTDZ}} = 0.6 \text{ MPa}$  for a gas temperature of  $T_{\text{HTDZ}} = 300 \text{ K}$  (for non evaporating conditions). Even though the design pressure of an A-injector is 20 MPa [114] the reference injection pressure was set to  $\Delta p_{\text{inj}} = p_{\text{Rail}} - p_{\text{HTDZ}} = 12 \text{ MPa}$ , in order to investigate the influence of a higher and a lower injection pressure. The needle lift for the reference point was set to  $\varepsilon = 23 \text{ }\mu\text{m}$ . It was varied between 11  $\mu\text{m}$  and 75  $\mu\text{m}$ . For all variations of injection pressure and needle lift the injected fuel mass was kept constant by adjusting the injection duration. In order to investigate the influence of evaporation on the spray morphology two temperatures have been employed: at 300 K the spray has been investigated under non evaporating conditions. For the evaporating cases the temperature was set to  $> 580 \text{ K}$ . This guaranteed the temperature to be above the boiling temperature of all components of the applied fuels; Isooctane (373 K) and gasoline ( $\geq 323 \text{ K} \leq 573 \text{ K}$ ). Table 3 gives an overview over the parameters and their variation performed in this work. All the measurement points shown in Table 3 have been investigated for evaporating and non evaporating conditions.

Measurement Conditions		Gas density	Injection pressure	Needle lift
		[kg/m <sup>3</sup> ]	[MPa]	[μm]
1	Reference conditions	6.6	12	23
2	Low density	2.2	12	23
3	High density	13.2	12	23
4	High inj. pressure	6.6	18	23
5	Low inj. pressure	6.6	6	23
6	Big needle lift	6.6	12	75
7	Small needle lift	6.6	12	11
8	Low density, low injection pressure	2.2	6	23
9	Low density, high injection pressure	2.2	18	23
10	Low density, big needle lift	2.2	12	75
11	Low density, small needle lift	2.2	12	11
12	High density, low injection pressure	13.2	6	23
13	High density, high injection pressure	13.2	18	23
14	High density, big needle lift	13.2	12	75
15	High density, small needle lift	13.2	12	11

**Table 3 –Operating conditions for the conducted measurements**

## 5.1 Reference case

### 5.1.1 Reproducibility of the Spray structure

As a result of the piezo driven pintle valve, the A-injector has an excellent reproducibility. Figure 5-2 shows a series of single images at identical conditions: atmospheric, very low injection pressure ( $p_{inj} = 0.7$  MPa) and medium needle lift ( $\epsilon = 23$  μm). The fluid exits the nozzle as a liquid sheet. Some individual droplets form around the cone. The comparison of the individual images reveals that these droplets change their position only by very small amounts ( $< 0.5$  mm). About 4 mm ( $\approx 87 \cdot d_h$ ) downstream the nozzle, the

liquid sheet starts to build waves. These are enhanced due to interaction between gas and fluid until the sheet breaks up.

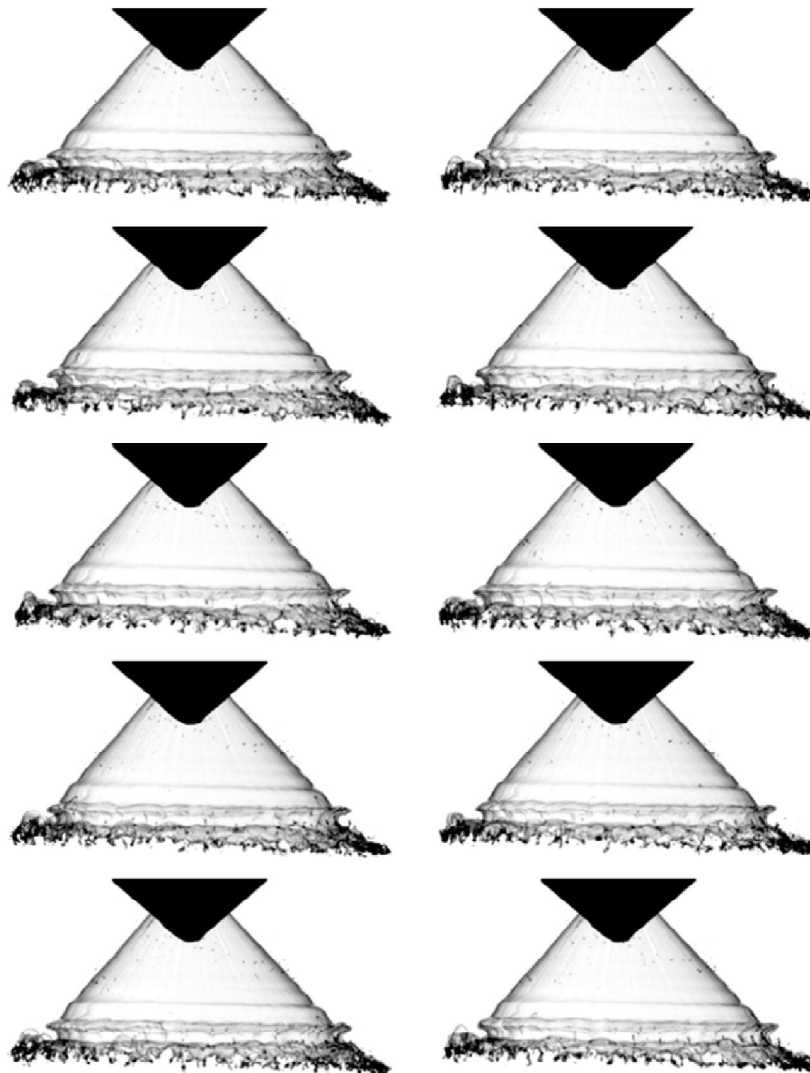


**Figure 5-2 – Reproducibility of the A-injector shown at a very low injection pressure. (individual shadow images, 800  $\mu$ s after SOI, atmospheric conditions,  $p_{inj} = 0.7$  MPa,  $\varepsilon = 23$   $\mu$ m)**

According to the Ohnesorge diagram (Figure 2-7, low pressure case) the breakup regime for these conditions lies within the 2<sup>nd</sup> wind-induced breakup regime. The investigation of the injection rate with the Injection Analyzer showed very high reproducibility too. Standard deviation for 500 injections was about 0.6 mg/ms during opening and closing of the injector which is about 10% of the actual injection rate and at most 3% of the maximum injection rate (compare Figure 7-1 in the appendix). The cases listed in Table 3 show a similar reproducibility.

### 5.1.2 Spray shape of an A-injector

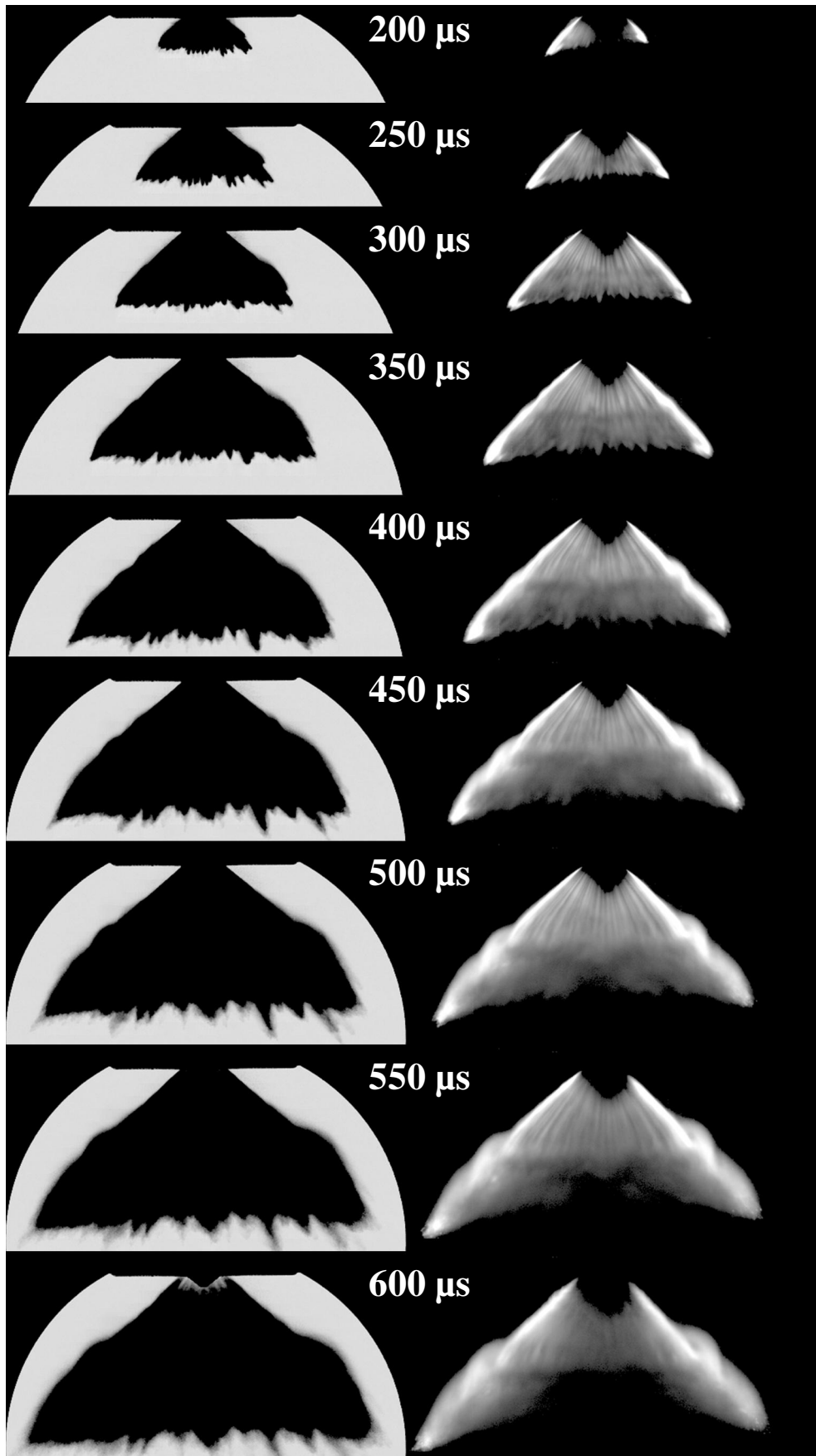


Figure 5-3 – Spray development of an A-injector, Shadowgraphy (left) and Mie (right) for reference case ( $T=300\text{K}$ ,  $6.6 \text{ kg/m}^3$ ,  $p_{inj}=12\text{MPa}$ ,  $\varepsilon=23\mu\text{m}$ )

Compared to other injectors applied for gasoline direct injection (e.g. multihole or swirl injectors), the A-injector has a very distinct shape (also compare [22]). Figure 5-3 shows the development of the injection from the electronic start of injection (injection trigger) until end of injection (EOI) under reference case conditions (temperature 300 K, gas density 6.6 kg/m<sup>3</sup>, injection pressure 12 MPa, needle lift 23 μm, injected mass 5 mg isooctane). The Shadowgraphy images on the left as well as the Mie images on the right are averaged over ten images. In the beginning the spray exits smoothly and the edge of the spray cone is almost perfectly linear (200 μs – 300 μs, on Shadowgraphy and Mie). After another 150 μs the spray surface starts to develop a bump on the outer side. This also shows on the inside of the spray (compare Mie images). Especially from 400 μs on the bump in the middle of the spray starts to interact with the jet and grows steadily. For the A-injector the interesting things from a fluid-dynamical view happen after end of injection (EOI) as can be seen on the Mie images in Figure 5-4. To allow a more detailed investigation of the inner structure the Laser power was increased by about 50 %. This provokes an overexposure of the images during the injection (and shortly after) but the vortices can be tracked much longer and their inside structure is visualised much more detailed. Additionally the injection duration was reduced to visualise the vortices at an earlier stage. As soon as the injection is over, the strong Mie signals from the jet decays as the liquid mass is distributed. This allows the observation of the vortices. As can be seen 500 μs after SOI, two vortices form about 10-12 mm underneath the injector tip. They form on the inner and outer side of the hollow cone. As soon as the injection stops the outer vortex is pushed towards the inner and the two vortices are in an almost steady position. They travel very slowly in axial direction: Between 500 μs and 1750 μs, the centre of the vortices travel about 6 mm downwards and about 2 mm in radial direction. Keeping their position, the two vortices push droplets in axial direction and towards the spray centre. As shown in [34] the vortices and their position can be influenced by injection strategy (e.g. pulsed injection, normal injection or with increased duration injection at reduced needle lift). This allows the shaping of the spray up to a certain degree; the position of the main spray cloud can be influenced.



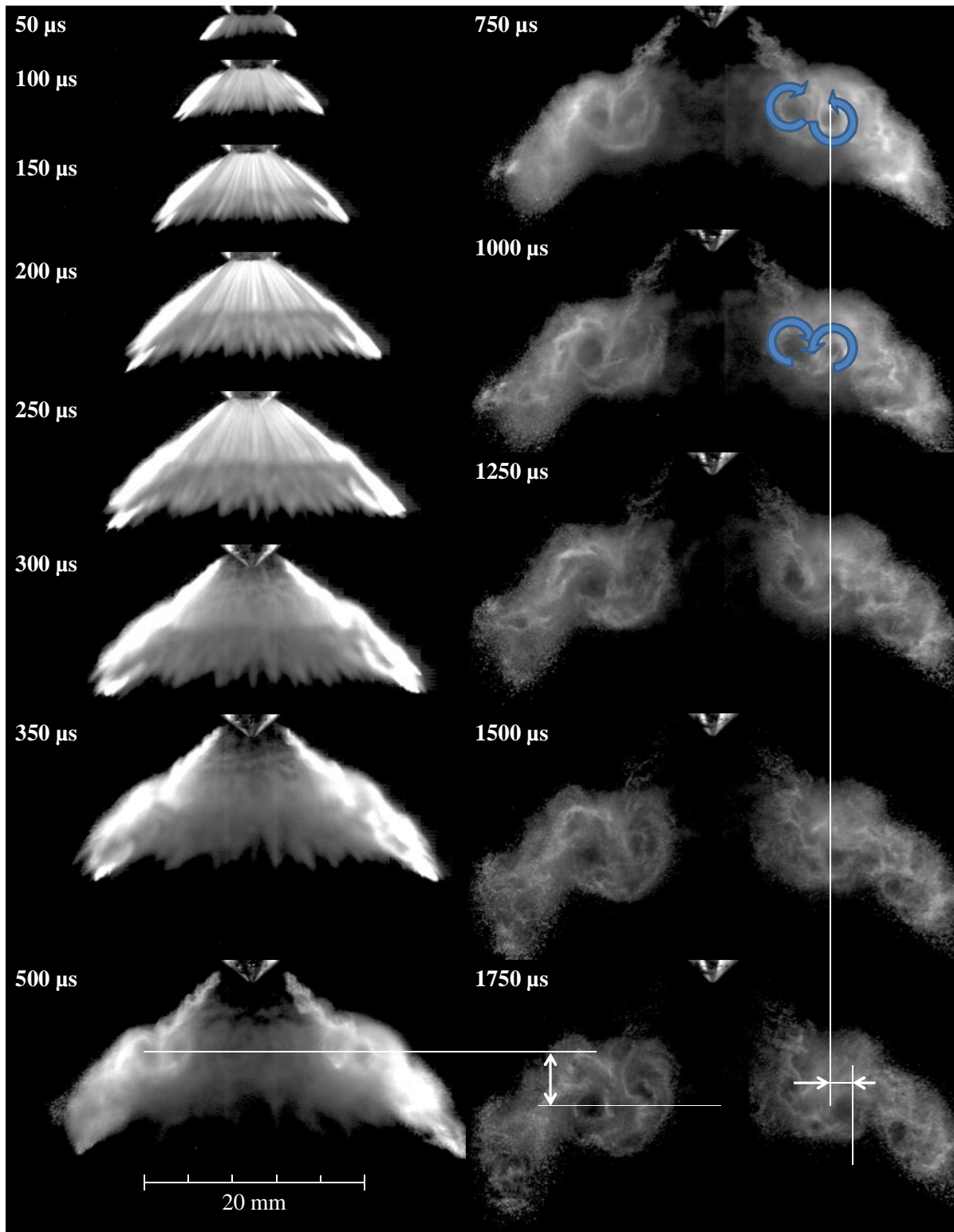
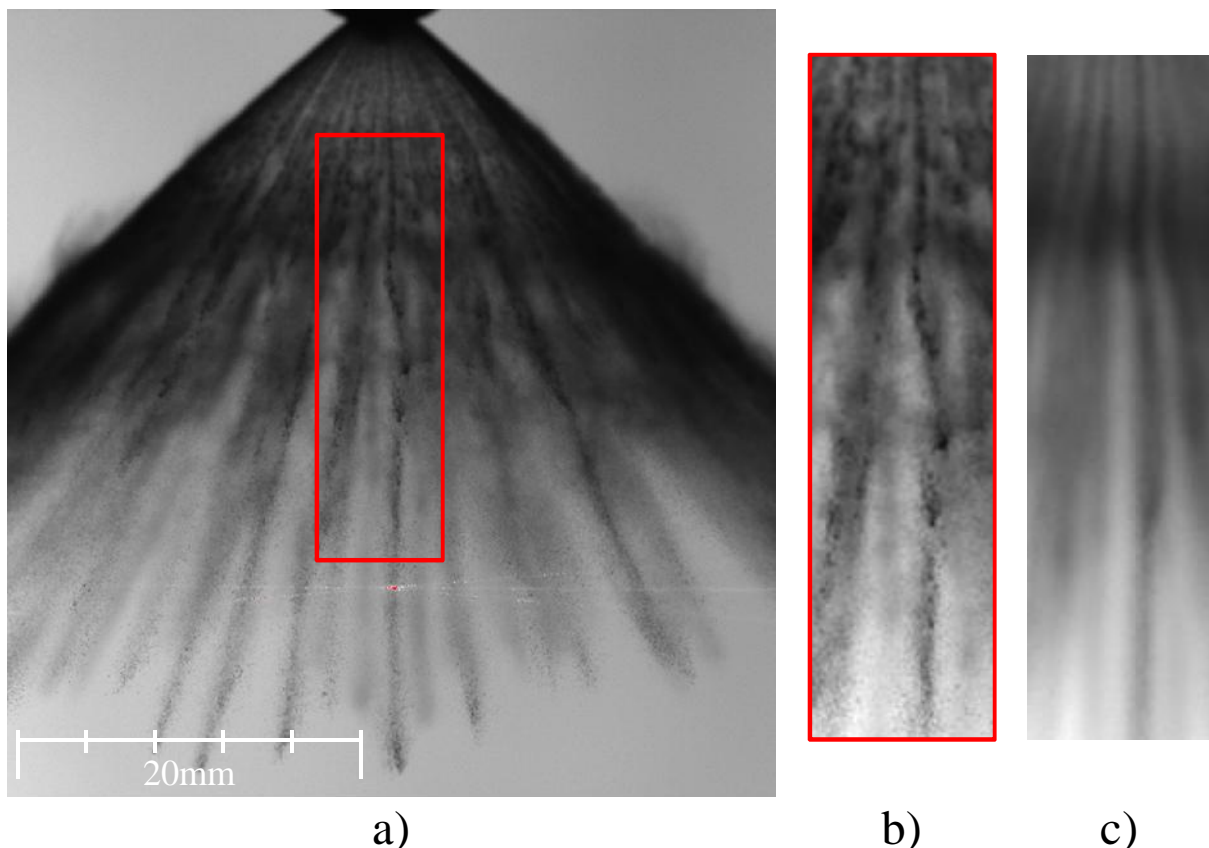


Figure 5-4 – Axial motion of the vortices (Mie scattering, single images,  $\rho = 7 \text{ kg/m}^3$ ,  $T = 300 \text{ K}$ ,  $\Delta p_{inj} = 12 \text{ MPa}$ ,  $m_{inj} = 2.2 \text{ mg}$ ,  $\varepsilon = 23 \mu\text{m}$ )

### 5.1.3 Streak Behaviour

As mentioned in various former works [78], [84], the spray of a hollow cone injector has a very distinguished shape. Strings form in the nozzle due to pockets of entrained air (as discussed earlier, in chapter 2.2.6). For a low density of the surrounding gas, individual strings stand out and give the impression as if they would propagate as single jets. A closer look reveals that these strings are not stationary but move tangentially and as will be shown later (page 90) radially during the first part of the injection. On the images this movement can be recognised as the strings seem to bend along their path. In the highlighted rectangle a streak describes a curve. This occurs when the pockets of entrained air move sideways in the nozzle and the streak is pushed sideways. That this bending is very reproducible can be seen in Figure 5-5 c), where the mean of 32 images show the same bending of the streak.



**Figure 5-5 – Single shot image of streaky spray structure with bending string a), magnified bending string b) and mean of 32 images of the same string (atmospheric conditions,  $p_{inj}=12\text{MPa}$ ,  $\varepsilon=23\mu\text{m}$ )**

As can also be seen in Figure 5-5, the streaks are not continuously filled with droplets. The spray is intermittent and travels in packages of droplets, just like in the primary breakup when the ligaments and blobs detach from the liquid core.

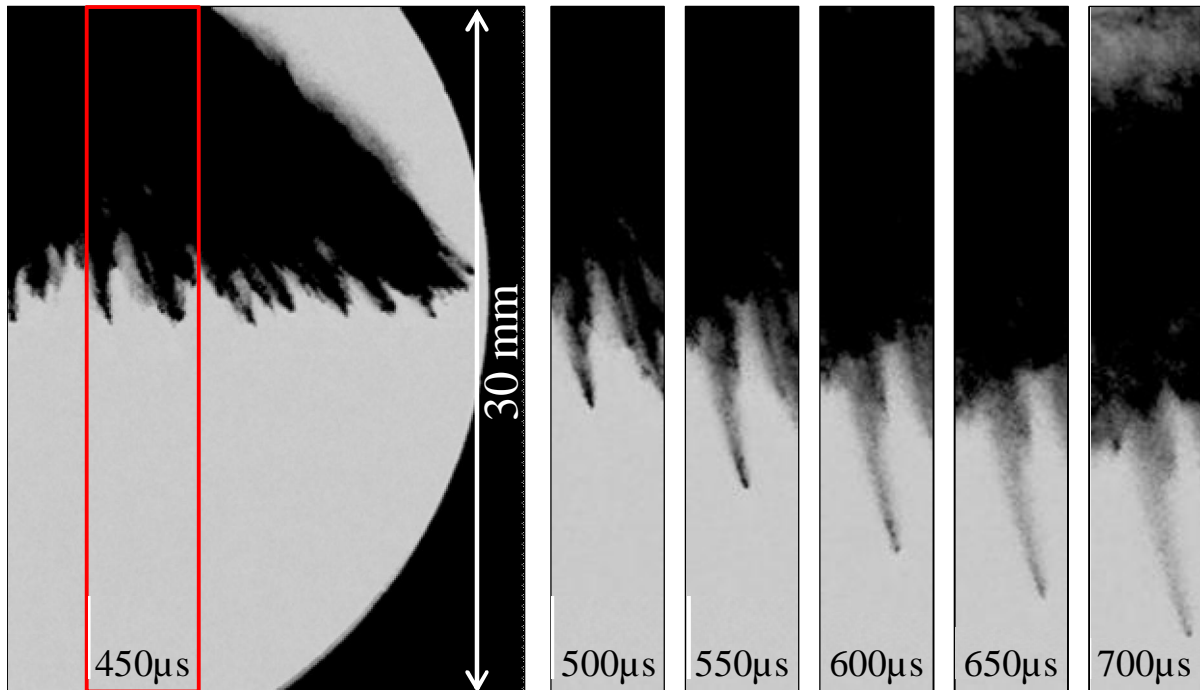


**Figure 5-6 – Time series of single images showing the development of a string tip (Shadowgraphy,  $\rho=2.2\text{kg/m}^3$ ,  $T=300\text{K}$ ,  $p_{inj}=12\text{MPa}$ ,  $\varepsilon=23\mu\text{m}$ )**

On closer examination of such a streak in Figure 5-6, it seems as the streaks are formed by large droplets or blobs which undergo primary atomisation. According to the threshold definition from a previous chapter (“Optical setup in the cell” on page 68 ff) the dark tip in the earlier images is in fact dense spray with a pixel intensity of 20 counts. In the first image (450  $\mu\text{s}$  after SOI) this tip has an axial distance of 18.7 mm from the injector tip, which is a nominal distance of about 26.5 mm (compare Figure 5-7). As will be seen in the next section (page 85) the primary breakup for these conditions is not yet completed therefore the hypothesis can be made that this dark region travelling downwards is fuel in the late stage of primary breakup. About 600  $\mu\text{s}$  after SOI the dense spray has vanished which implies that the primary breakup for this individual streak is fulfilled. This also shows in the penetration over time as also will be seen in the next sub chapter (page 109).

### 5.1.4 Spray Penetration of the reference case

For a quantitative description of the spatial spray development the penetration of the tip was measured in axial and nominal penetration direction. The axial

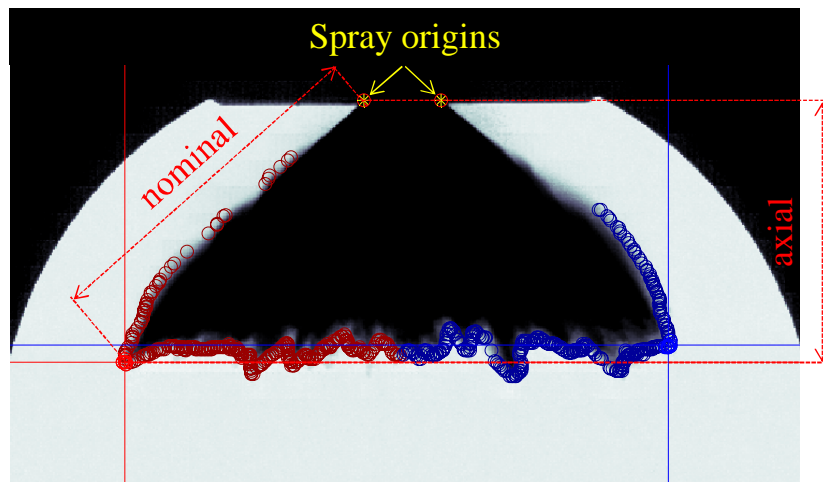


**Figure 5-7 – Shadowgraphy image with the points detected by the Matlab routine.**

penetration is defined as the distance between the nozzle and the spray parallel to the injector's axis. The nominal penetration is defined as the distance between the nozzle and the spray tip in the direction of the spray axis ( $\approx 45^\circ$ ). This was done for the individual as well as for the mean movies generated for each measurement point. A Matlab code has been written to track the spray tips on the images. The code automatically detects the tips and identifies the side of the corresponding spray origin. Figure 5-7 shows a Shadowgraphy image with the highlighted points found by the script. The lines indicate the two spray tips tracked, the different colour of the points stand for the spray origin to which the different edges have been related by the script. As the spray tips are propagating towards the side of the window, their observation is only possible until approximately 25 mm from the nozzle. For most of the investigated cases this distance is still within the breakup length of the spray or very short after it. This makes it hard to properly investigate the spray development. Therefore the axial spray penetration was measured with the help of the points in front of the tip of the injector. With the assumption that the cone angle is close to  $45^\circ$ , the nominal penetration was calculated as the axial penetration multiplied with  $\sqrt{2}$ . To derive the standard deviation, the spray tip was measured for ten individual pictures and from the pictures made out of the mean images.

Out of the ten penetration curves of the spray tip, the mean values and the standard deviation have been calculated. In Figure 5-8 the mean curve has been plotted as a line with the standard deviation added and subtracted and plotted as the area flanking the curve. Figure 5-8 shows the nominal spray tip penetration for the conditions specified in the legend (reference case). The penetration of the tip can be divided into three phases (part A, B and C). The first two phases are equal to most known multihole injectors and exhibit a behaviour as described in the literature and discussed earlier in section 2.2.3.2 (page 22). In the first part, during the linear penetration before the liquid breakup, the tip is pushed by the liquid core, large ligaments and blobs.

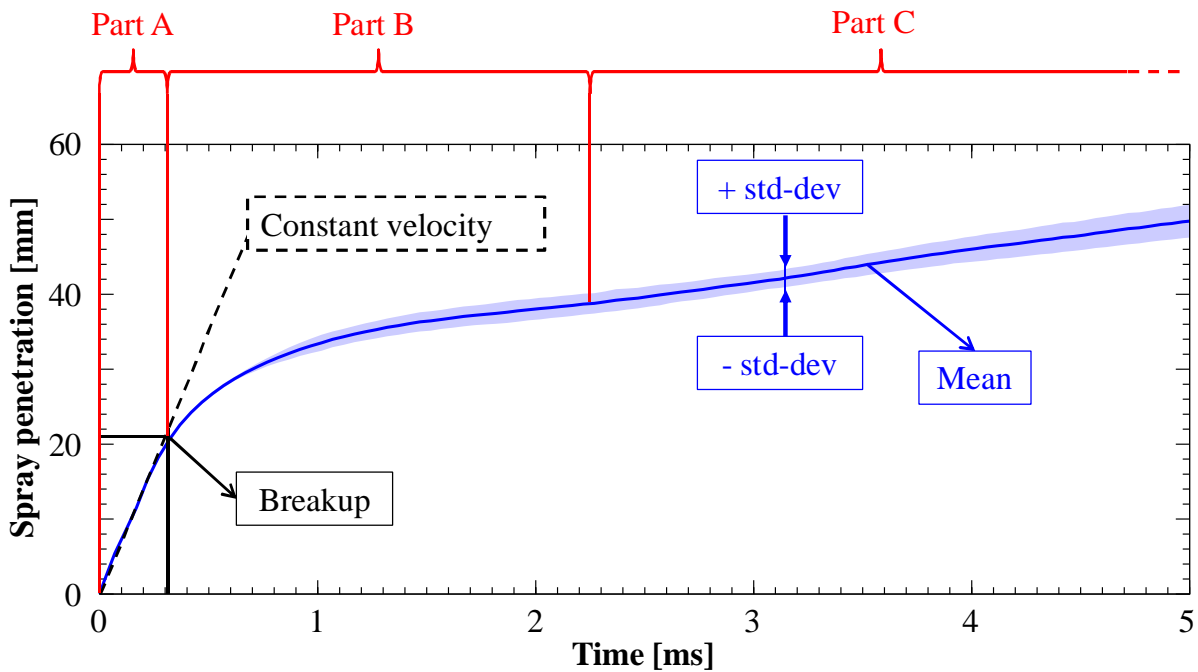


**Figure 5-8 – Nominal penetration of the spray tip for the Reference case, non evaporating conditions ( $\rho = 6.6 \text{ kg/m}^3$ ,  $T = 300 \text{ K}$ ,  $\Delta p_{inj} = 12 \text{ MPa}$ ,  $m_{inj} = 5 \text{ mg}$ ) Average (solid line) with standard deviations (shaded area) from eleven measurements.**

In the second phase (part B) the tip is formed by large groups of droplets which are slowed down by the surrounding gas in such a way that the curve of the tip penetration describes a square root-like shape. About 2.25 ms after SOI, during the second phase, the spray of the A-injector shows an interesting behaviour. The tip seems to accelerate again and continues its propagation with constant velocity. The reason for this can be found in the two circumferential vortices which form around and in the hollow cone as can be seen in Figure 5-4. To ensure that the spray tips remain within the observable domain and the effect is

fully visible, the high density case has been chosen to visualize the behaviour of the vortices. As can easily be seen, the tip slows down its nominal expansion and starts becoming wider (around  $770 \mu\text{s}$  after SOI), while in the hollow cone a vortex travels further in axial direction. By doing so, it overtakes the spray tip (for the high density case between  $920$  and  $970 \mu\text{s}$  after SOI). For line-of-sight methods, as the Shadowgraphy and shadow imaging for example, this top point will be interpreted as the spray tip. From this point on, the measurement of penetration via the axial penetration is not correct anymore. As a result of the high reproducibility of the spray, the standard deviation is very small until primary breakup. For the chosen line thickness the standard deviation is hardly visible in the linear part before and the first part shortly after the breakup.

A closer look on the linear phase (Figure 5-9) reveals that the curve is not perfectly linear, but shows a variation in the spray tip velocity ( a weak ‘dent’

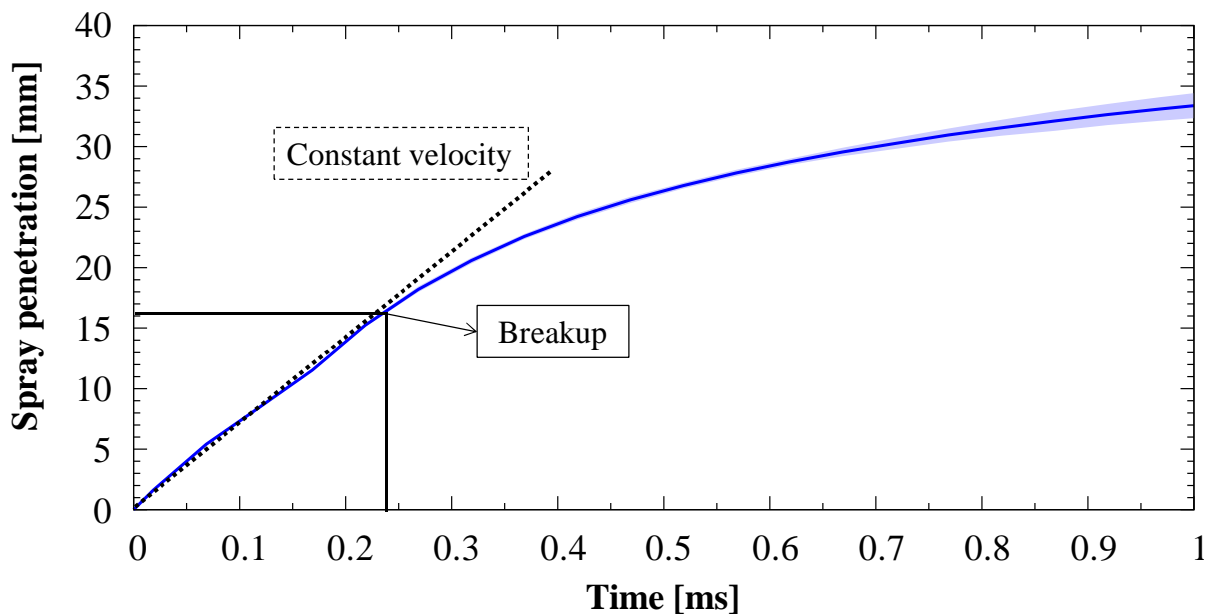
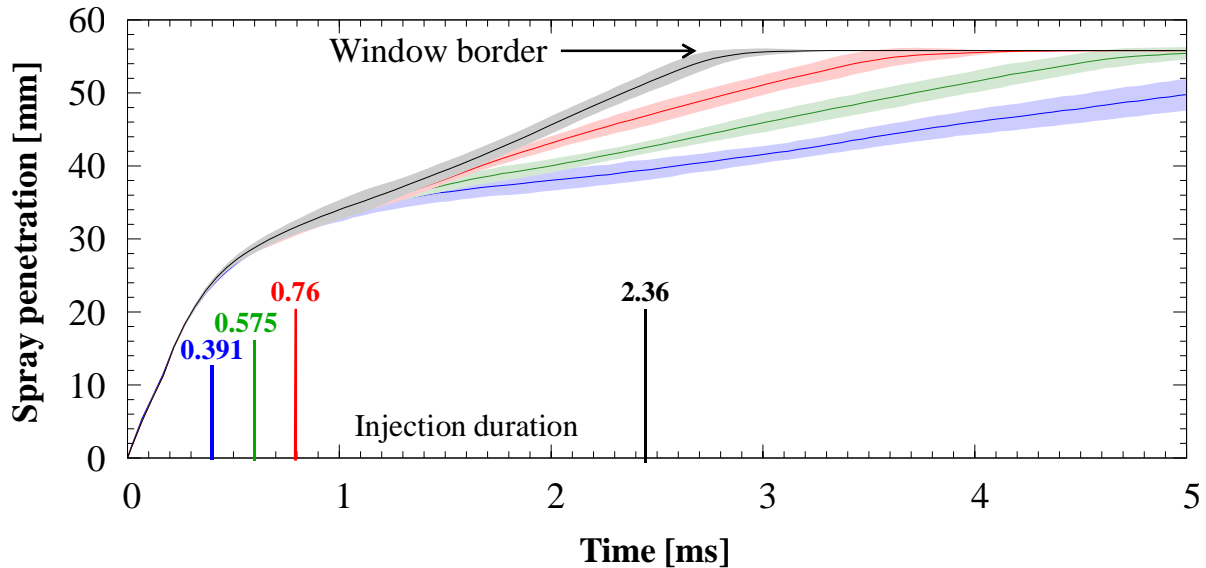


Figure 5-9 – Time and penetration: enlargement of Figure 5-8

from  $0.1$  until  $0.18$  ms). This probably occurs due to an oscillation of the needle combined with pressure oscillations in the rail (compare Figure 7-3 or Figure 7-4). For a system without such distortions, the curve should have a perfectly linear shape. The effect becomes stronger with increased injection pressure and with increased needle lift. (compare Figure 7-4 in the appendix). To define a spray tip velocity in the linear regime, the derivation of the curve was calculated. At the point where the velocity of the spray tip is lower than 90% of the linear velocity, breakup time and breakup length were defined.

### 5.1.5 Influence of injection duration on vortex development

The multihole spray, as it can be seen for non swirling injectors with cylindrical nozzles, is not influenced by a variation of the injection duration. The vortices which occur with hollow cone injectors on the other hand are strongly influenced by the injection duration.



**Figure 5-10 – Axial penetration for different injection durations (2.36 ms / 30 mg in black, 0.76 ms / 10 mg in red, 0.575 ms / 7.5 mg in green and 0.391 ms / 5 mg in blue) under non evaporating conditions ( $\rho = 6.6 \text{ kg/m}^3$ ,  $T = 300 \text{ K}$ ,  $\Delta p_{inj} = 12 \text{ MPa}$ )**

Figure 5-10 shows the axial penetration curves for different injection durations (and therefore a variation of the injected mass). To compare the different propagation behaviours, the penetration in Figure 5-10 is shown in axial direction. It can easily be seen that increased injection duration results in higher propagation velocity in axial direction. The reason for this can be found in the vortices themselves and how the liquid phase interacts with them. The vortices start to form very early, close to the nozzle. They travel along downwards the jet, driven by the liquid phase which is supplying the vortices with kinetic energy and – in case of non evaporating conditions – with liquid phase in the form of small droplets. During the injection the main vortex grows and gains strength, as the fast jet passes along its side and transfers its momentum to the vortex (Figure 5-11). While the vortices grow they gain influence until they are strong enough to have a noticeable influence on the spray. Due to the high velocity and the large size of the liquid structures in the jet, it needs a high force to deform the flanks of the spray. Therefore the spray of short injections is not

significantly influenced by the vortices, as they are too weak and too far upstream. But if the injection duration is longer, the vortices have more time to travel further downstream, where the spray has been broken up. In the mean time the main vortex had time to grow and to build up momentum and starts to bend the breakup region of the spray towards the inner side of the hollow cone. By doing so the spray is directed in the axial direction, transporting the droplets away from the nozzle. The radial component has been transferred, to a great extent, to the vortex. Therefore the sprays' preferred travelling direction is along the injectors axial. Around  $950\ \mu\text{s}$  to  $1000\ \mu\text{s}$  after SOI the droplets accelerated by the vortices are further away from the injector tip (in axial direction) than the spray tip and start to accelerate the penetration (separation point in Figure 5-10).

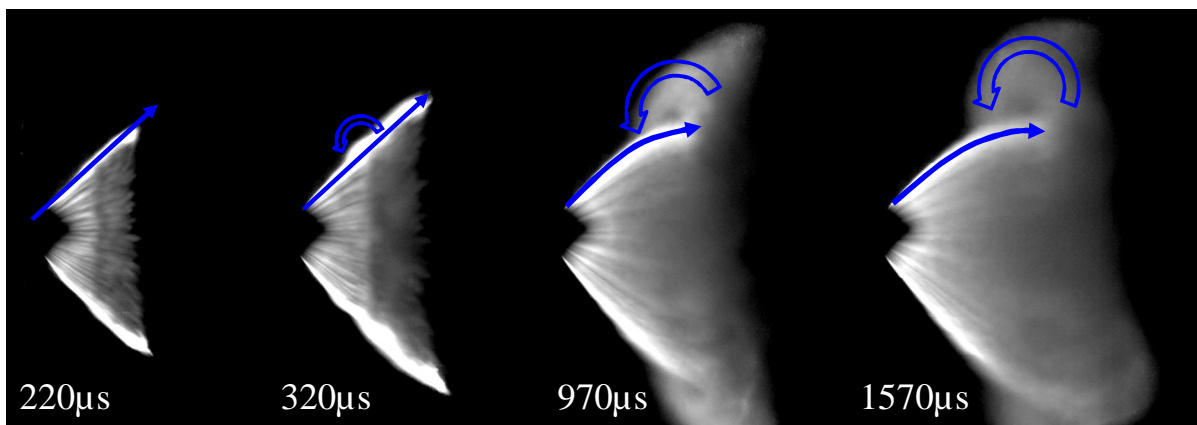


Figure 5-11 – Deviation of the jet from the nominal axis due to the ring vortices around the hollow cone (Reference case, 30 mg injected mass)

### 5.1.6 Droplet size and velocity distribution

With the assumption that the droplet size distribution of the short injection is not effected when injection duration is increased, the PDA measurements have been performed with the injection duration of 1 ms for all cases. The measurement of drop sizes and velocities was done at various positions for the standard case with  $23\ \mu\text{m}$  needle lift and at carefully selected positions to visualize the variations of injection pressure, needle lift and fuel. The measurements have been performed at atmospheric conditions. Unlike the measurements in the HTDZ, the reference case for the PDA measurements has been performed with gasoline (gasoline was the standard fuel; Isooctane was used as a variation).



### 5.1.7 Measurement grid

The flow field of a non swirling hollow cone injector is very interesting and it is dependent on numerous factors. In the atmospheric spray rig in Loughborough some of these influences have been investigated. The flow field in general has been investigated with a large grid. Figure 5-12 and Table 7 (in the appendix) give an overview of the different locations where the measurement volume was positioned in the spray. The horizontal and the vertical axis show the radial and the axial distance of the measurement volume from the injector tip. Where necessary (e.g. within the streaks or close to the nozzle) the grid was refined in radial direction down to distances of 0.25 mm. The arrows indicate the positive direction of the velocity components for the LDA and PDA measurements.

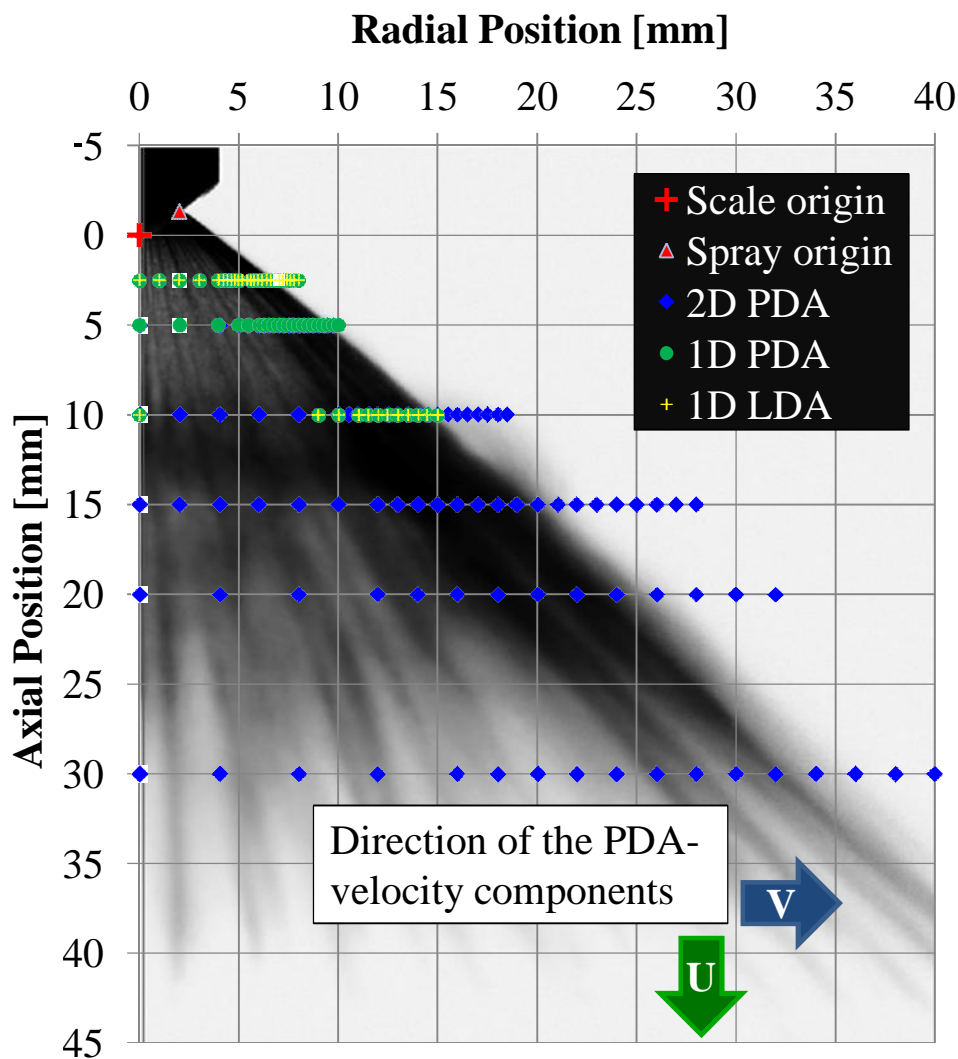
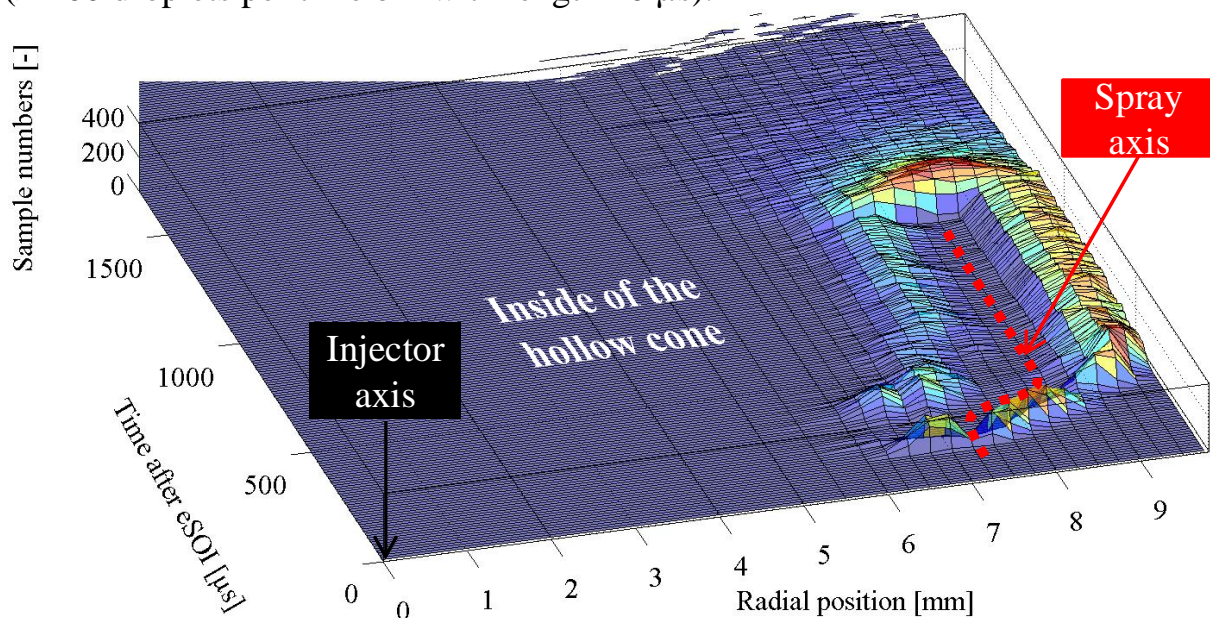


Figure 5-12 – Grid of the positions of the measurement volume for the LDA (green dots and yellow crosses) and PDA (blue) investigation superimposed over atmospheric injection.

### 5.1.8 External observation of a streak by means of sample number

For the investigation of the streaks and their evolution in time, the single bursts have been combined to time bins of  $10\mu\text{s}$ . If the time bins are bigger (e.g.  $50\mu\text{s}$ ) information of the temporal distribution is lost. For example little movements of the streaks would be lost due to the averaging in the time bins (also compare Figure 7-6 and Figure 7-7 in the appendix). Figure 5-13 shows the behaviour of a streak with the help of the sample number on several radial positions plotted along time. The measurement was carried out at  $z = 5\text{ mm}$ , thus close to the origin of the spray. It shows the temporal development (y-axis) of the sample number (z-axis) for each radial position (x-axis). The zones with no or very few samples have been coloured blue. Red shows areas with high droplet densities ( $> 200$  droplets per time bin with length  $10\mu\text{s}$ ).



**Figure 5-13 – Sample number as a function of radial position and time (2D PDA, 5mm underneath the injector tip, atmospheric conditions, needle lift  $\varepsilon = 23\mu\text{m}$ , injection pressure 12 MPa)**

Eye-catching is the valley that forms between two rows of peaks with high sample number. This is in the middle of the jet, where no or very few samples could be detected. As can be seen, the position of a streak is not stable. In the early development it moves outwards, increasing the cone angle. This can be seen from 250 to 300  $\mu\text{s}$  after the electric start of injection where the valley starts at radial position 6 mm from the injector axis. It then moves outwards to the stable position where it stays until the injector is closed. The region on the

inner side of the streak shows fewer droplets than the outer side of the spray. The geometry of the spray is such that the laser beams forming the measurement volume have to pass the dense spray of the neighbouring streaks. Therefore the chance to have a measurement volume is reduced, as the laser beams are deflected and obscured. This has an effect on the sample number. Due to the reduced chance of forming a measurement volume, fewer samples are detected. That the inner and outer side of the spray produce the same droplet density can be seen in the fact that as soon as the injection stops (1100  $\mu$ s), and the chance to form a measurement volume inside the hollow cone is increased again, the number of samples rises drastically from 100 to 200 samples per time bin; the same number as it was on the outer side of the streak during the whole injection. The spray can roughly be divided into three time regimes. In the first regime the leading droplets are contained (forming the spray tip in front of the streak). Also in the first part the development of the stable streak takes place. The streak forms and moves towards the outside, increasing the cone angle. The next part is the stable injection where the streak doesn't move anymore and a steady flow takes place. In the third and last temporal part of the spray the injection is over and the residual droplets move in the flow field generated by the vortices.

### **5.1.9 Development of the streaks inner structure**

At an axial distance of 2.5 mm from the injector tip or about 3.8 mm (about  $116 \text{ s}/d_n$ ) from the orifice the droplets have been investigated. The very first droplets arriving are travelling around the spray tip. A cross-section of the spray tip and the following development is shown in Figure 5-14.

The curves refer to a cross-section the spray around the tip, a set of LDA measurements has been compared for a streak 2.5 mm underneath the injector tip. The values are averaged for each radial position over the time bin between 120 and 130  $\mu$ s after SOI. To describe with a set of PDA data. The big difference between the two techniques is the quantification of droplet diameters by the PDA technique. This only works with spherical particles. LDA on the other hand detects anything that passes the measurement volume and produces a Doppler burst. The difference in number of detected samples must in part come from the state of breakup. It can be said that only few droplets break off the

liquid tip. Most of the structures are non spherical, maybe some blobs or small ligaments.

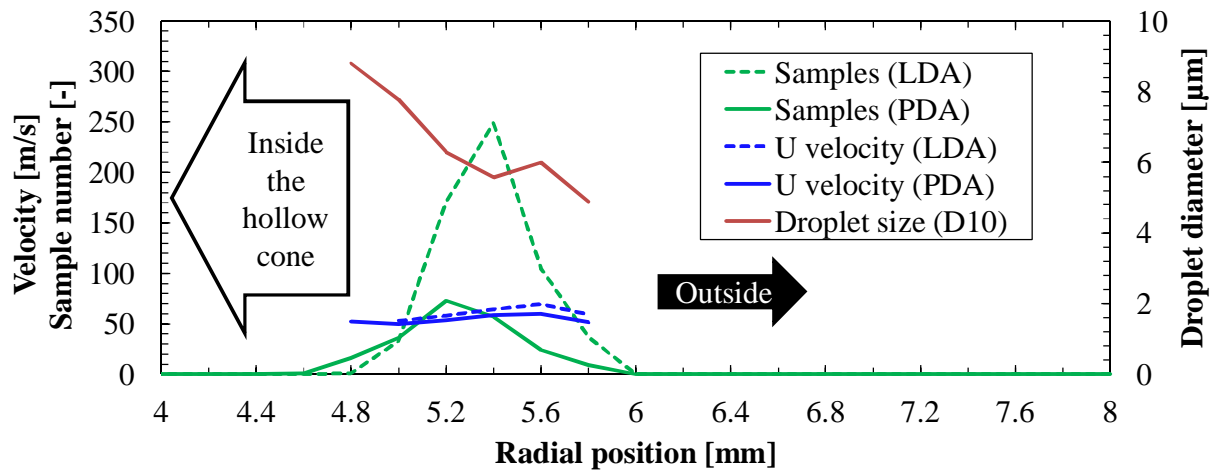


**Figure 5-14 – Sample number and velocity for 1D-LDA (dashed line) and 1D-PDA (solid line) measurements and droplet size under atmospheric conditions, 12 MPa injection pressure and medium needle lift ( $\epsilon = 23 \mu\text{m}$ ),  $z = 2.5 \text{ mm}$  underneath the injector tip, time bin = 120 – 130  $\mu\text{s}$  after SOI**

The centre of the streak can easily be identified with the sample number: From the centre of the hollow cone towards the outer side of the spray the sample number increases. Its maximum is at 5.2 mm for the PDA and 5.6 mm for the LDA data from the injector axis. This is another sign for the weak breakup of the young streak. The PDA detects the maximum number of samples at another location than LDA does. The LDA-maximum does not contain many droplets. The velocity of these first droplets is not very high (for velocity and droplet diameters the minimum sample number has been set to 5 samples per 10  $\mu\text{s}$ ). The velocities measured with LDA are a bit higher than with PDA which fits nicely to the theory of the weakly broken up spray, as the non-spherical droplets coming from the liquid core are faster than the droplets built in the very early breakup. The droplet diameters are in the range of 6 to 8  $\mu\text{m}$ .

About 10  $\mu\text{s}$  later, the streak has arrived and develops further. Its shape is shown in Figure 5-15. Here both techniques, PDA and LDA, show very similar results. Starting on the injector axis, the sample number starts to increase towards the outer region, reaching a local maximum at 5.2 mm. The relative velocity between the liquid spray and the gaseous surrounding is very high here. Therefore very high shear forces tear the droplets apart and form smaller droplets, as can be observed on the basis of the droplet sizes (red curve).

Going further towards the outer spray, the sample number drops towards a local minimum. Here the spray axis was defined. The velocity of the droplets has its maximum at the same position, as has the droplet diameter. The velocity of the droplets has not increased, compared to the foregoing time bin, neither has the droplet diameter. Interesting though is that the position of the streak has changed and is now very easily visible, as all 5 curves have their maxima and minima, respectively at the same position.

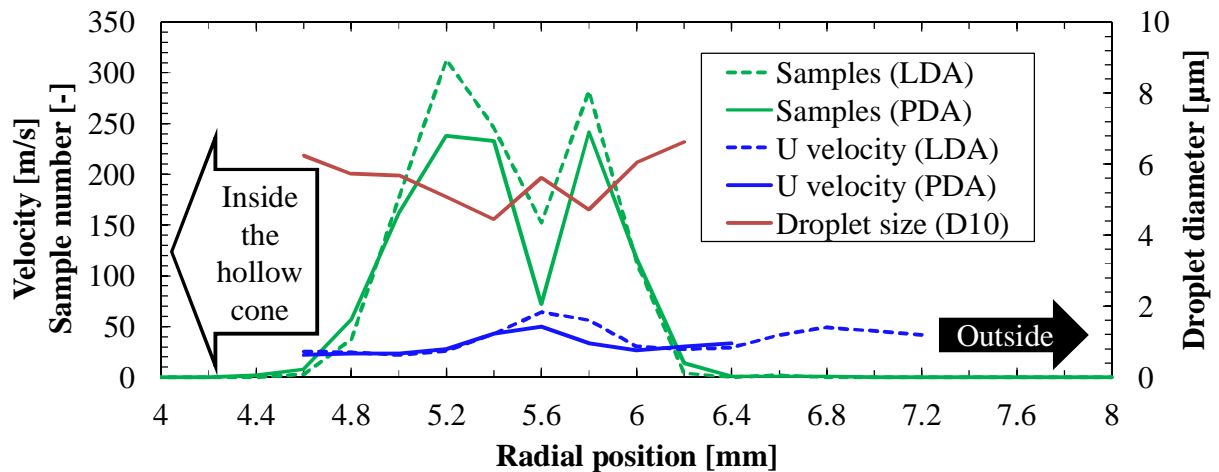


**Figure 5-15 – Sample number and velocity for LDA (dashed line) and 1D-PDA (solid line) measurements and droplet size under atmospheric conditions, 12 MPa injection pressure and medium needle lift ( $\epsilon = 23 \mu\text{m}$ ),  $z = 2.5$  underneath the injector tip, time bin = 130 – 140  $\mu\text{s}$  after SOI**

### 5.1.10 Cone and Spray Angles

From the spray axis the cone angle and the spray angle can be defined. Figure 5-16 gives an overview on how the relevant angles have been defined. The cone angle is defined as the angle between the injector axis and the spray axis. The spray angle is defined across the lateral spray directions (perpendicular to the spray propagation direction) where, averaged over 10  $\mu\text{s}$ , more than 10 samples per measurement (from the 250 measurements taken in total) can be measured and the spray axis.

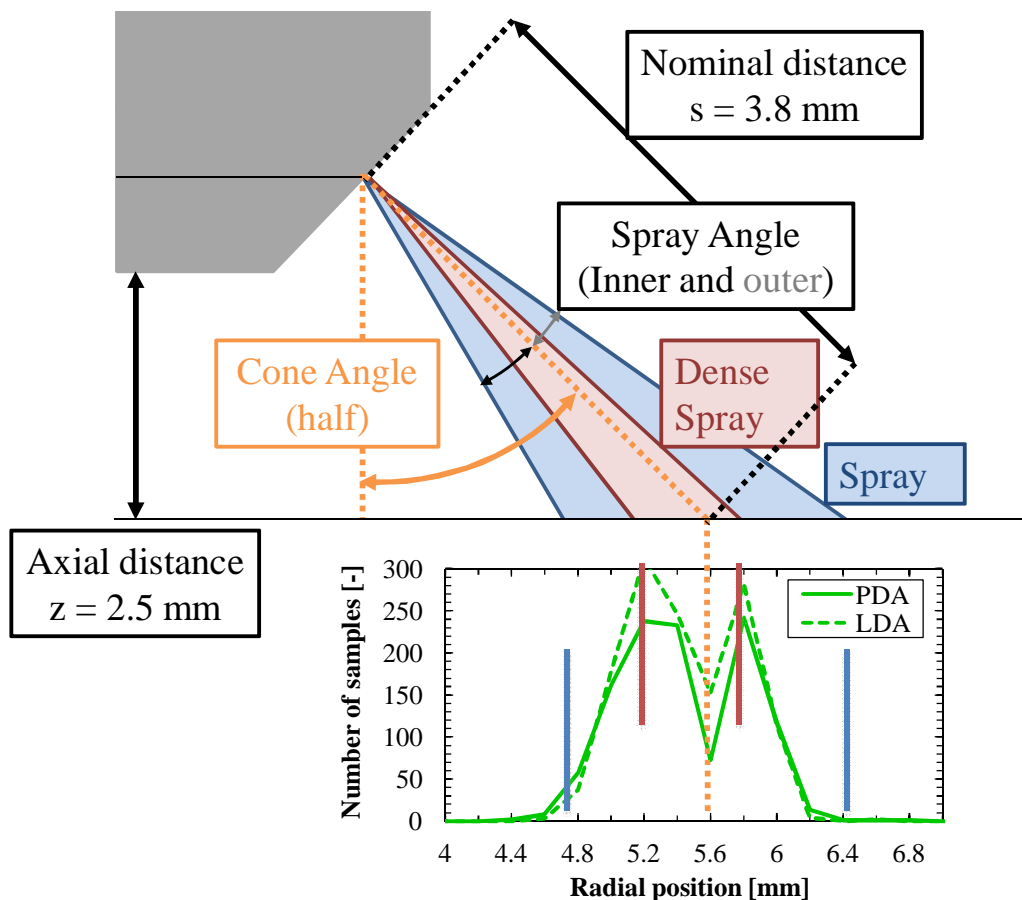


**Figure 5-16 – Definition of spray axis, cone and spray angle for PDA/LDA measurements (Reference conditions,  $z = 2.5$  mm, 130-140  $\mu\text{s}$  after SOI)**

Figure 5-17 shows the development of the cone angle at a level of 2.5 mm under the injector tip. In the basic case with the medium lift and 12 MPa injection pressure the first droplets arrive under a cone angle of  $41^\circ$ . During the injection the cone angle grows steadily up to  $49^\circ$  where it remains until the end of injection. Unlike in Figure 5-13 which shows a measurement at  $z = 5$  mm, the angle at  $z = 2.5$  mm is unsteady until 600  $\mu\text{s}$  after SOI. Due to the larger spray

further downstream, the movement of the spray might be blurred in such a way that it can't properly be detected anymore. After end of injection the definition of the spray axis is not possible anymore, as the dense spray disappears.

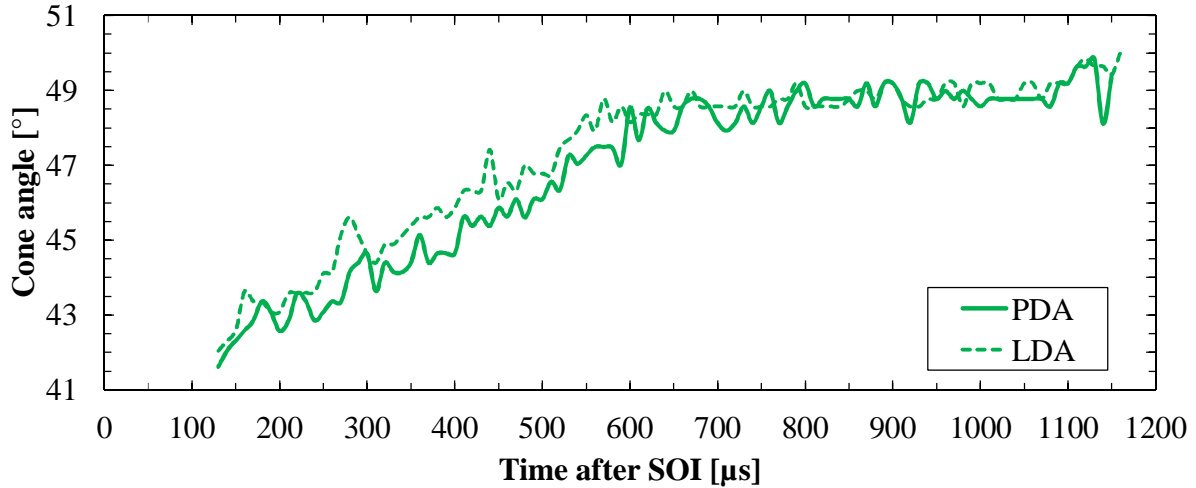


**Figure 5-17 – Cone angles during the injection (atmospheric conditions, inj. Pressure 12 MP, medium needle lift ( $\epsilon = 23 \mu\text{m}$ ),  $z = 2.5 \text{ mm}$  or  $82 \text{ s/d}_h$ )**

Therefore the cone angle is not defined anymore. The inner and outer spray angle shown in Figure 5-18, are quiet stable during the injection process. While the streak is moving laterally the spray angles are changing, as the outermost droplets need some time to react to the movement of the spray axis. Once the streak stabilised itself at  $49^\circ$ , the inner and outer spray angle stabilise as well. They are symmetrical, both in the range of  $8^\circ$ .

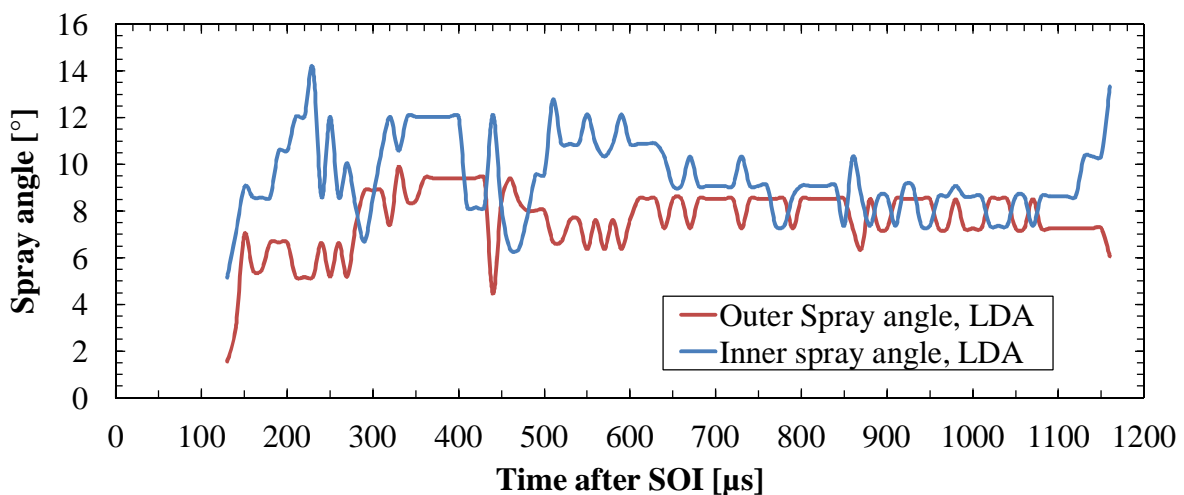


**Figure 5-18 – Spray angle during the injection (LDA, atmospheric conditions, inj. Pressure 12 MP, medium needle lift ( $\epsilon = 23 \mu\text{m}$ ),  $z = 2.5 \text{ mm}$ )**

### 5.1.11 Inside a streak

To investigate the inside part of a streak it is necessary to have steady-state conditions. Therefore the part where the streaks are stable has been looked at more closely. Figure 5-19 shows the mean values (600 – 1100  $\mu$ s after SOI) of a cross-section in the spray at  $z = 2.5$  mm. Again the LDA and the PDA measurement show very similar data. The droplets measured in this region are now very small and in the middle they became about 15% faster (87 ms/s) than in the beginning.

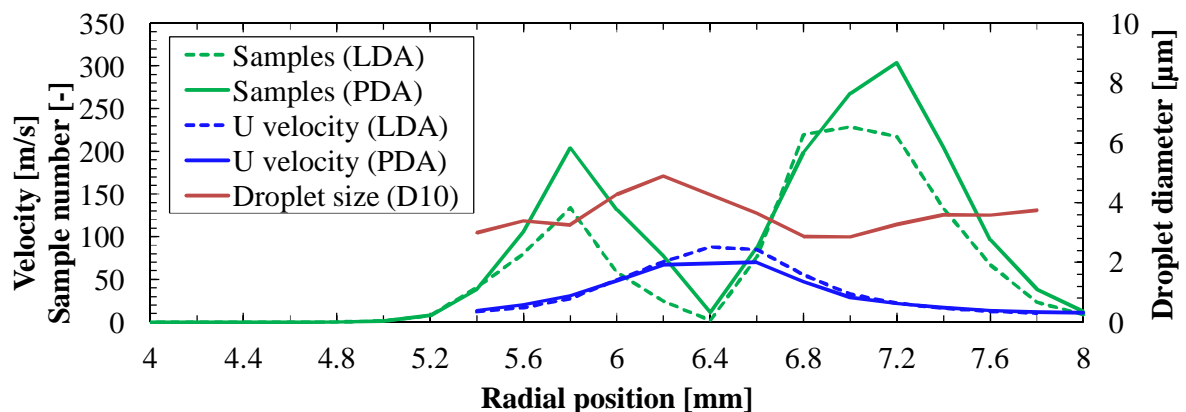


**Figure 5-19 – Sample number and velocity for LDA (dashed line) and 1D-PDA (solid line) measurements and droplet size under atmospheric conditions, 12 MPa injection pressure and medium needle lift ( $\epsilon = 23 \mu\text{m}$ ),  $z = 2.5$  underneath the injector tip, time bin = 600 – 1100  $\mu$ s after SOI**

The velocities of the droplets measured on the spray axis have been investigated and used to compare different needle lifts and an increased injection pressure against the reference case. Figure 5-20 shows the velocities of the droplets in the spray axis plotted over their nominal distance from the spray origin. The velocities are measured during the steady-state period. Therefore a time window for each nominal distance was calculated. The length of the time window is 240  $\mu$ s. The first window begins 680  $\mu$ s after SOI. Based on the spray velocity measured in the foregoing measurement volume the time was calculated for the spray to reach the next measurement volume. The velocities of all droplets which have been measured in the spray axis and which arrived in the defined time window have been averaged. By doing so, the droplets appearing in the first measurement volume could be tracked to the lowest measurement volume (nominal distance to spray origin  $s = 45$  mm), where the spray breakup for atmospheric conditions lies. Figure 5-20 shows the averaged velocities along the



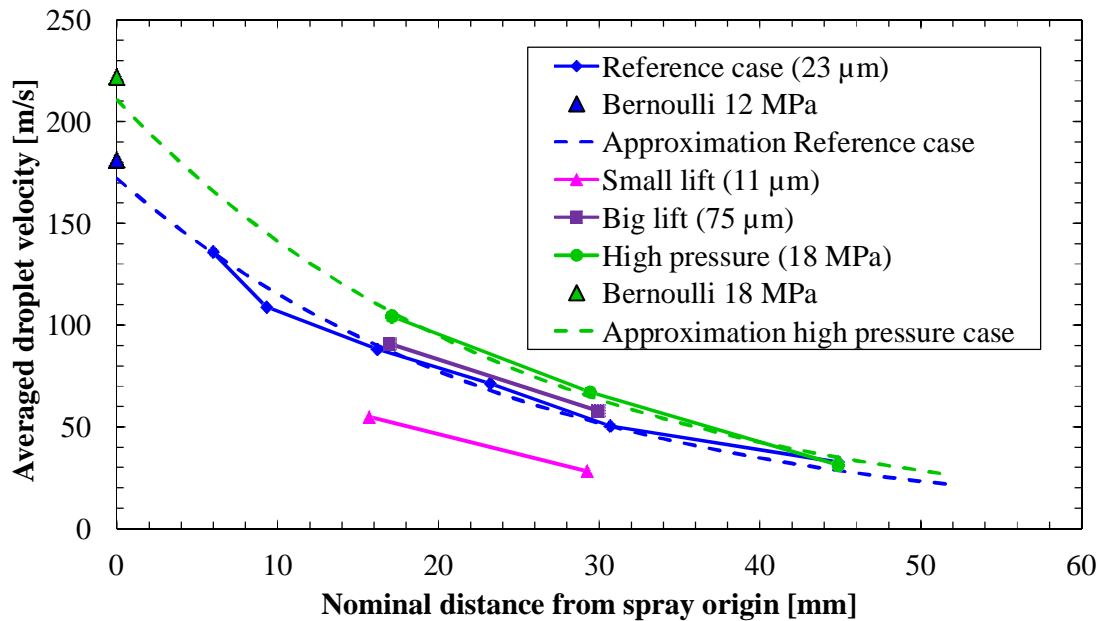


**Figure 5-20 – Velocity of the droplets in the spray axis for atmospheric conditions. With the theoretical nozzle velocities (Bernoulli) and an approximation of the velocity decay along the path ( $v = 0.95 \cdot v_{\text{Bernoulli}} \cdot e^{(-0.04 \cdot s)}$ )**

injection path for two different injection pressures (12 and 18 MPa) and three needle lifts (11, 23 and 75 μm). The Bernoulli velocity for the applied injection pressures has also been plotted as an initial velocity in the nozzle (nominal distance = 0). An estimation of the data as a function of the nominal distance from the nozzle, “*Approximation*”, has been plotted, using 95% of the Bernoulli velocity within the nozzle as initial velocity:

$$v_{(s)} = 0.95 \cdot v_{(\text{Bernoulli})} \cdot e^{-0.04 \cdot s} \quad (31)$$

The five percent of velocity losses come from estimated pressure losses in the range of 10% between pressure measurement and nozzle exit, which roughly results in a 5% velocity reduction. Together with exponential velocity decay along the path, this gives a good estimation of the droplet velocities within the fully developed hollow cone spray. Higher injection pressure leads, as would be expected, to higher droplet velocities. Again the exponential approximation fits well. A bigger needle lift brings no increase in droplet velocity whereas a smaller needle lift reduces the velocity by about 40%. The reason for this is not yet fully understood but must be linked to the different breakup scenarios of the different needle lifts (compare Chapter 5.4.3 on page 121).

### 5.1.12 Droplet size distribution along a streak

For the droplet size measurement the droplets arriving during the stable injection (600 - 1100  $\mu\text{s}$ ) have been compared. As explained earlier (chapter 5.1.11) the spray within a time window of 400  $\mu\text{s}$  has been investigated. The droplet diameters have been averaged to describe the droplet sizes within the spray.

Figure 5-21 shows the Sauter mean diameter for different axial distances from

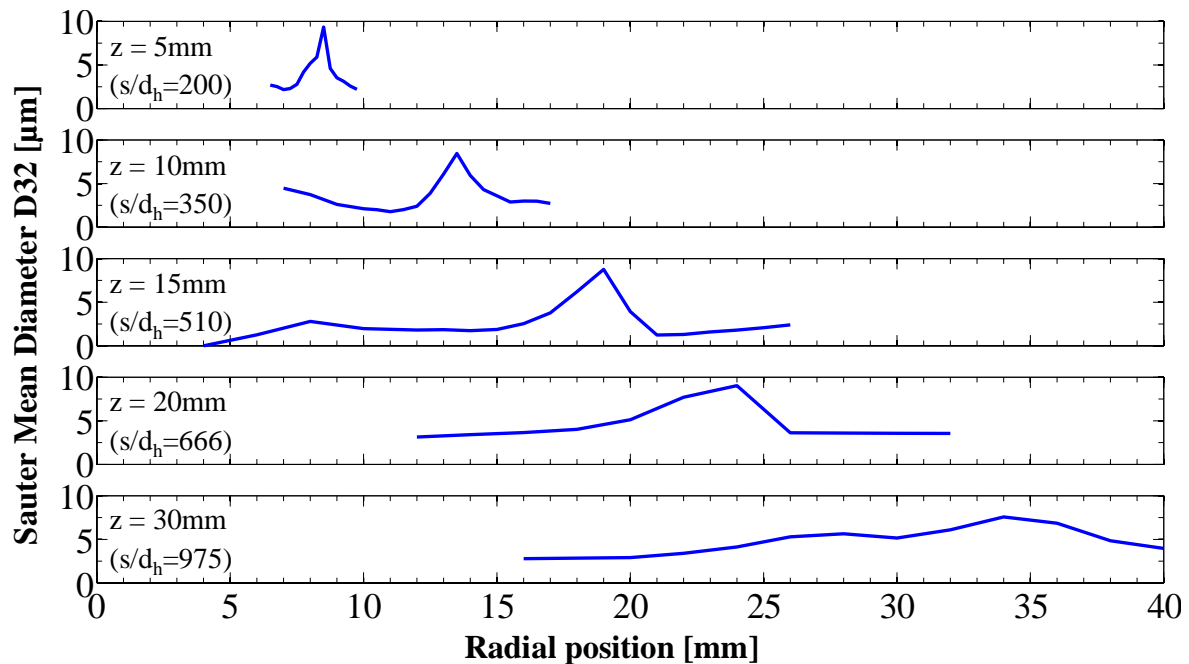


**Figure 5-21 – Sauter mean diameter as a function of the radial position for several axial positions 5, 10, 15, 20, 30 mm underneath the injector**

the injector tip. The axial distance to the injector tip is indicated on the left side of the plot. The nominal distance of the spray axis to the spray origin is shown in brackets underneath. Close to the injector tip, in a nominal distance of 9.1 mm from the spray origin, the fast spray containing the larger droplets is very thin. The further the spray travels, the wider becomes this region. Also the area in which droplets can be found becomes wider. A region with very small droplets can be found on the outer side of the hollow cone at all levels. Around the hollow cone droplets are very small; The Sauter Mean Diameters (SMD) are smaller than 4  $\mu\text{m}$ . As shown earlier the measurements on the inner side of the spray (especially close to the jet where the obscuration due to the other streaks is high) show fewer samples and bigger droplets as the probability for a big droplet to be detected is higher. In the dense zone the droplets are not exposed to high shear forces. Therefore these droplets will be broken down to smaller droplets

later; as soon as they are exposed to the much slower surrounding gas outside the dense spray, they will be broken up. To objectively compare the different cases, the outer side of the hollow cone, more precisely the area next to the dense spray, was used (e.g. Figure 5-19, the radial positions  $> 6.8$  mm). These

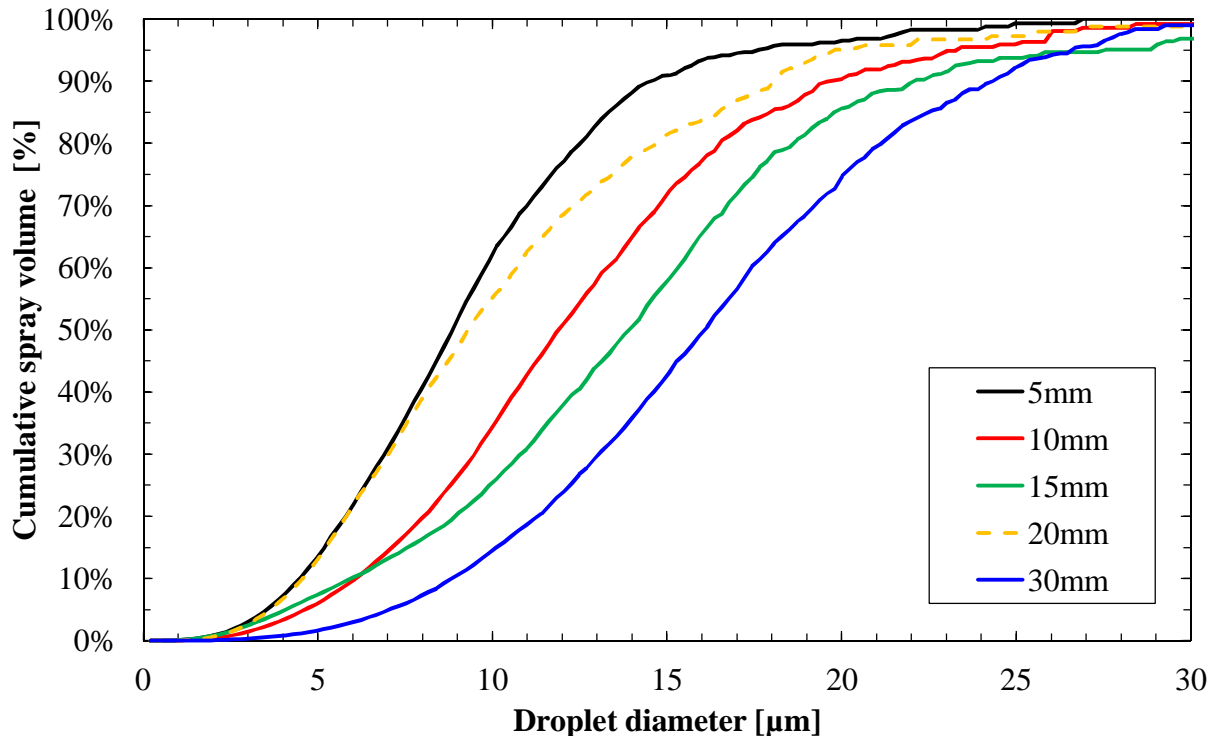


**Figure 5-22 – Cumulative spray volume of the outer spray (outside the dense spray on the outer side) over the droplet diameters for different measurement locations in the reference case. (Injection pressure 12 MPa, medium needle lift  $\varepsilon = 23$   $\mu\text{m}$ , atmospheric conditions, gasoline)**

droplets are not going to be broken up much further, as their Weber number is too low (compare image Figure 7-8 in the appendix). Due to this fact they are important for evaporation.

The cumulative volume of all droplets measured for the different axial distances to the needle tip have been plotted over the droplet diameter on Figure 5-22. It shows the total volume of all droplets measured in the outer spray (from the edge where the dense spray begins, to the outer side, e.g. Figure 5-19 between 6.8 mm and 8 mm) during the stable period (when the streaks didn't move anymore), plotted over the droplet diameter. Such a plot reveals for example that 15 mm underneath the injector tip, 50% of the total liquid volume is captured within droplets smaller than 14  $\mu\text{m}$ . The graph tells the story of a streak: Very early in the spray development small droplets are torn away from the liquid core (and other liquid structures upstream) by the shear forces. These droplets are

very small and can be observed already 5mm under the injector tip. Almost 90% of these droplets are smaller than 14  $\mu\text{m}$ . As the small droplets are carried away by the vortices while the bigger droplets travel further down in the main jet (as they are less influenced by the gas phase around the spray), the droplet distribution changes along the jet. The further away from the nozzle the measurement volume is (in nominal direction) the larger become the droplets measured in the spray. An exception can be seen at 20 mm axial distance (nominal: 666 s/d<sub>h</sub>). Here the drop size distribution looks similar as at 5mm. Almost 50% of the mass is contained in droplets smaller than 9  $\mu\text{m}$ . This can be explained when having a look at the spray images taken between 960 and 1200  $\mu\text{s}$  after SOI: Figure 5-4 shows a cut through the hollow cone spray made with the Mie scattering method. On the two images on the right it can easily be seen that during the measurement at 20 mm the circumferential vortices are around that area, transporting large amounts of small droplets from further downstream to the 20 mm-position.

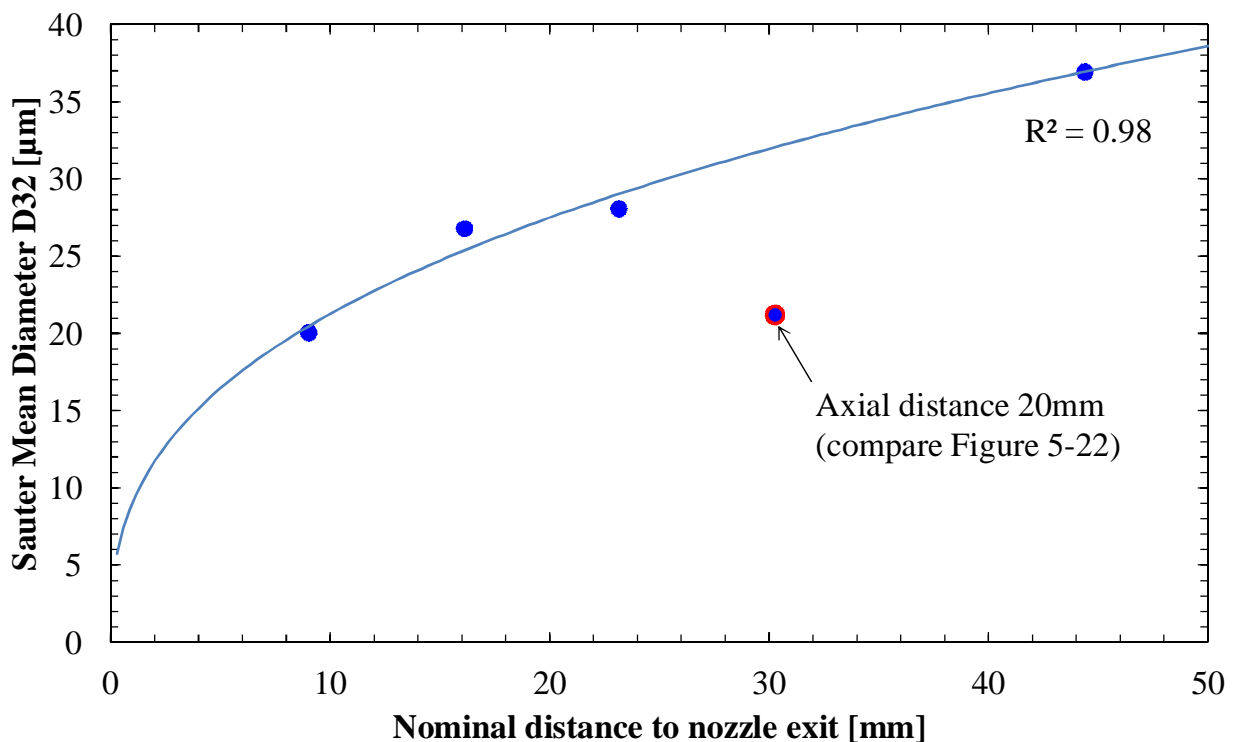


Figure 5-23 – Sauter Mean Diameters as function of distance to the nozzle.

Figure 5-23 shows the corresponding  $D_{32}$  to Figure 5-22 as function of the nominal distance to the nozzle. A curve was fitted with:

$$D_{32} = 0.7 \cdot s^{0.37} \quad (32)$$

The curve fits nicely to the data set with a  $R^2$  of 0.98. Only the droplet diameters 20  $\mu\text{m}$  underneath the injector tip, at a nominal distance of about 30 mm are much smaller. As already discussed in Figure 5-22 these are droplets from the vortex which are transported to this position as can be observed in Figure 5-11.

### 5.1.13 Vapour phase

Figure 5-24 shows the reference case (isooctane, gas density:  $6.6 \text{ kg/m}^3$ , injection pressure: 12 MPa, needle lift 23  $\mu\text{m}$ ) for two gas temperatures. Under non-evaporating conditions (gas temperature 300 K) the spray penetrates into the combustion chamber, the strings form a fine spray fog along their path and the distinctive shape of the hollow cone forms (left). The images taken 50  $\mu\text{s}$  after end of injection (EOI) show how the last fuel exits the nozzle. At the injector tip, a slight part starts to brighten again where the injection is finished and the spray leaves a fog of fine droplets behind. On the right hand side the same situation is visible, but under evaporating conditions (gas temperature  $T = 580 \text{ K}$ ). A wavy structure of bright and dark areas is visible around the dark spray. This is evaporated fuel visualised by the Shadowgraphy technique (compare chapter 3.3). Due to the evaporation of the spray, the penetration of the liquid phase is significantly reduced.

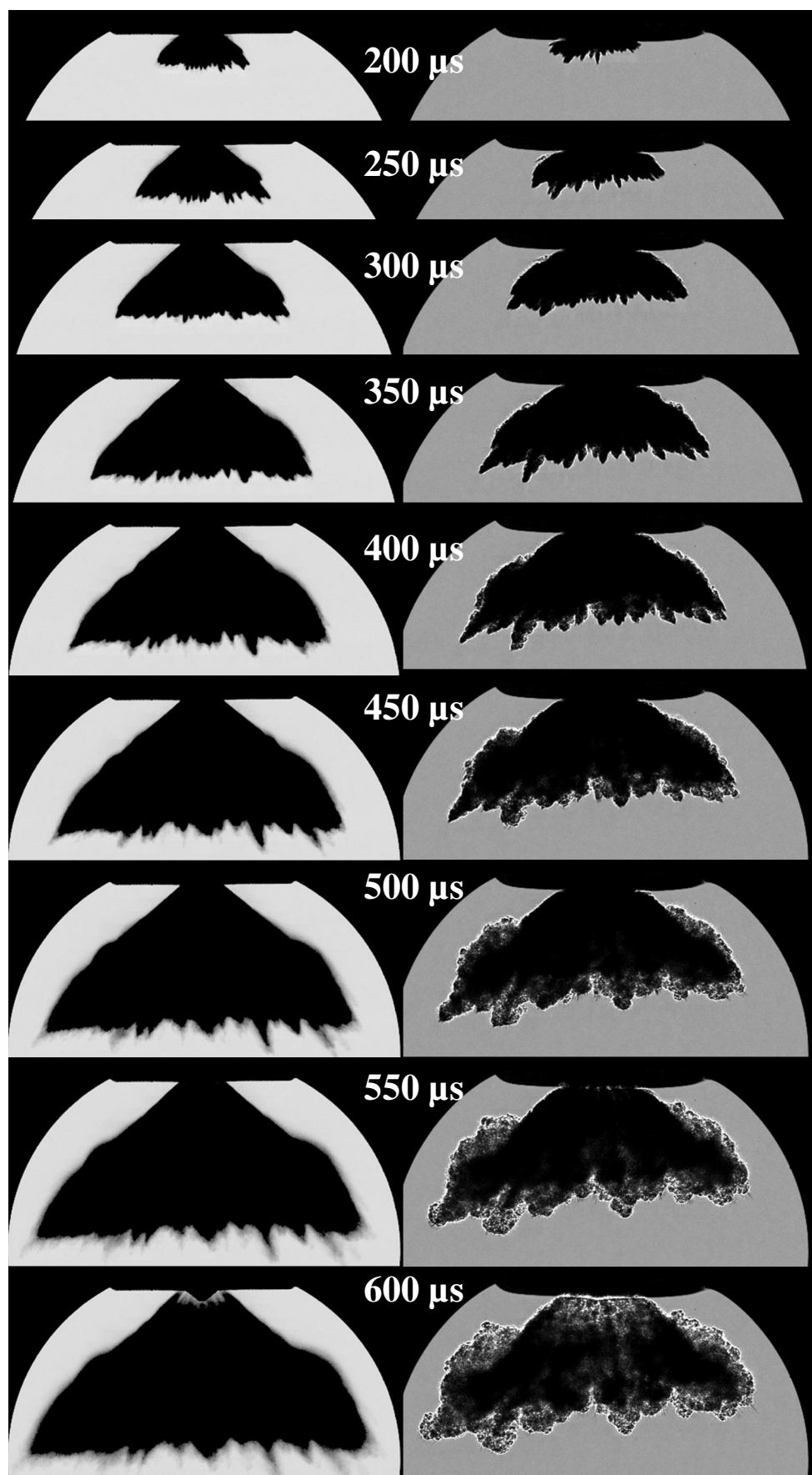
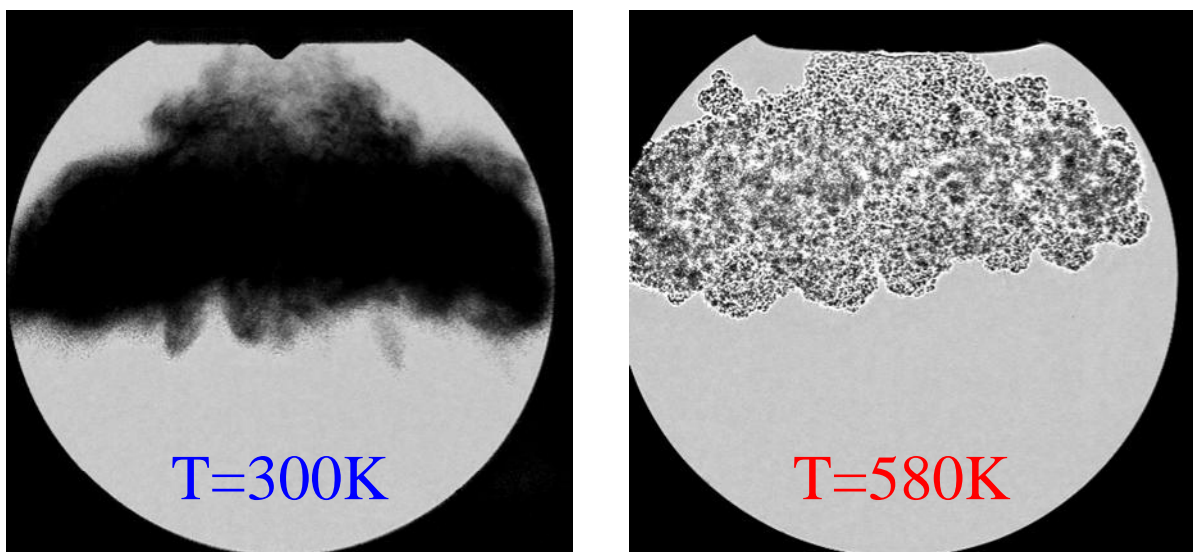


Figure 5-24 – Spray morphology at evaporating (right) and non evaporating conditions (left). (Shadowgraphy, mean (left) and single images (right),  $\rho = 6.6 \text{ kg/m}^3$ ,  $\Delta p_{inj} = 12 \text{ MPa}$ ,  $m_{inj} = 5 \text{ mg}$ ,  $\varepsilon = 23 \text{ } \mu\text{s}$ )

As soon as all the fuel is evaporated (Figure 5-25) and no more liquid phase is present, the dark areas vanish. The large area of dark and bright waves (right hand picture) is the vapour cloud. Even though the images shown in Figure 5-24 and Figure 5-25 are single images, it is possible (due to the sprays high reproducibility) to compare the shape of the liquid phase with the shape of the vapour volume. For the two cases the spray and the vapour shape look very similar. In both cases a heavily flattened ellipsoid is located underneath the injector tip. Under evaporating conditions the distance to the tip is smaller (refractive effects, also compare Figure 7-5). Also the axial penetration of the cloud is smaller. The reason for this is the fact that the evaporated fuel can better follow the vortices than the droplets. That means that the fuel vapour is transported further back upstream towards the nozzle than droplets do. The mechanism for this is later explained in Figure 5-31.



**Figure 5-25 – Evaporating (right) and non evaporating conditions (left).**  
 (Shadowgraphy, single images,  $\rho = 6.6 \text{ kg/m}^3$ ,  $\Delta p_{inj} = 12 \text{ MPa}$ ,  $m_{inj} = 5 \text{ mg}$ ,  $\varepsilon = 23 \text{ }\mu\text{m}$ ,  
 $t = 1000 \text{ }\mu\text{s}$  after SOI)

#### 5.1.14 Evaporation and Vapour Phase

A method was found to estimate the evaporated mass. It works with the help of Shadowgraphy images. It's in the nature of the Schlieren method that the standard deviation (STD) on the images is very high within the Schlieren. The liquid phase on the other hand shows a very high reproducibility (as discussed earlier in chapter 5.1.1). These facts offer a possibility to distinguish the vapour

phase from the liquid phase (at least approximately). For each operating point 10 experiments have been carried out. This results in 10 individual images for each time step. In Figure 5-26 (left image) a single Shadowgraphy image can be seen, showing the liquid phase (dark areas) and the vapour cloud (wavy structure around the liquid phase) shortly after the needle was closed. The right upper image shows the average of the ten images. As can easily be seen the cloudy structures around the spray are washed out, while the dark regions with the spray remain. The image underneath, following the red path, shows the standard deviation for the ten Shadowgraphy images. The region around the spray, where the fuel already evaporated, is bright. With thresholds for both images (averaged and STD-image), the area containing the liquid and the area containing the vapour phase can be estimated. If these areas are rotated around the injector axis by  $180^\circ$  the

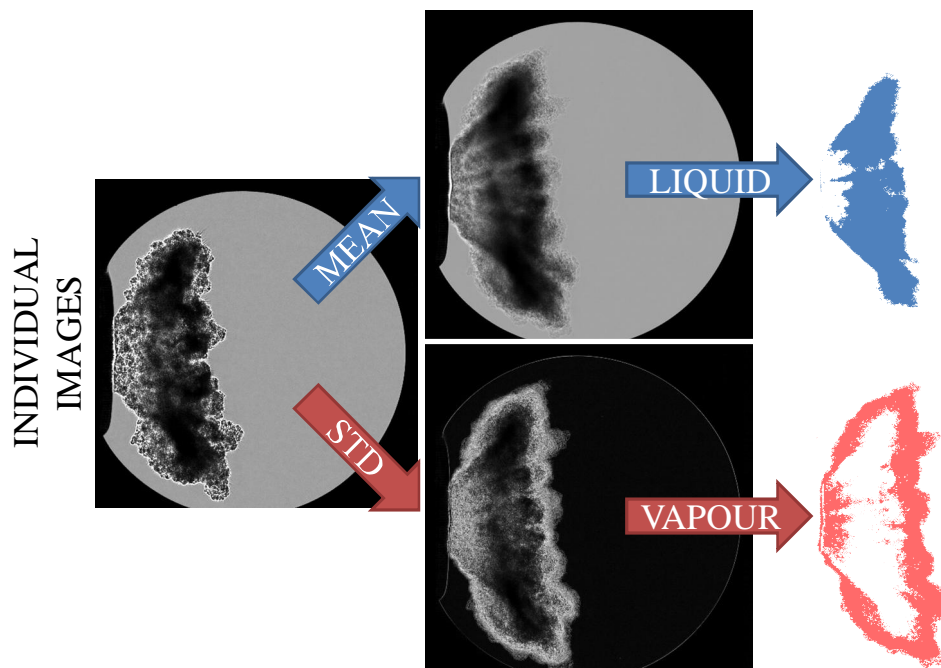


**Figure 5-26 – Estimation of liquid and vapour phase area based on Shadowgraphy.**  
 (Evaporating conditions:  $T = 580 \text{ K}$ ,  $\rho = 6.6 \text{ kg/m}^3$ ,  $\Delta p_{inj} = 12 \text{ MPa}$ ,  $m_{inj} = 5 \text{ mg}$ ,  
 $\varepsilon = 23 \text{ }\mu\text{m}$ ,  $t = 100 \text{ }\mu\text{s}$  after EOI)

volume occupied by the vapour phase – and correspondingly the liquid phase – can be calculated (assuming the homogeneous, circumferential fuel distribution, this had been shown by [80]). To determine the thresholds for the vapour and the liquid phase, a comparison with the non-evaporating case has been made:



Figure 5-27 shows six curves. The red curves show the evaporating case and the blue curves correspond to the case without evaporation. The intermittent line shows the injection rate for both cases (the rail pressure has been increased in case of higher pressure, to keep constant injection pressure). The volume calculated from the mean images, the liquid phase, has been plotted as a solid line and the volume calculated from the standard deviation image, the vapour phase, is represented by a dotted line. For both cases, evaporating and non evaporating conditions, the liquid exits the nozzle in the same way. Therefore the size of the liquid volume is the same in the beginning (Figure 5-28). Also the area of the standard deviation (vapour phase) is the same; the deviation in the spatial evolution is the same for both cases. As soon as the fuel starts to evaporate, things change completely. A look at the volume of liquid phase

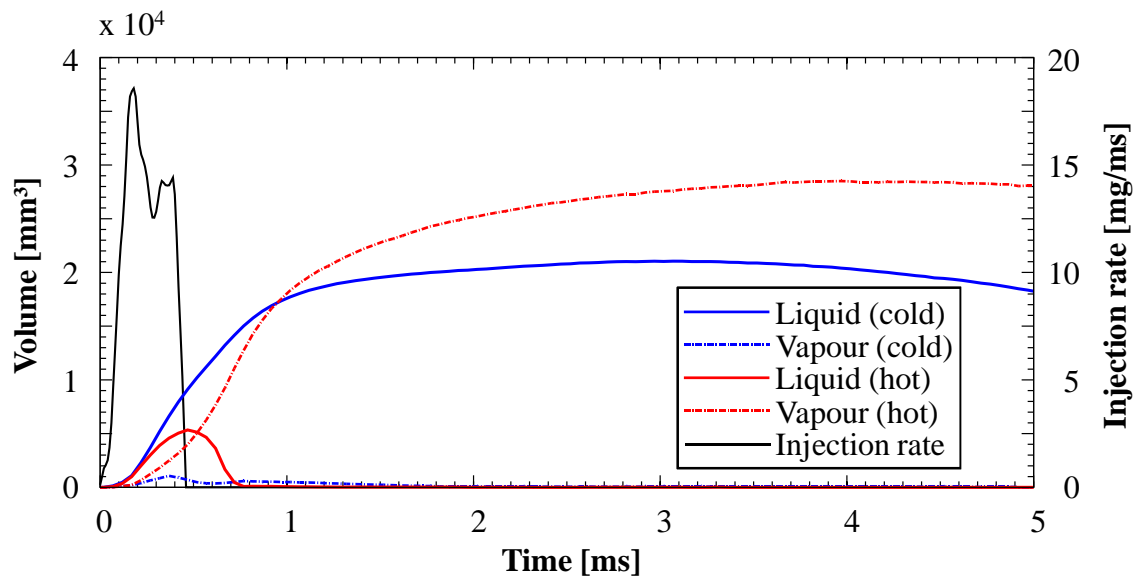


**Figure 5-27 – Injection rate (black line), Volume of vapour (dotted line) and volume of the liquid phase (solid line), Reference case.**

reveals the start of evaporation approximately 170  $\mu$ s after start of injection, where the red curve (evaporating case) starts to deviate from the blue curve (non evaporating case). Under non evaporating conditions the volume of the liquid phase grows fast, as the spray tip penetrates into the combustion chamber. In the case with evaporation (at the same air density) the liquid fuel is heated up to boiling temperature and evaporates around the surfaces of the hollow cone. Therefore the volume growth of the liquid phase is reduced and comes to an end. As soon as the injection stops, the volume containing the liquid fuel shrinks

fast until all the fuel is evaporated. If the injection duration is increased, equilibrium is reached where the injection rate is equal to the evaporation rate and the volume of the liquid phase has a constant size (compare Figure 5-48).

For the non evaporating case a small volume of fuel vapour seems to form in the beginning. This volume is not the vapour phase but the deviation in spray penetration. Both, the evaporating and the non evaporating cases show this increase in standard deviation as a result of the deviation in spray penetration. This (pseudo) vapour volume was subtracted from the volume of the vapour zone. Comparing the evaporating and the non-evaporating case, it can be seen that at the same time when the liquid volume of the evaporating case reduces growth, the vapour volume starts to grow (0.18 ms after SOI). This is when the evaporation starts.

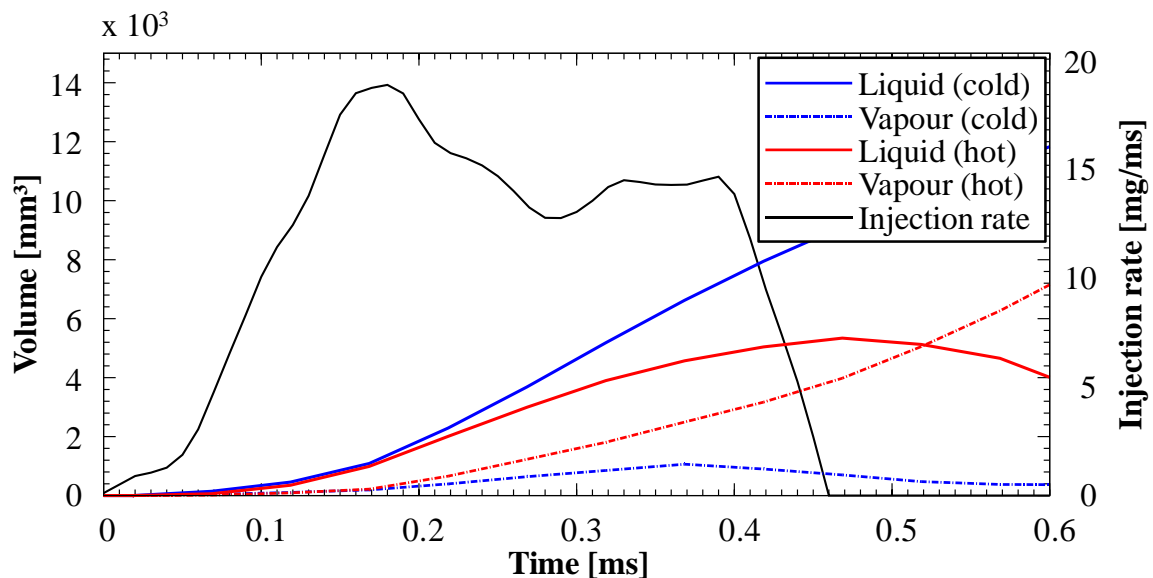
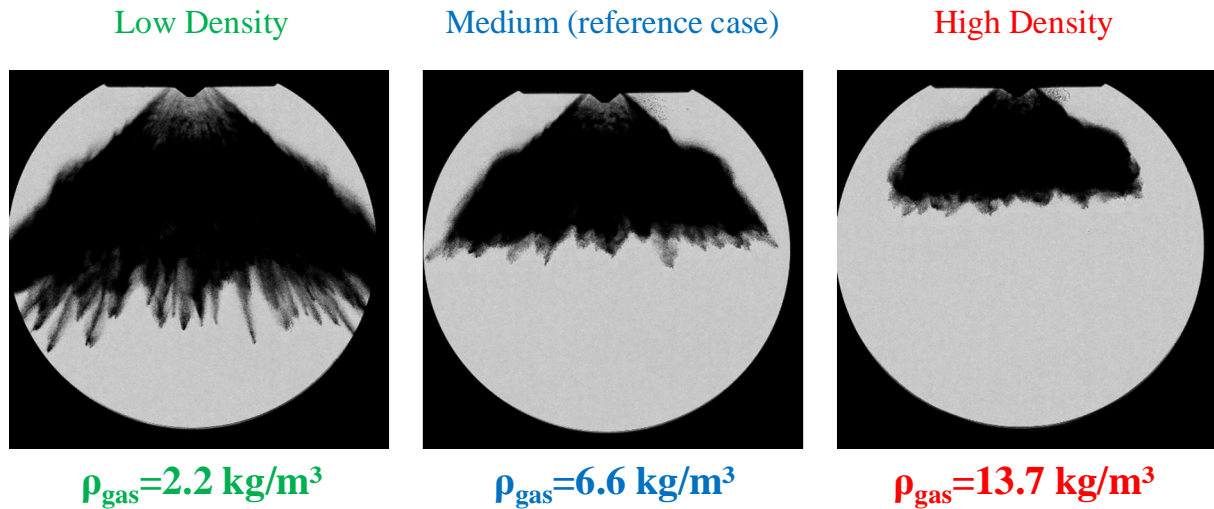


Figure 5-28– Early evolution of the volumes shown in Figure 5-27

In Figure 5-27 can be seen that the final volume of the vapour zone is bigger than the liquid volume in the non evaporating case (1 ms after SOI). With the knowledge about the volume of the vapour phase and the mass of injected fuel for each time step, estimation about the average lambda in the total volume can be made. With the assumption that the fuel within the volume is homogeneously mixed and by replacing the nitrogen mass by the same mass of air (as the experiments have been performed in nitrogen) a global lambda for the vapour zone can be calculated (hypothetically).

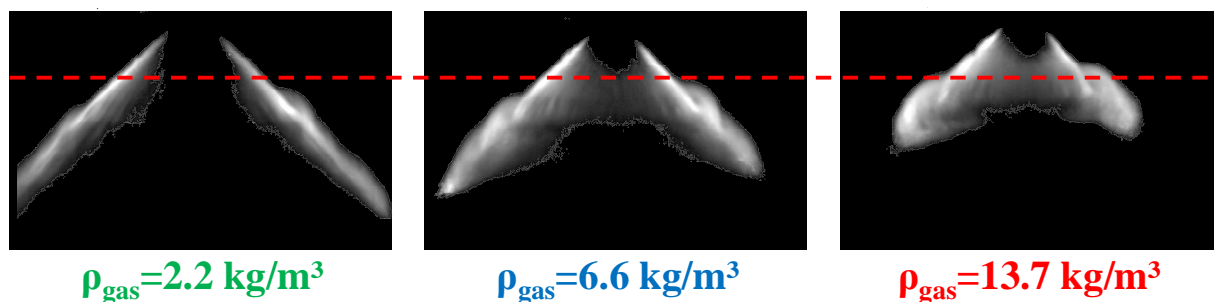
## 5.2 Influence of gas density

### 5.2.1 Influence of gas density on spray morphology



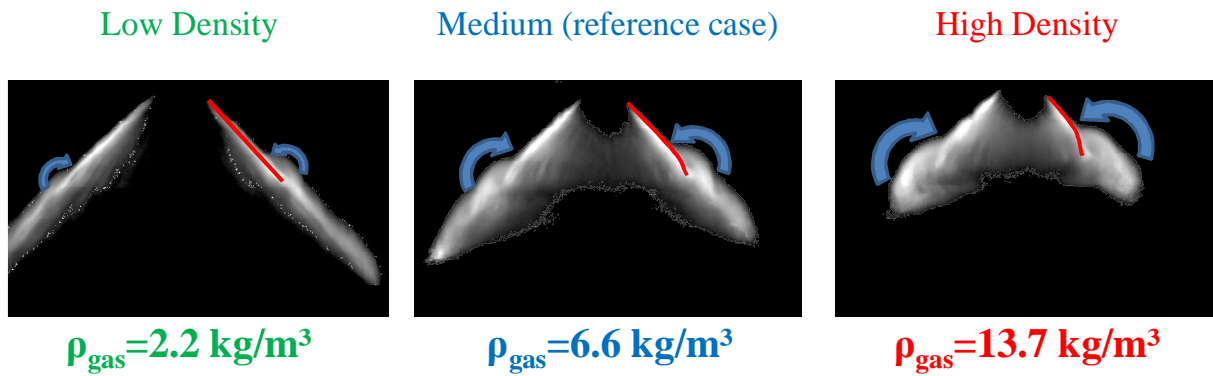
**Figure 5-29 – Influence of gas density on spray morphology.**  
(Shadowgraphy, single images,  $T = 300 \text{ K}$ ,  $\Delta p_{\text{inj}} = 12 \text{ MPa}$ ,  $m_{\text{inj}} = 5 \text{ mg}$ ,  $\varepsilon = 23 \mu\text{m}$ ,  
 $t = 500 \mu\text{s}$  after SOI)

Figure 5-29 shows Shadowgraphy images of the hollow cone spray  $500 \mu\text{s}$  after SOI for three different gas densities. All other parameters have been kept constant (rail pressure was increased in order to maintain constant injection pressure in case of higher gas density). Towards higher densities the string structure is less noticeable and the individual streaks are more and more prevented from emerging out of the main cloud. The spray shape in general becomes bushier and, as showed in earlier works [80], [81] or [82][118], the penetration of the spray is reduced towards higher surrounding gas densities. For



**Figure 5-30 – Influence of gas density on liquid phase and vortex position.**  
(Mie-scattering, mean images,  $T = 300 \text{ K}$ ,  $\Delta p_{\text{inj}} = 12 \text{ MPa}$ ,  $m_{\text{inj}} = 5 \text{ mg}$ ,  $\varepsilon = 23 \mu\text{m}$ ,  
 $t = 500 \mu\text{s}$  after SOI)

high gas densities the injector creates a fuel cloud just below the injector tip. This is desirable for stratified charge applications which the hollow cone injector actually has been designed for. The images obtained by means of 2D-Mie scattering (Figure 5-30) reveal also the inside of the hollow cone. The



**Figure 5-31 – Influence of gas density vortex momentum and its effect on liquid jet.**  
 (Mie-scattering, mean images,  $T = 300 \text{ K}$ ,  $\Delta p_{inj} = 12 \text{ MPa}$ ,  $m_{inj} = 5 \text{ mg}$ ,  $\varepsilon = 23 \text{ }\mu\text{m}$ ,  $t = 500 \text{ }\mu\text{s}$  after SOI)

intermittent line indicates the upper edge of the outer vortex for the reference case (middle image). In the case of lower density the edge is at higher distance from the nozzle, whereas the higher density shortens the distance to the nozzle. The two vortices forming on top and underneath the leading edge gain more momentum with higher gas densities. Containing more mass due to a higher liquid mass fraction and the higher gas density in general, the effect of the deflected liquid jet (described in chapter 5.1.5) is amplified as can be seen in Figure 5-31.

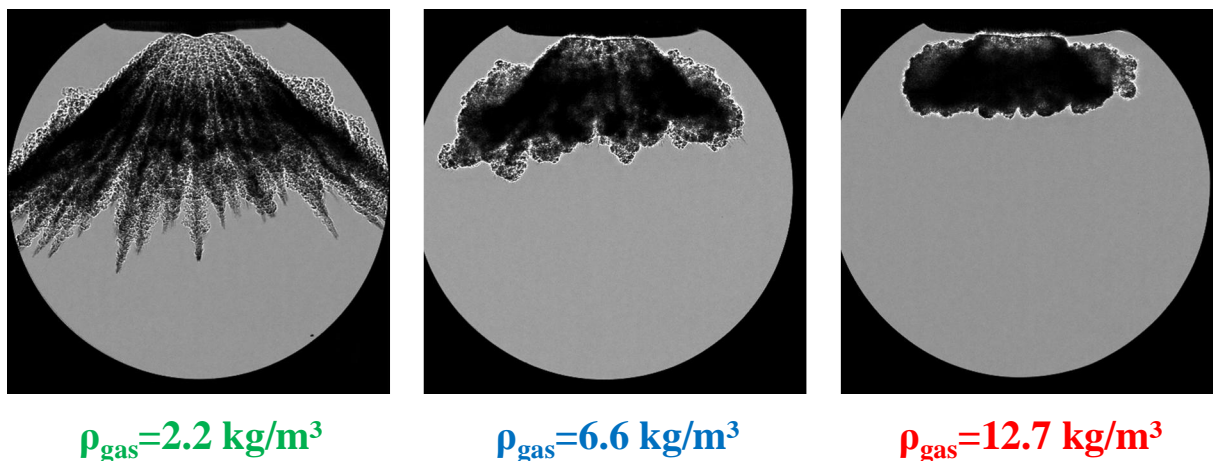


**Figure 5-32 – Influence of gas density on vapour phase (Shadowgraphy, single images,**  
 $T = 580 \text{ K}$ ,  $\Delta p_{inj} = 12 \text{ MPa}$ ,  $m_{inj} = 5 \text{ mg}$ ,  $\varepsilon = 23 \text{ }\mu\text{m}$ ,  $t = 500 \text{ }\mu\text{s}$  after SOI)

For evaporating conditions the density variation exhibits the same influence on the spray behaviour as for non evaporating conditions (Figure 5-32). The cloud of evaporated fuel along the envelope of the cone is directed further in radial direction, whereas the penetration in the axial direction is reduced.

### 5.2.2 Influence of air density on spray tip penetration

To investigate the influence of the gas density on the spray penetration, the air pressure in the HTDZ was varied. To maintain the same injection pressure (pressure difference), the rail pressure was adapted according to the pressure in the HTDZ. As for gasoline injectors with cylindrical holes, the A-injectors spray tip penetration is strongly influenced by the surrounding gas density as can be seen in Figure 5-33.

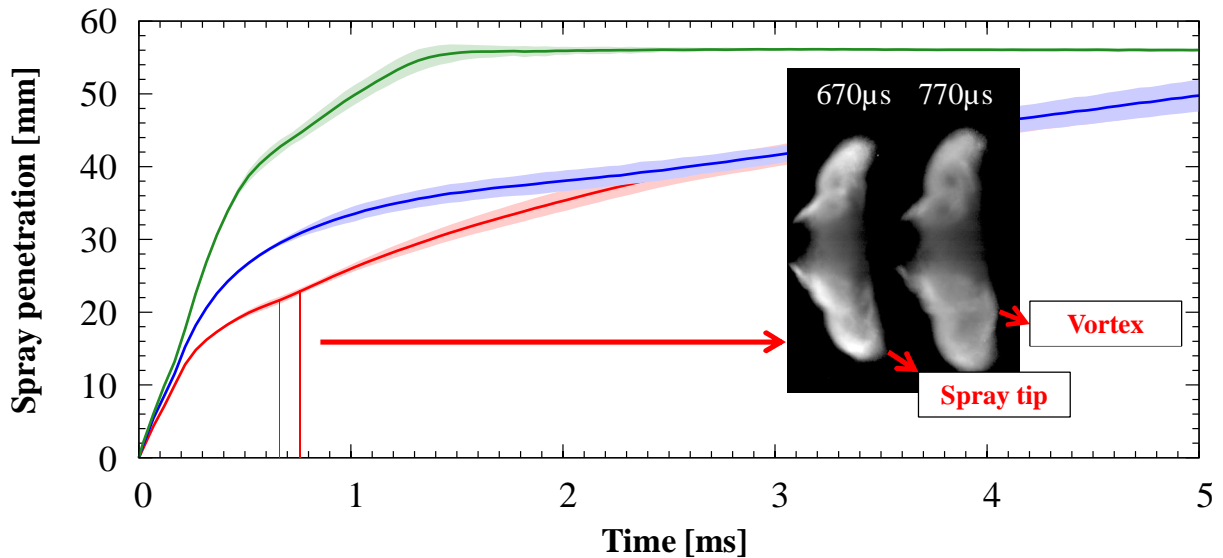


**Figure 5-33 – Nominal penetration for different gas densities (2.2 kg/m<sup>3</sup> in green, reference case with 6.6 kg/m<sup>3</sup> in blue and 13.7 kg/m<sup>3</sup> in red, T = 300 K,  $\Delta p_{inj} = 12$  MPa,  $m_{inj} = 5$  mg,  $\epsilon = 23$   $\mu$ m)**

With a low surrounding gas density the spray tip penetrates much faster than under conditions with increased gas density. This behaviour would be expected, as the drag is a linear function of the gas density. This also affects the breakup process. Towards lower gas density, the forces which tear the liquid structures apart become weaker. Therefore the core sustains longer and the larger structures in the spray can travel further until they break up. The Weber number is also linearly dependent on gas density. Higher Weber number implies faster droplet breakup. As soon as the spray is broken up, the surface is drastically increased and the spray faces a higher resistance. As can easily be seen in Figure 5-33; with small gas density (2.2 kg/m<sup>3</sup>) the spray tip quickly reaches the edge of the window and can't be tracked any further. As already discussed the penetration for medium gas density (6.6 kg/m<sup>3</sup>) shows three different phases. A linear propagation with constant velocity during the liquid breakup, the square

root shaped deceleration of the droplets and a third phase where the droplets are transported within the two strong circular vortices. This can also be observed in the case with the high gas density. But with increased density the effect of the overtaking vortices starts much earlier. A comparison of Figure 5-4 and Figure 5-33 reveals how the vortex becomes the leading edge 770  $\mu\text{s}$  after SOI. Unlike the reference case, the high density case shows a decrease in propagation velocity after approximately 2.3 ms from SOI. For both cases the vortices propagate with the same velocity.

### 5.2.3 Influence of air density on evaporation rate

Figure 5-34 shows the comparison in the Lambda development of three different gas densities. In all three cases evaporation starts 170  $\mu\text{s}$  after start of injection. During the injection the lambda within the vapour zone cannot be calculated correctly, as the evaporation rate cannot be measured and the droplet density within the liquid fuel zone can only be estimated with the help of the non evaporating case. But as soon as all the liquid fuel is evaporated the fuel mass in the vapour zone is known. Assuming a homogenous gas density distribution

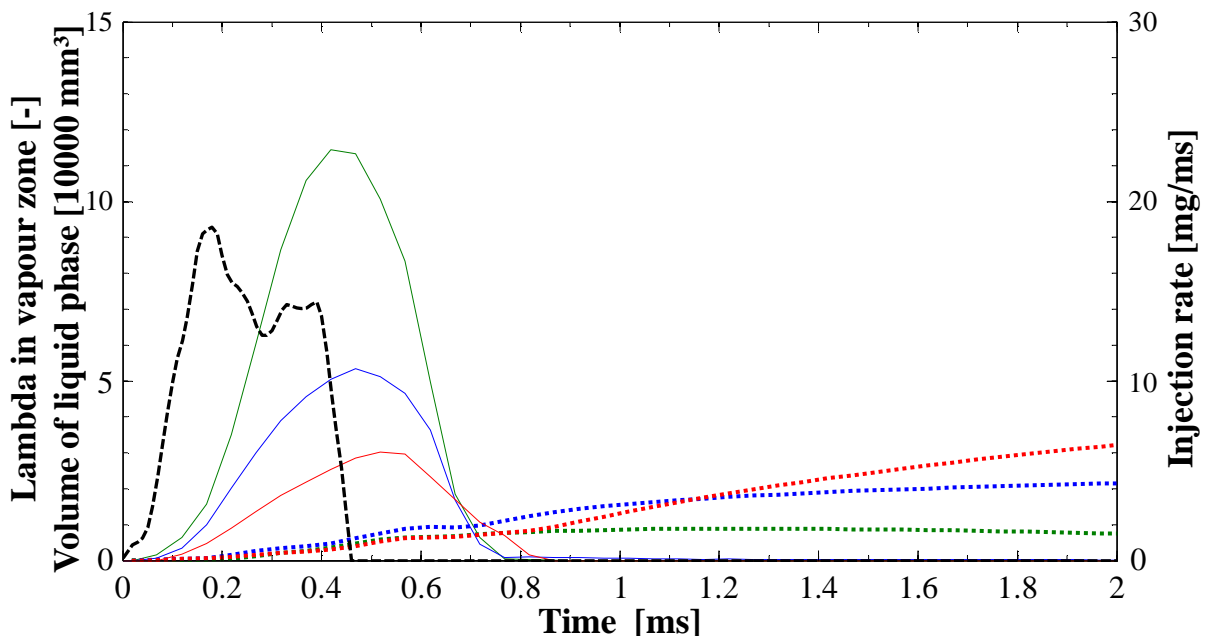


Figure 5-34 – Lambda in the vapour zone (dashed line), volume of the liquid zone (solid line) and injection rate (intermittent line) for three different gas densities; 2.3  $\text{kg/m}^3$  in green, 6.5 in blue and 12.7  $\text{kg/m}^3$  in red ( $T = 580 \text{ K}$ ,  $\Delta p_{\text{inj}} = 12 \text{ MPa}$ ,  $m_{\text{inj}} = 5 \text{ mg}$ ,  $\varepsilon = 23 \mu\text{m}$ )

within the vapour zone the lambda can be estimated, as the volume is known and the density of the air is assumed to be the same as outside the vapour cloud.

In reality the gas density will not be homogeneously distributed. Neither will the vapour phase. The density of the air in the vapour zone might be higher than on the outside, due to lower temperature as a result of the fuel evaporation. About 300  $\mu\text{s}$  after the injection ended, the evaporation is finished (no more liquid fuel). For the high density case it takes a bit longer to evaporate the fuel. The reason for this is the stratification of the fuel. Because penetration is strongly reduced due to the high gas density, the liquid fuel is in a much smaller volume. For the evaporation of the fuel, heat from the surrounding gas is used. In the case of the high density the energy is consumed locally by the fuel, therefore temperature drops and the evaporation process is slowed down. The local  $\lambda$  is low during the injection. As soon as the injection is over and the latest injected fuel is evaporated,  $\lambda$  increases as the fuel vapour is diluted with fresh air. This mixing is faster, the faster the vapour volume expands and the higher the density of the entrained air is. In case of the smallest density ( $2.3 \text{ kg/m}^3$ )  $\lambda$  never becomes stoichiometric. This is mostly because of the low density of the surrounding gas. At higher gas densities the curves look quite different: As soon as the evaporation is over and the vapour volume expands into the combustion chamber, the dilution is stronger, the higher the gas density is. Even though the effective expansion of the vapour cloud is slower than in the case with lower density, dilution is faster, as, due to the higher density, more air mass is mixed with the fuel.

### ***5.3 Influence of injection pressure***

#### **5.3.1 Influence of injection pressure on spray morphology**

Figure 5-35 shows the hollow cone spray for three different injection pressures. To allow an objective discussion of the spray shape, images 50  $\mu\text{s}$  after end of injection (EOI) have been compared. At this time the injected mass is the same and the vortices have had time to develop. The other parameters have been kept constant in all three cases: gas temperature  $T = 300 \text{ K}$ , gas density  $\rho = 6.6 \text{ kg/m}^3$ , injected mass  $m_{\text{inj}} = 5 \text{ mg}$  and the needle lift  $\varepsilon = 23 \mu\text{m}$ . The influence of higher injection pressure is not clearly visible on the Shadowgraphy

images. The vortices seem stronger and more pronounced in case of higher injection pressure.

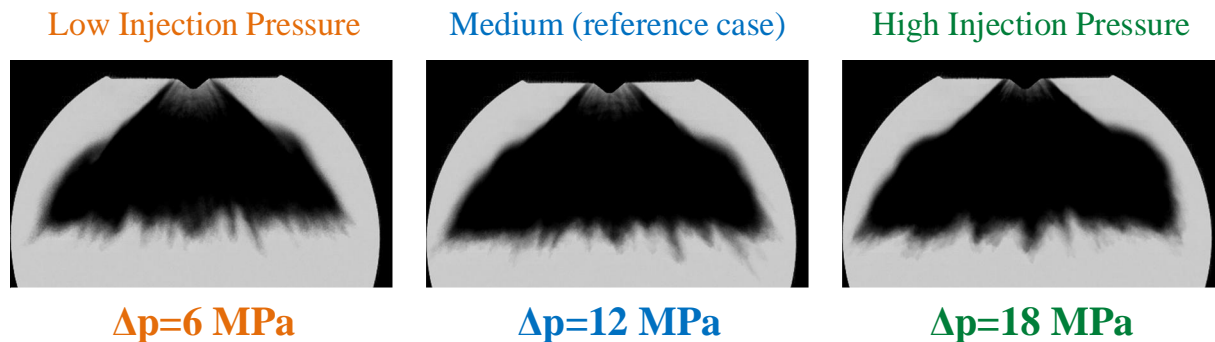


**Figure 5-35 – Influence of injection pressure on spray morphology under non evaporating conditions. (Shadowgraphy, mean images,  $\rho = 6.6 \text{ kg/m}^3$ ,  $T = 300 \text{ K}$ ,  $m_{inj} = 5 \text{ mg}$ ,  $\varepsilon = 23 \text{ }\mu\text{m}$ ,  $t = 50 \text{ }\mu\text{s}$  after EOI)**

The Mie scattering images presented in Figure 5-36 support these findings. The images are  $50 \text{ }\mu\text{s}$  after end of injection. At that moment all the fuel has been injected and the maximum possible momentum for each case has been transmitted to the gas phase. The images clearly show a thicker recirculation zone for the higher injection pressure. The penetration at this moment seems not to be influenced much by the higher injection pressure.

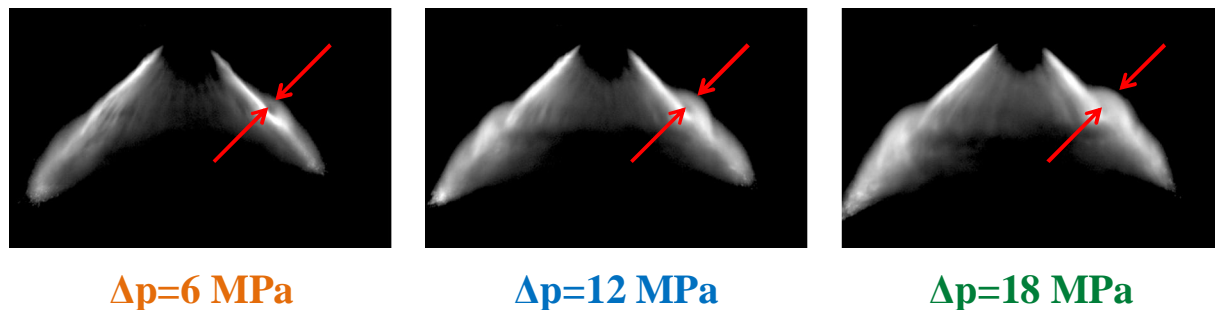


**Figure 5-36 – Influence of injection pressure on liquid phase and vortex position under non evaporating conditions. (Mie scattering, mean images,  $\rho = 6.6 \text{ kg/m}^3$ ,  $T = 300 \text{ K}$ ,  $m_{inj} = 5 \text{ mg}$ ,  $\varepsilon = 23 \text{ }\mu\text{m}$ ,  $t = 50 \text{ }\mu\text{s}$  after EOI)**

Under evaporating conditions (Figure 5-37) the differences become much more significant. In order to provide information concerning the evaporation process, the images were taken  $200 \text{ }\mu\text{s}$  after the end of each injection. At this time the fuel for the high pressure case is fully evaporated (as will be seen in Figure 5-41) and the effects can better be visualised. What catches the eye is that in case of low injection pressure (6 MPa) still large regions of non evaporated fuel (dark area) are visible.



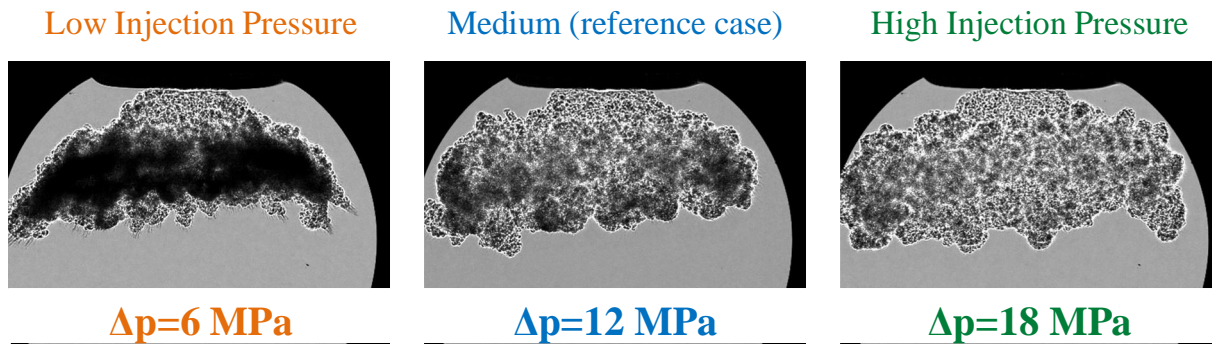


**Figure 5-37 – Influence of the injection pressure on the vapour phase. (Shadowgraphy, single images,  $\rho = 6.6 \text{ kg/m}^3$ ,  $T = 580 \text{ K}$ ,  $m_{\text{inj}} = 5 \text{ mg}$ ,  $\varepsilon = 23 \text{ }\mu\text{m}$ ,  $t = 200 \text{ }\mu\text{s}$  after EOI)**

Towards higher injection pressure these areas diminish, as due to a better atomisation of the fuel and therefore better surface to volume ratio a better heat transfer to the droplet is achieved. At higher injection pressures also the shape of the hollow cone becomes wider and due to the large circumferential vortices, the edges are rounder. For low injection pressures, the shape remains much more a

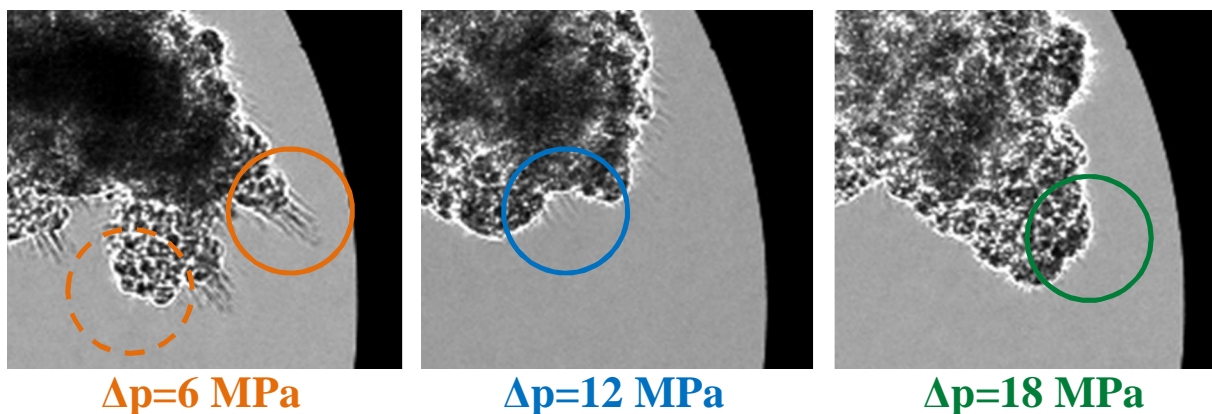


**Figure 5-38 – Zoom in on Figure 5-37, with droplets exiting the border of the vapour cloud, the range is highlighted by a circle**

triangular shape, as the recirculation zone is not as strong as with higher injection pressure. Another interesting observation is shown in Figure 5-38. A closer look at the fuel cloud in case of low injection pressure reveals strings exiting the cloud. These strings are large droplets which travelled in the slip stream of the droplets in front of them. Therefore they have not yet evaporated and pierce now the fuel cloud, leaving a trail of fuel vapour along their path. In the dotted circle no such lines are visible. The reason for this is the high momentum of the larger droplets. The cloud was formed perpendicular to the nominal spray penetration direction. It consists of fuel vapour which perfectly follows the local flow field. The big droplets have too high momentum to follow this flow field and maintain their velocity in nominal spray direction. Towards higher injection pressure this phenomena diminishes. The strings become

thinner and shorter, as the droplets producing them become smaller towards higher injection pressure.

### 5.3.2 Influence of injection pressure on spray tip penetration

As can be seen in Figure 5-39, the variation of the injection pressure has a significant influence on the spray tip velocity, the spray breakup length and the development of the vortices towards the end. According to Bernoulli's law, the velocity of the spray tip at the nozzle exit is increased with injection pressure (the velocity at the nozzle exit is proportional to the square root of the pressure drop along the nozzle). This can easily be seen before breakup, the spray tip propagates faster with higher injection pressure. After the breakup, when the larger fragments have been broken up and only droplets are left, the spray is decelerated much slower in the case of low injection pressure. Due to the high relative velocities between droplets and the surrounding gas in cases with higher injection pressure (12 and 18 MPa), the droplets face much higher drag forces as soon as they overtake the droplets in front. The vortices formed by the hollow cone travel faster with higher injection pressure. This can be seen in the fact that the nominal spray is overtaken much earlier by the vortices than in the cases

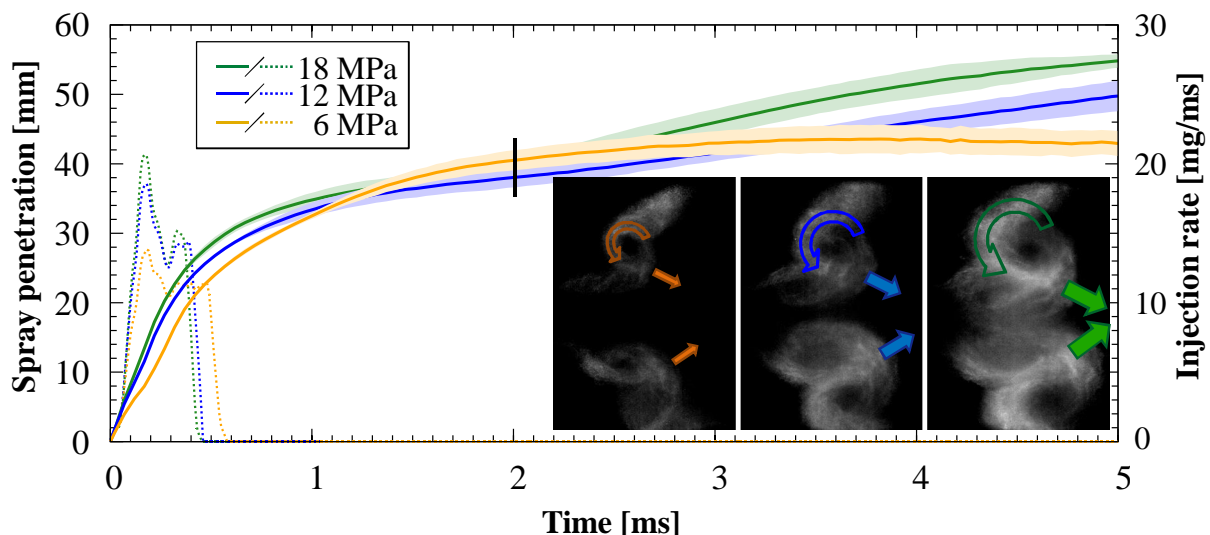


**Figure 5-39** – Nominal penetration for different injection pressures (18 MPa in green, reference case with 12 MPa in blue and 6 MPa in orange,  $T = 300 \text{ K}$ ,  $\rho = 6.6 \text{ kg/m}^3$ ,  $m_{inj} = 5 \text{ mg}$ ,  $\varepsilon = 23 \text{ }\mu\text{m}$ )

with medium or low injection pressure. The reason for this is the higher kinetic energy transferred to the vortices due to the higher injection pressure. In case of low injection pressure (6 MPa) the vortices hardly form.

Afterwards they stay small and travel at very low speed before they stop and disappear. In case of high injection pressure (18 MPa) the penetration is strongly decelerated until about 2 ms after SOI. Afterwards the vortices drive the spray further away. This transport is much faster with high injection pressure because more rotational energy is stored within the vortices. In case of high pressure the spray tip enters the combustion chamber with higher velocity, a strong deceleration due to the increase in surface area and the therefore higher drag forces is followed by a strong acceleration due to the vortices. The low pressure case on the other hand penetrates with low injection velocity. Due to the lower relative velocity the droplets don't break up as fast as in the high pressure case and therefore a weak deceleration and no further transport by the weak vortices are the result. As can be seen from these findings the interaction with the gas phase can be enhanced by increasing the injection pressure. Additionally can be assumed that the higher turbulence and kinetic energy in the vortices increases the transport of hot gas from the surrounding gas to the evaporation zone and to the liquid phase what enhances the evaporation process.

### **5.3.3 Influence of injection pressure on droplet size distribution**

That higher injection pressure has a positive influence on the spray behaviour is well known and has been properly investigated in the past decades, especially for Diesel engine and multi-hole applications. Also the spectra of droplet sizes produced by an A-injector can be shifted towards smaller droplet diameters by an increased injection pressure. Figure 5-40 shows the cumulative spray volume of the droplets measured in the outer spray for two different injection pressures. The measurement was taken 30 mm underneath the injector tip. With an increase in injection pressure by 6MPa (50%), the maximum droplet size can be reduced by about 30%. The fuel mass contained in droplets smaller than 15  $\mu\text{m}$  is more than doubled, from about 40% to 90%. Half of the liquid is within droplets smaller than 10  $\mu\text{m}$ . For an injected mass of 5mg with a droplet size distribution as shown in Figure 5-40 (18 MPa) this results in a total droplet surface area of 4  $\text{mm}^2$  whereas in case of the medium injection pressure the total surface is 2.5  $\text{mm}^2$ . This gives an increase in surface of about 60% and therefore an enhanced heat transfer from the gas to the liquid phase, which enhances fuel evaporation. The reduced injection pressure (6 MPa) was not measured. 20 mm

underneath the injector tip increased injection pressure has a similar effect on the droplet size distribution. The differences are not as pronounced anymore but are still visible.

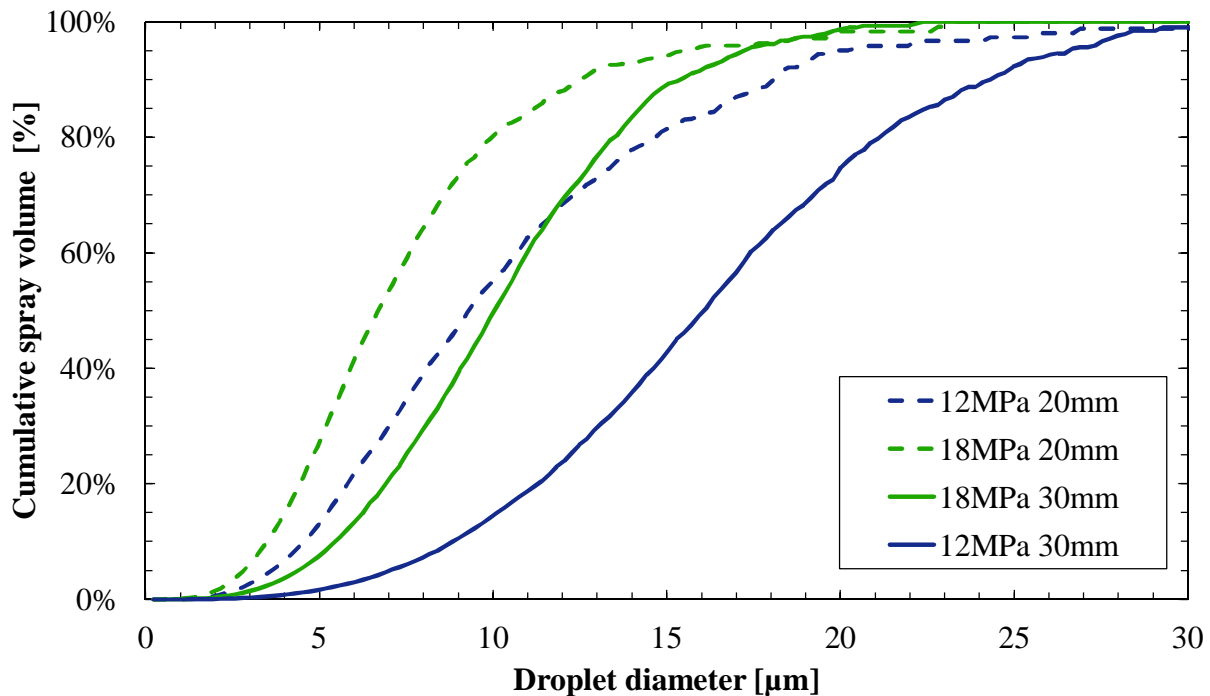


**Figure 5-40 – Cumulative spray volume over the droplet diameter 20 mm (dotted line) and 30 mm (solid line) underneath the injector tip. (18 MPa in green and reference case with 12 MPa in blue,  $T = 300$  K, atmospheric conditions,  $\varepsilon = 23$  μm, gasoline)**

### 5.3.4 Influence of injection pressure on evaporation rate

The influence of the injection pressure on the evaporation can be seen in Figure 5-41. The volume of the liquid phase grows faster with higher injection pressure. But, due to the smaller droplets (as discussed above) the evaporation is much faster. This can be seen in the fast decay of the liquid volume. For the case with high injection pressure (18 MPa, green curve) the evaporation process is completed 200 μs after end of injection. For the standard case (12 MPa, red curve) this takes about 300 μs. For the lowest injection pressure (6 MPa, orange curve) this delay is much bigger. It takes about 500 μs from the end of injection until the fuel is evaporated. The Lambda in the vapour cloud acts different for the three injection pressures once the liquid fuel is evaporated and the cloud of fuel drifts away from the injector. The high pressure case with the green curve is diluted faster. Due to its strong vortices which tunnel the fuel away from the

injector, the cloud entrains more fresh air than the cases with lower injection pressure (also compare Figure 5-39).

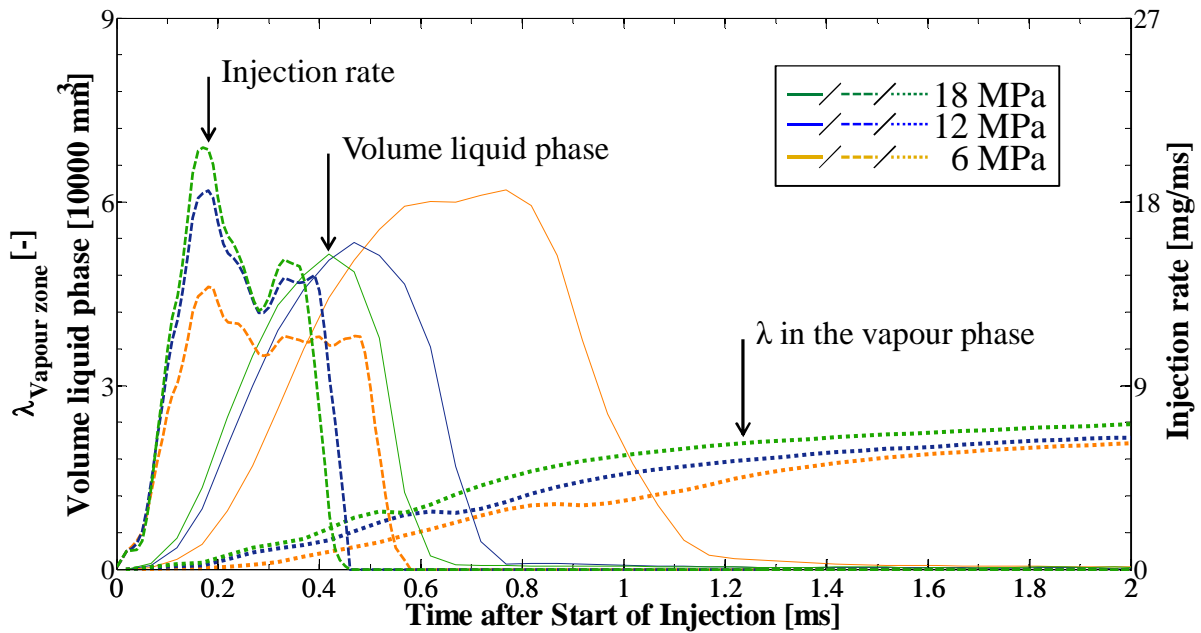


Figure 5-41 – Lambda in the vapour zone (dashed line), volume of the liquid zone (solid line) and injection rate (intermittent line) for three different injection pressures; 6MPa in orange, 12 MPa in blue and 18 MPa in green. ( $T = 580 \text{ K}$ ,  $\rho = 6.6 \text{ kg/m}^3$ ,  $m_{inj} = 5 \text{ mg}$ ,  $\varepsilon = 23 \text{ }\mu\text{m}$ )

## 5.4 Influence of needle lift

A big advantage of the piezo activated needle of the A-injector is its variable lift. The injectors design needle lift is about  $25 \text{ }\mu\text{m}$ . Its maximum needle lift (without damaging the injector) is around  $35 \text{ }\mu\text{m}$ . For these investigations the lift was massively increased (up to  $75 \text{ }\mu\text{m}$ ) to see what influence a large needle lift has on the spray propagation and spray shape.

### 5.4.1 Influence of needle lift on spray morphology

Due to the variation of maximal needle lift, the cross sectional area for the flow in the nozzle changes in a wide range (from  $0.12$  to  $0.25$  and up to  $0.78 \text{ mm}^2$ ). To maintain an injected mass of  $5 \text{ mg}$ , the injection duration had to be adjusted accordingly. It was set to  $1.35 \text{ ms}$  for the small and to  $0.19 \text{ ms}$  for the big needle lift. The influence in spray shape can be seen in Figure 5-42.

What catches the eye is the fact that 600  $\mu\text{s}$  after start of injection the medium and the big needle lift seem to have the same penetration length, whereas in case of a small needle lift (left image) the spray tips travelled about 6 mm less far. As

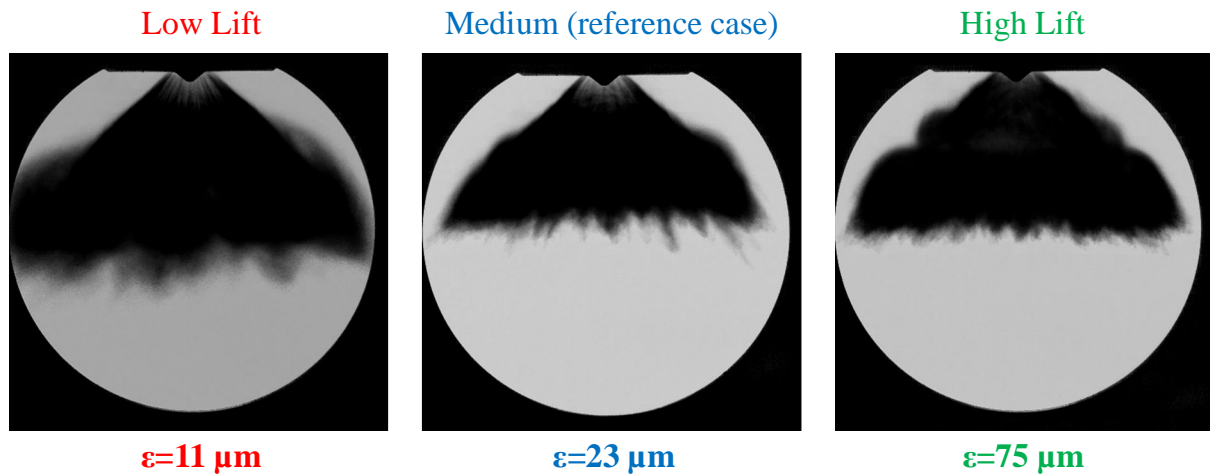


**Figure 5-42 – Influence of needle lift on spray morphology under non evaporating conditions. (Shadowgraphy, mean images,  $\rho = 6.6 \text{ kg/m}^3$ ,  $T = 300 \text{ K}$ ,  $\Delta p_{inj} = 12 \text{ MPa}$ ,  $m_{inj} = 5 \text{ mg}$ ,  $t = 50 \mu\text{s}$  after EOI)**

shown earlier (page 97) the injection velocity at the nozzle is not affected by the needle lift. But, due to the longer hydraulic delay caused by a slower opening of the needle (compare Figure 7-3 in the appendix), the fuel starts to exit the nozzle later. Towards a bigger needle lift a vanishing of the string structure can be observed. Another interesting fact is the shape of the spray edges. For the small and the medium needle lift only one recirculation zone is visible. For the large needle lift, it seems that two recirculation zones form. A look inside the spray (Figure 5-43) helps to understand this behaviour. The upper recirculation zone is a vortex which later moves to the inner side of the hollow cone. This

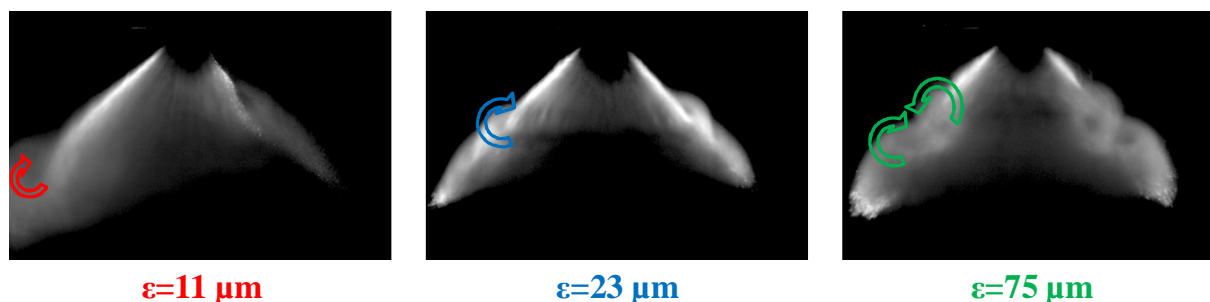


**Figure 5-43 – Variation of the needle lift under non evaporating conditions. (Mie scattering, mean images,  $\rho = 6.6 \text{ kg/m}^3$ ,  $T = 300 \text{ K}$ ,  $\Delta p_{inj} = 12 \text{ MPa}$ ,  $m_{inj} = 5 \text{ mg}$ ,  $t = 50 \mu\text{s}$  after EOI)**

vortex is much more present in the case of a big needle lift. It also forms with the medium needle lift but with a lower momentum. A look on the inside of the spray yet reveals another fact: With small needle lift, the spray becomes

asymmetric. The reason for this behaviour is the following: When the needle is lifted from the seat, the needle tends to move within the guidance of the needle seat. For a larger needle lift this does not affect the spray shape in a significant way. (But still one side of the spray is longer than the other, which can also be observed in the low pressure case (Figure 5-2)).

As the lift is very small the needle moves into its “neutral” position. Depending on the tolerance of the manufacturing process this movement might be bigger or smaller. The bigger it is, the stronger is the eccentricity between needle seat and needle and the stronger is the asymmetry of the spray.

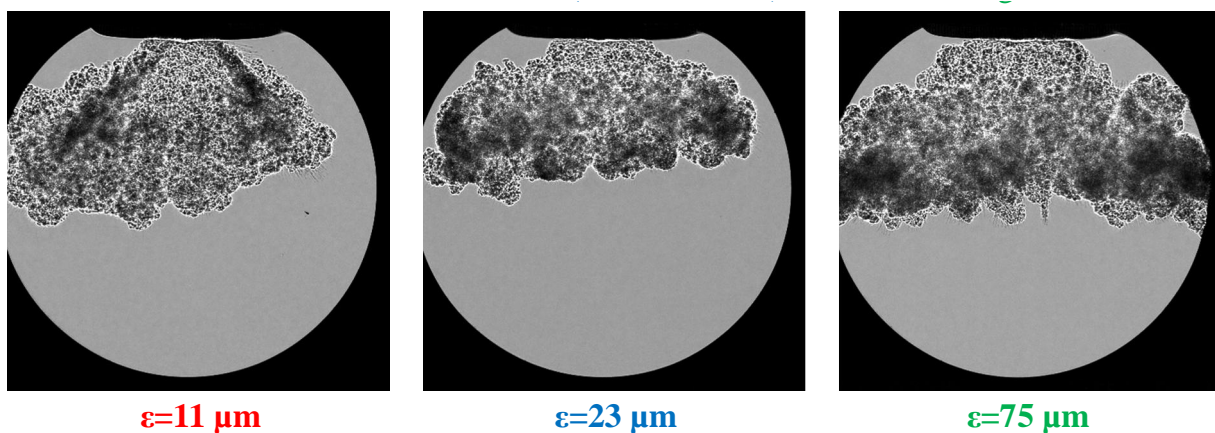


**Figure 5-44 – Influence of needle lift on the vapour phase.**

(Shadowgraphy, single images,  $\rho = 6.6 \text{ kg/m}^3$ ,  $T = 580 \text{ K}$ ,  $\Delta p_{inj} = 12 \text{ MPa}$ ,  $m_{inj} = 5 \text{ mg}$ ,  $t = 250 \text{ } \mu\text{s}$  after EOI)

The morphology under evaporating conditions is quite different for the three injection strategies. In case of a small needle lift, the long injection duration and the generated vortices force the fuel cloud downwards (compare Figure 5-44 ). The funnel effect becomes stronger with increasing injection duration (as described in Figure 5-10) and due to the weaker jet in case of the small needle lift (as a result decreased mass flow) the side of the hollow cone spray is bent more towards the injector axis. Therefore the fuel is directed in axial direction and transported away from the tip. For the very short injection with the large needle lift the fuel cloud forms a layer underneath the injector [34]. Due to the high mass flow in case of the big needle lift, the fuel builds clouds of higher density with a lower local  $\lambda$  and evaporates therefore less fast. The reason for this is the higher heat demand in these regions. Because of the inhomogeneity in liquid fuel distribution, locally more liquid mass has to be evaporated. Due to the reduced surface to volume ratio of these regions (more

droplets with about the same diameter are present in the same volume, therefore the liquid mass fraction is higher) the heat transport into these regions takes more time. Due to this higher density the vapour cloud also keeps its momentum and travels therefore further away from the injector than in case of the medium needle lift. The reference case (medium needle lift) is an intermediate between those two cases. Its axial penetration is the shortest.

### 5.4.2 Influence of the needle lift on spray tip penetration

The effect of a needle lift variation is shown in Figure 5-45. An increased needle lift results in a longer linear phase or, in other words, a later spray breakup. This was to be expected and has been observed in Diesel injectors in many investigations (e.g. [41], [55]). The spray tip velocity in the linear regime is not

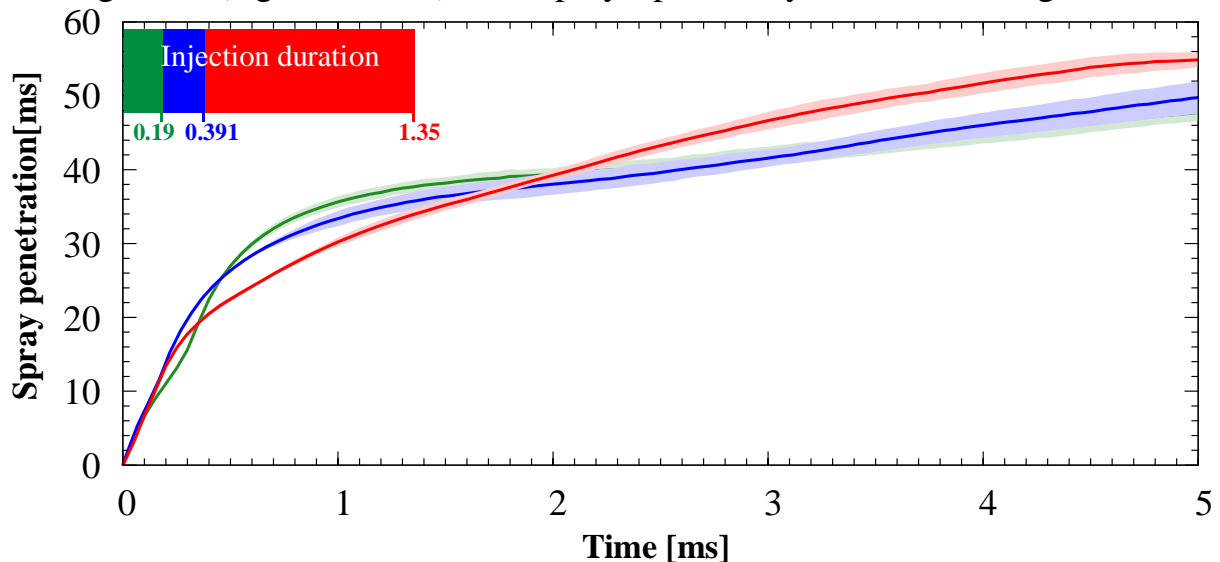


**Figure 5-45 – Nominal penetration for different needle lifts:  $\varepsilon = 75 \mu\text{m}$  in green, reference case with  $23 \mu\text{m}$  in blue and  $11 \mu\text{m}$  in red ( $T = 300 \text{ K}$ ,  $\rho = 6.6 \text{ kg/m}^3$ ,  $m_{\text{inj}} = 5 \text{ mg}$ ,  $\Delta p_{\text{inj}} = 12 \text{ MPa}$ , isooctane)**

influenced by the needle lift. The little bump in the linear regime of the case with big needle lift is expected to come from a pressure drop within the rail followed by a reopening of the needle as it bounced off the needle seat after end of injection. Due to the high mass flow and the fact that the fuel supply system was not fast enough to compensate this, the velocity in the linear regime decays until the pressure increases again and the velocity is back at the initial value again (the choking is expected to be in the injector itself, as it was never designed for such large needle lift). The axial propagation during the vortex phase is heavily influenced by the needle lift. As the needle lift is increased, the



influence of the vortices is reduced. Reducing the needle lift results in a higher axial spray velocity. This is mainly due to the shortened injection duration for the bigger needle lift and the longer injection duration in case of a smaller needle lift (these adjustments were necessary to keep the injected mass constant at 5 mg). As shown earlier, the spray penetration of an A-injector is influenced by the injection duration; the longer the injection is, the higher is the axial velocity.

### 5.4.3 Influence of a variation of the needle lift on droplet sizes

Figure 5-46 shows the cumulative spray volume over droplet diameter  $D_{10}$  for three different levels of needle lift. As can easily be seen, the smallest needle lift produces smaller droplets. This is what multi-hole correlations (e.g. [41], [55]) would predict and what was to be expected. The biggest droplets on the outside

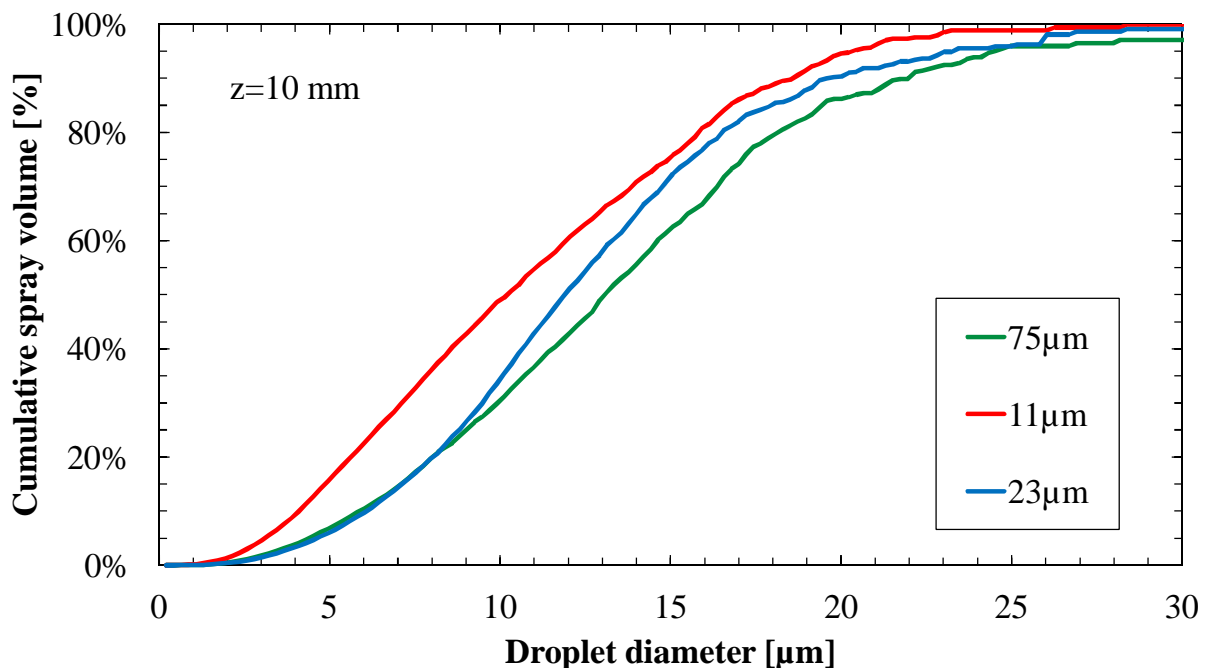


**Figure 5-46 – Percentage of cumulative spray volume depending on drop size for three different needle lifts under atmospheric conditions. The measurement was taken 10 mm underneath the injector tip at an injection pressure of 12 MPa.**

of the spray are 5  $\mu\text{m}$  smaller than the droplets of the case with 23  $\mu\text{m}$  needle lift. 50% of the liquid mass is within droplets smaller than 10  $\mu\text{m}$ . All in all this reduction in droplet diameter is not as strong as could be expected. A needle lift which is 7 times smaller than the maximum lift produces droplets which are about 3  $\mu\text{m}$  smaller than those from the case with maximum needle lift. Further downstream at an axial distance of 20 mm the distribution has changed a lot.

The reference case produces smaller droplets now and the big needle lift produces slightly bigger droplets whereas the smallest needle lift produces rather big droplets. The reason for this behaviour can be found in the different time evolutions of the spray penetration from the three different needle lifts. As has been shown in Figure 5-22 the droplet distribution is dependent on the distance from the nozzle. At an axial distance of 10 mm from the injector tip, which corresponds to a nominal distance of about 16 mm from the nozzle, the distance expressed in nozzle diameters is about  $732 \cdot d_h$  for the small needle lift. At the same height, the spray from the big needle lift travelled only  $107 \cdot d_h$  and in case of the medium needle lift only  $350 \cdot d_h$ . For the smallest needle lift the spray is in the range of the break up regime (about 10-15 mm nominal distance to the nozzle).

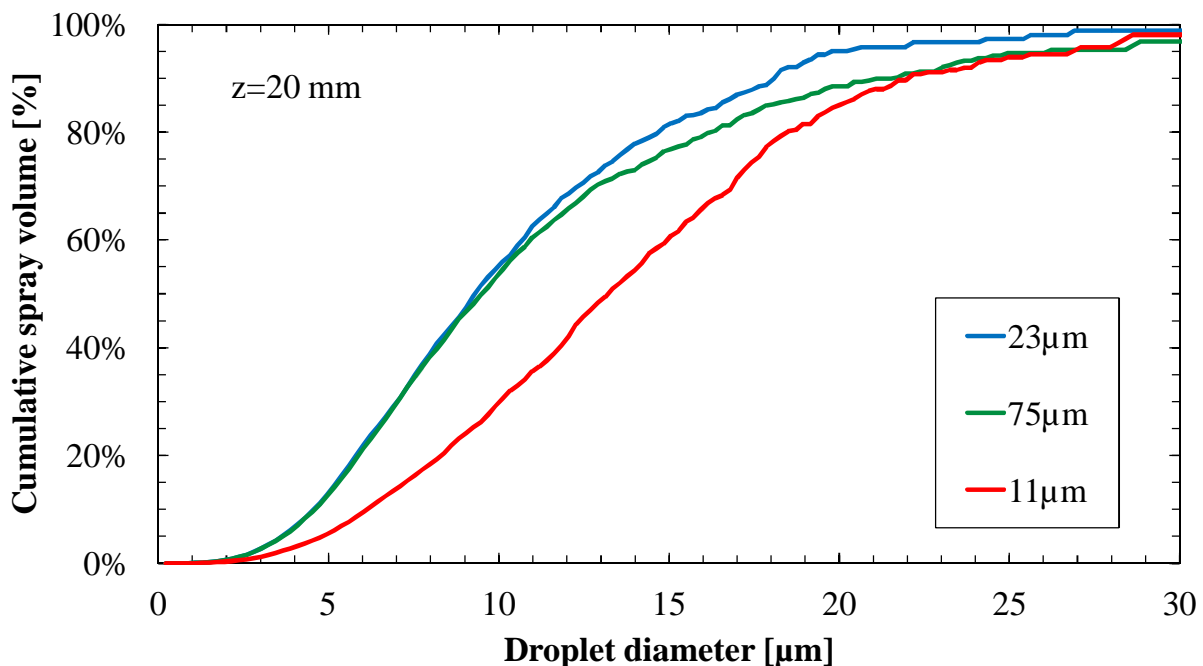


**Figure 5-47 – Percentage of cumulative spray volume depending on drop size for three different needle lifts under atmospheric conditions. The measurement was taken 20 mm underneath the injector tip at an injection pressure of 12 MPa**

#### 5.4.4 Influence of needle lift on evaporation rate

The influence of the needle lift on the evaporation is shown in Figure 5-48. As a result of the high mass flow rate in case of a high needle lift (75 μm), evaporation is much slower than with the medium needle lift. A possible explanation for this could be the high droplet density within the liquid phase cloud in the beginning. If the injection rate is compared with the volume of the

liquid phase, it can be seen that in case of medium needle lift the maximum in volume is reached shortly after the injection ends. In case of high needle lift, this maximum is reached 200  $\mu\text{s}$  after the injection ended. It takes about 200  $\mu\text{s}$  until evaporation starts and vapour is formed around the liquid phase. In this time about 60% of the fuel has already been injected. The volume which contains the droplets is about  $11\text{ cm}^3$ . For medium lift about 40% of the mass is injected 200  $\mu\text{s}$  after SOI whereas the volume occupied by the droplets is  $19\text{ cm}^3$ .

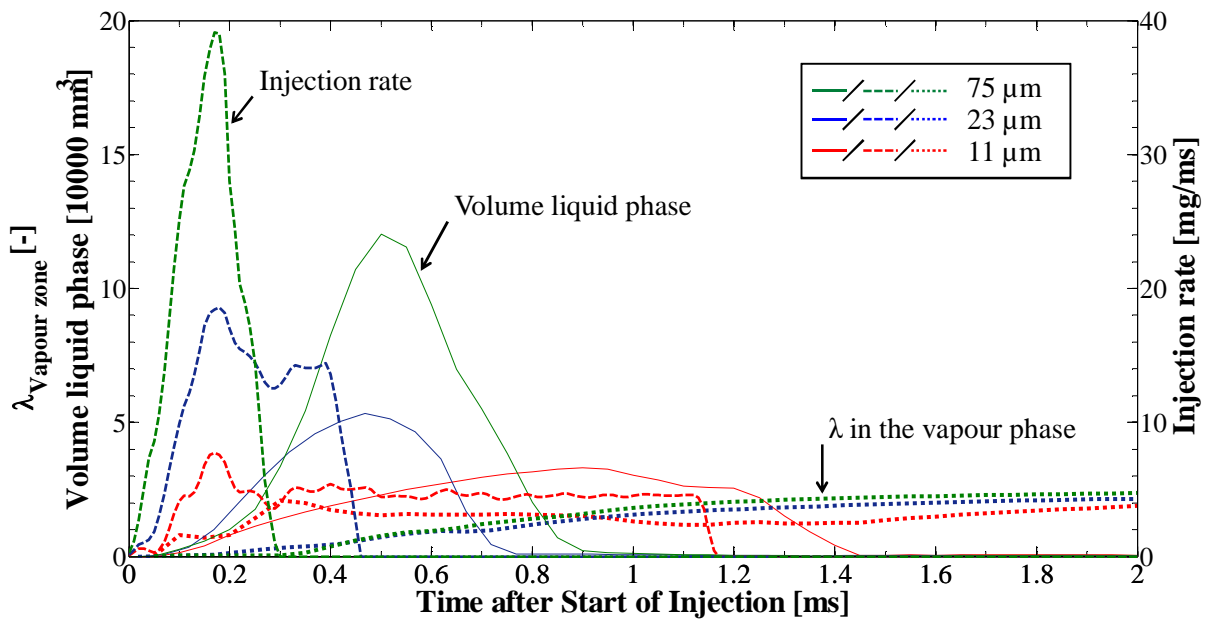


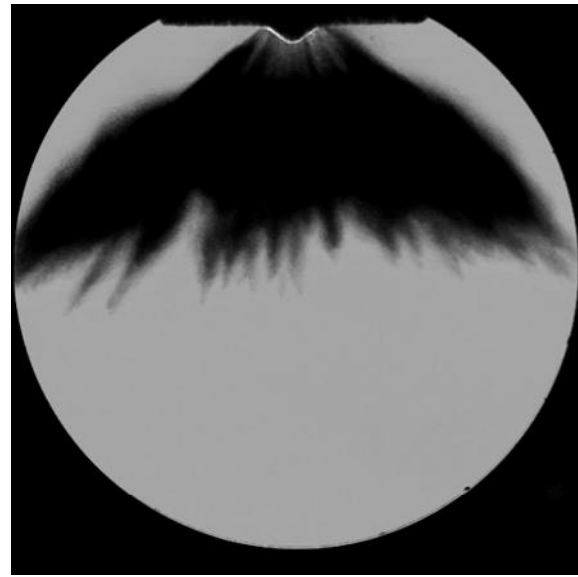
**Figure 5-48 – Lambda in the vapour zone (dashed line), volume of the liquid zone (solid line) and injection rate (intermittent line) for three different needle lifts;  $\epsilon = 75\ \mu\text{m}$  in green, reference case with  $23\ \mu\text{m}$  in blue and  $11\ \mu\text{m}$  in red. ( $T = 580\ \text{K}$ ,  $\rho = 6.6\ \text{kg/m}^3$ ,  $\Delta p_{\text{inj}} = 12\ \text{MPa}$ ,  $m_{\text{inj}} = 5\ \text{mg}$ , isooctane)**

The droplet number density in this volume is therefore about twice the density of the case with normal needle lift. This means that the heat transfer rate needed to evaporate all the fuel is twice as high. Within the evaporation zone the temperature can drop down to the boiling temperature of the fuel. This reduces the heat transfer to the droplet and slows down evaporation. It takes more hot gas within the droplet cloud to enhance the evaporation process. This is mostly done by entraining the gas from the “fresh gas zone” and mixing it with the “cold” saturated air around the droplets. This takes time and therefore evaporation is slower in case of large needle lift.

## 5.5 Influence of fuel properties



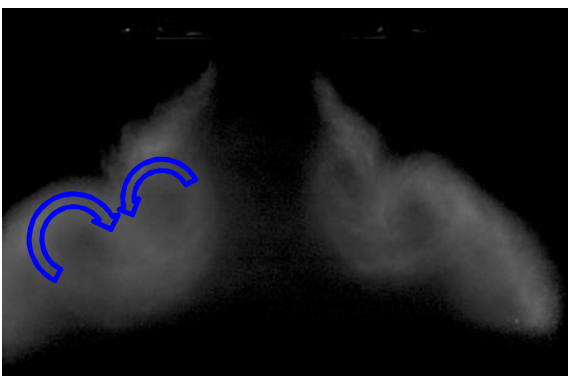
**Isooctane**



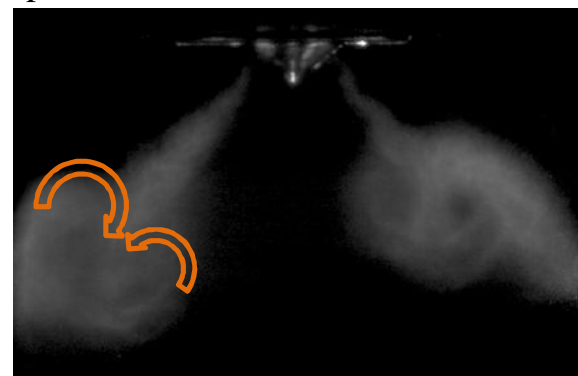
**Gasoline**

**Figure 5-49 – Influence of fuel properties on spray morphology under non evaporating conditions. (Shadowgraphy, mean images,  $\rho = 6.6 \text{ kg/m}^3$ ,  $T = 300 \text{ K}$ ,  $\Delta p_{inj} = 12 \text{ MPa}$ ,  $m_{inj} = 5 \text{ mg}$ ,  $\varepsilon = 23 \text{ }\mu\text{m}$ ,  $t = 50 \text{ }\mu\text{s}$  after EOI)**

As can be seen on Figure 5-49 the spray shape is heavily influenced by the fuel properties (which are given in detail in the appendix; Table 4 on page 156). With gasoline as fuel, the cloud tends to widen towards the side. The spray shape becomes asymmetric. The strings are more pronounced and areas without fuel can be seen within the hollow cone shape.



**Isooctane**



**Gasoline**

**Figure 5-50 – Influence of fuel properties on spray morphology under non evaporating conditions. (Mie, mean images,  $\rho = 6.6 \text{ kg/m}^3$ ,  $T = 300 \text{ K}$ ,  $\Delta p_{inj} = 12 \text{ MPa}$ ,  $m_{inj} = 5 \text{ mg}$ ,  $\varepsilon = 23 \text{ }\mu\text{m}$ ,  $t = 50 \text{ }\mu\text{s}$  after EOI)**

The reason for this could not entirely be identified. But as the inner nozzle flow has a significant influence on the spray shape (according to [36], [42] or [78]), this must play a major role in the influence of the spray shape. Further is a less

pronounced vortex noticeable: the bump on the edge of the spray is flatter and blurry. This has its nature in the different position and orientation of the vortices, as can be seen in Figure 5-50. In case of isooctane the outer vortex moves onto the nominal spray axis and so the two vortices direct the fuel almost perpendicular to the nominal spray axis into the inner region of the hollow cone. Gasoline shows a very different behaviour. The outer vortex stays outside the nominal spray axis and produces a flow which directs the fuel in the nominal spray axis.

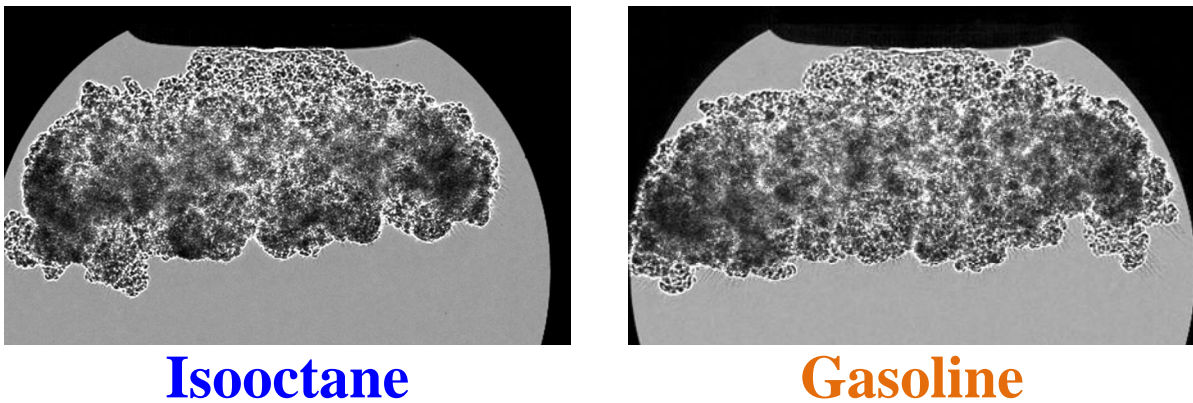


**Figure 5-51 – Influence of fuel properties on spray morphology under evaporating conditions. (Shadowgraphy, single images,  $\rho = 6.6 \text{ kg/m}^3$ ,  $T = 580 \text{ K}$ ,  $\Delta p_{inj} = 12 \text{ MPa}$ ,  $m_{inj} = 5 \text{ mg}$ ,  $t = 50 \text{ }\mu\text{s}$  after EOI)**

Under evaporating conditions (Figure 5-51) the differences between the two fuels seem to be much smaller. As seen under non evaporating conditions, the spray is wider in case of gasoline, but the dark areas, containing the non evaporated fuel are about the same.

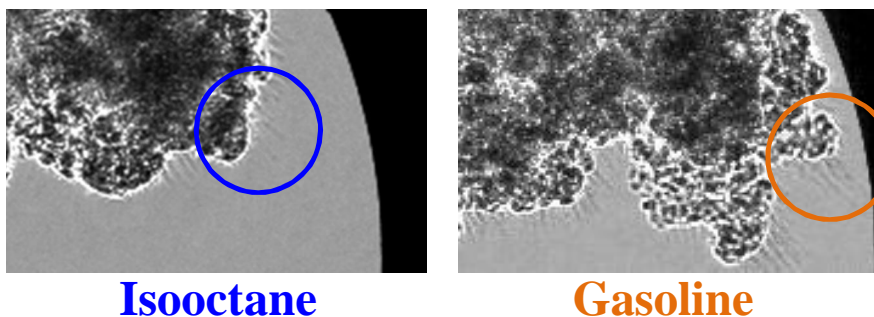


**Figure 5-52 – Zoom in on Figure 5-51**

Zooming onto the edges of the vapour cloud (Figure 5-52) yet reveals that like in the case of higher and lower injection pressure, the gasoline produces much more droplets shooting out of the vapour phase than isooctane. As gasoline and isooctane produce about the same size of droplets (Figure 5-54), the reason for

this phenomena must lie within the broad spectra of species contained in gasoline. While isooctane boils only at one temperature (99.2°C under atmospheric pressure), the lightest components in gasoline start to boil at 33°C and the heaviest components boil at 190°C. These heavier components need longer to evaporate and can therefore survive until the outside of the vapour cloud.

### 5.5.1 Influence of fuel properties on spray penetration

As can easily be seen in Figure 5-53 the influence on spray tip velocity before and after the spray breakup is negligible. Also the influence on breakup length is small. As seen earlier (Figure 5-50) the main difference between the two cases lies within the behaviour of the vortices. In case of gasoline as fuel, the vortices form in such a way that they push the fuel faster in nominal direction and lose their momentum earlier, whereas with isooctane the vortices are positioned in a way that the fuel is directed in axial direction.

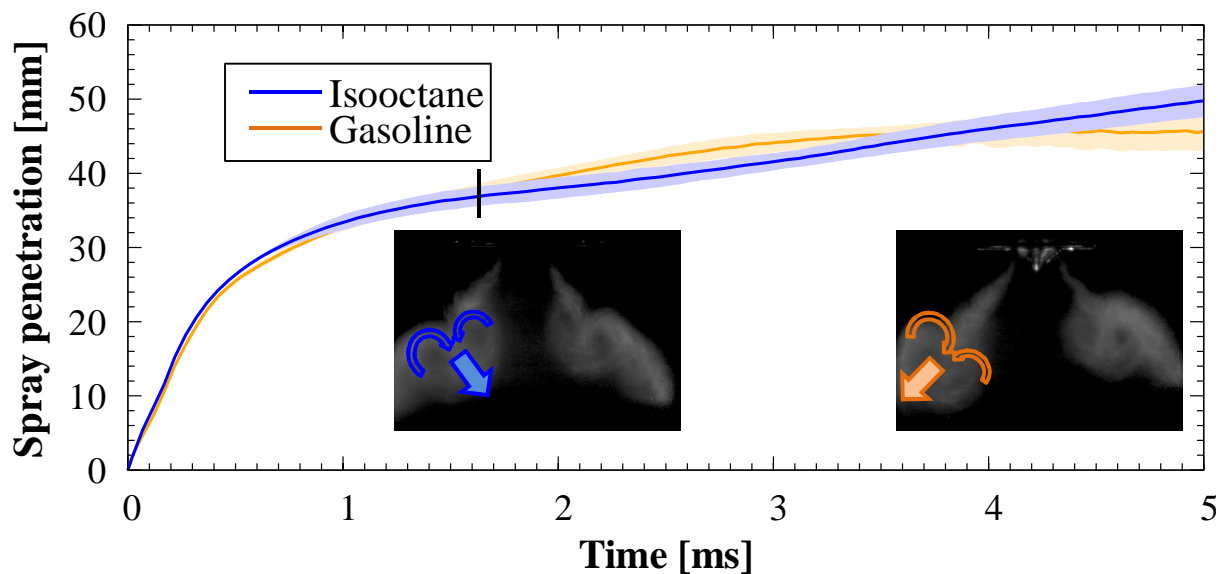


Figure 5-53 – Comparison of spray tip penetration for gasoline and isooctane under non evaporating conditions (Reference case)

### 5.5.2 Influence of fuel properties on droplet sizes

Figure 5-54 shows the droplet sizes for isooctane and gasoline. Obviously the droplet size is not tremendously influenced by the variation between the two fuels. While gasoline produces more small droplets (< 10 µm), isooctane produces more mid-sized droplets (10 to 15 µm). The largest droplets are about

the same size for both fuels. As seen earlier the differences in spray performance between the two fuels lie in the interaction with the gas phase.

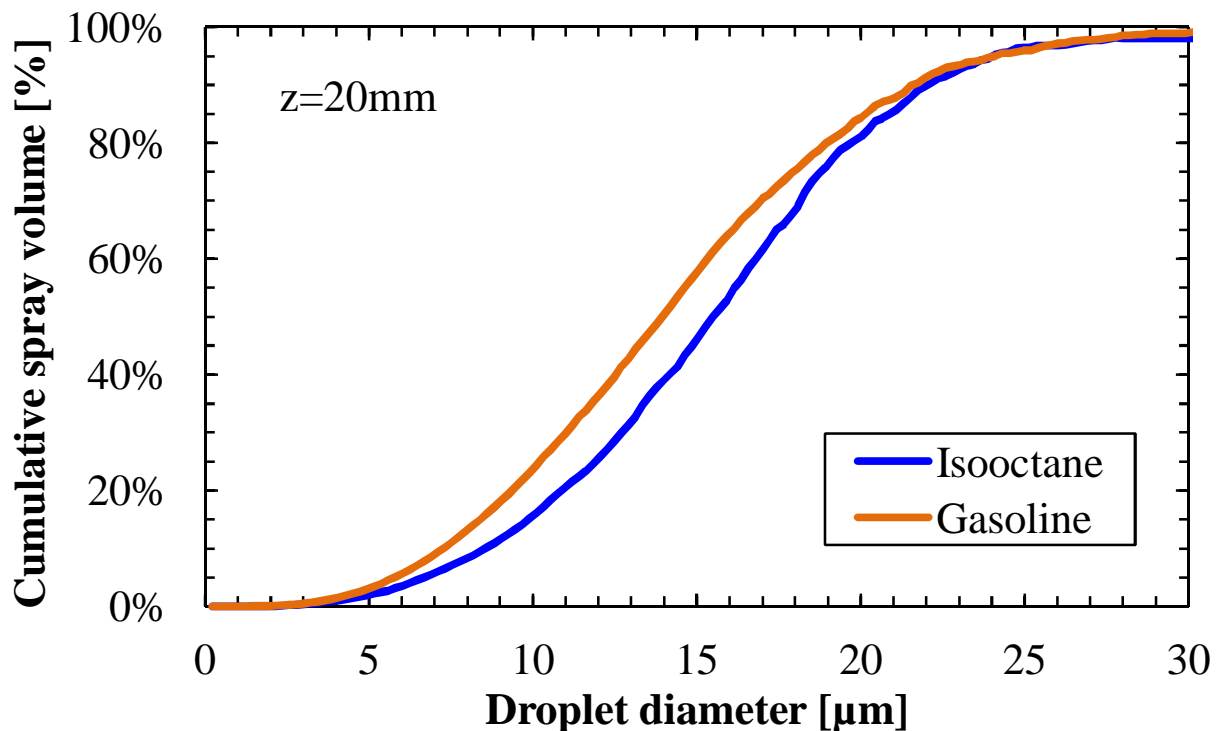


Figure 5-54 – Percentage of cumulative spray volume depending on drop size for gasoline and isooctane as fuel under atmospheric conditions (non evaporating conditions). The measurement was taken 20 mm underneath the injector tip.

### 5.5.3 Influence of fuel properties on evaporation

Isooctane is often used as a replacement fuel for gasoline. Due to its ignition behaviour which is similar to a 100 Octane gasoline fuel, it is a good substitute for CFD calculations with chemistry analysis and combustion. But being a single component fuel has some disadvantages, too. The evaporation process is not exactly the same as for the gasoline evaporation, which can be seen in Figure 5-55. The reason for the slower evaporation must be found within the fuel properties. Gasoline consists of more than 100 hydro carbon components which can be present in different concentrations. These individual components have boiling temperatures in the range of 70° up to 190° Celsius. Isooctane has a boiling temperature of about 99°C. The heavy components in the gasoline take longer to evaporate and are more sensitive to temperature drops in the gas phase, as just described before. Therefore in case of gasoline the volume of the liquid phase grows about 20% bigger before it collapses due to evaporation than isooctane does.

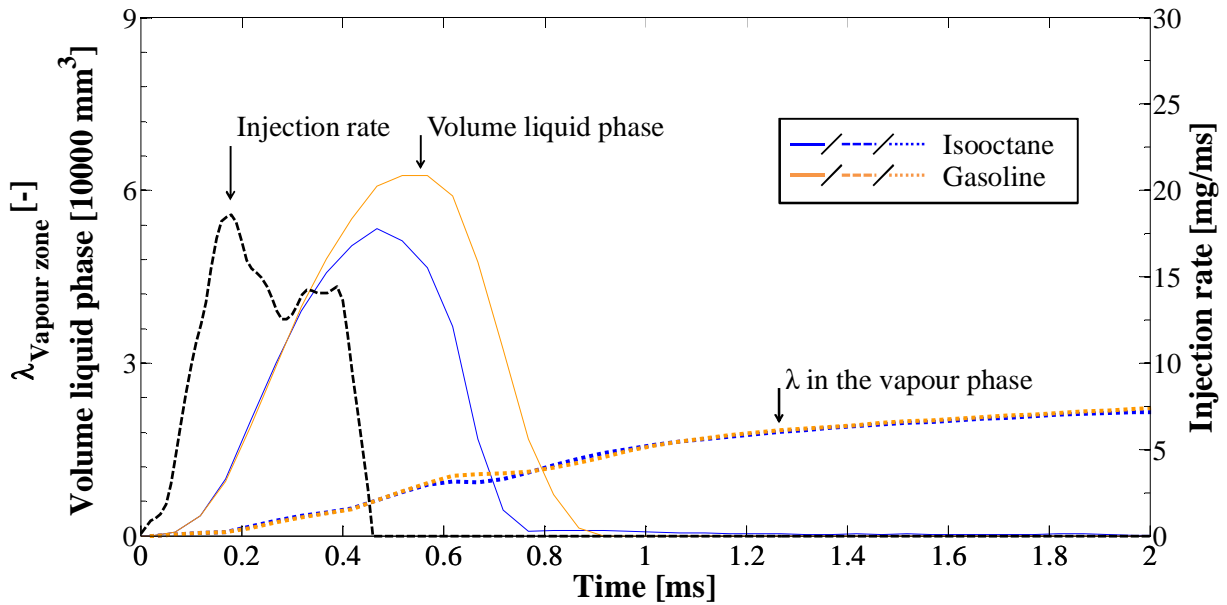


Figure 5-55 – Lambda within the vapour zone (dashed line), volume of the liquid zone (normal line) and injection rate (intermittent line) for gasoline (brown plot) and isooctane (red plot)

### 5.6 Comparison with literature

Different publications (e.g. [55], [61], [63]) give correlations to predict the spray tip penetration for hole-type injectors under engine-like conditions. Figure 5-56 shows a comparison of the spray tip penetration measured (reference case) and its prediction by several correlations. For the experiment breakup is reached if

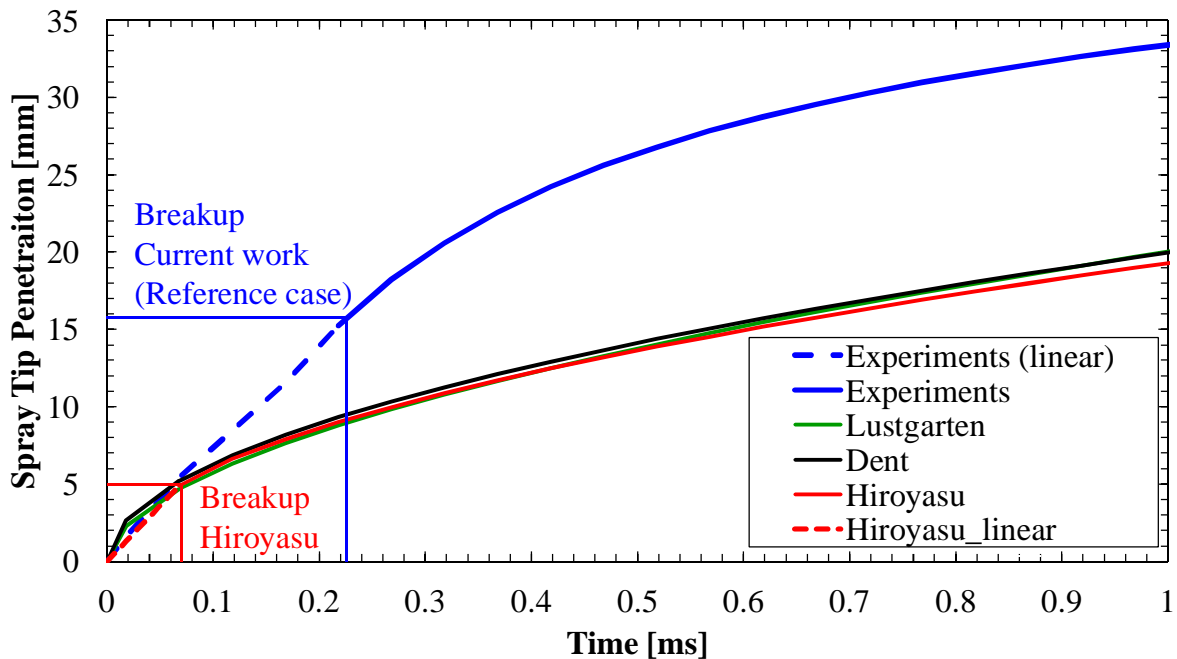


Figure 5-56 – Comparison of several penetration correlations from literature with the spray tip penetration of the Reference case



the velocity of the spray tip drops by more than 10% under the constant velocity from the linear phase. However these correlations have all been proposed for single or multihole Diesel injectors with nozzle-hole diameters around 100  $\mu\text{m}$ ; with injection pressures over 100 MPa and back pressures between 5 and 10 MPa. [41] gives a very good overview about the different models and their sensitivity on the different parameters. As can easily be seen in Figure 5-56, they overpredict the spray tip velocity during linear propagation and they heavily underpredict breakup and spray penetration. As far as the author knows, no correlation exists, therefore it was decided to define such a correlation for hollow cone injectors under Otto engine like conditions.

### 5.6.1 New correlation for spray penetration

To predict the break up length and the injection velocity for hollow cone injectors a new correlation was found. It was also found that the spray tip penetration was divided into two regimes: The part before breakup has a linear spray propagation behaviour. After the breakup different processes are involved in the braking of the droplets with regards to tip penetration. Therefore two correlations for two regimes were defined, as is common practice also for multi-hole injector sprays: Hiroyasu and Arai [55] define the spray tip velocity in the linear regime as

$$u_{Tip} = 0.39 \cdot \left( \frac{2 \cdot \Delta p}{\rho_{air}} \right)^{0.5} \quad (33)$$

For a hollow cone injector the correlation for linear spray tip velocity has been defined as

$$u_{Tip} = 0.75 \cdot \left( 1 + \frac{1}{CN} \right)^{1.1} \cdot \left( \frac{\Delta p}{\rho_{liquid}} \right)^{0.5} \cdot \left( \frac{\rho_{air0}}{\rho_{gas}} \right)^{0.25} \quad (34)$$

Where  $u_{Tip}$  is the spray tip velocity,  $CN$  is the cavitation number,  $\Delta p$  is the pressure drop over the nozzle (or the injection pressure  $p_{Rail} - p_{gas}$ ),  $\rho_{liquid}$  is the density of the injected fuel,  $\rho_{gas}$  is the density of the surrounding gas and  $\rho_{air0}$  is the standard density of air (1,293 kg/m<sup>3</sup>). The only difference to Hiroyasu and Arai's correlation for Diesel sprays is that the influence of the surrounding gas

(i.e. gas density) on the velocity is taken into account, as suggested by Schneider [41], already. A plot of the predicted vs. the measured spray tip velocity shows the performance of the new correlation, which has been calibrated with the present data. To give a comparison the linear velocities estimated with Hiroyasu have been plotted as well (Figure 5-57).

Unlike an injector with a cylindrical nozzle hole, a hollow cone injector has a “geometrical breakup length”. This means that due to its geometry the liquid sheet becomes broken up: Under idealized conditions (laminar flow, perfectly

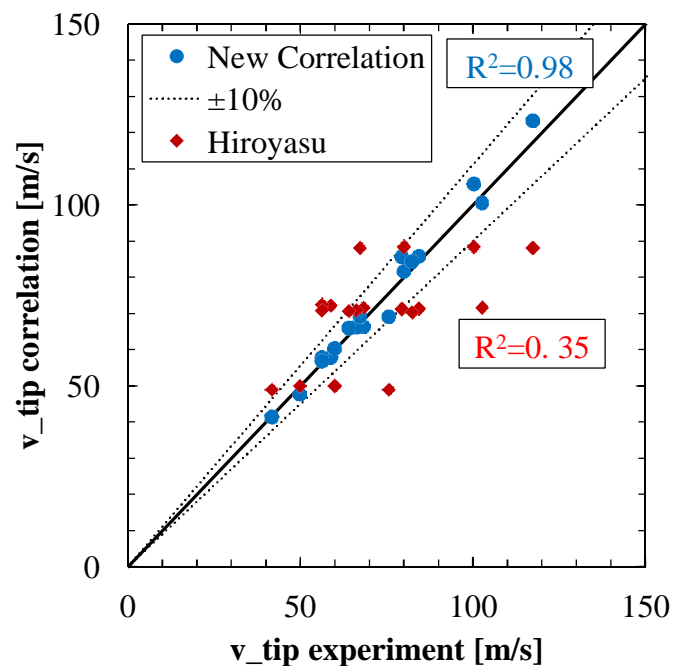
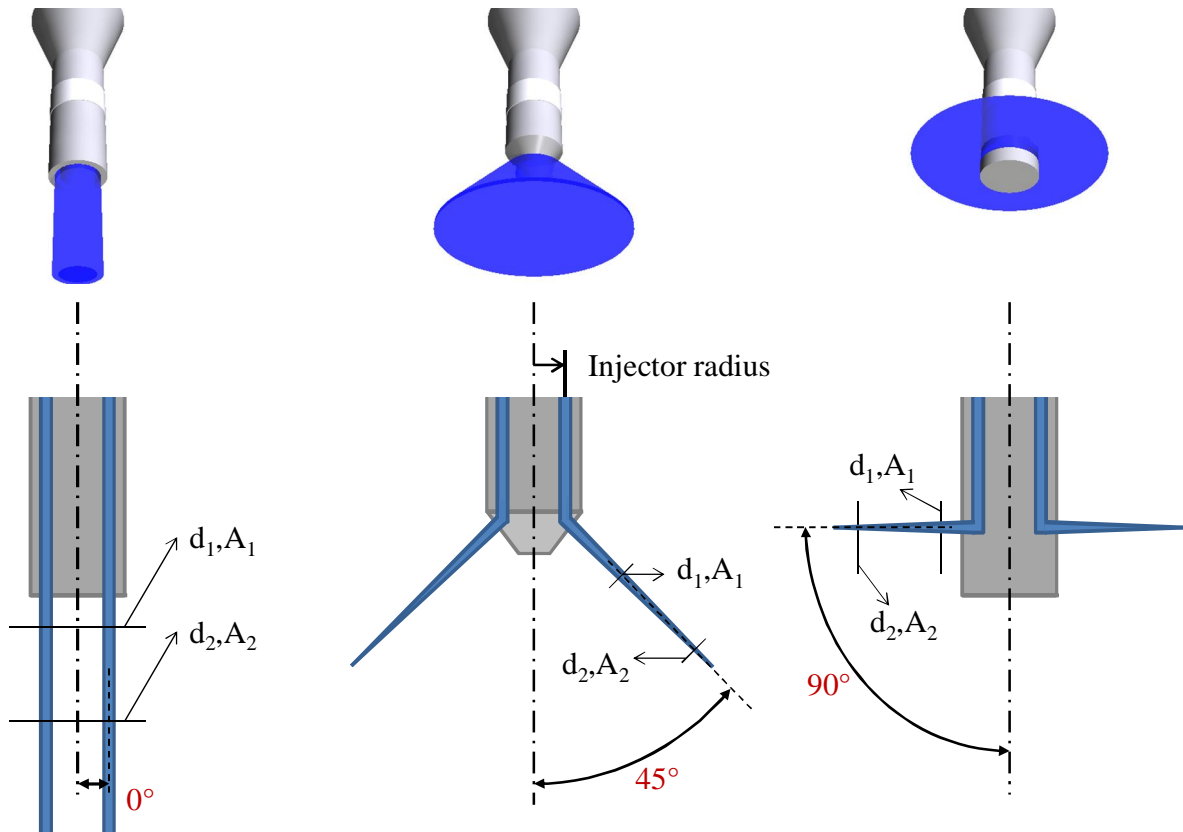


Figure 5-57 – Comparison between calculated and measured velocities

smooth surface and without influence from the gas phase) a liquid jet from a cylindrical nozzle (compare Figure 5-58, left image) would have an infinite penetration length. The surface tension would keep its cylindrical shape and due to the lack of irregularities (idealized conditions) it would not start to decay. A liquid sheet from a circumferential slit on the other hand (Figure 5-58, right image) becomes thinner while penetrating into the disk shaped volume. As its flow area grows in tangential direction its height/thickness has to reduce (or its velocity has to grow smaller) due to conservation of mass. At some point the liquid sheet is too thin and the surface tension tears it apart. In this work this point is defined as the geometric breakup length. It is, among others, depending on the radius of the injector and the angle of the needle seat. As can be seen in



**Figure 5-58 – Sketch of extreme nozzle angles (0° and 90°) for the A-injector and their influence on the *geometric breakup* compared to the 45° case**

Figure 5-58, the angle has a big influence on the geometric breakup. An injector with seat angle of 90° experiences the full influence of the geometric breakup whereas in case of a 0° (theoretical case) no influence can be seen. Furthermore the diameter of the injector has an influence on the geometric breakup. With an infinite radius, the liquid sheet does not grow in tangential direction and the geometric breakup length becomes infinite too. The smaller the radius of the injector is, the stronger is the tangential growth and the shorter becomes the geometric breakup. Geometrically the spray would grow infinitely small and therefore infinitely long. But even in an idealised environment without turbulence and no interaction with the surrounding gas, the spray would breakup when it reaches a certain thickness. This thickness is given by the fluid properties. For the presented correlation the geometric breakup length was empirically found and defined as:

$$S_{B_{Geometric}} = \frac{r_{Injector}}{\sin(\alpha)} \cdot \left( \frac{d_h}{l_{sheet}} \right)^{0.3} \quad (35)$$

The geometric breakup length grows infinite if the injectors radius ( $r_{Injector}$ ) becomes infinite or if the seat angle ( $\alpha$ ) is zero. It is further dependent on the initial thickness which is governed by the needle lift and therefore by the hydraulic diameter ( $d_h$ ). In case of a hollow cone injector the hydraulic diameter is twice the gap size. The geometric thickness ( $l_{sheet}$ ) where the sheet is broken up is depending on fuel properties (this thickness would have to be found empirically by means of low pressure injections in combination with a fuel variation). For the present work the relation between the initial and the final thickness before breakup was found to be to the 0.3<sup>rd</sup> power. As for injectors with cylindrical nozzles the breakup length was then found to depend on the density of the injected fuel and the surrounding gas. Additionally the geometric breakup has a linear influence on breakup length (instead of the nozzle-hole diameter):

$$s_{Breakup} = 0.37 \cdot s_{B_{Geometric}} \cdot \left( \frac{\rho_{liquid}}{\rho_{gas}} \right)^{0.5} \quad (36)$$

Figure 5-59 shows the performance of the breakup length predictions made with the new correlation. As can be seen, Hiroyasu’s correlation under predicts the breakup length by far. This is mostly due to the linear dependency of the

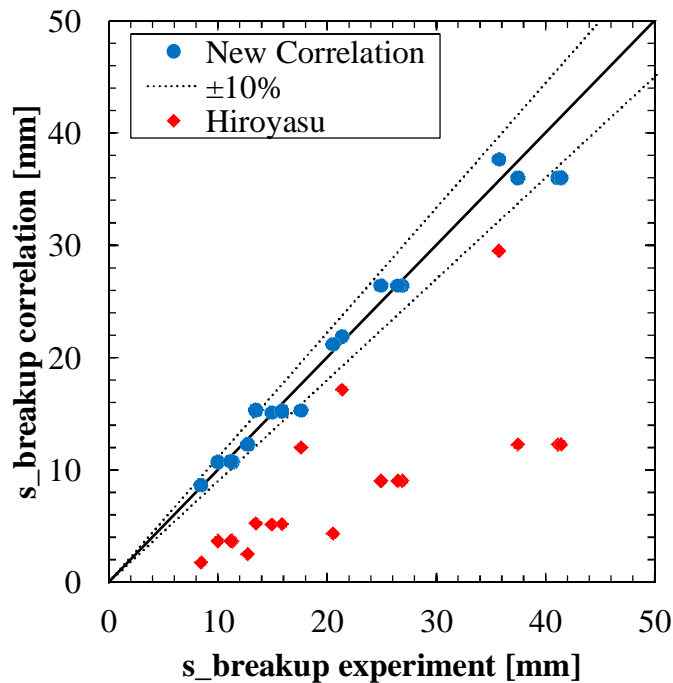


Figure 5-59 – Predicted spray breakup length, over measured breakup length

breakup length on the nozzle-hole diameter which has not been observed in the measurements taken.

For the sake of completeness the breakup time is calculated with the help of the linear velocity and the breakup length:

$$t_{Breakup} = \frac{s_{Breakup}}{u_{Tip}} = 0.5 \cdot \frac{s_{B_{Geometric}}}{\left(1 + \frac{1}{CN}\right)^{1.1}} \cdot \left( \frac{1}{\sqrt{\frac{\Delta p_{inj}}{\rho_{liquid}}}} \right) \cdot \left( \frac{\rho_{liquid}^2}{\rho_0 \cdot \rho_{gas}} \right)^{0.25} \quad (37)$$

For the time after the breakup no analytical solution for a correlation could be found. But as a numerical integration approach the following approach can be used:

Assuming that after the breakup only droplets are left over, a new time was defined. This starts after the breakup at zero again ( $t_{sqrt} = t - t_{Breakup}$ ) and is valid for the square root shaped propagation. A spherical droplet with the initial velocity from the linear part can be looked at. The forces acting on the model droplet are the aerodynamic and inertia forces, only (this means no surface tension etc.). Therefore the momentum equation to the problem is:

$$\dot{s}_{(t+\Delta t)} = \dot{s}_{(t)} - \ddot{s}_{(t)} \cdot \Delta t \quad (38)$$

with

$$F = \frac{1}{2} \cdot c_w \cdot A \cdot \rho_{gas} \cdot \dot{s}_{(t)}^2 = \frac{1}{2} \cdot c_w \cdot \pi \cdot r^2 \cdot \rho_{gas} \cdot \dot{s}_{(t)}^2 \quad (39)$$

With (39) in (38) and the mass calculated with droplet diameter and fluid density:

$$\dot{s}_{(t+\Delta t)} = \dot{s}_{(t)} - \frac{\frac{1}{2} \cdot c_w \cdot \pi \cdot r^2 \cdot \rho_{gas} \cdot \dot{s}_{(t)}^2}{\frac{4}{3} \cdot \pi \cdot r^3 \cdot \rho_{liquid}} \cdot \Delta t = \dot{s}_{(t)} - \frac{3}{8} \cdot \frac{c_w}{r} \cdot \frac{\rho_{gas}}{\rho_{liquid}} \cdot \dot{s}_{(t)}^2 \cdot \Delta t \quad (40)$$

The droplet diameter for a droplet exiting the linear part is not constant. Due to further breakup the droplet diameter is going to be reduced, whereas the number of droplets will increase. As the drag force on the droplet is strongly depending on the relative velocity and the droplet diameter, the change in velocity is a function of the initial velocity and the droplet diameter. The droplet diameter is

a function of the initial droplet size and the relative velocity. The droplet radius can therefore be defined as:

$$r = r_{(t)} = \frac{d^*}{\left(t_{sqr} / t_0\right)^\tau} \quad (41)$$

Where  $d^*$  is the initial droplet diameter at the nozzle,  $t_0$  is a characteristic time (1 ms) and  $\tau$  is the exponential decay number (range 0.92 – 1.6). The initial droplet diameter  $d^*$  and the time constant  $\tau$  were assumed to depend on injection pressure, density of the surrounding gas and needle lift. They have empirically been defined as (also compare Figure 7-9, Figure 7-10 and Figure 7-11 in the appendix, The 33  $\mu\text{m}$  are the design needle lift.):

$$d^* = 33\mu\text{m} \cdot \left(\frac{\rho_{gas}}{\rho_0}\right)^{0.378} \cdot \left(\frac{p_0}{p_{inj}}\right)^{0.6} \cdot \left(\frac{16000 \cdot d_h \cdot C_d}{5\mu\text{m}^{-5}}\right)^{0.25} \quad (42)$$

$$\tau = 4.7 \cdot \left(\frac{\rho_{gas}}{\rho_{fuel}}\right)^{0.223} \cdot \ln\left(\frac{d_h \cdot C_d}{3\mu\text{m}}\right) \quad (43)$$

When the droplets decay, two effects can be seen; due to the bigger surface to volume ratio the droplets face a stronger force reducing their velocity. In the mean time the droplets travelling in the drag of the first droplet overtake them. For a macroscopic observer these two effects can't be identified individually.

Their sum appears as the tip penetration velocity. As the spray tip is formed by

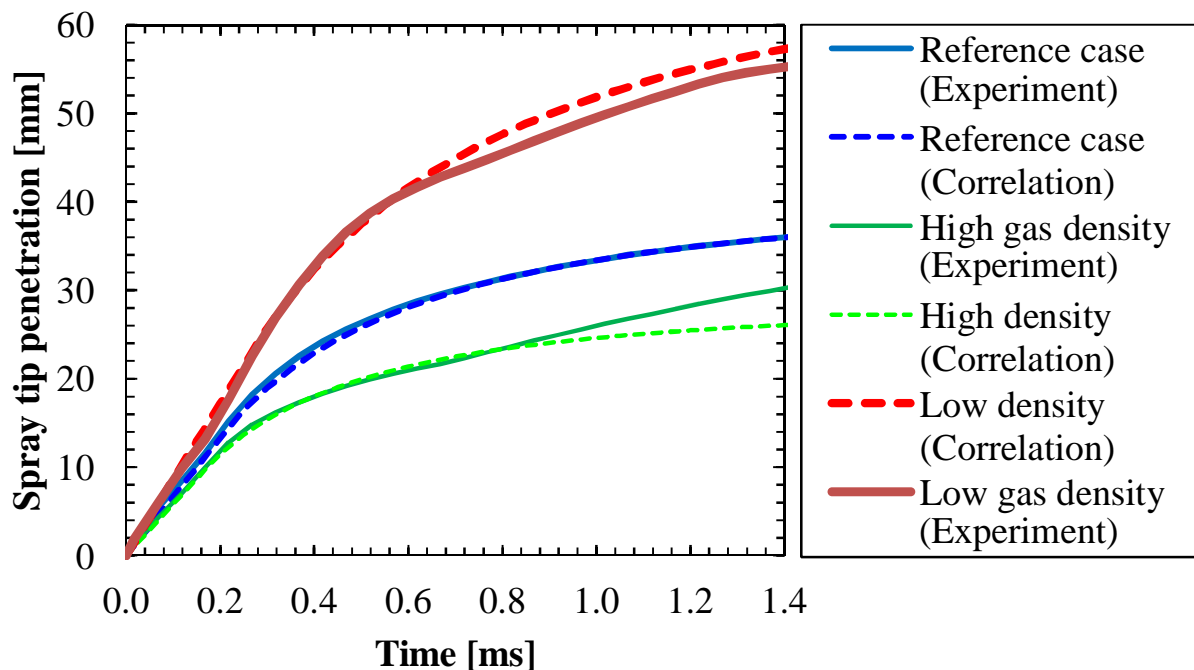
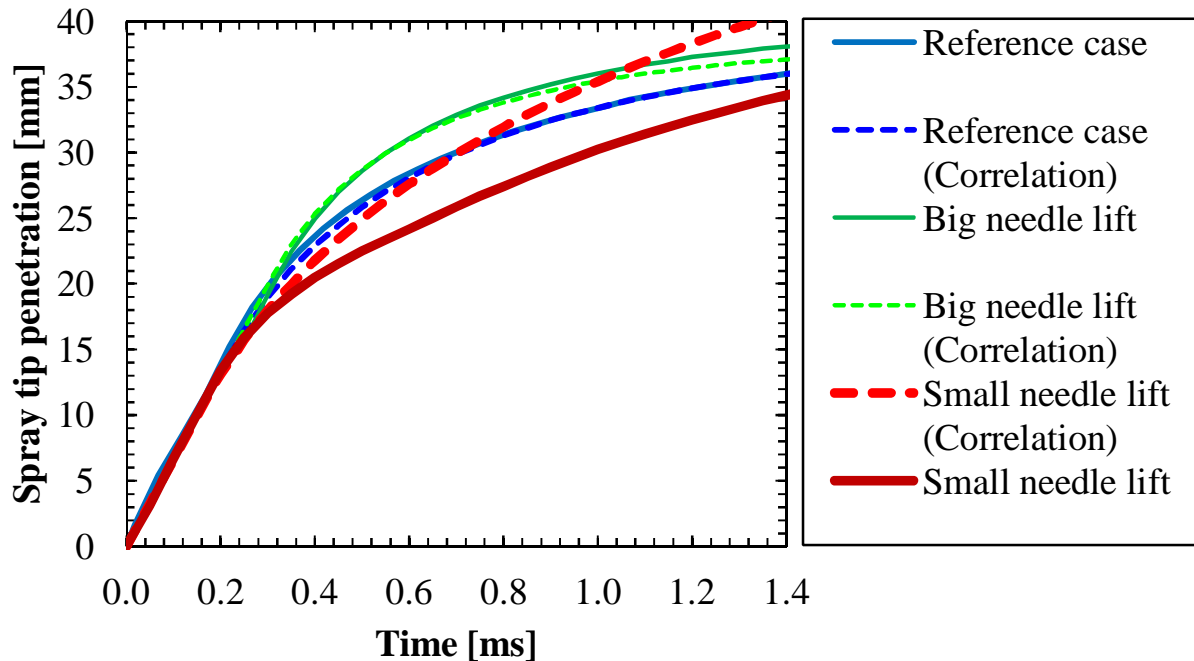


Figure 5-60 – Comparison of the new correlation with experiments at different gas densities (2.2, 6.6 and 13.2  $\text{kg/m}^3$ )

groups, the droplets on the inside are protected from the strong aerodynamic forces on the outer. The droplets facing the propagation direction are exposed to the still standing gas and are therefore slowed down and broken up by the aerodynamic forces. They are torn away from the group revealing the droplets behind. To take into account this effect a correction factor  $K$  has been introduced. It could empirically be defined as linearly depending on time constant  $\tau$ .



**Figure 5-61 – Comparison of the new correlation with experiments for a needle lift variation (11, 23, 75  $\mu\text{m}$ )**

Figure 5-60 gives an overview of the new correlations performance for different gas densities. The reference case is nicely predicted. Also the trend for the low density case is well reproduced, whereas in case of high gas density the curve of the correlation seems to drift away from the experimental findings. This is due to the acceleration induced by the vortices. The interaction between the gas phase and the vortices is not taken into account by the correlation. Figure 5-61 shows the performance of the new correlation with regards to needle lift. As can be seen, the increased needle lift is well reproduced by the correlation whereas the spray tip penetration in case of reduced needle lift is underestimated. The reason for this might be found in a too big assumption of the initial drop size. Figure 5-62 gives an overview on the performance when injection pressure is varied. As can be seen the correlation predicts the spray tip penetration well.

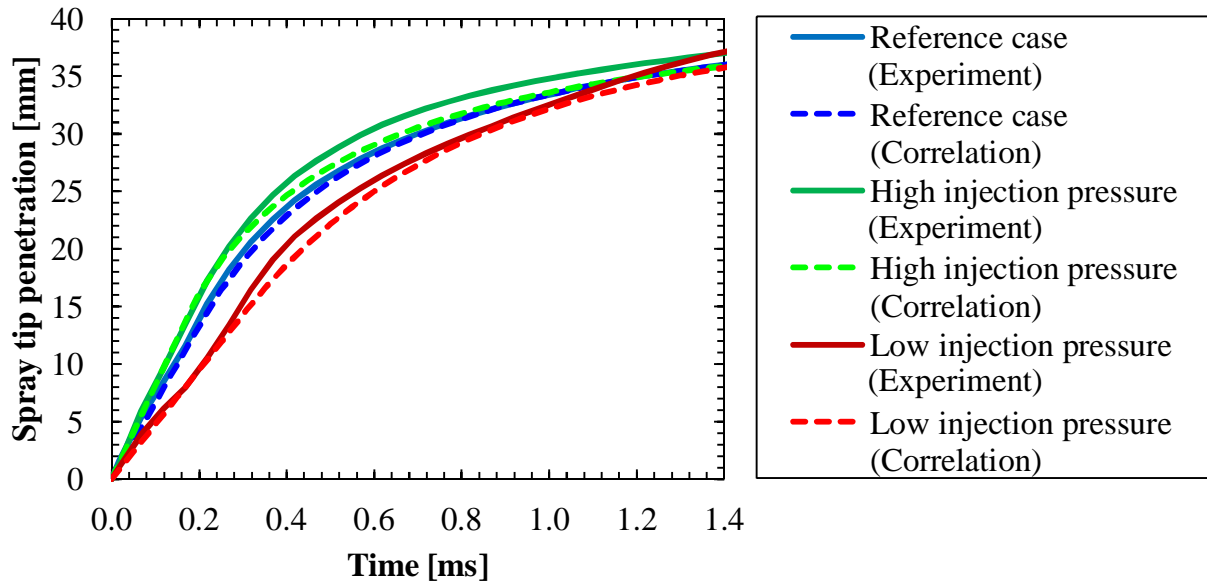


Figure 5-62 – Comparison of the new correlation with experiments for an injection pressure variation (6, 12, 18 MPa)



## 6 Conclusions and Outlook

*Es ist nicht deine Schuld, dass die Welt ist, wie sie ist. Es wär nur deine Schuld, wenn sie so bleibt.*

*-Die Ärzte*

The results shown in the previous chapter deal with investigations on the spatial evolution of sprays with short duration produced by a piezo driven, outward opening, hollow cone direct injector under engine like conditions. The experiments have been carried out in the high pressure high temperature cell (HTDZ) of ETH Zürich and at the atmospheric spray rig of University Loughborough in the UK.

The HTDZ allowed a wide and independent variation of gas pressure and gas temperature and good optical access for the observation of the spray. This was done with two optical measurement techniques: With Mie scattering the inside of the hollow cone has been visualised by the illumination of the liquid phase and with the Shadowgraphy method the liquid and the vapour phase have been visualized both to see the relation between these. The following parameters have been varied to investigate their influence on spray morphology: Gas density, gas temperature, injection pressure, needle lift, injection duration and fuel properties. All in all over 60 parameters and parameter combinations have been investigated. For each operating condition 10 experiments have been carried out. At the atmospheric spray rig in Loughborough Phase Doppler Anemometry (PDA) has been applied to measure droplet size and velocity. The influence of the following parameters has thereby been investigated; needle lift, injection pressure and fuel properties. The spray was measured at 7 axial distances. At each distance more than 14 measurement locations have been placed and for each location 250 injection events have been recorded.

The presented results help to understand the mechanisms of spray breakup, the formation and evolution of circumferential vortices (which are characteristic for the A-injector) and the evaporation processes of a so called A-injector. In addition they build a solid data base for development, validation and tuning of spray models and numerical simulations.

In *general* the *spray shape* of an A-injector is very reproducible. Its characteristic string structure shows an interesting behaviour: In the first phase of the injection the liquid streaks bend individually in radial and in circumferential direction. This behaviour diminishes after the first hundreds of microseconds after start of injection and the strings become steady. The fact that the strings may occur due to air pockets and cavitation in the nozzle (cf. [36],[39]) allows the building of the hypothesis that these pockets must wander or change their size in such a way that they push the strings and make them bend. Together with the surrounding gas, the A-injector forms circumferential vortices around its hollow cone shaped spray sheet. These vortices grow with increased injection duration and can become strong enough to influence the spray in such a way that the liquid phase is bent towards the inside of the cone until the spray is directed in axial direction. The spray tip penetration with time shows the linear and the square root shaped behaviour as it has been observed for injectors with cylindrical nozzles. With the help of PDA measurements it could be shown that the droplet velocity on the spray axis decreases exponentially downstream. An extrapolation of the velocity profile towards the nozzle reveals that the exit velocity lies close to the prediction made with Bernoulli's law for incompressible nozzle flow. The PDA measurements showed further that the droplets produced by the A-injector are very small; at an injection pressure of 12 MPa the Sauter Mean Diameter of a gasoline spray is smaller than 10  $\mu\text{m}$  when injected in quiescent, atmospheric air. Close to the big vortices the droplets are very small, whereas close to the spray tip larger droplets can be found.

The spray shape of an A-injector is heavily influenced by the surrounding *gas density*. As shown earlier by [80], [81] or [82], the gas pressure at constant temperature has significant influence on the spray phase. But unlike a pressure swirl injector [118], the A-injector does not collapse towards higher gas pressure. The penetration in axial and nominal direction of the spray is reduced

and the spray shape becomes bushy. Injection velocity is influenced as well by the gas density, as already shown for Diesel injectors by [41]. The circumferential vortices become more compact and have higher density as the same amount of fuel (droplets) is contained in a smaller volume. The vortices have bigger influence on the spray with higher gas density.

Increased *injection pressure* has a negligible influence on the spray shape. But spray tip velocity becomes higher and this has two effects: On one hand the droplets become smaller due to the higher relative velocity between the liquid phase and the surrounding gas what leads to faster evaporation. On the other hand the kinetic energy transferred to the gas phase is increased which lets the circumferential vortices grow and gain more influence on the hollow cone.

For the first time the influence of *needle lift* on spray morphology, spray tip penetration, droplet diameter and evaporation could be shown. Towards smaller needle lift the mass flow is reduced and the spray becomes less dense. The individual streaks protrude stronger what prevents them from mutual interaction. Therefore the single streaks exhibit individual atomisation processes; this means that each string has its own breakup length. With bigger needle lift the spray is denser and has a higher momentum. Individual streaks are less present; instead they merge and a spray sheet is visible. This is due to the proximity of the streaks which therefore prevent one another projecting from the fuel cloud. Towards smaller needle lift, the spray becomes very sensitive to needle motion what leads to an asymmetric spray shape. Evaporation becomes slower towards higher needle lift. This is due to the higher local demand in heat to evaporate the droplets. An influence of the needle lift on the droplet size could not clearly be identified. The reason for this lies in the difficulty to fairly compare the different cases as the distance in function of the needle lift ( $s/d_h$ ) is not the same whereas the distance of the measurement was constant for all three cases. The influence of the *fuel properties* on spray morphology has been investigated with the comparison of gasoline and isooctane. It showed that the spray shape is heavily influenced by the fuel properties. The spray becomes wider and less symmetrical. The position of the vortices shows strong dependencies on fuel properties. The difference in droplet diameters is small between gasoline and isooctane. Evaporation on the other hand is influenced by the fuel properties in such a way that gasoline takes longer to evaporate. The reason for this are the

bigger hydro carbons in the gasoline which need higher temperature to evaporate.

A comparison with literature showed that the existing correlations for spray penetration from multihole injectors do not meet the requirements of non swirling hollow cone injectors. Therefore a new correlation was introduced in this work. The correlation shows very good agreement with the experimental data for the linear and the square root phase of the propagation.

The main goals defined in Chapter 2.2.6 have been achieved.

- The general spray of the injector has been elaborately described giving new information on the spray of an A-injector and on the streaks behaviour and the circumferential (toroidal) vortices in particular
- The main injection parameters have been successfully isolated and their influence on spray morphology, spray penetration and evaporation could be shown in detail
- A correlation could be found to accurately predict spray tip penetration lengths of an A-injector under the influence of the different parameters

The conducted investigations showed that the large circumferential vortices around the hollow cone have a strong influence on spray morphology and spray penetration. For new measurements it would be interesting to quantify these findings by means of rotational energy of the vortices and influence on the spray jet. Investigations with Particle Image Velocimetry (PIV) could help to identify and understand the relation between the liquid phase and the vortices.

Another interesting effect is the unsteadiness of the strings during the first phase of the injection. With the help of low injection pressure ( $< 0.7$  MPa) the influence of needle lift on the string structure could be investigated and by a continuous increase of the injection pressure the transition between the two situations shown in Figure 2-12 could help to understand the influences on the nozzle. Large Eddy Simulations might additionally help to characterise the pockets which form the strings in order to better understand the streaks behaviour.

Ballistic Imaging (an optical method to investigate the area close to the nozzle [54]) can resolve the dense core close to the orifice and probably show the

streaks and their primary breakup. This would deliver helpful information to understand the forming and development of a streak. Especially the length of the liquid core could help to understand the additional forces destructing the liquid sheet (as discussed with Figure 5-58).

The influence of needle lift on droplet diameter could not clearly be identified. A PDA measurement series in combination with a grid of measurement locations which is depending on the needle lift could help to understand the relationship between needle lift and droplet size.

For quantitative information on the local  $\lambda$  as well as information on the distribution of the liquid and the vapour phase, PLIF measurements should be conducted.

Based on these new information a more detailed description of the spray of a piezo activated, outwards opening hollow cone injector could be achieved. It would also allow the description of different aspects of the spray (e.g. liquid/vapour volume, surface area, cone angles, evaporated mass etc.) with additional correlations.

# Nomenclature

## *Abbreviations*

<i>2D</i>	Two Dimensional
<i>ACEA</i>	European Automobile Manufacturers' Association
<i>AR</i>	Anti Reflective
<i>Ar<sup>+</sup></i>	Argon Ion (-laser)
<i>BOS</i>	Background Oriented Schlieren
<i>CAI</i>	Controlled Auto Ignition
<i>CMOS</i>	Complementary Metal Oxide Semiconductor
<i>CN</i>	Cavitation Number
<i>DI</i>	Direct Injection
<i>DICU</i>	Direct Injection Control Unit
<i>DISI</i>	Direct Injection Spark Ignition
<i>EOI</i>	End Of Injection
<i>ETH</i>	Eidgenössische Technische Hochschule
<i>GDI</i>	Gasoline Direct injection
<i>geTDC</i>	Gas exchange Top Dead Centre
<i>HCCI</i>	Homogenous Charge Compression Ignition
<i>HSS6</i>	High Speed Star 6 (LaVision)
<i>HTDZ</i>	Hochtemperatur-Hochdruckzelle (High pressure high temperature cell)
<i>IC</i>	Internal Combustion
<i>ISB</i>	Inner Seal Band
<i>LDA</i>	Laser Doppler Anemometry
<i>LDI</i>	Laser Doppler Interferometry
<i>LFT</i>	Laser Flow Tagging
<i>PDA</i>	Phase Doppler Anemometry

---

<i>PDI</i>	Phase Doppler Interferometry
<i>PIV</i>	Particle Image Velocimetry
<i>PLIF</i>	Planar Laser Induced Fluorescence
<i>PM</i>	Particular Matter
<i>SI</i>	Spark Ignited
<i>SMD</i>	Sauter Mean Diameter ( $D_{32}$ )
<i>STD</i>	Standard Deviation
<i>SOI</i>	Star Of Injection
<i>TDC</i>	Top Dead Centre
<i>UHC</i>	Unburned Hydro Carbon
<i>UK</i>	United Kingdom

## ***Symbols***

$A$	Surface	[m <sup>2</sup> , mm <sup>2</sup> ]
$C_a$	Area contraction coefficient	[-]
$C_d$	Discharge coefficient	[-]
$C_v$	Velocity coefficient	[-]
$d$	Droplet diameter	[μm]
$d_n$	Nozzle diameter	[μm]
$d_0, d^*$	Initial droplet diameter	[μm]
$d_f$	Fringe spacing	[μm]
$d_l$	Diameter of the laser beams before the front lens	[mm]
$d'_l$	Beam waist diameter	[mm]
$d_p$	Particle diameter	[μm]
$d'_z$	Length of measurement volume	[μm]
$D_{1(2,3)}$	Detector 1 (2, 3)	[-]
$f$	Frequency	[Hz]
$f$	Focal length of lenses	[mm]
$F$	Force	[N]
$m$	Mass	[kg]
$n$	Refractive index	[-]
$Oh$	Ohnesorge number	[-]

## Nomenclature

---

$p_b$	Back pressure (pressure outside the nozzle)	[MPa]
$p_{HTDZ}$	Gas pressure in the HTDZ	[MPa]
$p_{inj}$	Injection pressure (pressure drop over the nozzle)	[MPa]
$p_{rail}$	Rail pressure	[MPa]
$r$	Radius	[m, mm]
$Re$	Reynolds number	[-]
$s$	penetration length	[mm]
$s_{B(geometric)}$	Geometric spray Breakup	[mm]
$s_{Breakup}$	Spray breakup length	[mm]
$s_{punkt}$	penetration velocity	[m/s, mm/ms]
$t$	Time	[ms, $\mu$ s]
$T$	Temperature	[K, °C]
$t_{Breakup}$	Breakup time	[ $\mu$ s]
$u_0$	initial relative velocity	[mm/ms]
$u_{nozzle}$	Velocity of the fuel in the nozzle	[mm/ms]
$u_{Tip}$	Nominal penetration velocity of spray tip	[mm/ms]
$v$	Velocity component	[m/s]
$We$	Weber number	[-]



***Greek symbols***

$\lambda$	Air to fuel ratio	[-]
$\theta$	Angle between the laser beams before the measurement volume	[°]
$\psi$	Angle between the photomultipliers	[°]
$\alpha$	Angle of the flanks at the nozzle	[°]
$\chi$	Cavitation number	[-]
$\varepsilon$	Deflection of a light beam	[ $\mu\text{m}$ ]
$\rho$	Density	[ $\text{kg}/\text{m}^3$ ]
$\eta$	Dynamic viscosity	[ $\text{mPas}$ ]
$\nu$	Kinematic viscosity	[ $\text{mm}^2/\text{s}$ ]
$\varepsilon$	Needle lift	[ $\mu\text{m}$ ]
$\Phi$	Phase shift between two detectors (PDA)	[°]
$\varphi$	Scattering angle in the X-Y-plane (70° in the present work)	[°]
$\sigma$	Surface tension	[ $\text{kg}/\text{s}^2$ ]
$\tau$	Droplet decay exponent	[-]

## References

- [1] EPA and U. S. E. P. Agency (2011). "Summary of the Clean Air Act"  
<http://www.epa.gov/lawsregs/laws/caa.html>
- [2] European Conference of Ministers of Transport, E. (2007). "Cutting Transport CO2 Emissions"
- [3] Noembrini, F. (2009). "Modeling and Analysis of the Swiss Energy System Dynamics with Emphasis on the Interconnection between Transportation and Energy Conversion". P.h.D. thesis. Department of Mechanical and Process Engineering. Zürich, ETH Zürich.
- [4] [http://unfccc.int/kyoto\\_protocol/items/2830.php](http://unfccc.int/kyoto_protocol/items/2830.php)
- [5] Thring, R. H. (1989). "Homogeneous Charge Compression Ignition (HCCI) engines" SAE TECHNICAL PAPER SERIES.
- [6] Duret, P. and J. Lavy (2000). "Gasoline controlled auto-ignition (CAI<sup>TM</sup>)~Potential and prospects for the future automotive application". SAE TECHNICAL PAPER SERIES
- [7] Hübner, W., Gerke U., Boulouchos, K., Peters, N., Schulz, C. and Spicher, U. (2009). "Influence of pre-injection on controlled auto-ignition combustion – a theoretical and experimental study". THE SPARK IGNITION ENGINE OF THE FUTURE. Strasbourg, Universität Karlsruhe.
- [8] VanDerWege, B., Han, Z., Iyer, C., Muñoz, R. et al. (2003). "Development and Analysis of a Spray-Guided DISI Combustion System Concept." SAE TECHNICAL PAPER SERIES.
- [9] Schaupp, U., F. Altenschmidt, F., Bertsch, D., Laudenschach, N., Voigtländer, D., (2005). "Das strahlgeführte Mercedes-Benz-Brennverfahren: Robustheitsanforderung unter Serienaspekten." Direkteinspritzung im Ottomotor 5: 27.

- 
- [10] Sauter, W., J. Pfeil, et al. (2006). "Application of Particle Image Velocimetry for Investigation of Spray Characteristics of an Outward Opening Nozzle for Gasoline Direct Injection." SAE TECHNICAL PAPER SERIES 2006-01-3377: 13.
- [11] Skogsberg, M., P. Dahlander, et al. (2007). "Spray Shape and Atomization Quality of an Outward-Opening Piezo Gasoline DI Injector." SAE TECHNICAL PAPER SERIES 2007-01-1409.
- [12] Hermann, A., C. Krüger, et al. (2008). Numerical and Diagnostic Analysis of Spray Propagation and Vortex Formation of Piezo-A-injectors and their Sensitivity to the Internal Nozzle Flow. 8th International Symposium on Internal Combustion Diagnostics. Baden Baden: 23.
- [13] Meinig, U. (2008). „Geschichte der Benzin-Direkteinspritzung“. Ottomotor mit Direkteinspritzung, van Basshuysen, R.: 3 - 27.
- [14] Otto, N. A. (1877). Germany. 46: 5,  
<http://v3.espacenet.com/publicationDetails/originalDocument>
- [15] Düll, R. (1935). "Übersicht über den heutigen Stand niedrig verdichtender Einspritzmotoren mit Fremdzündung." ATZ 38.
- [16] Scherenberg, H. (1955). "Rückblick über 25 Jahre Benzineinspritzung in Deutschland." MTZ 16(9): 9.
- [17] Hütten (1994). „Schnelle Motoren seiert und frisiert“, Motorbuchverlag.
- [18] Krämer (1998). „Untersuchung zur Gemischbildung, Entflammung und Verbrennung beim Ottomotor mit Direkteinspritzung. Institut für Kolbenmaschinen“. P.h.D. thesis. Karlsruhe, Karlsruhe Institute of Technology.
- [19] Spicher, U., T. Heidenreich, et al. (2008). Gemischbildungs- und Verbrennungsverfahren. Ottomotor mit Direkteinspritzung, van Basshuysen, E. h. R. 2: 29 - 116.
- [20] Dietsche, K-H, Reif, K., Kraftfahrtechnisches Taschenbuch, 2002
- [21] Stan, C. (1999). „Direkteinspritzsysteme für Otto- und Dieselmotoren“. Berlin, Heidelberg, New York, Springer-Verlag (VDI-Buch).
- [22] Ruthenberg, I. (2006). „Laserspektroskopische Analyse eines strahlgeführten Brennverfahrens der Benzindirekteinspritzung“. P.h.D.-Thesis. Institut für Verbrennungsmotoren und Kraftfahrwesen. Stuttgart, Universität Stuttgart.
- [23] Audi AG

- [24] Manz, A. (2005). „Experimentelle Optimierung der Benzinzerstäubung mit Hilfe eines neuartigen Strömungsmodells basierend auf der Weberzahlanalogie“. Aalen, Fachhochschule Aalen.
- [25] Spicher, U. and T. Heidenreich (2008). „Abgasemissionen und Schadstoffreduzierung“. Ottomotor mit Direkteinspritzung. Wiesbaden, Richard van Basshuysen. 2: 213-249.
- [26] Kemmler, R., A. Frommelt, et al. (2002). „Thermodynamischer Vergleich ottomotorischer Brennverfahren unter dem Fokus minimalen Kraftstoffverbrauchs“. 11. Aachener Kolloquium Fahrzeug- und Motorentechnik.
- [27] Lückert, P., E. Rau, et al. (2004). Weiterentwicklung der Benzin-Direkteinspritzung bei Mercedes-Benz. DaimlerChrysler-Sonderdruck zum 13. Aachener Kolloquium Fahrzeug- und Motorentechnik. Aachen.
- [28] Hübner, W., A. Witt, et al. (2003). „Methodeneinsatz bei der Entwicklung eines weiterführenden DI-Brennverfahren“. Direkteinspritzung im Ottomotor IV. Essen, Expert-Verlag.
- [29] Spicher, U., T. Heidenreich, et al. (2004). „Stand der Technik strahlgeführter Verbrennungssysteme“. Essen, Expert-Verlag.
- [30] Ganser, M. (1984). „Akkumuliereinspritzung: theoretische und experimentelle Untersuchung eines elektronisch gesteuerten Dieselemspritzsystems für Personenwagenmotoren“. P.h.D. thesis, Diss. ETH Nr. 7462. Department of Mechanical and Process Engineering. Zürich, ETH Zürich.
- [31] Buri, S., H. Kubach, et al. (2010). "Effects of increased injection pressures of up to 1000 bar – opportunities in stratified operation in a direct-injection spark-ignition engine." International Journal of Engine Research 11(Special Issue): 473 - 484.
- [32] Delphi Injectors  
(<http://delphi.com/manufacturers/auto/powertrain/gas/injsys/homogenous/>)
- [33] Tokuda, H., T. Yoshinaga, et al. (2006). “Flexible Design of Fuel Injection Systems for Gasoline Direct Injection Engines”. Internationales Wiener Motorensymposium. Wien. 27: 364 - 387.
- [34] Schmid, A., Schneider, B., et al. (2010). “Experimental investigation on the spray behaviour for a hollow cone piezo injector with a multiple injection strategy”. ILASS. Brno.

- 
- [35] Varble, D., M. Xu, et al. (1998). "Development of a Unique Outwardly-Opening Direct Injection Gasoline Injector for Stratified-Charge Combustion". 7th Aachen Colloquium Automobile & Engine Technology. Aachen. 7.
- [36] Befrui, B., G. Corbinelli, et al. (2009). "Cavitation and Hydraulic Flip in the Outward-Opening GDi Injector Valve-Group." SAE TECHNICAL PAPER SERIES 2009-01-1483.
- [37] Chryssakis, C. and D. N. Assanis (2008). "A unified fuel spray breakup model for internal combustion engine applications." *Atomization and Sprays* 18: 52.
- [38] Abdelkarim, N. B. H., S. S. Ibrahim, et al. (2007). "Gasoline sprays injected at different back pressures : calculatuions using two atomization models." *Atomization and Sprays* 17: 32.
- [39] Marchi, A., J. M. Nouri, et al. (2007). "Internal Flow and Spray Characteristics of Pintle-Type Outwards Opening Piezo Injectors for Gasoline Direct-Injection Engines." SAE TECHNICAL PAPER SERIES 2007-01-1406.
- [40] Carvalho, I. S., M. V. Heitor, et al. (2002). "Liquid film disintegration regimes and proposed correlations." *International Journal of Multiphase Flow* 28: 16.
- [41] Schneider, B. (2003). „Experimentelle Untersuchung zur Spraystruktur in transienten, verdampfenden und nicht verdampfenden Brennstoffstrahlen unter Hochdruck“. P.h.D. thesis Diss. ETH Nr. 15004. Department of Mechanical and Process Engineering. Zürich, ETH Zürich.
- [42] Gavaises, M. and A. Andriotis (2006). "Vortex cavitation inside multi-hole injectors for large Diesel engines and its effect on the near- nozzle spray structure " SAE TECHNICAL PAPER SERIES (2006-01-1114).
- [43] Nurick, W. H. (1976). "Orifice cavitation and its effect on spray mixing." *Journal of Fluid Engineering* 98.
- [44] Soteriou, C., R. Andrews, et al. (1995). "Direct injection Diesel sprays and the effect of cavitation and hydraulic flip on atomization." SAE TECHNICAL PAPER SERIES (950080).
- [45] Chaves, H., M. Knapp, et al. (1995). "Experimental study of cavitation in the nozzle hole of Diesel injectors using transparent nozzles." SAE TECHNICAL PAPER SERIES (950290).
- [46] Kolokotronis, D., Y. Hardalupas, et al. (2010). "Experimental Investigation of Cavitation in Gasoline Injectors." SAE TECHNICAL PAPER SERIES.

## References

---

- [47] Reitz, R. D. and F. V. Bracco (1982). "Mechanism of Atomization of a liquid jet." *Physics of Fluid* 25(10): 12.
- [48] Brennen CE (2005) *Fundamentals of multiphase flows*. Cambridge University Press
- [49] Shamsborhan, H., Coutier-Delgosha, O., Caignaert, G., Nour, F.A., « Experimental determination of the speed of sound in cavitating flows”, *Exp Fluids* (2010) 49:1359–1373, DOI 10.1007/s00348-010-0880-6
- [50] Ohnesorge V.W., “Anwendung eines kinematographischen Hochfrequenzapparates mit mechanischer Regelung der Belichtung zur Aufnahme der Tropfenbildung und des Zerfalls flüssiger Strahlen“. Dissertation Techn. Hochschule Berlin 1937
- [51] Reitz R.D., „Atomization and other Breakup Regimes of a liquid jet”, Ph.D. Thesis, Princeton University, 1978
- [52] Brown R. and Y. L. (1962). "Sprays formed by Flashing Liquid Jets." *AICHE Journal*.
- [53] Lin, S. P. and R. D. Reitz (1998). "Drop and Spray Formation from a Liquid Jet." *Annu. Re. Fluid Mech* 30: 20.
- [54] Linne, M. (2009). "Ballistic imaging of liquid breakup processes in dense sprays." *Proceedings of the Combustion Institute*.
- [55] Hiroyasu, H. and M. Arai (1980). Fuel spray penetration and spray angle in Diesel Engines. *Trans. of JSME*.
- [56] Charalampous, G., Y. Hardalupas, et al. (2009). "Novel Technique for Measurements of Continuous Liquid Jet Core in an Atomizer." *AIAA* 47(11).
- [57] Chehroudi, B., S. H. Chen, et al. (1985). “On the intact core of full-cone sprays”.
- [58] Lefebvre, A. H. (1989). “Atomization and Sprays”. Hemisphere Publishing Corporation.
- [59] Eifler, W. (1990). „Untersuchung zur Struktur des instationären Dieselöleinspritzstrahles im Düsennahbereich mit der Methode der Hochfrequenz-Kinematografie“. Kaiserslautern, University of Kaiserslautern. Doctor.
- [60] Soteriou, C., R. Andrews, et al. (1999). "Further studies of cavitation and atomization in Diesel injection." *SAE TECHNICAL PAPER SERIES* (199-01-1486).
- [61] Dent, J. C. (1971). "A basic for the comparison of various experimental methods for studying spray penetration." *SAE TECHNICAL PAPER SERIES* (710571).

- 
- [62] Naber, J.D., Siebers, D.L., „Effect of Gas Density and Vaporization on Penetration and Dispersion of Diesel Sprays” SAE TECHNICAL PAPER SERIES (960034, 1996).
- [63] Lustgarten, G. (1973). Modelluntersuchung zur Gemischbildung und Verbrennung im Dieselmotor unter Anwendung der Modelltheorie. Zürich, ETH. Doctor.
- [64] Marchi, A., J. Nouri, et al. (2010). "Spray stability of outwards opening pintle injectors for stratified direct injection spark ignition engine operation." *International Journal of Engine Research* 11(Special Issue): 24.
- [65] Faeth, G. M., L.-P. Hsiang, et al. (1995). "Structure and breakup properties of sprays." *Int. J. Multiphase Flow* 21
- [66] Pilch, M. and C. A. Erdman (1987). "Use of breakup time data and velocity history data to predict the maximum size of stable fragments for acceleration-induced breakup of liquid drop." *Int. J. Multiphase Flow* 13
- [67] Orme, M. (1997). "Experiments on droplet collisions, bounce, coalescence and disruption." *Prog. Energy Combust. Sci* 23
- [68] Abbott, C.E. "A Survey of Waterdrop Interaction Experiments," *Reviews of Geophysics and Space physics*, 15, 3, 363 - 374, 1977
- [69] Bower, G., Chang, S.K., Corradini, M.L., Foster, D.E., Martin, J.K., 1988. "Physical mechanisms for atomization of a jet spray: a comparison of models and experiments", SAE 881318
- [70] Rotondi, R., Bella, G., Grimaldi, C., and Postrioti, L., "Atomization of High-Pressure Diesel Spray: Experimental Validation of a New Breakup Model," SAE Technical Paper 2001-01-1070, 2001, doi:10.4271/2001-01-1070.
- [71] Rayleigh, L. (1900). *Scientific Papers* (Cambridge University) 11.
- [72] Taylor, G. I. (1950). "The Instability of Liquid Surfaces when Accelerated in a Direction Perpendicular to their Planes." *Proceedings of the Royal Society* 201(1065): 4.
- [73] Sharp, D. H. (1984). "An overview of Rayleigh-Taylor instability."
- [74] Hsiang L.P., Faeth G.M., "Drop deformation and Breakup due to shock wave and steady disturbances", *Int. J. Multiphase Flow*, Vol 21, No. 4, pp. 545-560, 1995
- [75] Ranger, A. A. and J. A. Nicholls (1969). "Aerodynamic shattering of liquid droplets." *AIAA*: 5.
- [76] Schmid, A. Wigley, G. (2013) "Experimental investigation of needle lift of a piezo activated hollow cone injector and its influence on spray" *Int. J. of engine research*

- [77] VanDerWege, B. A., Z. Han, et al. (2003). "Development and Analysis of a Spray-Guided DISI Combustion System Concept." SAE TECHNICAL PAPER SERIES.
- [78] Nouri, J. M., M. A. Hamid, et al. (2007). "Spray characterization of a piezo pintle-type injector for gasoline direct injection engines." Journal of Physics: Conference Series 85: 012037-012037.
- [79] Mathieu, F., M. reddemann, et al. (2010). "Experimental Investigation of Fuel Influence on Atomization and Spray Propagation Using an Outwardly Opening GDI-Injector." SAE TECHNICAL PAPER SERIES: 13.
- [80] Wislocki, K., I. Pielecha, et al. (2010). "The Influence of Injection Parameters on the Indexes of Fuel Atomization Quality for a High Pressure Injection." SAE TECHNICAL PAPER SERIES: 12.
- [81] Martin, D., J. Stratmann, et al. (2010). "Experimental Investigation of the Interaction of Multiple GDI Injections Using Laser Diagnostics." SAE TECHNICAL PAPER SERIES.
- [82] Schmid, A., C. Lämmle, et al. (2008). Sprayuntersuchungen in einer Hochtemperatur-Hochdruckzelle. Diesel- und Benzindirekteinspritzung V. Berlin, expert Verlag: 11.
- [83] Baecker, H., A. Kaufmann, et al. (2007). "Experimental and Simulative Investigation on Stratification Potential of Spray-Guided GDI Combustion Systems." SAE TECHNICAL PAPER SERIES 2007-01-1407: 10.
- [84] Martin, D., J. Stratmann, et al. (2010). "Experimental Investigation of the Interaction of Multiple GDI Injections Using Laser Diagnostics." SAE TECHNICAL PAPER SERIES.
- [85] Mitroglou, N., J. M. Nouri, et al. (2008). "Spray structure from double fuel injection in multihole injectors for gasoline direct-injection engines." Atomization and Sprays 19(6): 16.
- [86] Einecke, S., Schulz, C., (1998). "Two-Dimensional Temperature Measurements in an SI Engine Using Two-Line Tracer LIF", SAE 982468
- [87] Schulz, C. Sick, V. (2005), "Tracer-LIF diagnostics: quantitative measurement of fuel concentration, temperature and fuel/air ratio in practical combustion systems", Progress in Energy and Combustion Science, Volume 31, Issue 1, Pages 75–121
- [88] Settles G.S. Schlieren und Schadowgraph techniques, Springer, Berlin 2001



- 
- [89] Ramanah, D., S. Raghunath, et al. (2007). "Background oriented schlieren for flow visualisation in hypersonic impulse facilities." *Shock Waves* 17(1-2): 65-70.
- [90] Kristensson, E., Berrocal, E., et al. (2009). "Ultra-fast Structured Laser Illumination Planar Imaging (SLIPI) for single-shot imaging of dense sprays", ICLASS, Vail, Colorado, USA
- [91] Ibrahim , K., Bachalo, W.D. (1989). "Invention of digital signal detection methods for reliable detection and processing of Doppler signals".
- [92] Hiller, B., Booman, R. A., Hassa, C., Hanson, R. K., "Velocity visualisation in gas flows using laser-induced phosphorescence of biacetyl". *Review of Scientific Instruments*, 55 (1984), Dezember, Nr. 12, S. 1964–1967
- [93] Orlemann, C., Schulz, C., Wolfrum, J., "NO flow-tagging by photodissociation of NO<sub>2</sub> - a new approach for measuring small-scale flow structures"
- [94] Durst, F. and M. Zaré (1975). *Laser-Doppler Measurements in Two-Phase Flows. LDA-Symposium, Copenhagen, Denmark.*
- [95] Hirleman, E. D. (1996). "History of Development of the Phase-Doppler Particle Sizing Velocimeter." *Particle and Particle Systems Characterization* 13(2): 18.
- [96] Pitcher, G. and G. Wigley (1989). "Laser and Phase Doppler Anemometry Measurement Techniques in Fuel Sprays. International Conference on Laser Anemometry - Advances and Applications". Wales, University College Swansea.
- [97] Pitcher, G. and G. Wigley (1992). "Application of Phase Doppler Anemometry to Combusting Diesel Fuel Sprays - Measurement Technique, Precision Data and Interpretation". 6th Workshop on Two-Phase Flow Predictions, Erlangen.
- [98] Tropea, C. (1999). "The Development of the Phaser Doppler Technique". *Applied optical measurements: 279-292.*
- [99] Ochs, M., Gass, J., Reh, L. (1996) "Phase Doppler Reflection Configurations for Size Measurements of Evaporating Feul Droplets", 1<sup>st</sup> European Conf. On Small Burner Techn. And Heating Equipment.
- [100] Herrmann, K., Schneider, B., Obrecht, P. (2011). "Diagnostics in Combustion Research", Lecturing script
- [101] Sankar, S. V. and Bachalo W. D. (1995). "Performance Analysis of Various Phase Doppler Systems". 4th Int. Congress on Optical Particle Sizing. Nürnberg.
- [102] Wigley, G., G. K. Hargrave, et al. (1998). "A high Power, High Resolution LDA/PDA System Applied to Dense Gasoline Direct Injection Sprays". 9th Int.

- Symposium on Applications of Laser Techniques to Fluid Mechanics. Lisbon, Portugal.
- [103] Araneo, L., N. Damaschke, et al. (2000). "Measurement and Prediction of the Gaussian Beam Effect in the Phase Doppler Technique". 10th Int. Symp. on Applications of Laser Techniques to Fluid Mechanics. Lisbon.
- [104] Hardalupas, Y. and H. C. Liu (1997). "Implications of the Gaussian Intensity Distribution of Laser Beams on the Performance of the Phase Doppler Technique Sizing Uncertainties." Prog. Energy Combust. Sci 23: 23.
- [105] Xu, T. H. and C. Tropea (1994). "Improving the performance of two-component phase Doppler anemometers." Meas. Sc. Technology 5: 7.
- [106] Schneider, B. (1999 - 2011). PDA Grapher (Software for PDA Data analysis). Zürich, Switzerland.
- [107] Herrmann, K., von Rotz B., Schulz R., Weisser G., Boulouchos K., and Schneider B., ILASS-Europe 2010, Brno, Czech Republic, 2010
- [108] Kistler 7061BK, (<http://www.kistler.com/mediaaccess/000-052m-08.98.pdf>)
- [109] Coura, T., Salles, L. P., "Quantum-efficiency enhancement of CMOS photodiodes by deliberate violation of design rules", Sensors and Actuators A 171 (2011) 109-117
- [110] Schneider, B. (1999 - 2012). PCOPictures (Software for Image Processing). Illnau, Switzerland.
- [111] Carlucci, P., A. Ficarella, et al. (2005). "Effects on combustion and emissions of early and pilot fuel injections in Diesel engines." International Journal of Engine Research 6.
- [112] Badami, M., Mallamo, F. et al. (2003). "Experimental investigation on the effect of multiple injection strategies on emissions, noise and brake specific fuel consumption of an automotive direct injection common-rail Diesel engine" International Journal of Engine Research 4: 15.
- [113] Mancaruso, E., Merola, S. S. et al. (2008). "Study of the multi-injection combustion process in a transparent direct injection common rail Diesel engine by means of optical techniques." International Journal of Engine Research 9(6): 15.
- [114] Achleitner, E., S. Berger, et al. (2004). "Benzin-Direkteinspritzsystem mit Piezo-Injektor für strahlgeführte Brennverfahren." MTZ: 11.
- [115] Strehlow, R.A., „Fundamentals of Combustion“, International Textbook: Scranton (1968)

- [116] Heywood, J.B., „Internal Combustion Engine Fundamentals“, McGraw-Hill Book Company, 1988
- [117] Cham, J. „<http://www.phdcomics.com/comics/archive.php?comid=848>”
- [118] Hargrave, G. K, Wigley, G., Allen, J. and Bacon, A. “Optical Diagnostics and Direct Injection of Liquid Fuel Sprays”, *Journal of Visualization*, Vol. 2, Nos. 3/4 (2000) 293-300

## 7 Appendix

### 7.1 Fuel properties

Property	Unit	Gasoline	Isooctane
Density (@15°C)	[kg/m <sup>3</sup> ]	732.1	692.2
Vapour pressure (@37.8°C)	[kPa]	84.4	15.1
Boiling start temperatur	[°C]	33	99.2
Boiling end temperatur	[°C]	192	99.2
RON	[-]	95.2	100
Carbon	[% of mass]	86.48	84.21
Hydrogen	[% of mass]	13.7	15.79
Heating value	[MJ/kg]	42.98	43.95
Viscosity	[cSt]	0.46	0.4661
surface tension	[mN/m]		18.2(303.15K)
refractive index (@25°C)	[-]	1.426	1.38898
Heat of evaporation	[kJ/kg]		300.2
Stoichiometric air to fuel ratio	[-]	14.2	15.09

Table 4 – Comparison of fuel properties for gasoline and isooctane

### 7.2 Injection rates and needle lifts

With an injection rate analyser from IAV, the flow rate through the A-injector has been measured for different needle lifts and rail pressures. To visualise the reproducibility of the injection rate, the average over 500 injections for the reference case have been plotted in Figure 7-1 with the standard deviation.

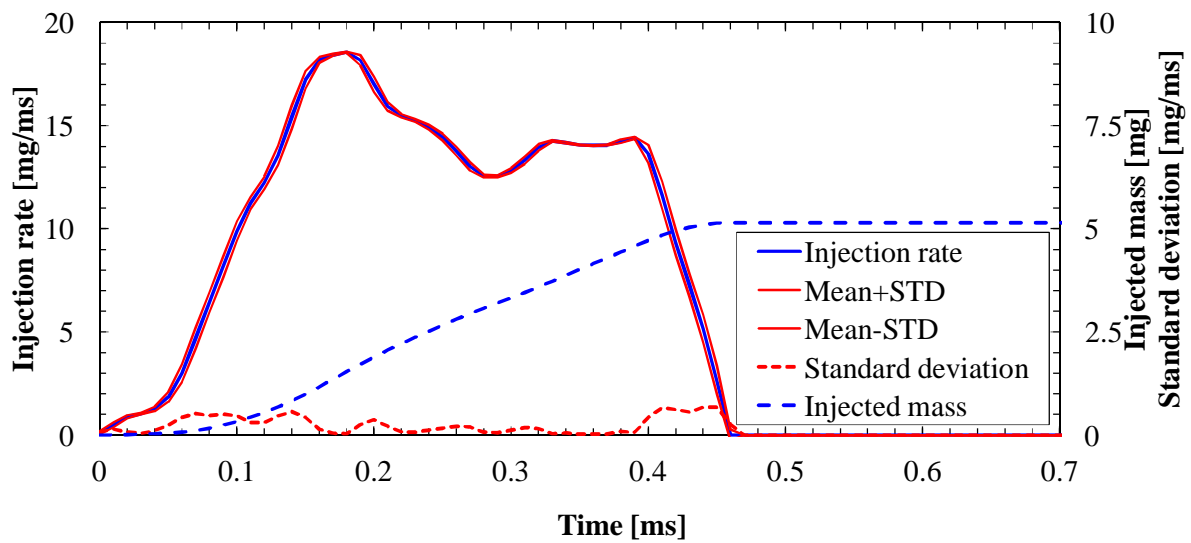


Figure 7-1 – Injection rate for the reference case ( $p_{inj} = 12 \text{ MPa}$ ,  $\varepsilon = 23 \text{ }\mu\text{m}$ , isooctane)

The injection curves for the applied needle lifts and injection pressures have been plotted in Figure 7-2.

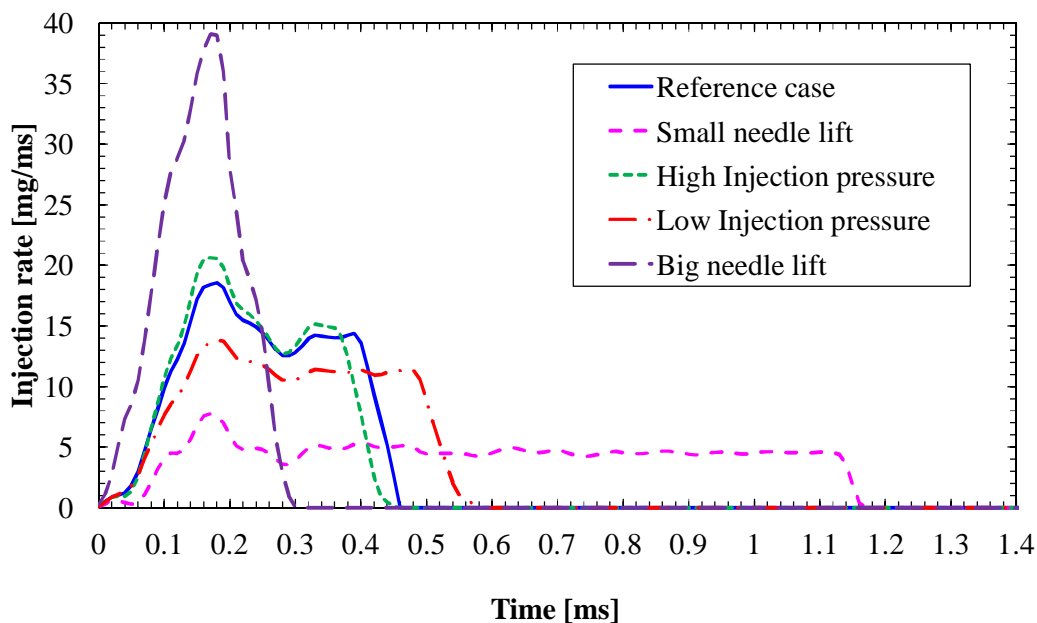
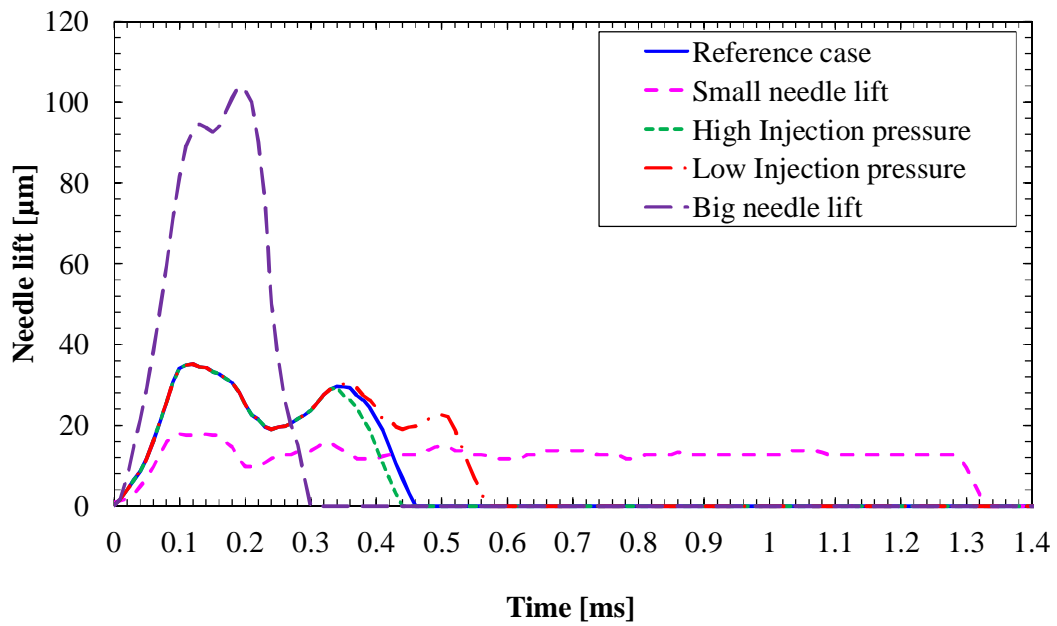
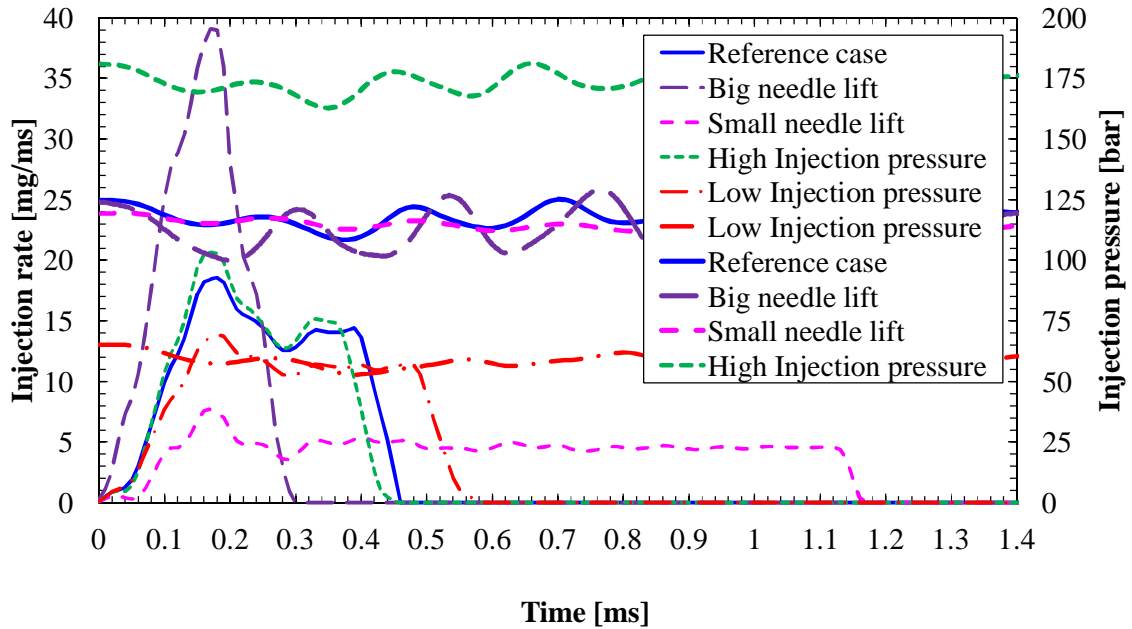


Figure 7-2 – Injection rates for different measurement points. Total injected mass 5mg. With a microscope and a high speed camera the needle lift was measured under dry conditions (the injector was not pressurized and empty – dry – inside). The results of this needle lift measurements are shown in Figure 7-3.



**Figure 7-3 – Needle lift for the different measured points. Total injected mass for each case is 5mg.**



**Figure 7-4 – Injection rate with rail pressure.**

Name	Charge	Current shape	Opening duration	Closing duration	Rail pressure
[-]	[mC]	[-]	[ms]	[ms]	[MPa]
Reference case	0.5	Rectangular	0.1	0.1	Backpressure + 12MPa
Big Needle Lift	1.1	Rectangular	0.1	0.1	Backpressure + 12MPa
Small Needle Lift	0.35	Rectangular	0.1	0.1	Backpressure + 12MPa
High Injection Pressure	0.5	Rectangular	0.1	0.1	Backpressure + 18MPa
Low Injection Pressure	0.5	Rectangular	0.1	0.1	Backpressure + 6MPa

Table 5 – Setting parameters for the Direct Injection Control Unit (DICU) and pressure system

### 7.3 Distortion of Shadowgraphy images

An eye catching detail is the wall where the injector is mounted. The wall seems to bend into the combustion chamber. This is a result of the temperature differences along the wall. The heated wall reaches temperatures of about

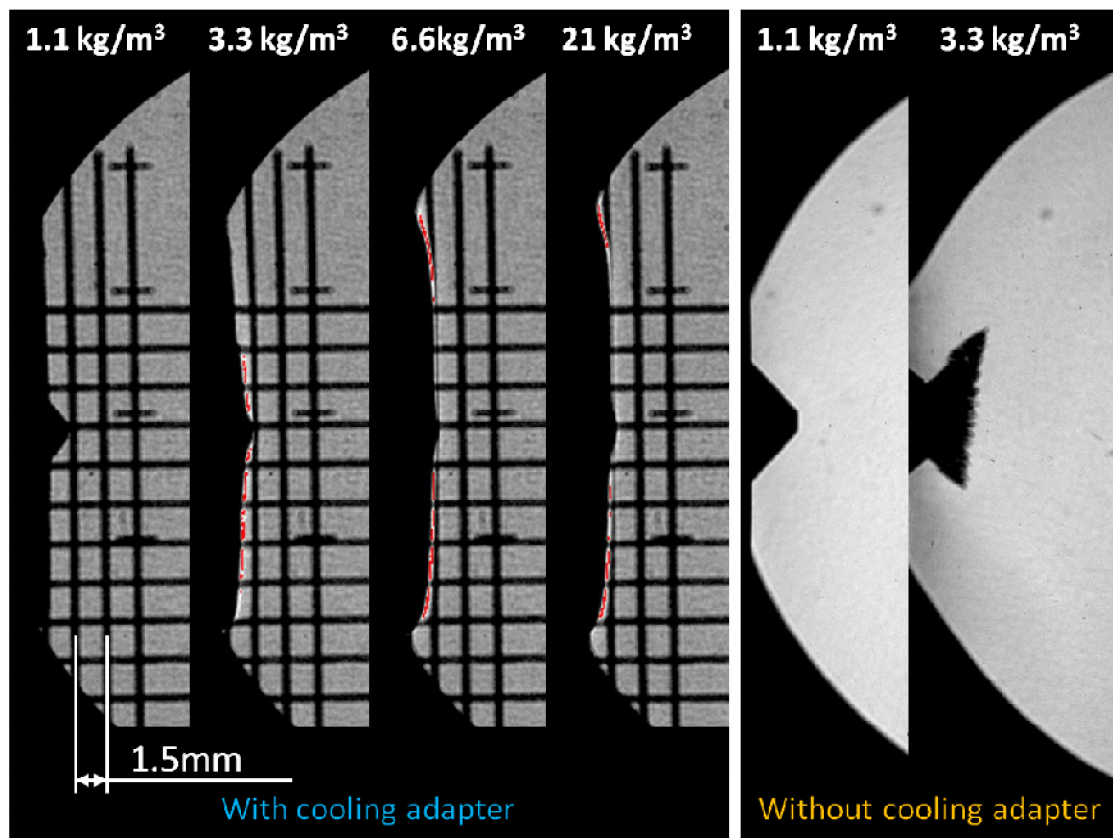


Figure 7-5 – Visualisation of the distortion due to cooled surface (left) and hot surface (right)

650 K, whereas the cooled injector reaches temperatures not higher than 350 K.

This temperature gradient generates a boundary layer with increased density towards the injector cooler and the injector tip. As the Schlieren and Shadowgraphy methods are sensitive to such density gradients the former parallel light rays are bent into the wall, giving the impression that the wall would be bent outwards and the injector tip was swallowed by the wall. The effect was more present towards higher gas pressure. The influence on the spray measurement is very small: Just the regions very close to the wall are effected (compare Figure 7-5); in fact only the first image of spray penetration is distorted by the phenomena.

## 7.4 PDA settings

<b>Laser Transmission System</b>	Axial	Radial	<b>Receiver</b>	
Wavelength [nm]	<b>514.5</b>	<b>488</b>	Phase Factor U1-U3 [ $^{\circ}/\mu\text{m}$ ]	<b>2.621</b>
Beam Power [mW]	<b>200</b>	<b>100</b>	Max. Drop Size Range [ $\mu\text{m}$ ]	<b>99.2</b>
Beam Diameter [mm]	<b>5</b>		Lens Focal Length [mm]	<b>310</b>
Beam Separation [mm]	<b>50</b>		Lens Aperture [mm]	<b>80</b>
Polarization Plane [-]	<b>Parallel</b>		Scattering Angle [ $^{\circ}$ ]	<b>70</b>
Front Lens Focal Length [mm]	<b>300</b>		Refractive Index	<b>1.47</b>
Measurement Volume - Diameter [ $\mu\text{m}$ ]	<b>39</b>	<b>37</b>	Aperture Size	<b>0.5</b>
Fringe Spacing [ $\mu\text{m}$ ]	<b>3.1</b>	<b>2.9</b>	<b>Processor</b>	
Velocity Measurement Range [m/s]	<b>-30.9 to 108.4</b>		Bandwidth [MHz]	<b>45</b>

**Table 6 – Setting parameters for the PDA system**





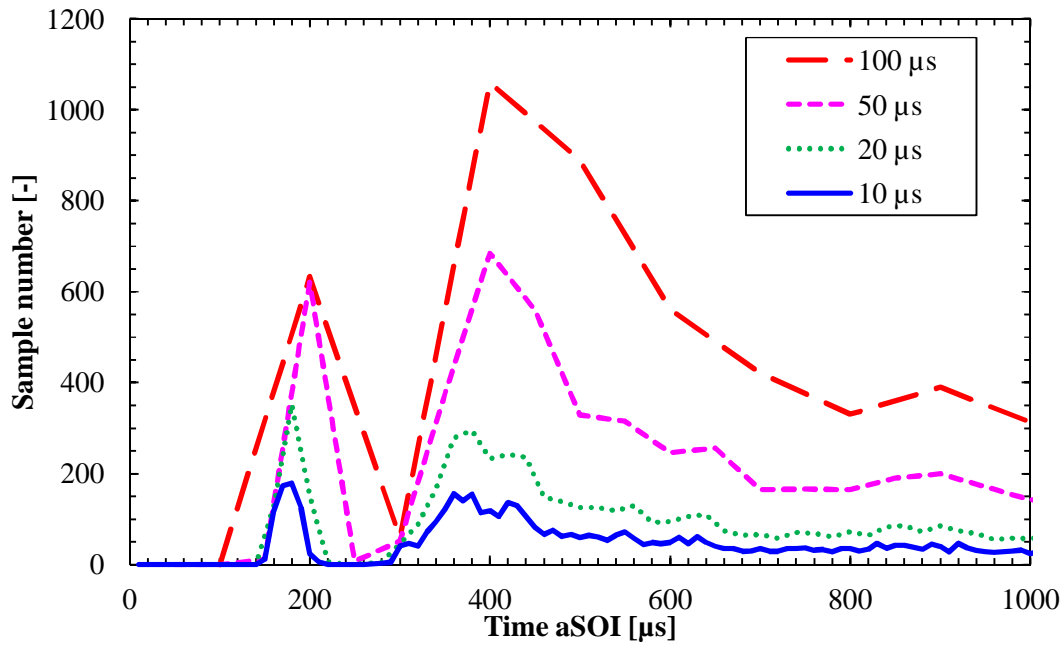


**Figure 7-6 – Sample number for different time bin lengths, plotted over time (Reference case: 23 μm needle lift; 12 MPa injection pressure; z = 5 mm; r = 7mm)**

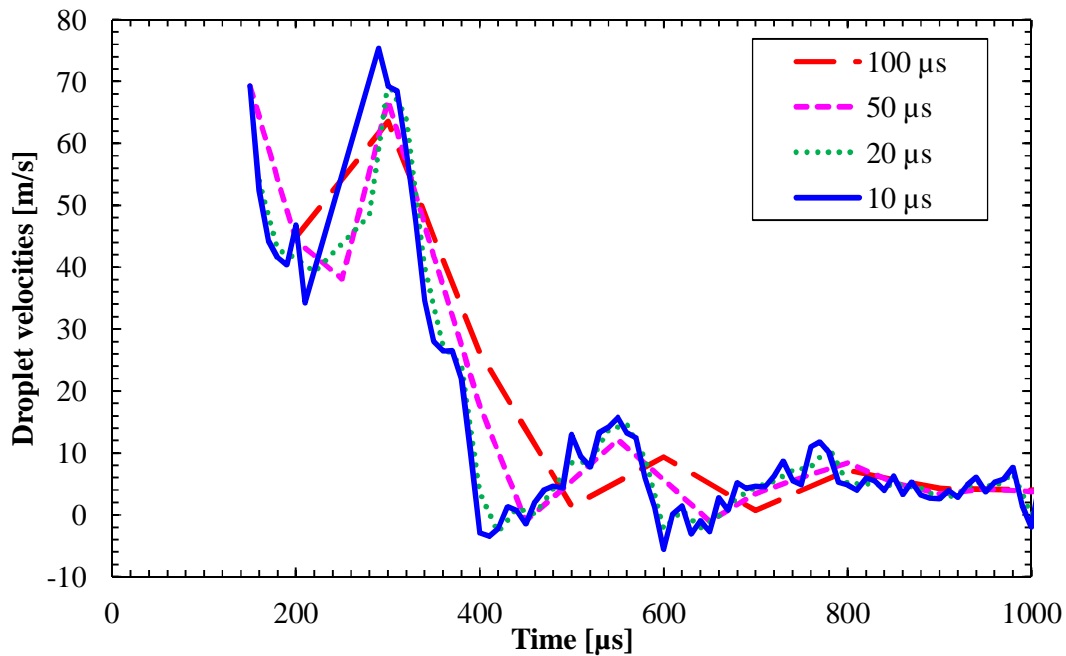


**Figure 7-7 – Axial velocity for different time bin lengths, plotted over time (Reference case: 23 μm needle lift; 12 MPa injection pressure; z = 5 mm; r = 7mm)**

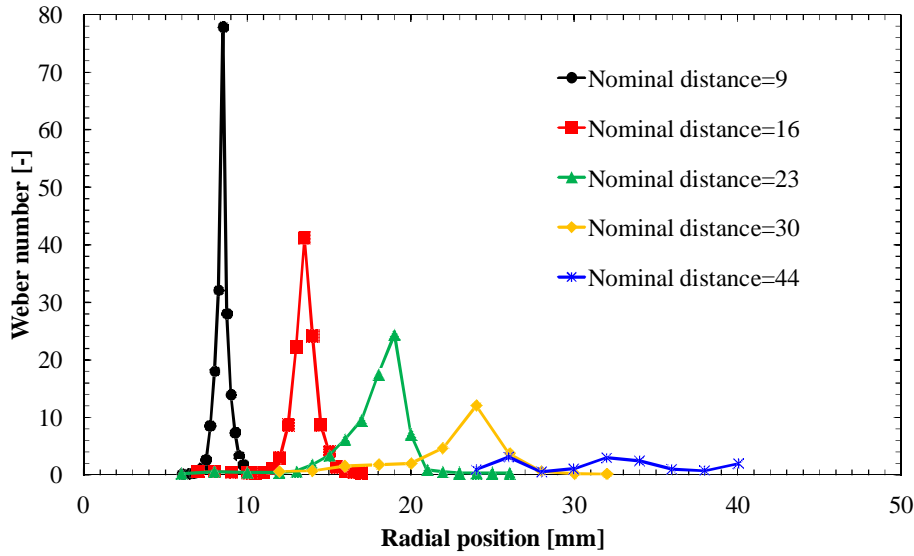


Figure 7-8 – Weber number along spray axis

Figure 7-9 shows the dependency of the initial droplet diameter  $d_h$  and the droplet decay exponent on density. Even though a physical correlation is not visible in case of the initial drop size, the droplet decay exponent nicely grows with increasing gas density what could be expected. Figure 7-10 shows the dependency of  $\tau$  and  $d_h$  on injection pressure. Here a clear trend is visible:

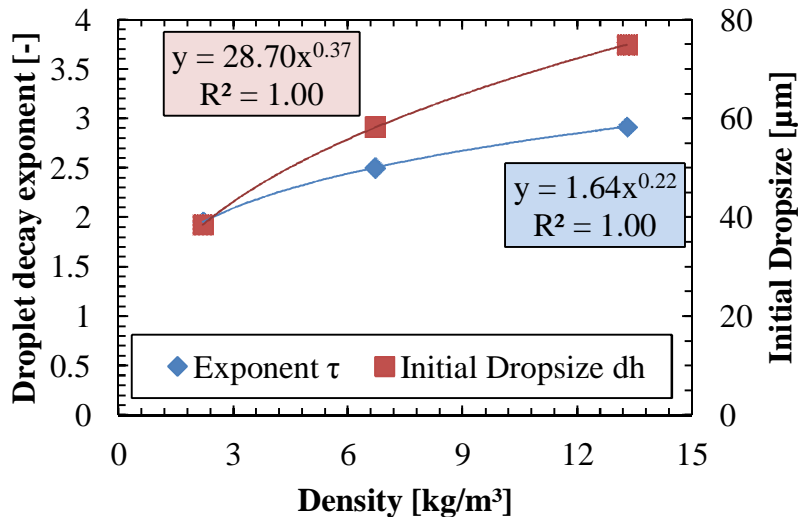
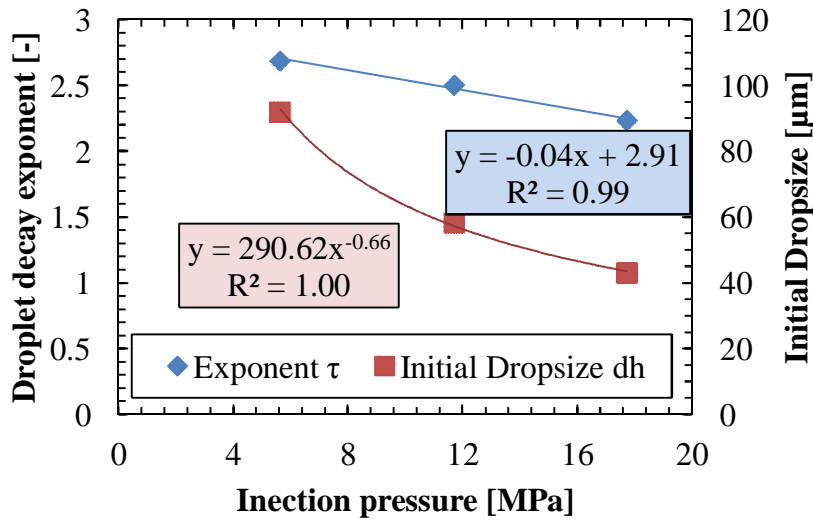


Figure 7-9 – Dependency of droplet decay exponent  $\tau$  and initial droplet diameter  $d_h$  on density

Increasing injection pressure results in higher relative velocity between the exiting liquid and the surrounding gas phase. Therefore the droplets are faster



**Figure 7-10 – Dependency of droplet decay exponent  $\tau$  and initial droplet diameter  $d_h$  on injection pressure**

broken up and decay into smaller droplets, therefore the initial drop size declines. The linear trend of the decay exponent on the other hand is not yet fully understood.

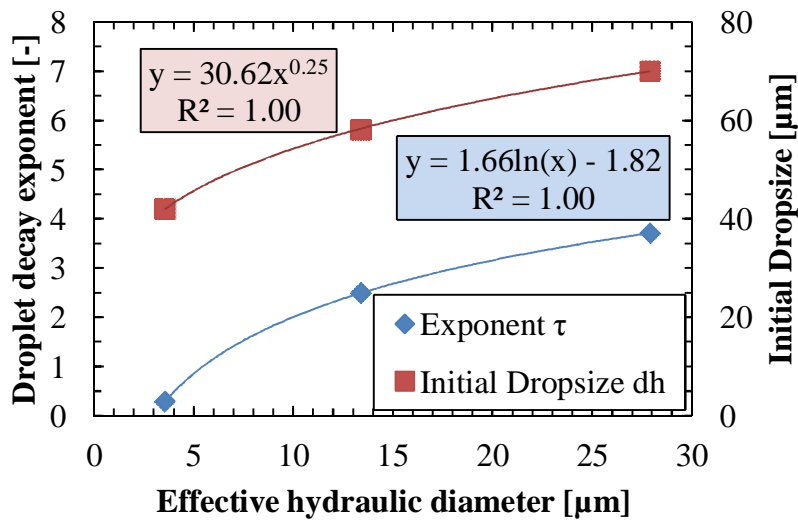


**Figure 7-11 – Dependency of droplet decay exponent  $\tau$  and initial droplet diameter  $d_h$  on effective hydraulic diameter**

The dependency on needle lift could not be found as such. But  $\tau$  and  $d^*$  showed a dependency on the effective hydraulic diameter, which was defined in this work as the hydraulic diameter multiplied with the discharge coefficient  $C_d$ .

---

## 7.5 List of publications

### Peer reviewed articles

### Conferences with proceedings

1. Andreas Schmid, Christian Lämmle, Yuri Martin Wright, Konstantinos Boulouchos , “*Sprayuntersuchungen in einer Hochtemperatur-Hochdruckzelle*” Presentation and Conference paper, 6. Tagung “Diesel- und Benzindirekteinspritzung“, Berlin (D)
2. Andreas Schmid, Bruno Schneider, Konstantinos Boulouchos, Graham Wigley and Mehdi Mojitabi, „*Experimental investigation on the spray behaviour for a hollow cone piezo injector with a multiple injection strategy*“, Presentation and Conference paper ILASS 2010, Brno (CZ)
3. Andreas Schmid, Beat von Rotz, Rolf Bombach, German Weisser, Kai Herrmann and Konstantinos Boulouchos “*Investigation of Marine Diesel Ignition and Combustion at Engine-Like Conditions by means of OH\* Chemiluminescence and Soot Incandescence*”, COMODIA Conference 2012, Fukuoka, Japan

### Journal publications

1. Andreas Schmid, Bruno Schneider, Konstantinos Boulouchos and Graham Wigley „*Experimental investigations on a piezo activated hollow cone injector - Part I: Measurement of needle lift and its influence on spray morphology*“, submitted to *Atomization and Sprays*
2. Andreas Schmid, Bruno Schneider, Konstantinos Boulouchos and Graham Wigley „*Experimental investigations on a piezo activated hollow cone injector - Part II: The influence of needle lift on droplet size distributions and vortex formation*“, submitted to *Atomization and Sprays*

## **7.6 Curriculum vitae**

### **PERSONAL DATA**

Name:	Andreas Manuel Schmid
Date of birth:	21 <sup>st</sup> April 1979
Place of birth:	Brig, Switzerland
Bürgerort	
Place of citizenship:	Raron and Ausserberg, Switzerland
Place of residence:	Raron, Switzerland
Nationality:	Swiss Citizen

### **EDUCATION**

2007 – present	PhD studies, research scientist and teaching assistant at the Aerothermochemistry and Combustion Systems Laboratory of Prof. Dr. K. Boulouchos, Swiss Federal Institute of Technology (Eidgenössische Technische Hochschule ETH) Zürich, Switzerland
2001 – 2006	Diploma in Mechanical Engineering Swiss Federal Institute of Technology (Eidgenössische Technische Hochschule ETH) Zürich, Switzerland Specialisation: - Internal Combustion Engines - Biomedical Engineering
1995 –2001	High school with matriculation in math and science subjects Matura, mathematisch-naturwissenschaftlicher Typus General qualification for university entrance Kollegium “Spiritus Sanctus” Brig, Switzerland
1993 – 1995	Secondary education (Sekundarschule) Raron/ VS, Switzerland
1987 – 1993	Primary education (Primarschule) Raron/ VS, Switzerland

### **WORK EXPERIENCE**

2011 – present	Wärtsilä Switzerland Ltd. Spray and Combustion Research Scientist
----------------	--